Investigation on Intramolecular Charge Transfer in π-Conjugated Donor and Acceptor Ensembles

Inaugural dissertation

of the Faculty of Science,

University of Bern

presented by

Ping, Zhou (周 萍)

from China

Supervisor of the doctoral thesis:

PD Dr. Shi-Xia Liu

Prof. Dr. Robert Häner

The Department of Chemistry, Biochemistry and Pharmaceutical Sciences

Investigation on Intramolecular Charge Transfer in π-Conjugated Donor and Acceptor Ensembles

Inaugural dissertation
of the Faculty of Science,
University of Bern

presented by

Ping, Zhou (周 萍)

from China

Supervisor of the doctoral thesis:
PD Dr. Shi-Xia Liu
Prof. Dr. Robert Häner

The Department of Chemistry, Biochemistry and Pharmaceutical Sciences

Accepted by the Faculty of Science.

Bern, 20.09.2022

The Dean
Prof. Dr. Marco Herwegh

Acknowledgements

After four years of my study, I would like to thank many important people who sincerely supported and helped me.

First of all, I thank PD Dr. Shi-Xia Liu and Prof. Robert Häner for giving me this opportunity to work on such nice projects for my PhD study. I have always enjoyed working in their laboratory for the past four years. I appreciate their support, patience and kindness. I also thank Prof. Thomas Feurer, the chairman of my PhD examination, for his great help with ultrafast transient absorption spectroscopy measurements.

I would like to thank Prof. Dirk Michael Guldi (Friedrich-Alexander-Universität Erlangen-Nürnberg) for acting as an external referee and also for the successful collaboration during the project on the investigation of the electronic coupling between fused donor-acceptor conjugates and nanographene.

I would also like to thank Prof. Silvio Decurtins who encourages me all the time.

Many thanks to my colleagues and all the staff members of the department who always liked to help me when I needed them. Especially, I would like to thank Dr. Oleh Vybornyi and Dr. Henrik Peters for their kind suggestions about synthetic methodologies.

A big thank to all collaborators: Prof. Ernst Meyer (University of Basel), Prof. Roman Fasel (Empa), Prof. Wenjing Hong (Xiamen University), Prof. Colin Lambert (Lancaster University), Prof. Ulrich Aschauer (Bern University), Prof. Andrea Cannizzo (Bern University), Dr. Hans-Martin Frey (Bern University) and Dr. Chuancheng Jia.

Last, I would like to thank my family for supporting and accompanying me during my PhD studies and my friends for enriching my life.

Table of Contents

Abstract **1**

Abbreviations **6**

1. General introduction **8**

1.1 Donor-acceptor ensembles 9

1.1.1 Tetrathiafulvalene (TTF) chemistry 9

1.1.2 Tetraazapyrene (TAP) derivatives 14

1.1.3 Azulene derivatives 17

1.1.4 Paracyclophane (PCP) derivatives 26

1.2 Molecular electronics 34

1.3 Aim of the work 38

2. Chemically controlled charge flow in a compact TTF-fused dipyrrolylquinoxaline difluoroborate (QB) **41**

2.1 Article 43

3. TAP-based donor-acceptor (D-A) systems **48**

3.1 Electronic communication 50

3.1.1 Article 50

3.2 Modulate lifetime of charge separation state 55

3.2.1 Introduction 55

3.2.2 Results and discussion 56

3.2.3 Conclusions and outlook 66

3.2.4 Experimental section 66

4. π-Extended perylene diimide (PDI)-based D-A conjugates **70**

4.1 TTF-fused PDI 72

4.1.1 Article 72

4.2 Azulene-PDI triads 78

4.2.1 Introduction 78

4.2.2 Results and discussion 78

4.2.3 Conclusions and outlook 89
4.2.4 Experimental part 89
5. Through-space ICT in benzothiadiazole (BTD)-PCP-TTF conjugates 92
5.1 Introduction 93
5.2 Results and discussion 93
5.3 Conclusions and outlook 99
5.4 Experimental part 99
6. Molecular electronics 105
6.1 Atomically well-defined nitrogen doping in the cross-plane transport through graphene heterojunctions 107
6.1.1 Manuscript 107
6.1.2 Supporting information 124
6.2 Self-assembly and on-surface polymerization 138
6.2.1 Self-assembly of tetrabromotetraazapyrene (TBTP) on Ag(111) 138
6.2.2 Self-assembly of TBTP on superconducting Pb(111) 140
6.2.3 On-surface chemical reactions 142
Bibliography 162
Appendix 174
A.1 General methods 175
A.2 NMR and MS spectra 176

Abstract

π-Conjugated donor (D) and acceptor (A) ensembles have been widely investigated in the fields of (bio)chemistry, physics, medicine, materials chemistry and nanoscience because of their unique optical and electrochemical properties. Electronic interactions between D and A units have been widely explored for the development of advanced functional materials. Therefore, diverse π-conjugated ensembles containing different donors such as benzodifuran (BDF), tetrathiafulvalene (TTF), triphenylamine (TPA), and acceptors including 2,1,3-benzothiadiazole (BTD), perylene diimide (PDI), tetraazapyrene (TAP) and dipyrrolylquinoxaline (DPQ) have been investigated. It has been demonstrated that HOMO and LUMO energy levels and band gaps critically depend on the intrinsic electronic properties of D and A units as well as the nature of the linker between them. To optimize the electronic communication between D and A units for potential applications in molecular (opto)electronics, a variety of π-conjugated ensembles with different D-A architectures have been designed, synthesized, and characterized in this thesis. Importantly, efficient synthetic approaches to functionalize the TAP core *via* halogenation, hydrolysis, oxidation, and condensation have been developed, allowing the preparation of various kinds of TAP-based D-A molecules. Our keen interest in such π-conjugates has led us to comprehensively investigate the intramolecular charge-transfer (ICT) interactions through-bond or through-space between D and A moieties by UV-Vis-NIR spectroscopy, cyclic voltammetry (CV), transient absorption spectroscopy (TAS) and density functional theory (DFT) calculations. The thesis is organized as follows:

1. General introduction
2. Chemically controlled charge flow in a compact TTF-fused dipyrrolylquinoxaline difluoroborate (QB)
3. TAP-based donor-acceptor (D-A) systems
4. π-Extended perylene diimide (PDI)-based D-A conjugates
5. Through-space ICT in benzothiadiazole (BTD)-PCP-TTF conjugates
6. Molecular electronics

---

2. Chemically controlled charge flow in a compact TTF-fused dipyrrolylquinoxaline difluoroborate (QB)

In **section 2**, a new approach for a compact annulation of TTF and QB units has been developed, where strong electronic interactions occur between them. As depicted in **Chart 1**, the direction of ICT transitions changes upon the addition of fluoride or $NOSbF_6$. In the former case, an ICT occurs from the pyrrolylquinoxaline-fluoride adduct to the pyrrolylquinoxaline difluoroborate coordination pocket. In the latter case, the chemical oxidation of the TTF subunit to its radical cation $TTF^{\bullet+}$ leads to a reverse ICT from the QB to the TTF moiety. As a result, the direction of the photoinduced charge flow in this D-A system can be easily regulated, paving the way for manipulation of the photoinduced ICT by various chemical methods for potential applications in optoelectronic devices.

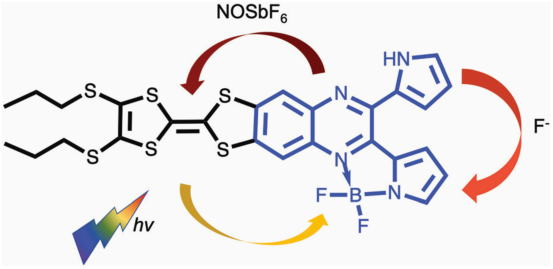

Chart 1 A schematic illustration of the ICT pathways in the TTF-QB dyad.

3. TAP-based donor-acceptor (D-A) systems

In **section 3**, TAP as an electron-deficient core was formed by an initial reduction of tetranitronaphthalene in the presence of tin and the subsequent cyclization with formic acid / pivalic anhydride. TAP was then brominated and sequentially functionalized with two TTF units by four bridging sulfur atoms, resulting in two different TAP based D-A triads. They differ in the substitution at 2- and 7-positions of the central TAP core (**Chart 2a**). Both only show weak intramolecular through-bond interactions between TTF and TAP units. The insertion of *tert*-butyl groups raises the TAP-localised LUMO level by 0.21 eV, in fairly good agreement with the 0.17 eV determined by DFT calculations. Our findings represent a novel concept for manipulating the relative HOMO and LUMO energetic positions of organic D-A ensembles through chemical modification. To enhance their electronic interactions, we have embarked on the preparation of fused TAP-TTF π-conjugates through Schiff base reaction of TAP-tetraone with TTF precursor and 4,5-diaminophthalonitrile (one example is given in **Chart 2b**). It turns out that the fusion of two TTF units with the TAP core leads to a long-lived charge separation (CS) state compared to the counterpart with only one TTF unit.

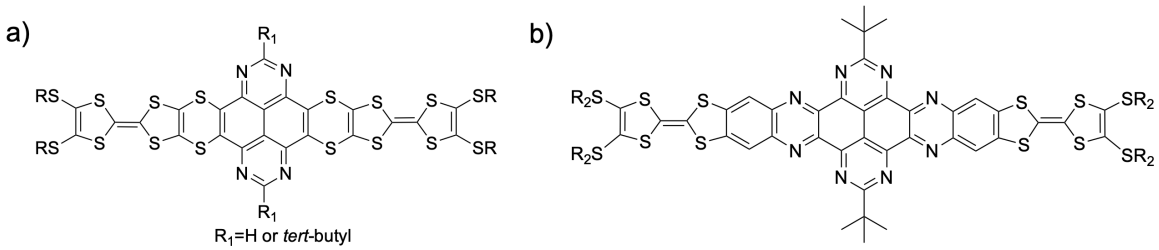

Chart 2 Chemical structures of TAP based D-A π-conjugates.

4. π-Extended perylene diimide (PDI)-based D-A conjugates

In **section 4.1**, it has shown that the annulation of TTF and PDI into a compact and planar π-conjugated system promotes ground-state and excited-state ICT. Due to a slight boat conformation of the TTF units and its coplanarity with the PDI core, this dyad can interact with pre-exfoliated nanographene (NG) forming a nanohybrid in situ. Coupling with NG has been found to occur preferentially through PDI rather than TTF, leading to the formation of the $PDI^{\bullet-}$ radical anion, which corresponds to p-doping of graphene (**Chart 3**).

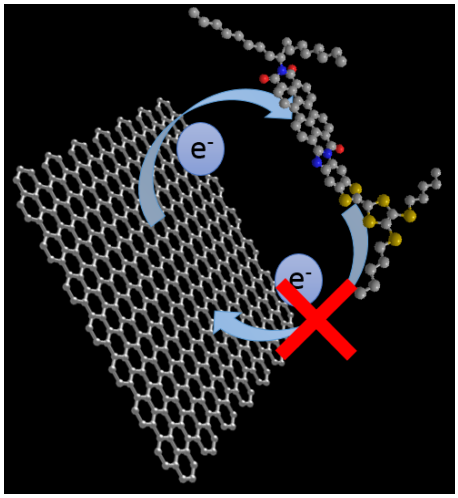

Chart 3 A schematic illustration of the interaction between TTF-fused PDI with NG.

In **section 4.2**, an electron donor, azulene, was incorporated as an alternative to TTF into a PDI core at 1- and 7-positions through either the carbon atom at 2- or 6-position of the azulene ring, leading to a series of azulene-PDI conjugates. Since azulene consists of an electron-rich five-membered ring and an electron-deficient seven-membered ring, the azulene-PDI systems exhibit a reversible colorimetric pH-response upon the addition of trifluoroacetic acid (TFA) and triethylamine (TEA), which renders them appealing for sensor development (**Chart 4**).

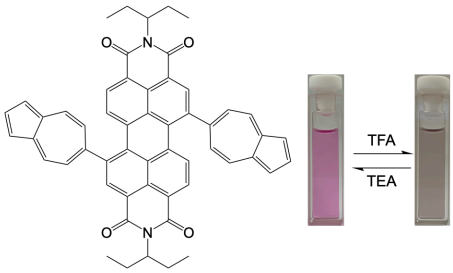

Chart 4 The pH-response of an azulene-PDI conjugate.

5. Through-space ICT in benzothiadiazole (BTD)-PCP-TTF conjugates

Not only ICT dynamics through-bond but also through-space plays a crucial role in the fabrication of high-performance organic electronics. In **section 5**, we describe D-A systems based on paracyclophane (PCP), in which TTF and BTD are connected either directly or through triple bonds to the 4- and 16-positions of the PCP core, respectively, (**Chart 5**). Their optical and electrochemical properties have been investigated. A mixture of a through-space ICT from the TTF to the BTD units and a through-bond ICT from the PCP to the BTD units probably occur, which is still under investigation by TAS measurements.

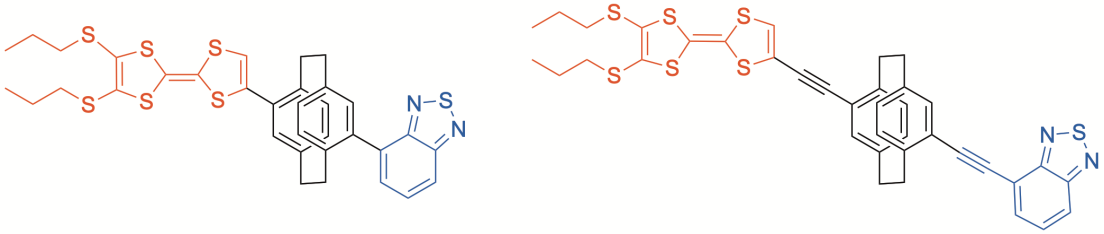

Chart 5 Chemical structures of PCP based D-A conjugates.

6. Molecular Electronics

Considering the unique properties of polycyclic aromatic hydrocarbons (PAHs) such as planarity, stability and easy halogenation, various building blocks (**Chart 6**) were synthesized. Atomically well-defined N-doping in cross-plane charge transport through graphene heterojunctions has been investigated, revealing the N-doping effects on their electrical conductance. The detailed information is discussed in **section 6.1**. Scanning tunneling spectroscopy (STS) on the self-assembled TBTP molecules on Ag(111) shows strong electron-vibrational coupling due to the Franck-Condon blockade effect. As the sample voltages are increased, nearly all the molecules show the feature of concentric rings, indicating that electron vibrations in TBTP are being coupled in the discharging stage. Besides, a fingerprint of a

charge-state switching from an anionic state $TBTP^{\bullet-}$ to a neutral state $TBTP^{0}$ is induced by the local electric field of the voltage applied to the tip on Pb(111). The polymerization of DBBA molecules on the superconducting Nb(110) substrate covered with thin Ag films has been performed, demonstrating the robust proximity-induced superconductivity on the Ag layer. Chemical reactions of Cu porphyrin on Au(111), including chlorine-induced hydrogen elimination and fusion of zigzag graphene nanoribbons have been explored.

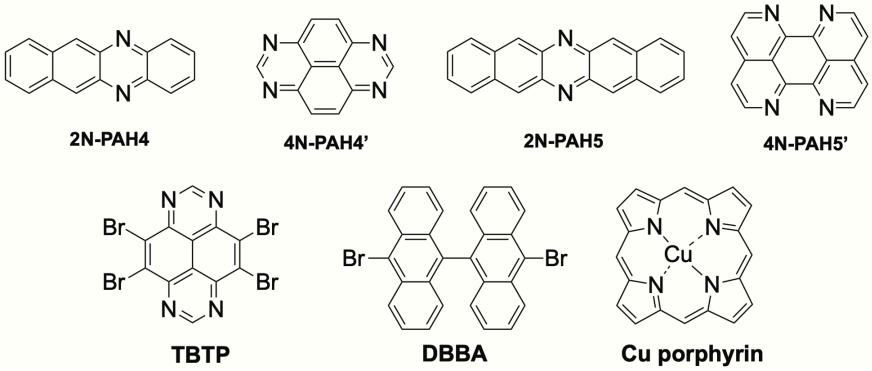

Chart 6 The chemical structures of the studied molecules.

Abbreviations

A	acceptor
AFM	atomic force microscopy
pin_2B_2	bis(pinacolato)diboron
BODIPY	boron dipyrromethene
$CHCl_3$	chloroform
CV	cyclic voltammetry
CT	charge transfer
D	donor
DCM	dichloromethane
DFT	density-functional theory
DTF	1,4-dithiafulvene
ESI-MS	electrospray ionization mass spectrometry
HOMO	highest occupied molecular orbital
HAT	hexaazatriphenylene
HRMS	high-resolution mass spectrometry
ICT	intramolecular charge transfer
LUMO	lowest unoccupied molecular orbital
ILCT	intra-ligand charge transfer
MALDI-TOF MS	matrix assisted laser desorption ionization-time of flight mass spectrometry
MLCT	metal-to-ligand charge transfer
NDI	1,4,5,8-naphthalene diimide
$NOSbF_6$	nitrosonium hexafluoroantimonate
OFET	organic field-effect transistor
PAHs	polycyclic aromatic hydrocarbons
PDI	perylene diimide
QB	dipyrrolylquinoxaline difluoroborate
STM-BJ	scanning tunnelling microscopy break junction
STS	Scanning tunneling spectroscopy
TAS	transient absorption spectroscopy
TAP	tetraazapyrene

$TBAF{\cdot}3H_2O$	tetrabutylammonium fluoride trihydrate
TEMPO	2,2,6,6-Tetramethylpiperidine-1-oxyl
TDI	tetracene diimide
THF	tetrahydrofuran
TFA	trifluoroacetic acid
TTF	tetrathiafulvalene
TVS	transition voltage spectroscopy
UPS	ultraviolet photoelectron spectroscopy
UHV	ultra-high vacuum
UV-Vis-NIR	ultraviolet-visible-near infrared

1. General introduction

1.1 Donor-acceptor ensembles

1.1.1 Tetrathiafulvalene (TTF) chemistry

Tetrathiafulvalene (TTF) is an effective π-electron-donating molecule that displays unique electrochemical behavior. Its characteristic feature is that it undergoes two reversible, single-electron oxidations at low potentials to form its radical cation ($TTF^{\bullet+}$) and dication (TTF^{2+}) species. The TTF core in its ground state is non-aromatic 14 π-electron system (2 for each sulfur atom and 1 for each sp^2 carbon atom) (**Figure 1a**) while the oxidation converts a ring to an aromatic 6 π-electron configuration. Interestingly, the TTF radical cation can form a mixed-valence state with its neutral species (**Figure 1b**).[1] TTF is stable in different chemical environments except in the presence of strong acids and oxidants. Thus, it is widely used as a building block in the formation of supramolecular assemblies and multifunctional materials for a multitude of applications in diverse fields such as chemsensors, conductors, switches, solar cells *et al*.[2]

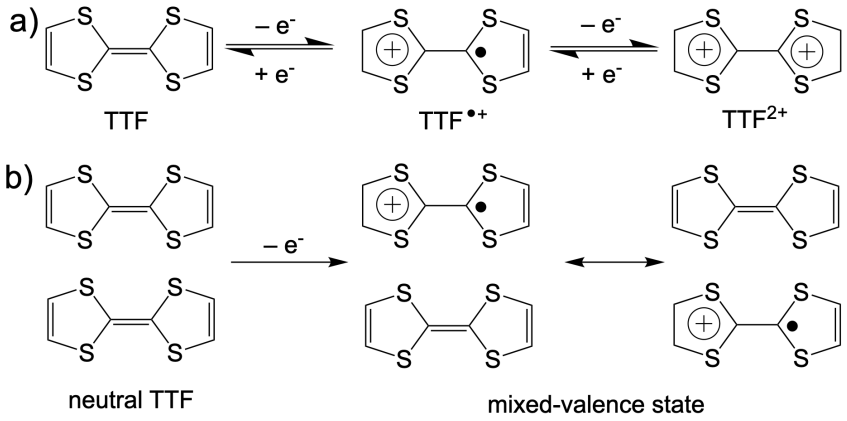

Figure 1 a) Reversible redox processes involving the neutral, radical cation and dication species, respectively. b) A mixed-valence state upon oxidation.

Before we start with the functionalization of TTF, we should mention the Schiff base reaction as one of the topics in carbonyl chemistry may need to mention. This reaction involves the condensation of an aldehyde or ketone with an aryl or aliphatic amine, catalyzed by an acid or base.

The amine acts as the nucleophile and attacks at the carbonyl carbon to give an unstable intermediate, called as carbinolamine, which then undergoes a dehydration to yield the imine or Schiff base.[3]

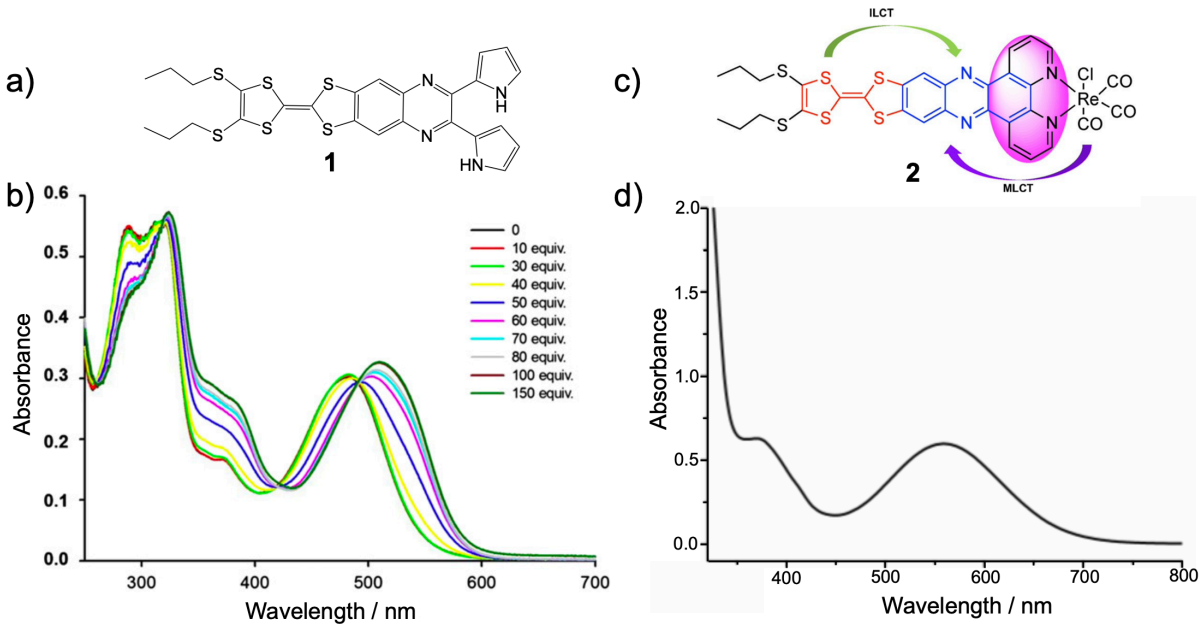

Figure 2 a) The TTF based sensor anion **1**. b) UV-Vis spectral changes of sensor **1** upon the addition of TBAF. c) The TTF based complex. d) The UV-Vis spectrum of complex **2** in DMF.

In this section, only TTF-fused D-A ensembles *via* Schiff base reactions are discussed. Our group and Langford *et al*. explored TTF-fused 2,3-di(1H-2-pyrrolyl)quinoxaline (DPQ) to form TTF-DPQ *via* the direct condensation reaction.[4, 5] As depicted in **Figure 2b**, TTF-DPQ shows exclusively selectivity to the fluoride anion as demonstrated by pronounced optical changes in the UV/Vis-absorption spectra upon the addition of TBAF (tetrabutylammonium fluoride). Recently, our group investigated a metal-to-ligand charge transfer (MLCT) and an intra-ligand charge transfer (ILCT) in the Re(I) complex (**2**) with a TTF based ligand (**Figure 2c**). The UV-Vis spectrum of this complex shows a strong and broad absorption band centred at 580 nm, which is attributed to a spin-allowed π-π* ILCT transition from the highest occupied molecular orbital (HOMO) localized on the electron donor TTF to the lowest unoccupied molecular orbital (LUMO) localized on the phenazine component. As expected, the MLCT transition peaks at 375 nm. Importantly, the ILCT transition is well separated from the MLCT transition (**Figure 2d**). An optical control of the direction of the photo-induced CT was confirmed, which is of high importance to develop an optoelectronic molecular switch that triggered by light of different wavelengths.

Also, our group synthesized TTF-fused hexaazatriphenylene (HAT, **3**) *via* Schiff base reaction of hexaketocyclohexane with the diamine-TTF precursor. The compound **3** undergoes three reversible reductions, which are assigned to the successive reduction of the electron deficient

HAT core. The six-electron oxidations of three TTF units are also observed. Moreover, it provides three potential metal binding sites, whereby transition metal ions can be chelated by nitrogen atoms.[6] Another example of the multiple uses of TTF units is **4** which comprises a nanosized fragment of graphene (coronene), largely extended by annulation with three π-electron donors. The intramolecular charge transfer (ICT) from the TTF units to the central core leads to the lowest energy absorption band at 750 nm.[7]

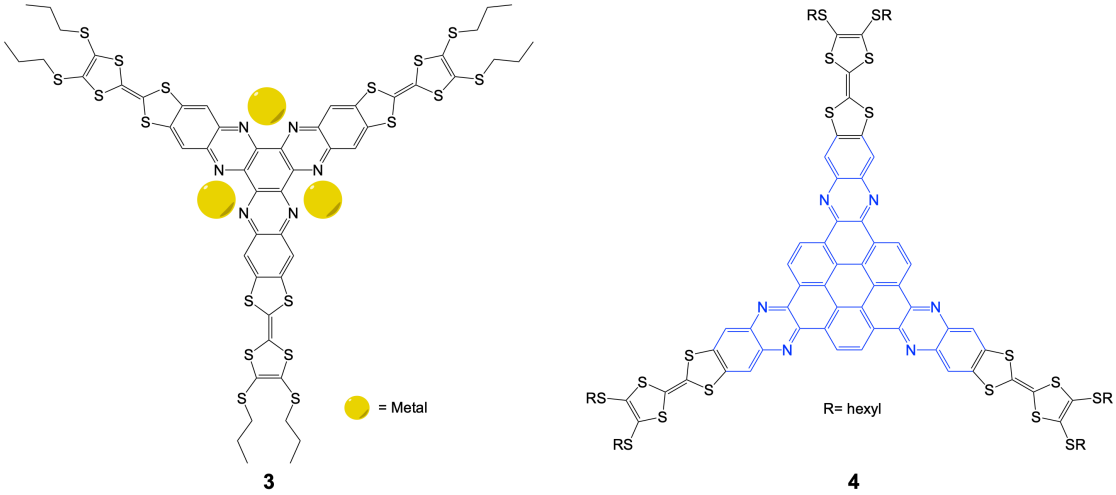

Figure 3 Star-shaped TTF fused D-A compounds.

Apart from the introduction of TTF units at the periphery of the π-conjugated core, a TTF unit can also be used as a bridge between two nanographene units as shown in **Figure 4**. The compound **5** displays multiple light-induced ICT processes between spatially separated electron-rich (red and purple) and electron-deficient (blue) fragments within this extended system.

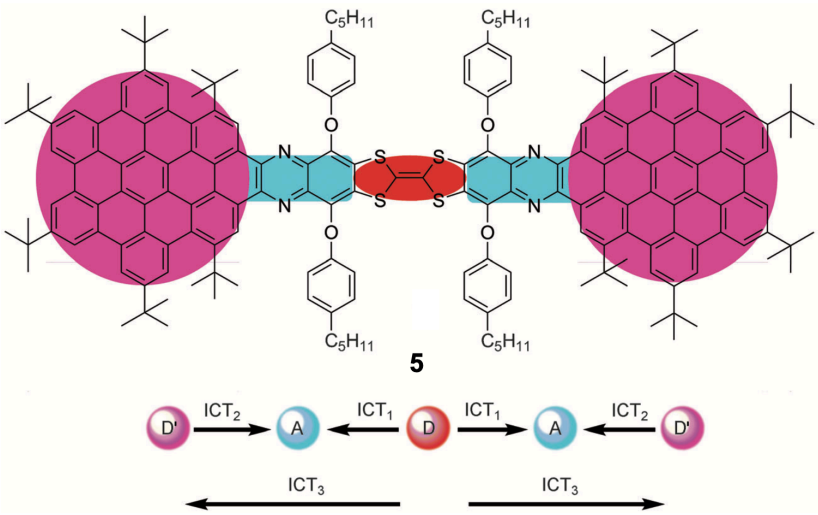

Figure 4 Chemical structure of compound **5** with the multiple ICT transitions.

Among electron acceptors, diimide chromophores have attracted much attention due to their excellent thermal and optical stabilities, high molar absorption coefficient, reversible redox properties, and feasible derivatization chemistry.[8, 9] For example, 1,4,5,8-naphthalene diimide (NDI) and its derivatives have been intensively investigated for n-type semiconductors. As shown in **Figure 5**, two TTF units are incorporated to the NDI core (**6**). The appearance of a new absorption around 780 nm indicates the electronic interactions between the TTF and NDI moieties. Calculations based on density functional theory (DFT) confirm that the NDI core and the four bridging sulfur atoms are almost co-planar while the TTF moieties are not co-planar with the NDI core, forming dihedral angles of 135 °C. The HOMO orbital is localized on the TTF moieties while the LUMO orbital is mainly on the NDI core. Cyclic voltammetric and absorption spectral studies reveal that electronic communication between two TTF units and NDI core through the sulfur bridges leads to a narrow band gap of ca. 0.9 eV.[10]

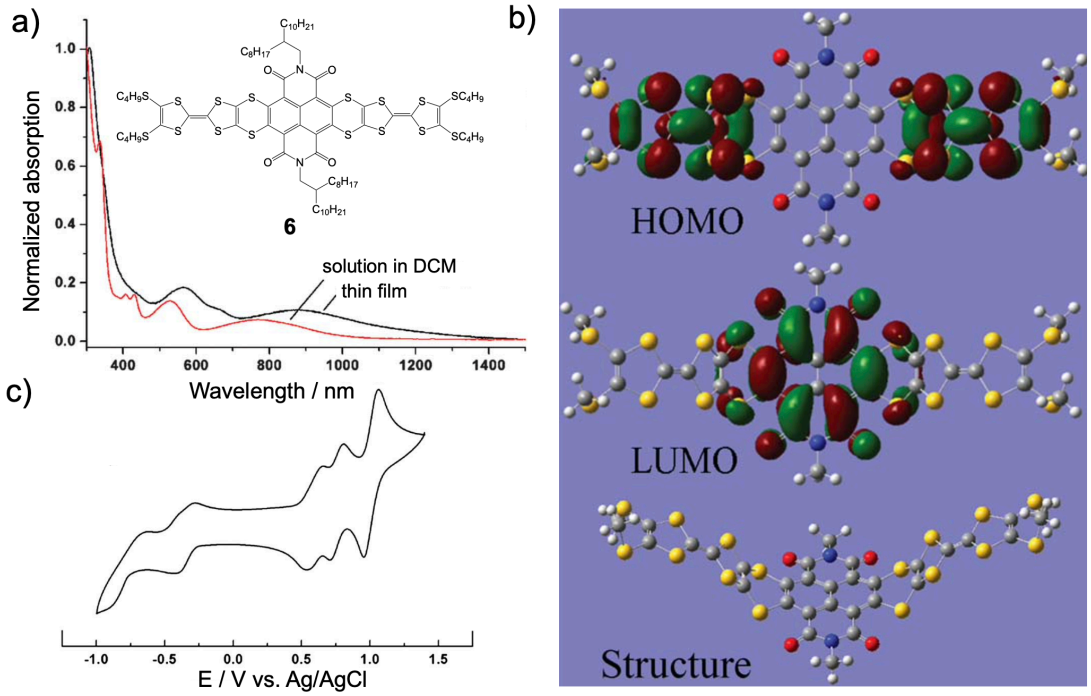

Figure 5 UV-Vis-NIR spectra (in solution and thin film) and cyclic voltammogram of a TTF-NDI triad together with the frontier molecular orbitals and the optimized structure.

With respect to NDI, perylene diimide (PDI) has a large π-conjugated backbone leading to n-type semi-conductivity, high thermo- and chemical stability, and superior photophysical properties. A rich derivatization chemistry at the bay (1,6,7,12) and ortho (2,5,8,11) positions has been explored (**Figure 6**).

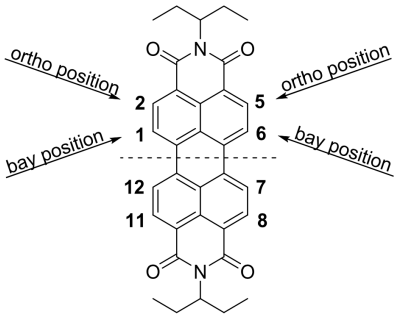

Figure 6 Chemical structure of a PDI chromophore.

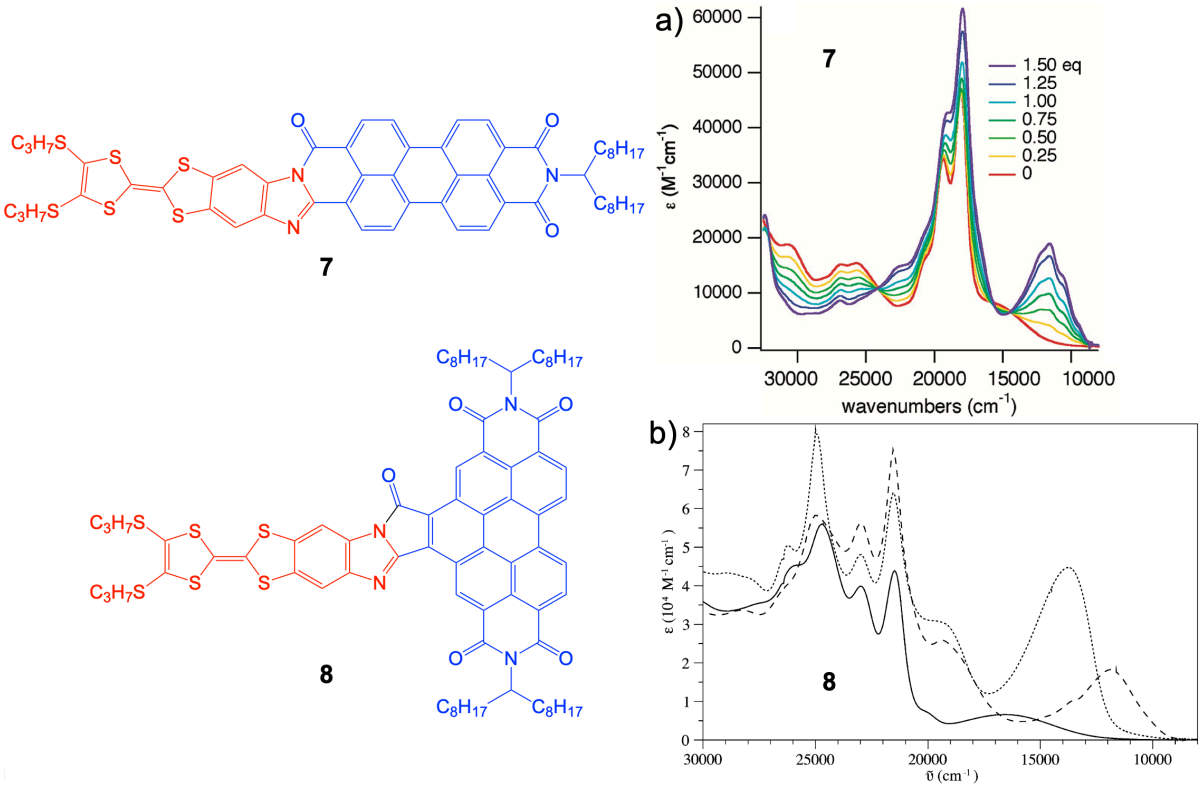

Figure 7 TTF fused-PDI at imide site (**7**) and bay position (**8**). a) Absorption spectra of **7** upon oxidation with different equivalents of $[Fe(bpy)_3](PF_6)_3$ in DCM. b) Absorption spectra of **8** (solid), $\mathbf{8}^{\bullet+}$ (dashed), and $\mathbf{8}^{2+}$ (dotted) in DCM (oxidizing agent: $[Fe(bpy)_3](PF_6)_3$).

Instead of connecting of D and A by flexible or rigid σ-spacers (D-σ-A) which keep the moieties apart from each other, TTF-fused PDI dyads (**7** and **8** in **Figure 7**) were synthesized. By comparison with the electronic spectra of **TTF** and **PDI** precursors, a new electronic transition is observed in **7** that is attributed to an intramolecular π-π* CT transition from the TTF unit to the PDI core. The positively-shifted oxidation and negatively-shifted reduction processes conform to the sizable electronic interactions between TTF and PDI units.[11] As depicted in **Figure 7a**, the spectral evolution of **7** upon chemical oxidation by $[Fe(bpy)_3](PF_6)_3$ clearly indicates the $TTF^{\bullet+}$ radical bands appeared at 830 nm and 430 nm. In addition, **7** has

successfully been used as a solution-processed active material for light sensitive field-effect transistors with balanced hole and electron mobilities.[12] In contrast to a fusion to the imide site, a direct annulation of TTF to the bay region of the PDI core (**8**) results in a strong ICT from the TTF to the PDI moieties which is well-separated from the π-π* transitions localized on the PDI unit (**Figure 7b**). Upon addition of $[Fe(bpy)_3](PF_6)_3$, the lowest-energy ICT absorption decreases with the appearance of a new band at 840 nm, corresponding to a combination of $TTF^{\bullet+}$ and back ICT from PDI to $TTF^{\bullet+}$. Further oxidation leads to the formation of the $\mathbf{8}^{2+}$ species as confirmed by the appearance of a new absorption at 730 nm at the expense of the band at 840 nm for $\mathbf{8}^{\bullet+}$.[13]

Inspired by electronic interactions between TTF and PDI units in such planar π-extended conjugates, application of **7** with long alkyl chains in exfoliation of graphite leading to the formation of nanographene (NG)-TTF–PDI hybrid material has been explored in collaboration with Prof. Guldi. A detailed investigation of CT will be discussed in **section 4.1**.

1.1.2 Tetraazapyrene (TAP) derivatives

1,3,6,8-Tetraazapyrene (TAP), a heteroaromatic compound including four nitrogen atoms, is an electron acceptor which displays n-type semiconducting behavior with unique optoelectronic and electrochemical properties. By functionalizing the TAP at 2-,7-positions or at the aromatic core, its electronic properties can be changed easily, which paves the way for its diverse applications in the field of organic (opto)electronics.[14-18] TAP was first reported by Roos and Dimroth in1927 and developed by Gerson and Marvel's groups until 1964 when they successfully synthesized 2,7-dimethyl- and 2,7-diphenyl-1,4,6,8-tetraazapyrene derivatives and explored the relative radical anion properties.[19-21] Initially, the synthetic approach to TAP involves the reduction of tetranitronaphthalene in a solution of hydrogen chloride in the presence of tin powder or stannous chloride followed by cyclo-condensation under formic acid and oxidation under air.[14, 22, 23] Later on, different approaches have been reported (**Figure 8**). Notably, all these methods rely on an oxidation step. Especially, Rubin and co-workers developed a protocol based on 1*H*-perimidine-6,7-diamines or naphthaene-1,4,5,8-tetraamine with nitroalkanes to get different TAP derivatives in good yields, in which nitroalkane may play a dual role, serving both as an electrophilic reagent in cyclization and as an oxidant (method **b** and **e**).[24]

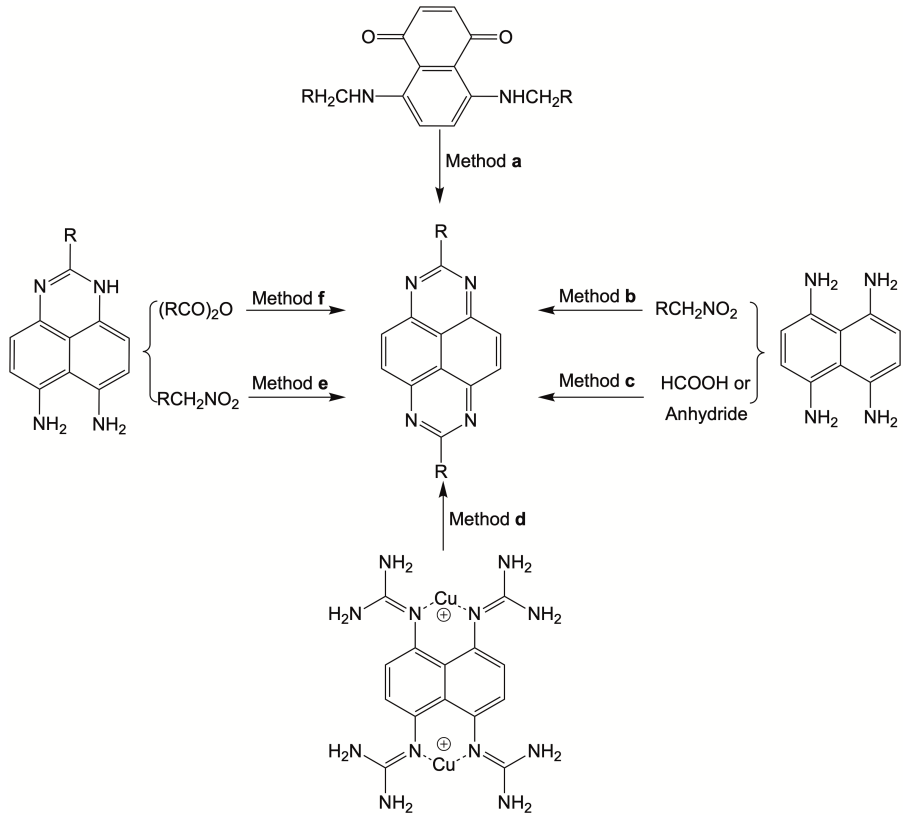

Figure 8 The different synthetic approaches to obtain TAP derivatives.

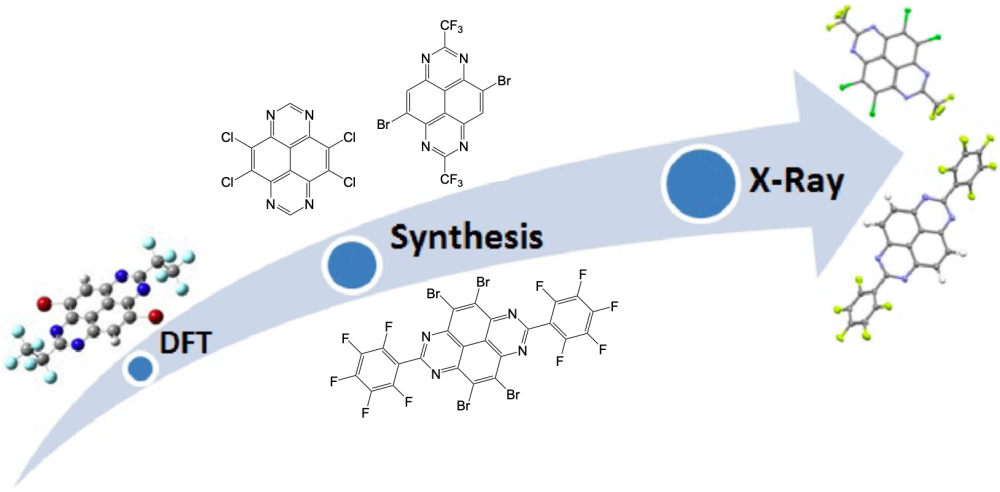

Figure 9 Synthesis of 2,7- and/or core-substituted TAP derivatives.

Introduction of perfluorinated substituents as well as halogens are known to lower the LUMO energy levels significantly, making such TAP derivatives interesting in the field of n-channel semiconducting materials. Gade and co-workers synthesized a series of 2,7- and/or core-substituted TAP derivatives with LUMO energy levels in a range from -3.57 to -4.14 eV (**Figure 9**). The **Figure 10** shows the Kohn-Sham HOMO and LUMO of TAP-based

compounds, suggesting that the longitudinal axis lies in a nodal plane of the frontier orbitals, which connects the carbon atoms at 2- and 7- positions. As a consequence, the substituents at these positions only have a small effect on the frontier orbital energies.[14]

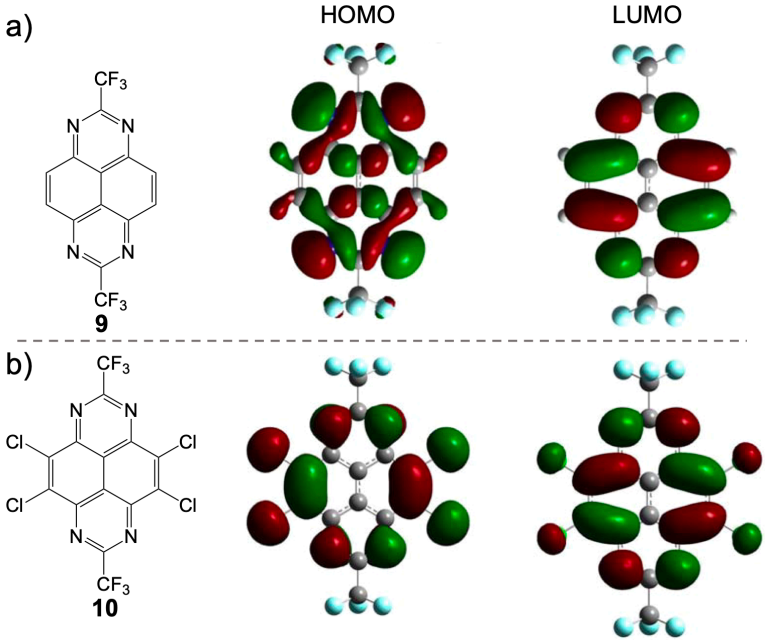

Figure 10 The Kohn-Sham HOMO and LUMO of 2,7- bis(trifluoromethyl)-TAP (**9**) (a) and 2,7-bis(trifluoromethyl)-4,5,9,10-tetrachloro-TAP (**10**) (b).

Later, the group of Gade found new types of annulated derivatives, in which the TAP is annulated with a furan or indolizine ring (**Figure 11**). The frontier Kohn-Sham orbitals of the furan-annulated TAP show that the HOMO and LUMO orbitals are distributed across the complete π-system of the molecule. For the indolizine-annulated TAP, the HOMO is mainly localized on the indolizine moiety whereas the LUMO is on the TAP unit, indicative of a considerable ICT character. Compared to the reference **9**, which shows two reversible reduction processes corresponding to the formation of the mono- and dianions of TAP, the reduction potentials of furan-annulated TAP (**11**) and indolizine-annulated TAP (**12**) are negatively shifted, due to the electron-donating effect of a furan or indolizine ring. Interestingly, compound **12** exhibits strong fluorescence (**Figure 11b**), in contrast to other TAP derivatives that have been found to be non-emissive. The emission spectra are seen to shift dramatically to longer wavelengths with increasing the polarity of solvents from cyclohexane to acetonitrile.[15]

Given that a limited study on TAP derivatization and intrinsic electronic properties of TAP, we decided to functionalize the TAP core for the synthesis of different TTF-TAP systems and a

detailed study of electronic couplings between an electron donor TTF and an electron acceptor TAP will be discussed in **Section 3**.

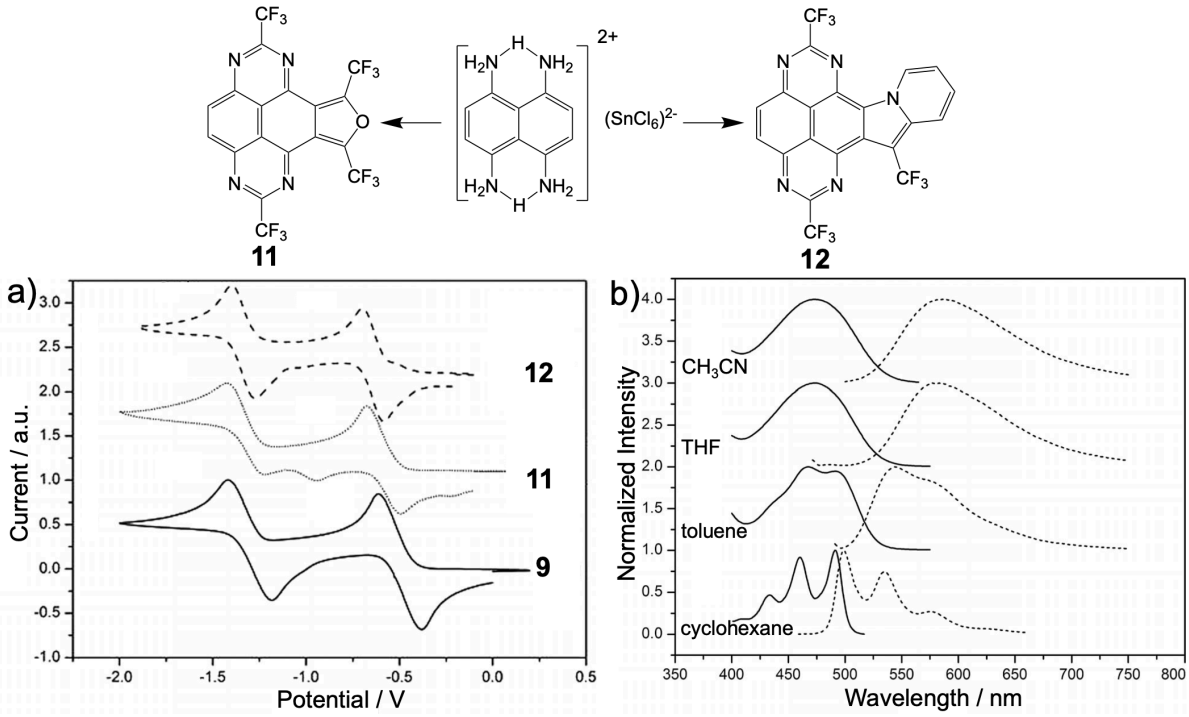

Figure 11 The new types of annulated heterocyclic derivatives of TAP. a) Cyclic voltammograms of **9**, **11** and **12** derivatives. b) Normalized UV-Vis absorption and emission spectra of compound **12**.

1.1.3 Azulene derivatives

Azulene, which was discovered by Piesse in 1863, is an isoelectronic isomer of naphthalene with 10 π-electrons. As shown in **Figure 12**, azulene is a parent non-alternant, non-benzenoid aromatic hydrocarbon and has attracted much interest of researchers in different fields due to its unusual chemical structure with a negatively charged 5-membered ring fused with a positively charged 7-membered ring, bringing out an inherent dipole moment of about 1.08 D while naphthalene is zero. The $S_0 \rightarrow S_1$ transition is observed as a weak absorption band in the visible range, leading to a blue color. This is rare for hydrocarbons without any heteroatom substitutions in the neutral state. In addition to this weak absorption band, there is a strong absorption band relating to the $S_0 \rightarrow S_2$ transition in the UV region. Another unique optical property is fluorescence from S_2 to S_0, thus violating Kasha's rule.[25] In contrast, naphthalene has a symmetrical HOMO and LUMO geometry, while azulene shows a non-mirror-related MO geometry with its HOMO located mainly at the odd positions and its LUMO at the even positions of the azulene ring.[26, 27] Considering its unique MOs and resonance delocalization,

the 1-, 3-, 5- and 7-positions of azulene are electron-rich and can readily react with electrophilic reactants, whereas the 2-, 4-, 6- and 8-positions of azulene are electron-deficient and prefer to undergo nucleophilic reactions.

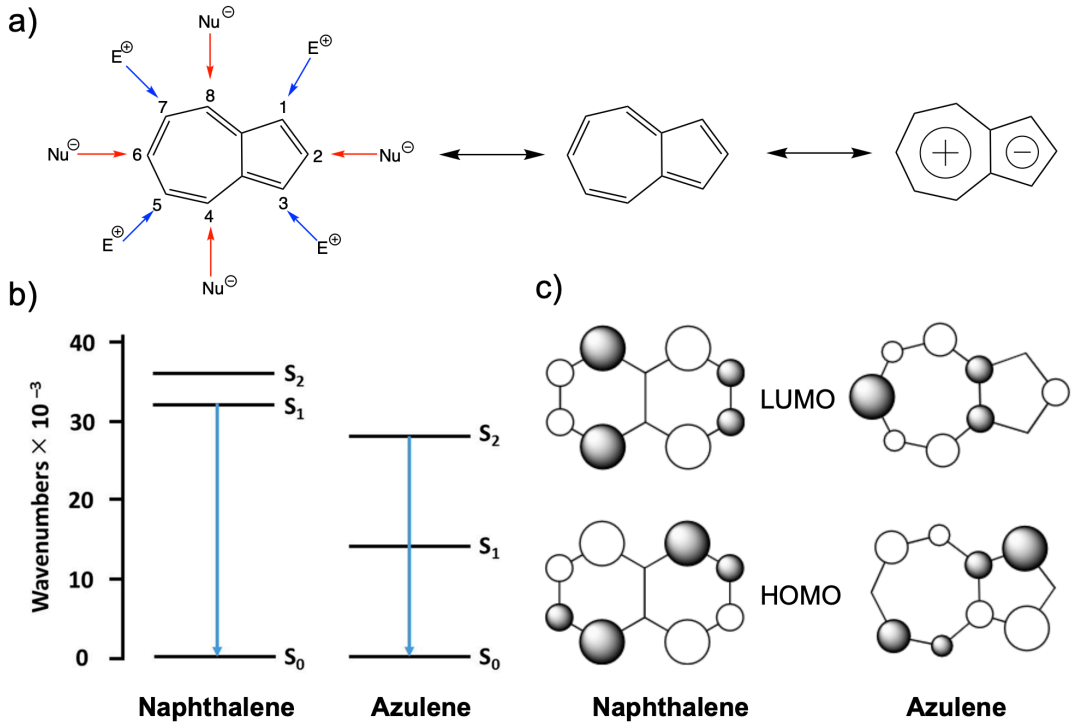

Figure 12 a) The resonance delocalization of azulene. b) Comparison of the electronic energy spacing and radiative transitions of azulene and naphthalene. c) Orbitals coefficients of HOMO and LUMO OF naphthalene and azulene.

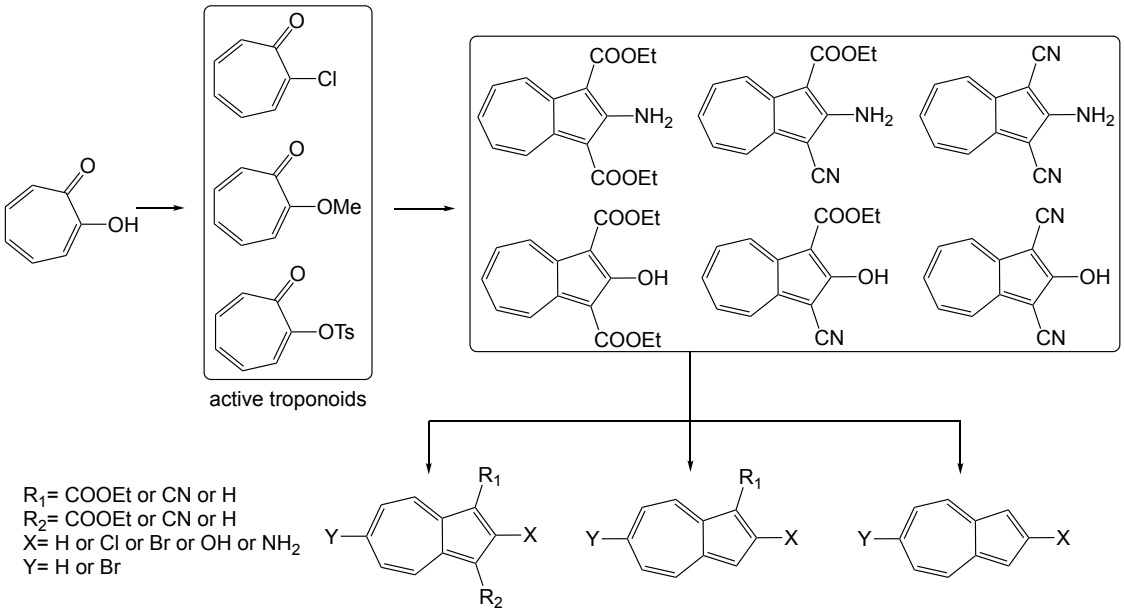

Figure 13 Some representative azulene derivatives synthesized from the starting material tropolone.

The synthetic routes to azulene derivatives were not practical because of low yields. Therefore, research on azulene-based molecules is less explored compared to naphthalene. Some representative azulene derivatives were synthesized starting from tropolone. The hydroxy group of tropolone can be easily converted into a chloro, methoxy, or tosyloxy group and these active troponoids can undergo nucleophilic reactions to yield substituted azulenes (**Figure 13**). Further conversion provides a variety of azulene derivatives with different functional groups. Some other important and efficient methods have been investigated by Ziegler, Hafner, Takase, Hawker *et al*.[28-30]

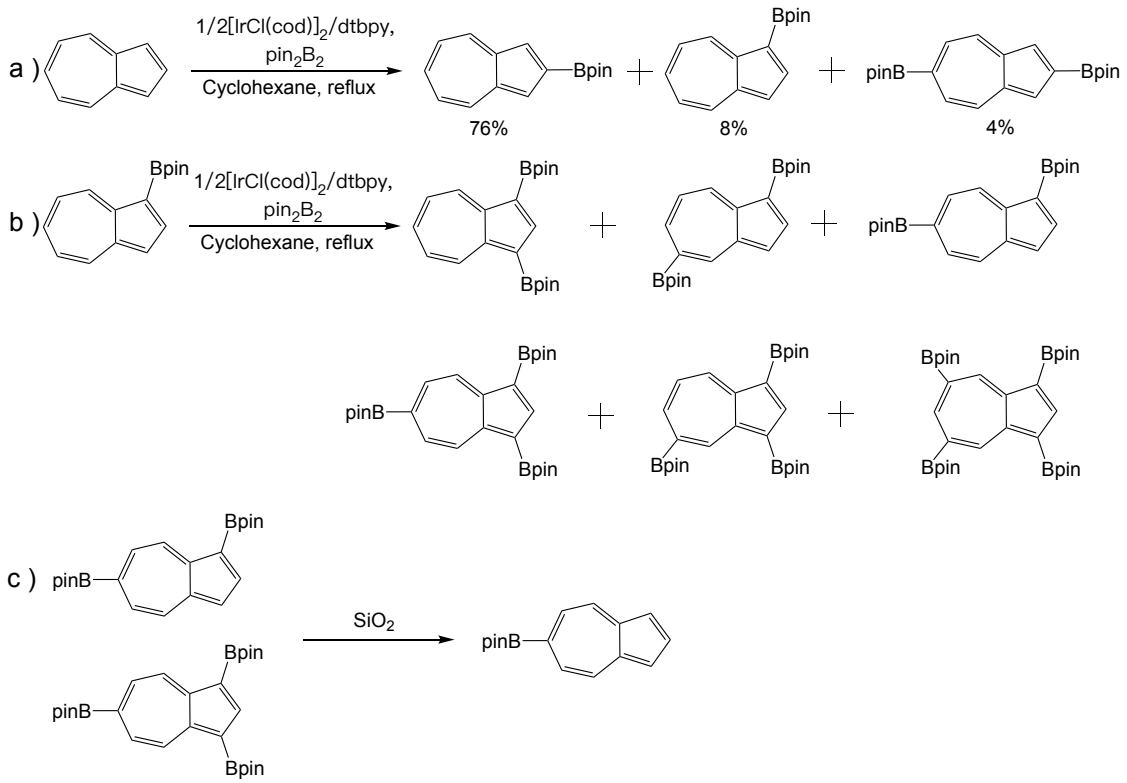

Figure 14 Borylation of azulene at the 2- and/or 6-positions.

The electron distribution in the MOs must be considered for functionalization of the azulene core. A direct functionalization at the electron-rich 1- and 3-positions has been developed as an effective method to prepare azulene derivatives, as reported by Daub, Marafuji, Sugihara, Dyker, Liu *et al.*[31-34] In contrast, direct functionalization at other positions appears to be much harder. For example, it is difficult to perform an electrophilic reaction at the 2-position where is the low electron density. In 1962, Matsumura's group reported the substitution of an amino group for a chloride group by using hydrochloride gas and subsequent decarboxylation. The resultant 2-chloroazulene can be further converted to organolithium species.[35] An alternative approach was explored starting from 1,3-dibromoazulene to form a 2-silylated-1,3-

dibromoazulene.[36] A big step was made by Sugihare's group towards direct borylation of azulene at the least-hindered 2-position in the presence of iridium catalysis to yield 2-borylazulene (**Figure 14a**). This is ascribed to the formation of a complex between an iridium center and the 5-membered ring, rather than the 7-membered ring. The selectivity for the 2-position over the 1-position is very likely governed by steric hindrance.[37] Besides, 2-silylated azulene was prepared with even higher regioselectivity than 2-borylazulene.[38]

The C-H borylation is also applicable to azulene to yield 6-borylazulene with exclusive regioselectivity. However, a very lengthy, six-step reaction from 2-chlorotropone or a 3-step reaction from azulene was reported for synthesis of 6-borylazulene.[38-40] Side-product 1-borylazulene (8-10%) can be obtained during borylation of azulene (**Figure 14a**). The subsequent borylation of 1-borylazulene with an excess amount of bis(pinacolato)diboron (pin_2B_2) afforded a series of di-, tri- or tetra-substituted borylazulene. Finally, during the isolation, they found that 1,6-di-borylazulene and 1,3,6-triborylazulene can be deborylated easily under chromatographic separation on silica gel to obtain 6-borylazulene. Until 2021, Yorimitsu's group has developed borylation at the 6-position of azulene in a single-step reaction in a high yield.[41] As shown in **Figure 15**, based on Brich reduction,[42] they chose sodium dispersion to reduce azulene in the presence of a reduction-resistant alkoxyborane forming a diborylation intermediate, which then underwent oxidative monodeborylation in the presence of 2,2,6,6-tetramethylpiperidine-1-oxyl (TEMPO) to yield a 6-borylazulene with exclusive regioselectivity. This allows to get access to various 6-substituted azulene derivatives.

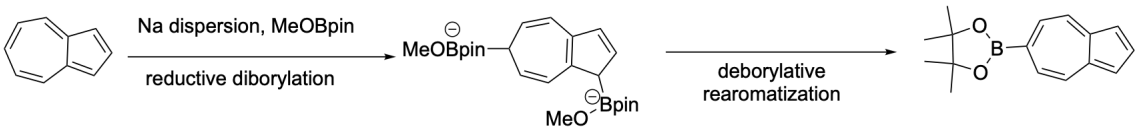

Figure 15 Reductive diborylation and oxidation to yield mono-borylation of 6-borylazulene.

Considering the unique asymmetric structure, azulene-based dimers are simple linear derivatives containing three regioisomers that are connected through different positions, revealing diverse optoelectronic properties. Katagiri and co-workers explored these isomers and found that all of them show relative lower HOMO-LUMO gap energies and good p-type characteristics compared to 2,2'-binaphthalene.[43] Moreover, linearly π-expanded azulene trimers including the four regioisomers also exhibit unique properties, such as different dipole moments, varied HOMO and LUMO density distributions as well as distinct charge carrier transport properties, which leads to the potential application for semiconductor materials.[44, 45]

DFT calculations on the tetraazulene isomers reveal that they have polarity-tunable OFET transport properties because of their different MO density distributions induced by the different directions of connection of the four azulene moieties.

Azulene-fused linear aromatic hydrocarbons have been investigated by Takai's group, showing a small band gap, good solubility and reversible stimuli responsiveness. As shown in **Figure 16**, upon addition of trifluoroacetic acid (TFA), compounds **13** and **14** exhibits a new absorption band at 458 nm and 414 nm with the longest wavelength absorption band at 587 nm, respectively. This is due to the formation of azulenium cation caused by the protonation at 5-memebered ring of azulene. Besides, these spectra changes are accompanied with color change from green to orange for **13** and light green to blue for **14**. Moreover, neutralization of acidic solutions of **13** and **14** with triethylamine (TEA) can regenerate original spectra.[46] This process of protonation/deprotonation was reversible by addition of TFA or neutralization with ammonia. However, the reversibility of the optical properties is easily affected by the spatial environment of the heptagon ring and the substitution as well as linkers between azulene moieties.[47]

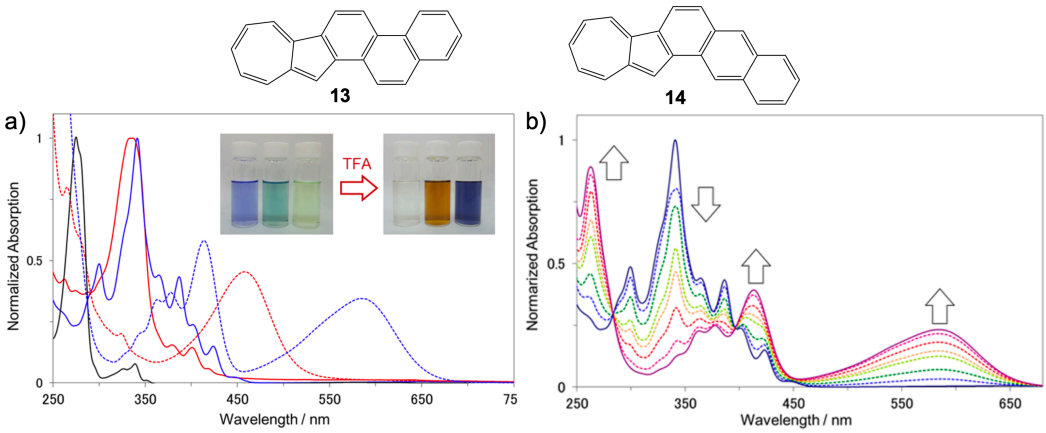

Figure 16 a) UV-Vis spectra of azulene (black), **13** (red), and **14** (blue) in the neutral state (solid line) and after protonation by TFA (dotted line) using TFA/DCM. b) Variation of UV-Vis absorption spectra of **14** upon the protonation by TFA.

Azulenes, especially functionalized at the 2,6-positions, are promising building blocks for organic optoelectronic materials owing to the considerable contribution of their resonance structures. It is, however, difficult to directly functionalize the azulene core at the 6-position until 2021. Therefore, such azulene derivatives are rarely explored. Azulene-fused aromatic diimides comprised of a 2,2'-biazulene moiety and two seven-membered imide rings (**15a** and

15b in **Figure 17**), were synthesized by Gao's group. They have relatively lower LUMO levels and narrower band gaps than the corresponding naphthalene diimides.[48] Later on, 2-ethynylazulene-NDI (**16a**) and 6-ethynylazulene-NDI (**16b**) were reported, exhibiting n-type semiconducting properties.[49] DFT calculations suggest that **16b** has a more delocalized LUMO over the backbone lying at a lower energy (-3.51 eV) than **16a** (-3.27 eV), which facilitates electron transport and injection (**Figure 18**). The lowest-energy absorption bands of **16a** and **16b** appear at 523 nm and 509 nm in DCM, respectively. Both of them show two reversible reduction processes, while **16b** (-0.45 V) has a higher onset potential leading to lower LUMO energy compared to **16a** (-0.50 V). The LUMO is more stabilized by a sizable contribution of the 7-membered ring of the azulenes in **16b**.

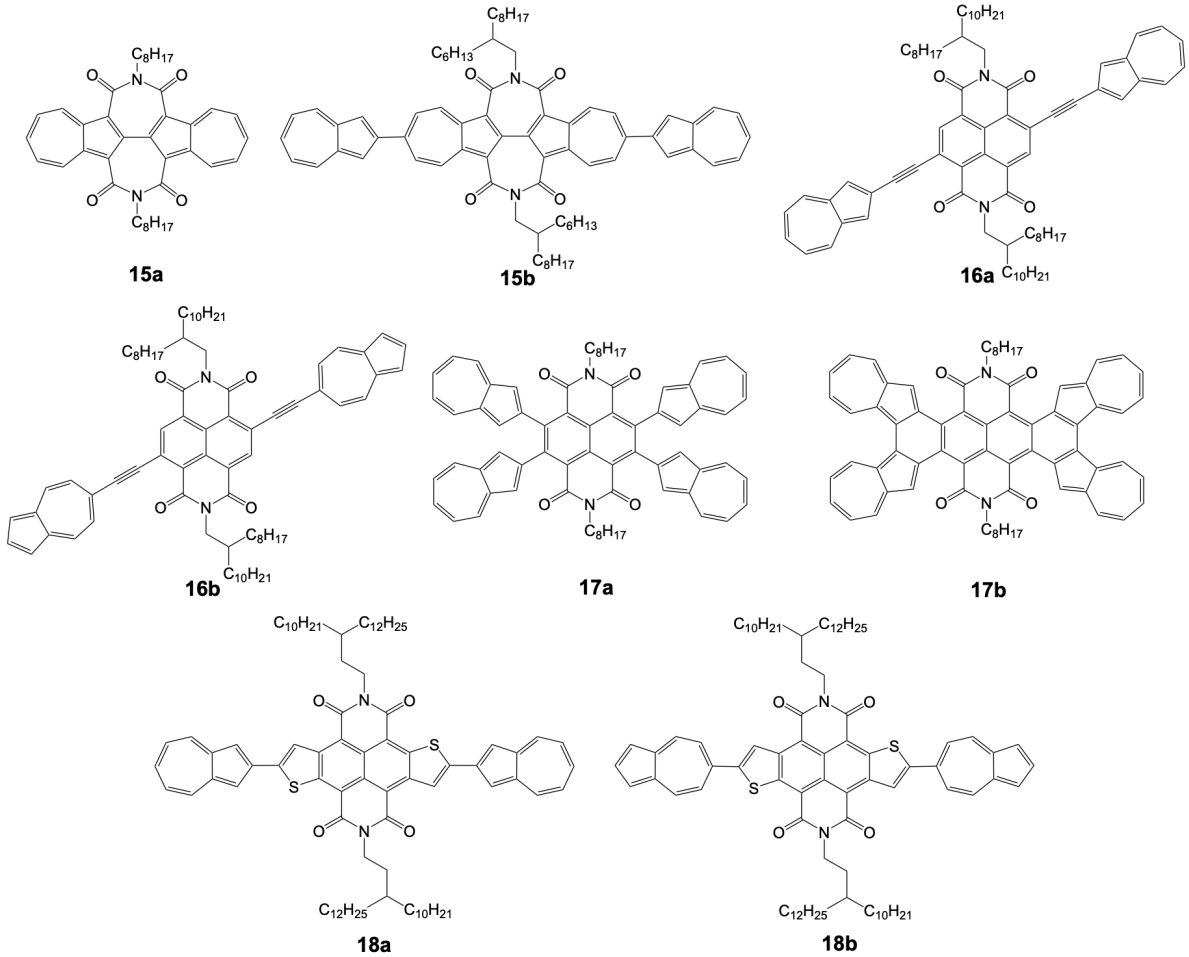

Figure 17 Chemical structures of the reported azulene-functionalized diimides.

The fusion of azulenes to a tetracene diimide (TDI) core leads to an effective π-extension and ICT from the azulene to TDI units. The compound **17b** possesses a small HOMO-LUMO gap of 0.96 eV, in good agreement with the appearance of one absorption band in the near-IR region.

It exhibits four reversible well-resolved reduction processes. The first and second reduction potentials are positively shifted compared to **17a**, indicative of the stabilization of LUMOs caused by the π-extension after cyclization (**Figure 19**).[50]

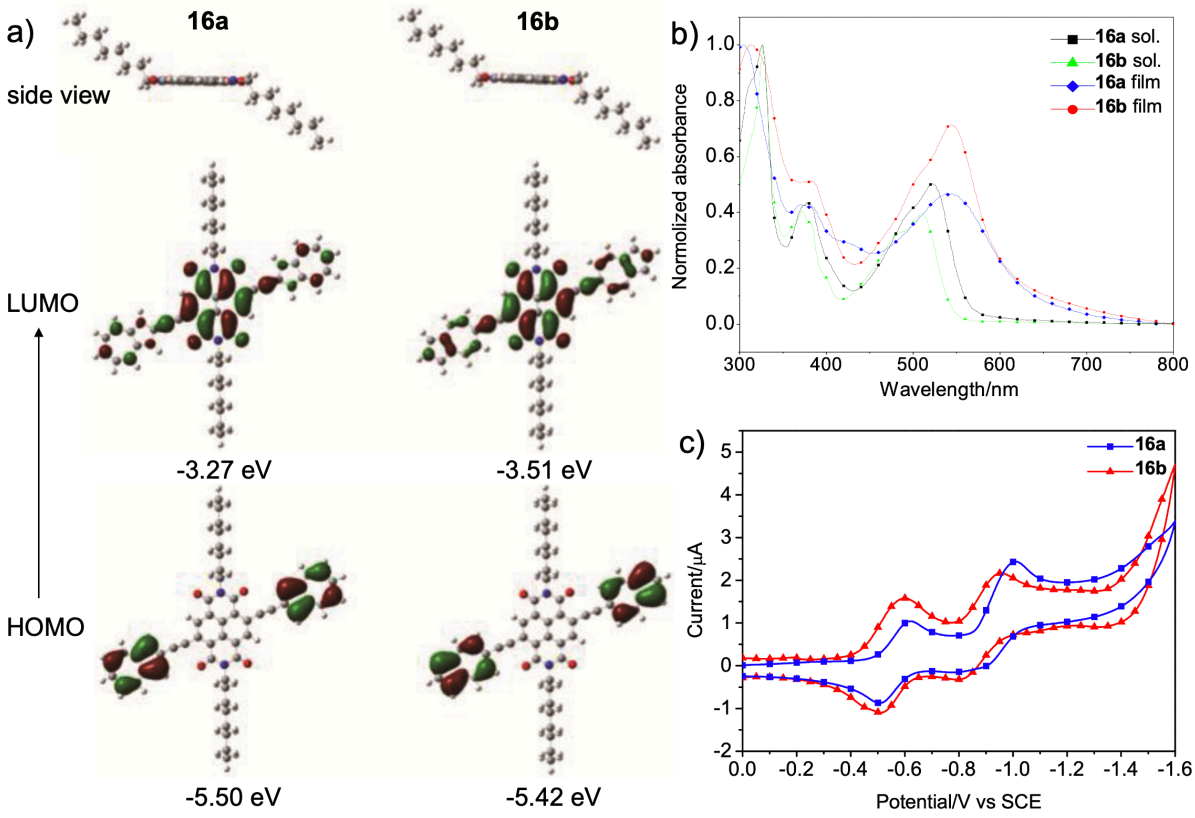

Figure 18 a) Molecular geometries, HOMO and LUMO distributions, and energy levels of **16a** and **16b** computed by DFT calculations. b) The UV-Vis spectra of **16a** (black) and **16b** (green). c) The cyclic voltammograms of **16a** and **16b.**

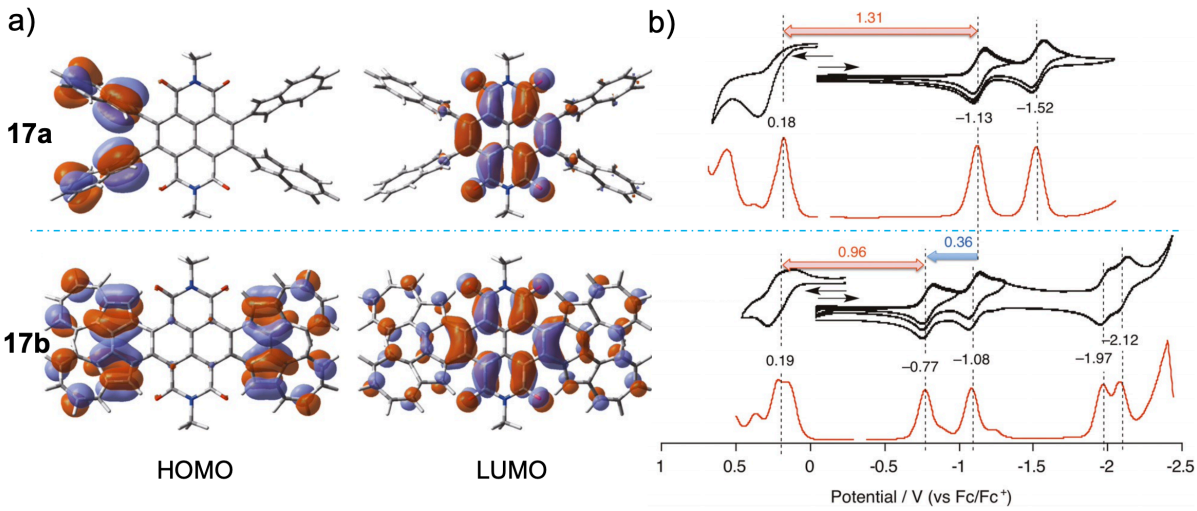

Figure 19 a) DFT-calculated HOMOs and LUMOs of **17a** and **17b**. b) Cyclic voltammograms and differential pulse voltammograms of **17a** and **17b**.

Similar to azulene-NDI systems (**16a** and **16b**), two isomeric azulene-decorated naphthodithiophene diimide (NDTI) triads (e.g., **18a** and **18b**), in which two azulene units are directly connected with the NDTI core through its 2- and 6-position, respectively, were reported.[51] DFT calculations reveal that in both cases, the LUMO is delocalized over the entire molecule but with a large amplitude on the NDTI core, whereas the HOMO is mainly delocalized over the entire molecule for **18a**, but only localized at two terminal azulene units for **18b**. It can be accounted for by the fact that **18a** is more planar while **18b** is non-planar with dihedral angles of ~30.35°/~38.82° between the two azulene units and the NDTI core (**Figure 20**). The compound **18a** exhibits an ambipolar OFET performance, whereas **18b** acts as a typical n-type semiconductor.

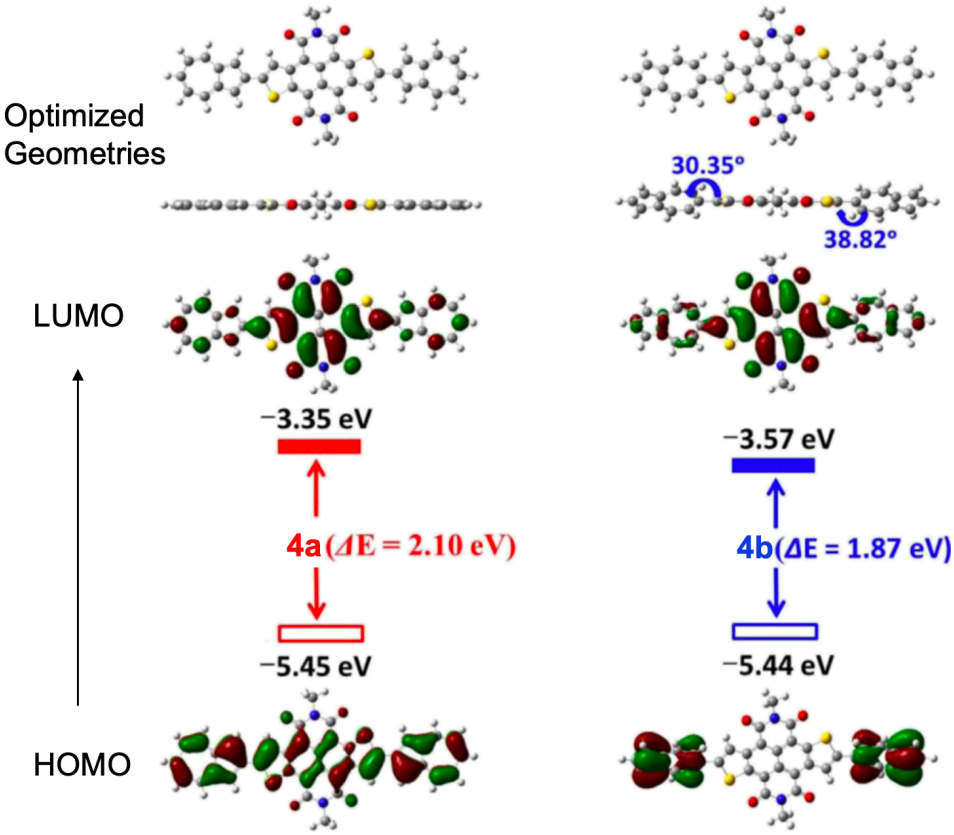

Figure 20 Molecular geometries, HOMO and LUMO distributions, and energy levels of **18a** and **18b** calculated using DFT.

It can be deduced that the azulene units are connected with NDTI and NDI through the 6-positions (**16b** and **18b**), leading to a lower LUMO energy compared to their counterparts which are connected through the 2-positions (**16a** and **18a**). The HOMO distribution depends on the nature of the linkers between azulene and NDI/NDTI which significantly affects the molecular geometries. For **16a**, the HOMO is localized on two azulenes while for **18a** the

HOMO is completely delocalized over the entire molecule because of coplanarity. In both **16b** and **18b**, the HOMO distribution mainly locates on azulene itself no matter what kinds of linkers between azulene and diimides. For the UV-Vis spectra of these four molecules, all of them show bathochromic shifts compared to references, indicative of the effective extension of the π-conjugation systems. The lowest-energy absorption bands of **16b** and **18b** show hypsochromic shifts compared to their counterparts **16a** and **18a**. The long-wavelength absorption bands for **16a** and **18a** come from the transitions of HOMO-2 → LUMO and HOMO → LUMO, for **16b** and **18b**, the long-wavelength absorption bands are attributed to the transition of HOMO-2 → LUMO. Clearly, electronic properties of azulene-based diimides are significantly affected by connectivity and the nature of the linkers.

Except for small molecules, azulene-incorporated D-A polymers (**19a-c**) were reported, demonstrating that their semiconducting behavior can be modulated by altering the connectivity of the azulene units.[52] In comparison to **19a** and **19b**, where 1,3-disubstituted azulene units are inserted to the polymer backbone, **19 c** containing 4,7-disubstituted azulene units has a lower LUMO energy and acts as an ambipolar semiconductor. Besides, these polymers can be used as electron donors in solar cells (**Figure 21**).

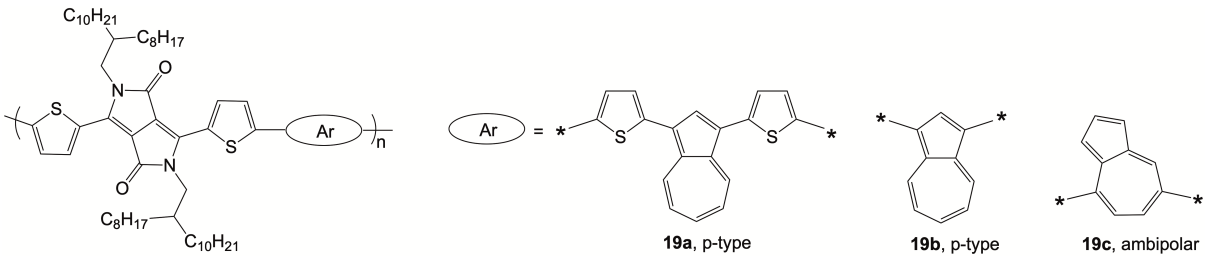

Figure 21 Chemical structures of azulene-based polymers with different connectivity.

Considering the stimuli-responsive behavior of azulene, incorporation of azulenes to different polymers turns out to be an effective strategy for novel switches, conductors and so on. In contrast to homopolymers, azulene-incorporated polymers exhibit pronounced changes in the visible and near-infrared region. Azulene is weakly fluorescent due to the S_2–S_0 transition while the azulenium cation is extremely fluorescent in a concentrated acidic environment. As illustrated in **Figure 22**, the addition of TFA leads to a significant increase in the emission intensity with a λ_{max} of 385 nm of azulene and a shoulder at 320 nm of fluorene.[53] The azulene-fluorene conjugated polymer provides a potential application of pH-sensing materials.[54] Moreover, protonated polymers containing 1,3-disubstituted azulene moieties show a stronger

fluorescence than those with 4,7-disubstituted azulene moieties.[55] Importantly, azulene-based conjugated polymers can absorb a significant portion of the NIR spectrum up to 2.5 μm. Together with high thermal stability, easy film-forming properties and good chemical and electrochemical stability, they appear to be promising candidates for the fabrication of novel organic near-IR electronic devices.[56]

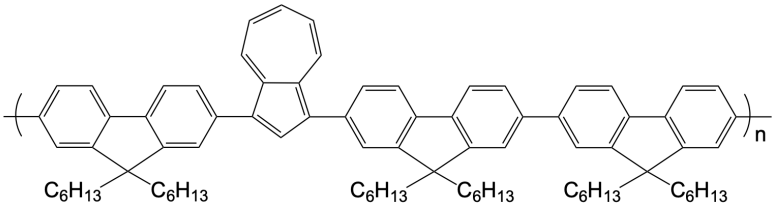

20

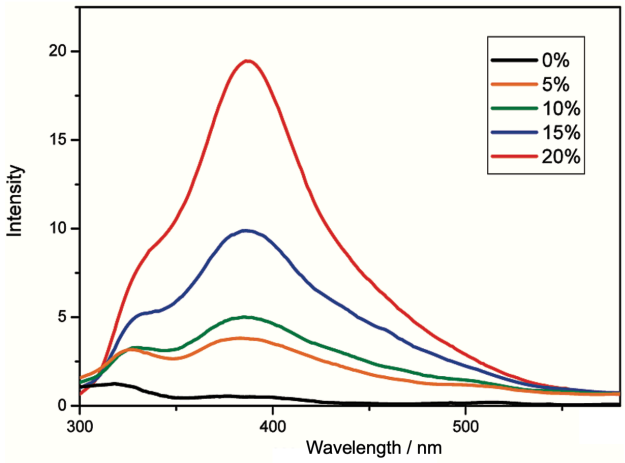

Figure 22 Fluorescence spectral changes of the azulene-incorporated polymer **20** with increasing amount of TFA.

Considering all unique properties of azulene, including a large dipole moment, a narrow HOMO-LUMO gap and colorimetric reversible stimuli-responsiveness with acids and bases, azulene-incorporated PDI derivatives with different connectivities have been studied. The detailed discussion will be presented in **section 4.2**.

1.1.4 Paracyclophane (PCP) derivatives

[2,2]Paracyclophane (PCP) was firstly reported by Farthing and Brown in 1949, and it was obtained as a byproduct from low-pressure pyrolysis of *para*-xylene.[57] [2,2]PCP consists of face-to-face stacked, strongly interacting benzene rings with an average ring-to-ring distance of 3.09 Å and linking by diethylene, leading to a rigid structure and good conformational stability. This ring-to-ring separation is far less than the standard van der Waals distance of 3.40 Å observed between layers in graphite (**Figure 23**). [2,2]PCP is chemically stable towards

light, oxidation, acids, bases, and temperature up to 180 °C.[58] It exhibits an abnormal absorption spectrum in a range of 200 to 400 nm compared to simple benzene derivatives and related hydrocarbons. A broad band around 356 nm in its emission spectrum is also unexpected compared to alkyl aromatics. These spectroscopic properties are attributed to strong σ-π interactions, as well as a π-π through-space delocalization that results in energy transfer throughout the entire cyclophane core.[59] Except [2,2]PCP, multilayered [3,3]PCP has been widely investigated as well. Compared to [2,2]PCP, [3,3]PCP has less strain between two benzene rings.

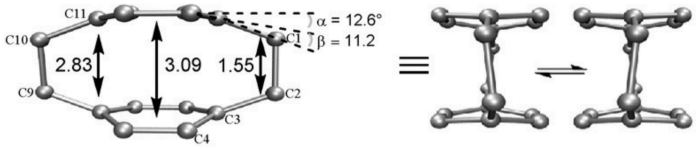

Figure 23 The aromatic-ring distance of [2,2]PCP of 3.09 Å.

The use of [2,2] or [3,3]PCP as a bridge in D-A ensembles can promote an ICT from the D to the A units and control electronic interactions between them by the π-π stacking within cyclophane. As a result, **D-PCP-A** ensembles are interesting candidates for molecular electronics and can be classified into three types according to the alignment of **D** and **A** units with respect to the PCP core: type A: the D-A cyclophanes; type B: cyclophanes with **D** and **A** incorporated into the bridge chains; type C: the cyclophanes substituted with **D** and **A** at the *pseudo-para*, *pseudo-geminal*, *pseudo-meta* or *pseudo-ortho* positions (**Figure 24**).

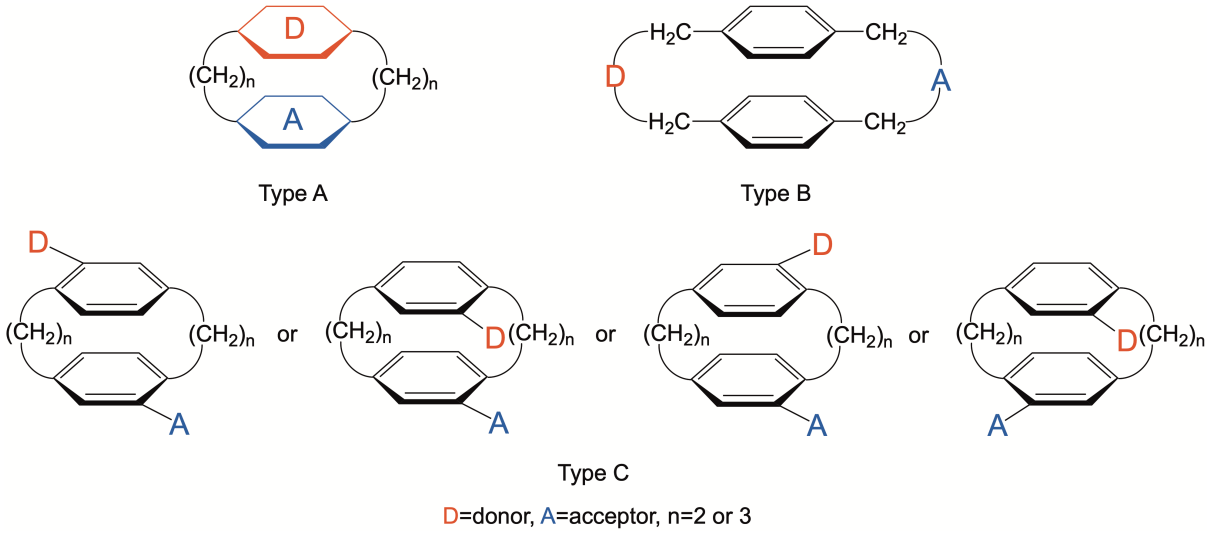

Figure 24 Chemical structures of different types of **D-PCP-A** ensembles.

Over several decades, **D-PCP-A** systems of type A were investigated to gain an insight into the CT dependence on transannular distance and relative orientation of **D** and **A**. For example,

Misumi *et al.* explored the double-layered **D** (1,4-dimethoxybenzene)-[2,2]PCP-**A** (*p*-benzoquinone), in which two benzene rings are replaced by **D** and **A** and a broad CT band was observed clearly in the spectral range of 600 to 1000 nm. As shown in **Figure 25**, the absorption maximum of double-layered compound **21** is shifted to a longer wavelength than those of triple-layered counterparts **22**. For the triple-layered systems **22** and **23**, the introduction of electron-donating methoxy group into the benzene ring leads to a red shift of an ICT band. The ICT transition also depends on the orientation of the D-A moieties as shown in the electronic spectra of **22a-c**.[60]

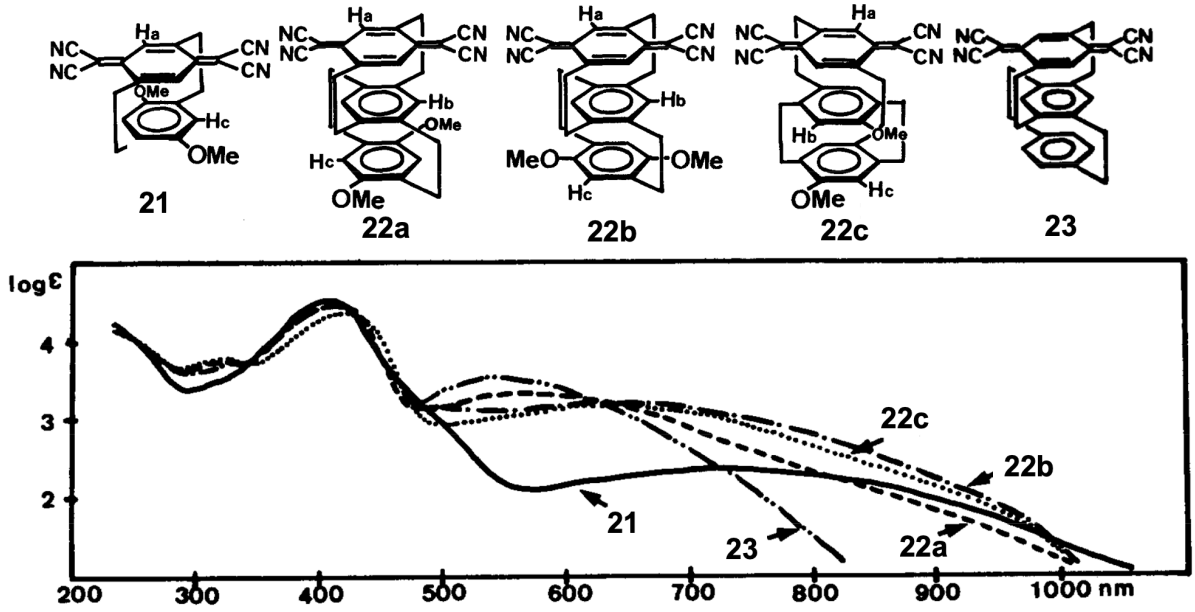

Figure 25 Chemical structures and electronic spectra of some examples of [2,2]PCPs of type A.

As shown in **Figure 26**, another example pointed out that the oxidation potential decreases as the number of the layers increases with -$CH_2CH_2CH_2$- bridges. The oxidation potential of the triple-layered compound **25** with -$CH_2CH_2CH_2$- bridges is 0.72 V, which is much lower than its double-layered counterpart **24** (1.08 V), **27** with -CH_2COCH_2- bridges (1.01 V) and the parent [3,3]PCP (1.07 V). The double-layered **26** with -CH_2COCH_2- bridges has only one reduction wave (-1.97 V) which is quite comparable to the triple-layered counterpart **27** (-2.03 V). However, there is no reduction process in **24** and **25**. These results clearly indicate that different bridges significantly affect electronic interactions between BTD and [3,3]PCP moieties in the ground state. Moreover, through-bond interactions are effective with the -$CH_2CH_2CH_2$- bridge. In contrast to UV-Vis spectra of reference compounds BTD and [3,3]PCP, double-layered **24** and **26** clearly show an ICT around 380 nm, while triple-layered

25 and **27** show a red-shift of the ICT band to 400 nm. These results suggest that a through-space ICT transition occurs in both double- and triple-layered PCP compounds. In addition, the triple-layered **25** and **27** show a broad fluorescence band with a low quantum yield compared to the double-layered **24** and **26**, probably due to a faster charge recombination in triple-layered **25** and **27** compared to double-layered **24** and **26**.[61]

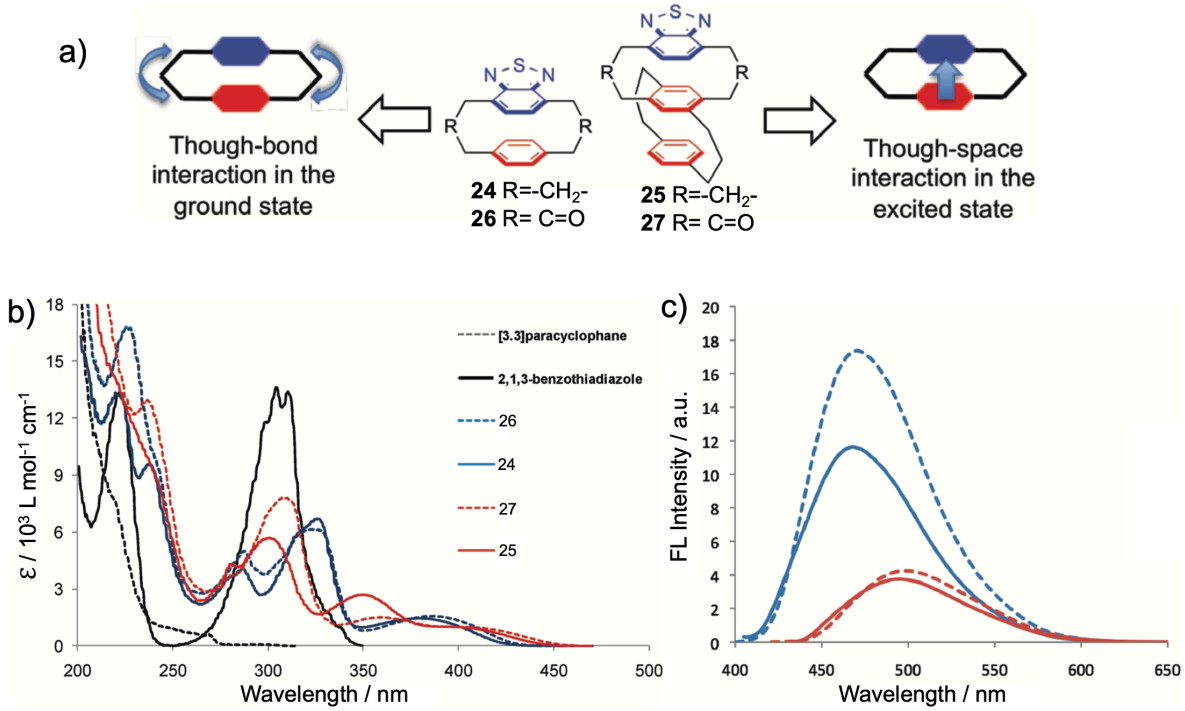

Figure 26 a) The double- and triple-layered [3,3]PCP-based D-A molecules of type A. b) UV-Vis spectra. c) Fluorescence spectra.

As far as we know, there is only one literature about **D-PCP-A** of type B that has been reported by Takemura's group, in which π-systems of **D** and **A** are orthogonal to the benzene rings of the cyclophane, which is distinct from spiro π-conjugation.[62] As shown in **Figure 27**, a fixed D-A distance in triad **28** was achieved with a [3,3]PCP as a rigid spacer. Its UV-Vis spectrum is a simple combination of the related references, indicative of the lack of an ICT process. The cyclic voltammetry measurement demonstrates only weak electronic interactions between 1,4-dithiafulvene (DTF) and dicyanomethylene. The appearance of two bands at 415 nm and 750 nm in its transient absorption spectra indicates the formation of a radical cation of **28** which has a lifetime longer than the reference bis(benzyl)DTF (black dashed part). The DFT calculations show that the positive charge of this radical cation species is predominantly located on the DTF ring and partly on the benzene rings, which is more stable than that of the reference bis(benzyl)DTF which shows a strong tendency to dimerize. The reason is probably due to its

rigid structure and the weak electronic interaction of DTF and dicyanomethylene moieties through [3,3]PCP.[62]

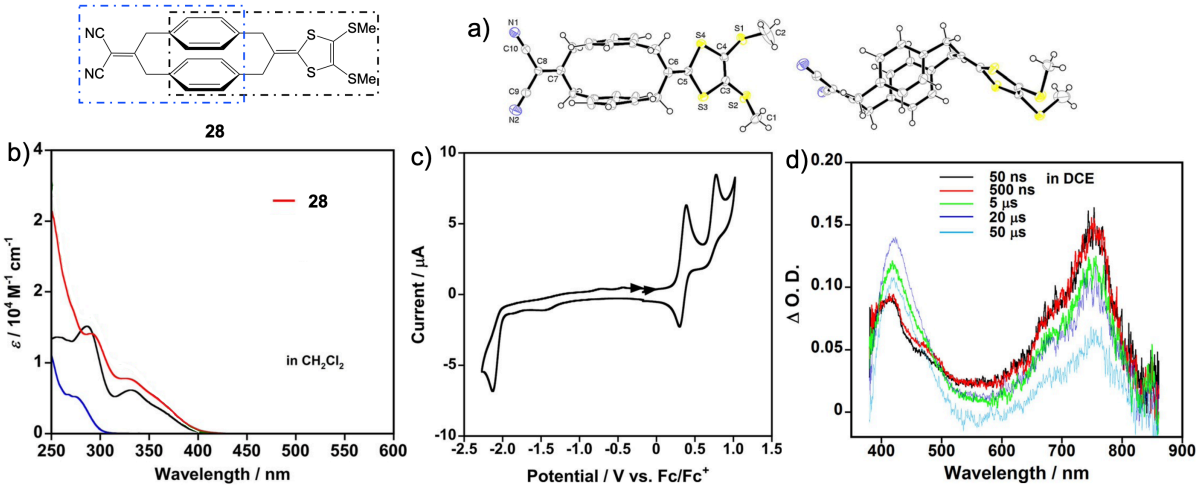

Figure 27 The type B: cyclophanes with **D** and **A** incorporated into the bridge chains. a) Molecular structure of **28**. b) UV-Vis spectra of **28** and reference compounds as shown in the black dashed part of **28** (black) and the blue dashed part of **28** (blue). c) Cyclic voltammogram of **28**. d) Transient absorption spectra of **28**.

Most importantly, **D-PCP-A** triads of type C using [2,2]PCP or [3,3]PCP) are expected to reduce the rate of charge recombination, leading to a charge-separation state with a long lifetime.[63, 64] In order to obtain a long-lived charge-separated state, the charge recombination rate has to be lowered. Among **D-PCP-A** triads of type C, the ones with a *pseudo-para*-orientation of D and A units can be one of the most interesting candidates to be explored in optoelectronic devices.[59]

The [2,2]PCP has been chosen as a skeleton with coplanar D and A groups at the *pseudo-geminal* or *pseudo-para* orientation (**Figure 28**) for developing through-space conjugated thermally activated delayed fluorescent (TADF) materials. The HOMO and LUMO are mainly located on the donor and acceptor moieties, respectively, and also on the adjoining benzene rings, suggesting that the strong transannular electronic communication between D and A units can be mediated by a PCP bridge, which enhances a through-space ICT interaction.[65] The clear separation of the frontier orbitals leads to a small energy gap between the singlet and triplet excited states, namely, 0.19 eV and 0.04 eV for trans- and cis-compounds, respectively, which render them appealing as TADF emitters.

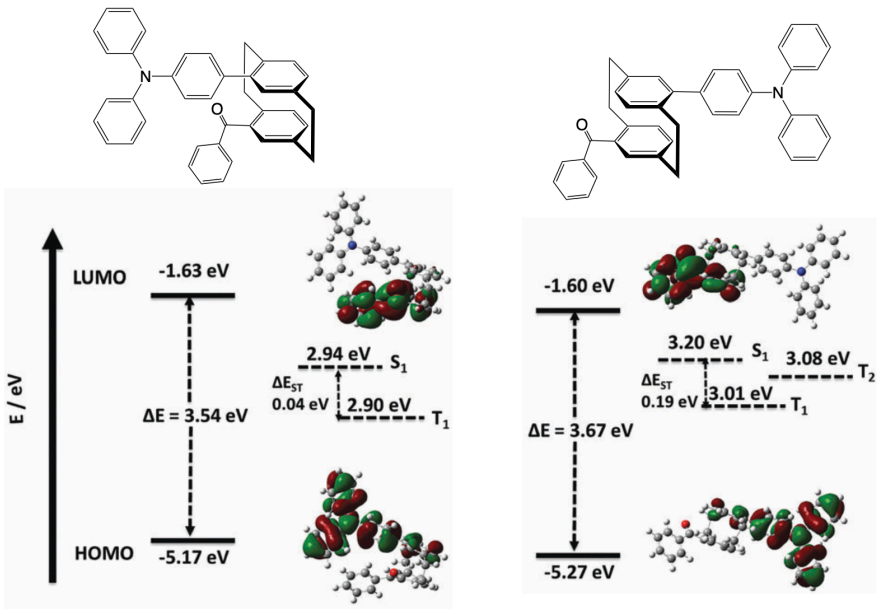

Figure 28 HOMO-LUMO profiles and excited state dynamics.

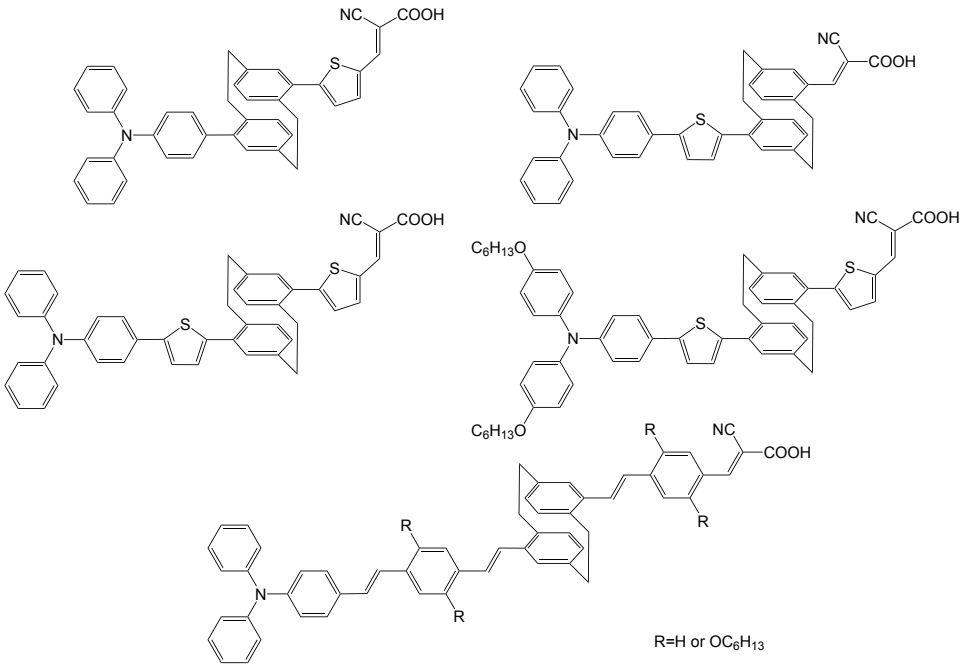

Figure 29 Chemical structures of **D-PCP-A** triads of type C with substitution at the *pseudo-para* position.

[2,2]PCP derivatives with D and A units in the *pseudo-para direction* have been applied in designing solar cell as well, in which D and A units are either directly linked to the PCP core or *via* vinyl groups, as shown in **Figure 29**. The UV-Vis absorption spectra demonstrate that all of them show electronic communications from D to A units through the PCP bridge. Moreover, the introduction of vinyl groups results in a red-shift of the lowest-energy absorption

band. In all cases, the electron distributions in the HOMO and LUMO are well separated by the PCP bridge, indicating that π-conjugation is severely interrupted.[66] Therefore, they have the potential to lower the charge recombination and generate a long-lived charge separated state.[64, 66]

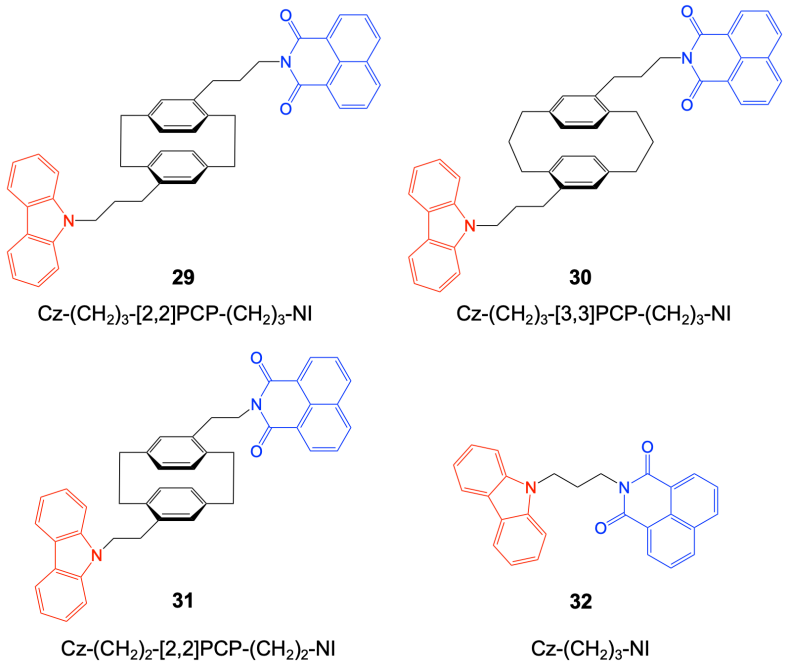

Figure 30 A series of **D-PCP-A** triads containing a [2,2]- or [3,3]PCP bridge with D and A units.

Shinmyozu and his co-worker synthesized a series of **D-PCP-A** triads of type C, which was prepared through incorporating D and A units to a PCP core *via* flexible alkyl chains (**Figure 30**). As expected, negligible electronic interactions between D and A moieties are confirmed by their UV-Vis spectra and cyclic voltammetry. This is in sharp contrast to type A (**Figure 26**).[63] The DFT calculations suggest that the HOMO and LUMO orbitals are mostly localized over donor moieties and completely localized over acceptor units, respectively, indicating no orbital interactions between D and A in the ground state. No doubt, their UV-Vis spectra are a simple superposition of related reference compounds. The same holds true for their redox potentials that are similar to those of the corresponding donor and acceptor references. In contrast to [2,2]PCP-based **29** and **31**, [3,3]PCP-based triad **30** with propyl chain shows stronger tendency to form an exciplex between PCP and NI units in the excited state in cyclohexane, probably resulting from better electron-donating ability of [3,3]PCP than [2,2]PCP because of reduced strain and also from a propyl chain, following the statistical rule known as Hirayama's n=3 rule.[63, 67] Besides, a multistep electron transfer process occurs in

CH_3CN, starting from D-(CH_2)m-[n,n]PCP-(CH_2)m-A* to $D^{\bullet+}$-(CH_2)m-[n,n]PCP-(CH_2)m-$A^{\bullet-}$ *via* D-(CH_2)m-[n,n]$PCP^{\bullet+}$-(CH_2)m-$A^{\bullet-}$. The transient absorption spectra (TAS) suggest that these PCP-based triads show longer CS states compared to Cz-$(CH_2)_3$-NI (454 ps). For example, Cz-$(CH_2)_3$-[2,2]PCP-$(CH_2)_3$-NI and Cz-$(CH_2)_3$-[3,3]PCP-$(CH_2)_3$-NI have a lifetime of 6.3 ns and 5.0 ns, respectively.[68]

Below is another example of **D-PCP-A** where D and A units are linked to a PCP core through triple bonds (**Figure 31**). It has been found that there are only weak interactions between triarylamine (TAA) and NDI units through [2,2]- or [3,3]PCP by UV-Vis and cyclic voltammetry. This is probably attributed to the electronic properties of the NDI core which shows negligible electronic interactions with substituents attaching to its nitrogen imide atoms, as the LUMO has a nodal plane along the molecular axis. The rate constants of CT and CS of **34** ($150 \times 10^{10}\ s^{-1}$, $5.6 \times 10^{10}\ s^{-1}$) are faster than those of **33** ($45 \times 10^{10}\ s^{-1}$, $2.4 \times 10^{10}\ s^{-1}$). Both of them show a singlet CS state with a lifetime of hundreds of nanoseconds and a triplet CS state with a lifetime of several microseconds.[69]

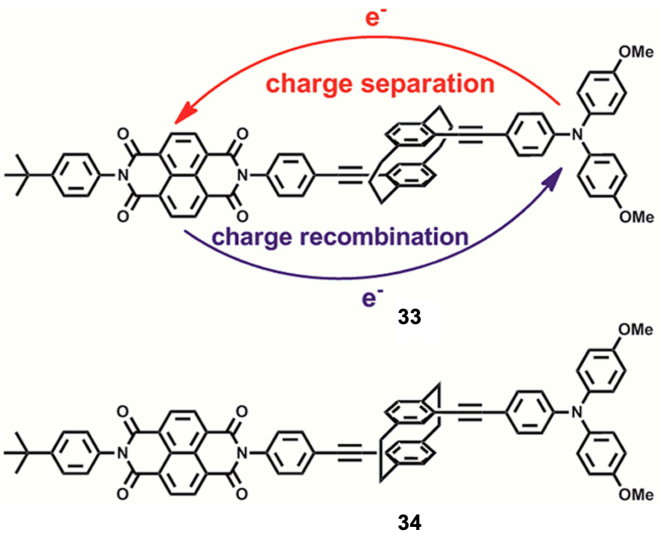

Figure 31 [2,2]- or [3,3] PCP-based NDI-PCP-TAA triads.

As aforementioned, D and A can be incorporated into the *pseudo-para*-positions of a [2,2]- or [3,3]PCP directly or by a π-linker (double or triple bond) or a σ-spacer (propyl or ethyl chain). So, how do these linkers affect the lifetime of a CS state? Here are some conclusions as follows: 1) the incorporation of a PCP bridge in D-A systems could lead to a long-lived CS state; 2) good spatial separation of HOMO on the D unit and LUMO on the A unit through a PCP bridge impedes the CR rate; 3) the nature of D and A has a strong effect on the CS processes; 4) an increase in the length of a σ-spacer between D or A with PCP could prolong the lifetime of a

CS state (e.g. D-propyl-PCP-propyl-A *vs* D-ethyl-PCP-ethyl-A); 5) electronic interactions between D and A through PCP can be enhanced by replacing a σ-spacer with a π-linker, but the lifetime of a CS state depends on the spatial arrangement of HOMO and LUMO.

Among different types of D-PCP-A systems, type A shows obvious ICT interactions between D and A units whereas only weak electronic interactions occur in type C, being beneficial for a long-lived CS state. As a result, BTD-PCP-TTF systems of type C in which TTF and BTD units are linked to the *pseudo-para*-positions of [2,2]PCP directly or through triple bonds have been synthesized. The interplay between through-bond and through-space CT interactions as well as lifetimes of CS states in such systems will be discussed in detail in **section 5**.

1.2 Molecular electronics

On-surface synthesis has become one of the hottest research fields with the assistance of ultra-high vacuum (UHV)-based surface science techniques, especially scanning tunneling microscopy (STM) and non-contact atomic force microscopy (nc-AFM). Compared to classical wet chemistry, on-surface reactions are catalysed by a substrate and done without solvents, thus no limitation of solubility is involved. Due to these unusual reaction environments, some organic reactions that are inefficient or prohibited in solution or in gas phase can occur on a surface. A key challenge for on-surface synthesis lies in a precise control of the reaction pathway. The appropriate choice of a surface should be a prerequisite to a successful on-surface chemical reaction, including its material, shape, and crystallographic orientation.[70] Although active Group VIII metals, such as Ni, Pd, Co, Pt, have often been used as catalysts in wet chemistry, their strong binding interactions with molecules lead to poor molecular diffusion rates on them, which reversely limits their utilizations in the on-surface synthesis. So far, coinage metals (Au, Ag, Cu) with moderate chemical reactivities, have been the most popular surfaces, as the requirement of both chemical reactivity and molecular diffusion can be met at the same time. The Ullmann coupling reaction is one of the most well-studied on-surface reactions, which is stimulated by the dissociation of the C-X (X = Cl, Br, I) bond, typically forming a C-metal-C organometallic intermediate by the capture of a metal adatom on surface. The organometallic intermediate subsequently transforms into a C-C covalent structure after further thermal treatment. As shown in **Figure 32**, 10,10'-dibromo-9,9'-bianthryl (DBBA) as a precursor couple into polymeric chains *via* Ullmann coupling at 200 °C (**Figure 32b**). Then,

the cyclodehydrogenation of the polymer occurs at 400 °C, leading to the formation of 7-graphene nanoribbon (GNR) (**Figure 32c**).[71] In contrast, it is surprising that DBBA follows a distinct reaction pathway on Cu(111) as reported by Fasel *et al.* (**Figure 32d**).[72] Therefore, these three coinage metal surfaces exhibit distinct efficiency for some reactions involving two or more reactive groups.

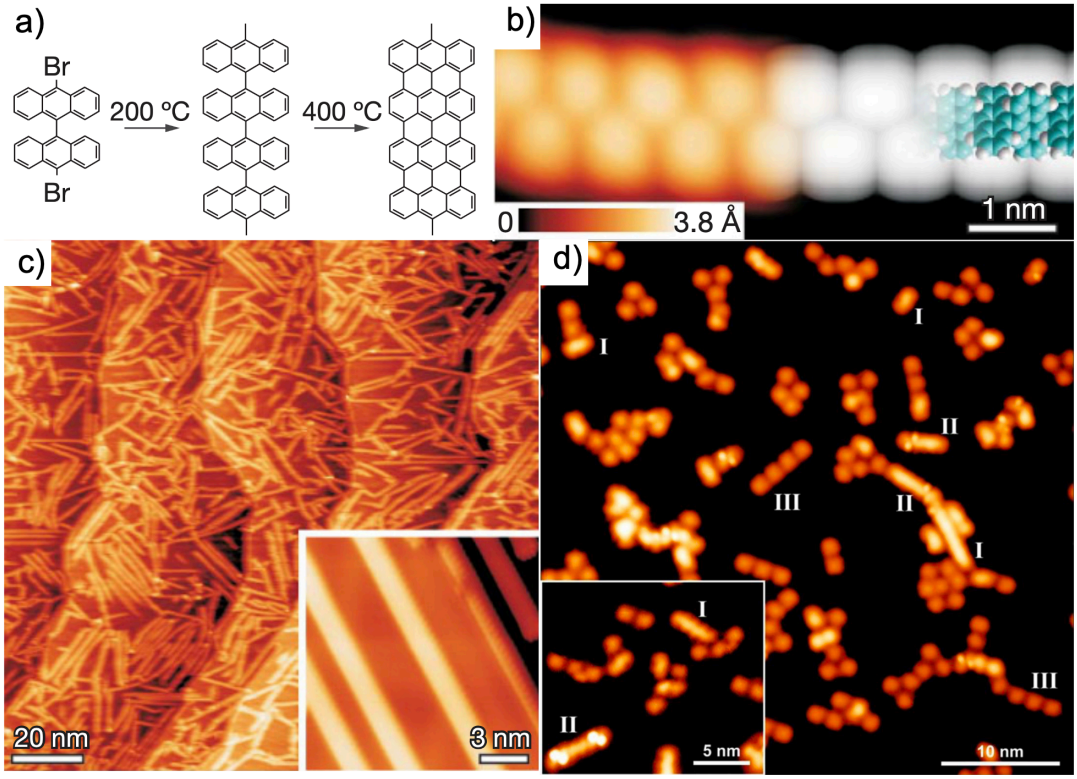

Figure 32 Bottom-up synthesis of graphene nanoribbons (GNRs) on Au(111), Ag(111) and Cu(111). a) A reaction scheme from the precursor DBBA to straight N = 7 GNRs on Au(111) and Ag(111). b) Zoom-in STM image of the formed polyanthrylene chain, overlaid with DFT-based simulated STM result. c) Overview STM image after cyclodehydrogenation, showing straight N = 7 GNRs. d) STM images recorded after deposition of DBBA on Cu(111) and subsequent annealing to 250 °C.

Another popular on-surface reaction is the reaction of terminal alkynes, aiming at the fabrication of carbon nanostructures made of sp-hybridized carbon atoms. The three coinage metal surfaces exhibit distinctly different efficiencies (**Figure 33**).[73] Fuchs *et al.* studied the Glaser coupling of 1,4-diethynylbenzene on Au(111) and Ag(111) upon annealing at 122 °C in yields of 43.3% and 73.6%, respectively. Compared to Ag(111) and Au(111), Cu(111) shows the lowest efficiency because it interacts too strongly with the alkynyl group, which inhibits the molecular diffusion and increases the reaction barrier.[74]

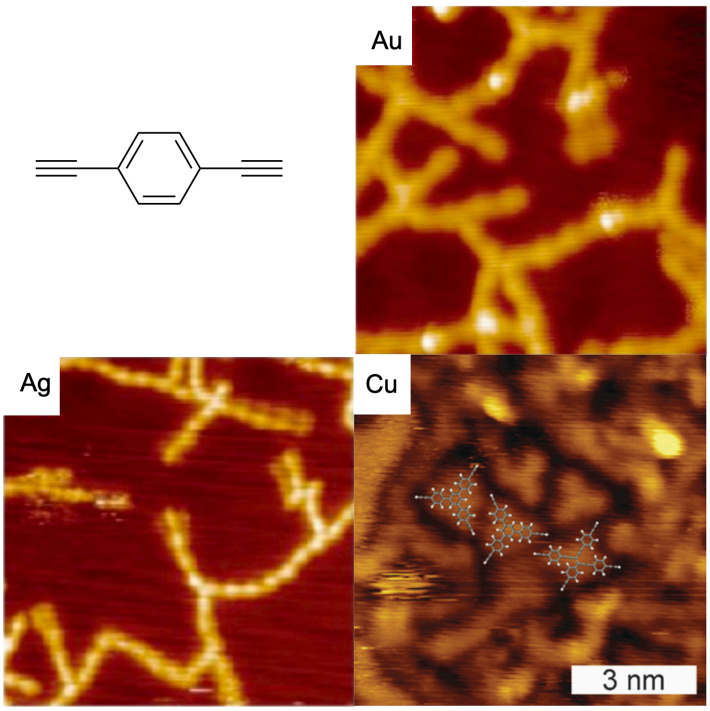

Figure 33 The reactions of 1,4-diethynylbenzene on Au(111), Ag(111) and Cu(111).

Porphyrin, with a total of 26 π-electrons, is of particular interest thanks to its planar structure with an aromatic core of 18 π-electrons, remarkable thermal stability, tunable redox properties, and intense optical features. Porphyrin nanotapes (PorNTs) are promising molecular wires due to a high degree of π-conjugation, low HOMO-LUMO gaps, and exceptional conductance. Fasel and his co-worker reported *meso-meso* triply fused PorNTs through a two-step synthesis on Au(111) (**Figure 34a**). The diradical character of the on-surface formed building block $PorA_2$, a phenalenyl π-extended $Zn^{II}Por$, facilitates the formation of laterally π-extended tapes *via* the intermolecular homocoupling (**Figure 34b**). Remarkably, the obtained PorNTs are featured with magnetic end states resulting from the presence of an unpaired electron at each end of the Au(111)-supported NTs. The reactivity of these radicals is particularly high at the β-pyrrolic positions of the porphyrin core, making the termini susceptible to hydrogenation. Indeed, a close inspection of PorNTs by constant-height nc-AFM imaging reveals doubly hydrogenated carbon atoms (CH_2) at the terminal b positions of some of the tapes (**Figure 34d**). It could selectively transform the terminal $C(sp^3)H_2$ into $C(sp^2)H$ by STM tip-induced atomic manipulation, thereby removing the "extra" hydrogen atom (**Figure 34e**).

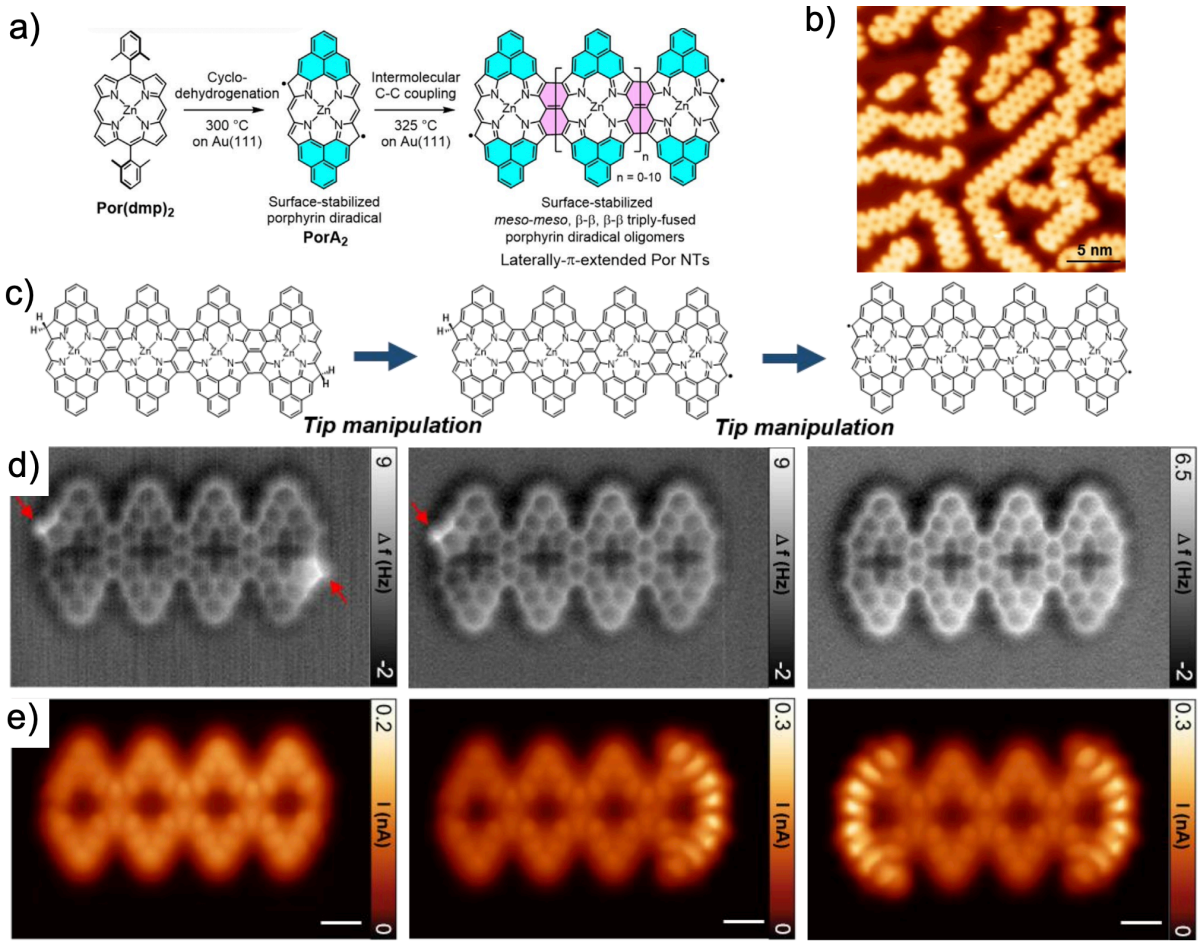

Figure 34 a) A two-step, on-surface synthesis of laterally π-extended PorNTs on Au(111). b) Overview STM image of the on-surface synthesis of PorNTs (V_s = -0.5 V, I_t = 40 pA). c) A chemical scheme of the tip-induced dehydrogenation of the CH_2 sites at the ends of Por_4NT. d) Constant-height nc-AFM images of Por_4NT. The arrows indicate the CH_2 structures at the β positions of the Por core. e) Constant-height STM images of the corresponding structures at –5 mV.

Heteroatom doping in graphene offers unique opportunities to fabricate D-A heterostructures and enhance magnetism of nanographene. Nitrogen is of particular interest for its electron-accepting character. In collaboration with Prof. Meyer at the University of Basel, we have investigated nitrogen-doped porous graphene nanoribbons (N-GNRs) *via* Ullmann coupling of 2,7,11,16-tetrabromotetrabenzo[*a,c,h,j*]phenazine (TBTBP) on Ag(111) surface (**Figure 35a**). With gradual annealing, TBTBP initially forms an organometallic intermediate upon debromination, and then the C-Ag-C bonds transform to C-C single bonds. The formed N-GNRs possess periodically spaced nanopores of 4.6 Å diameter and a high N-doping, which results in a semiconducting band gap of about 2.2 eV on Ag(111) and an interesting D-A

heterostructure.[75] Later on, we explored on-surface reaction of 3,6,14,17-tetrabromodibenzo[*a,c*]-dibenzo[5,6:7,8]quinoxalino-[2,3-*i*]-phenazine (TBQP) on Ag (111) (**Figure 35b**), indicative of a similar reaction mechanism to TBTBP. The formation of N-doped *Kagome* graphene (N-KG) is also triggered by an organometallic intermediate. It not only displays a semiconducting character due to the nitrogen doping, but also shows *Kagome* flat bands near the Fermi level. This work could set the scene for the attainment of graphene-based topological materials.[76]

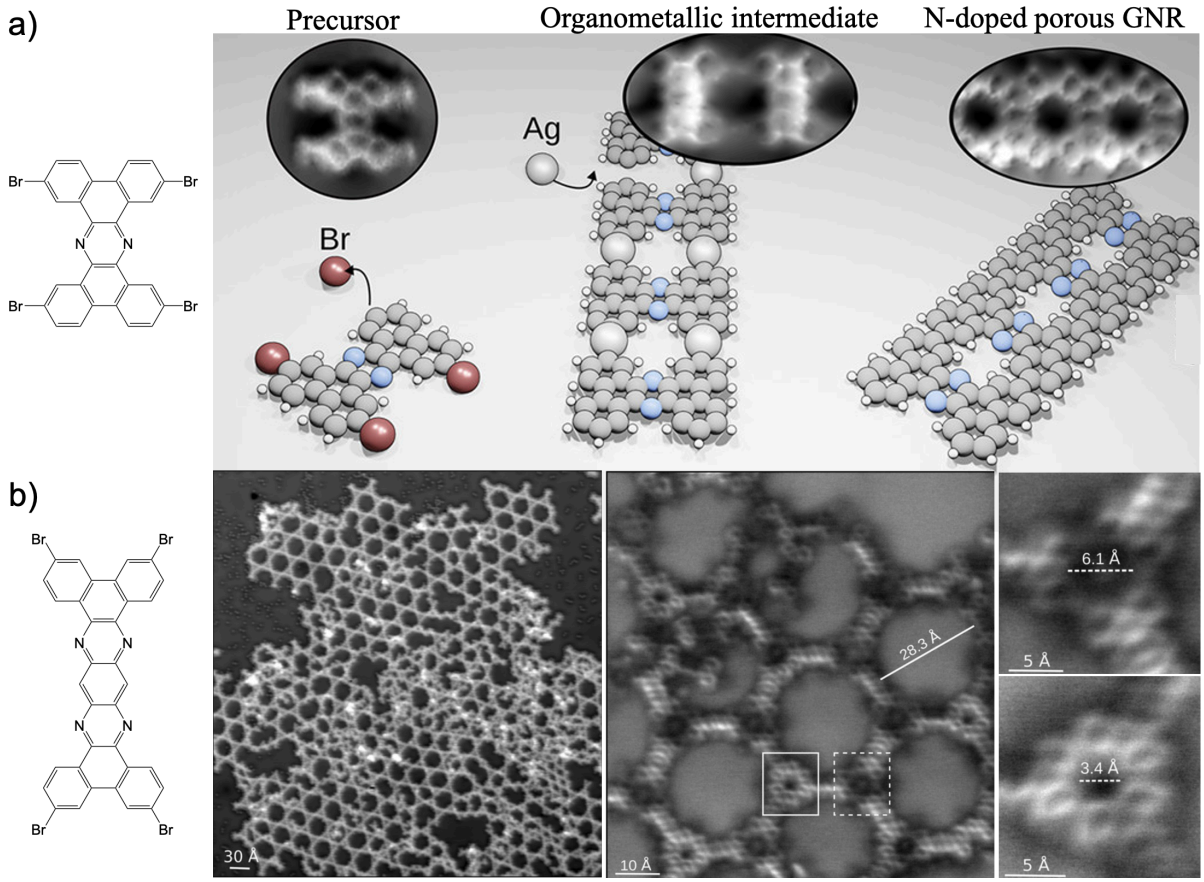

Fig.35 a) Ullmann coupling for the generation of porous-N-GNRs. b) On-surface synthesis of N-KG.

1.3 Aim of the work

Due to the remarkable electronic properties of tetrathiafulvalene (TTF), tetraazapyrene (TAP), perylene diimide (PDI), azulene, and paracyclophane (PCP) which are discussed in the **section 1.1**, my PhD work is mainly focused on the synthesis and characterization of π-conjugated D-A ensembles based on these building blocks for exploring ICT dynamics in the ground- and

excited-states in the hope of optically or chemically controlling charge flow direction. A series of new D-A ensembles (**Figure 36**) have been prepared and investigated in this thesis.

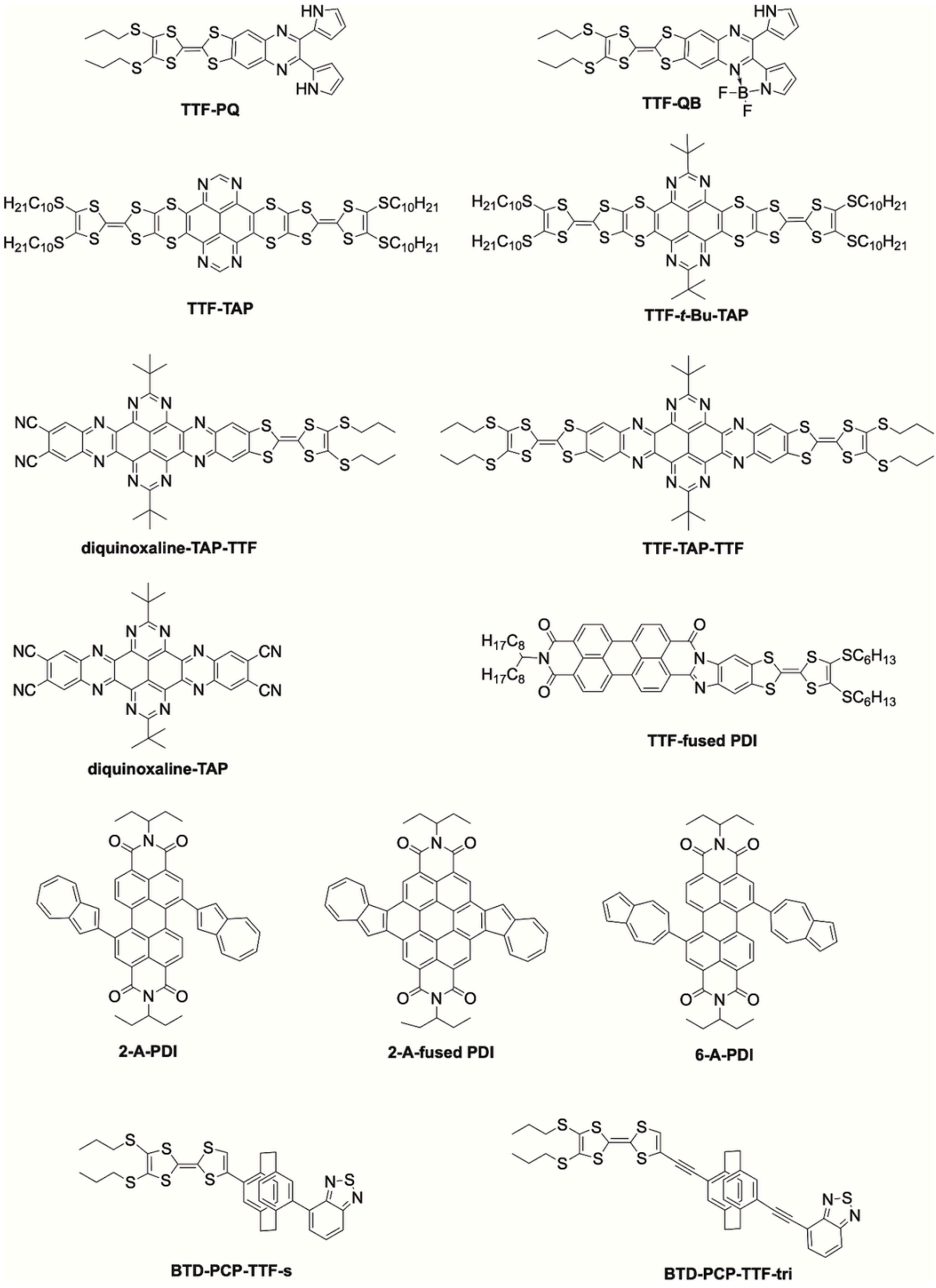

Figure 36 A series of new D-A ensembles.

Firstly, chemical regulation of direction of photoinduced charge flow is realized in a compact TTF-QB dyad. Thanks to the newly developed synthetic protocols for functionalization of the TAP core, TTF can be incorporated into the TAP core either through four sulfur bridges or by direct annulation through a quinoxaline. Following up the previous study, the π-extended TTF-PDI dyad has been used for exfoliation of graphite, and the resulting nanographene-dyad hybrid exhibits electronic interactions between nanographene and an electron acceptor rather than an electron donor. Furthermore, BTD-PCP-TTF ensembles have been studied for exploring through-space interactions between D and A affected by different linkers. Secondly, as an alternative to TTF, azulene was linked to the PDI core through different connectivities. The connectivity-dependent redox and optical properties have been investigated in detail. All of them show reversible colorimetric pH responsiveness.

As a result, through judicious choice of D and A units and linkers between them, different photoinduced ICT pathways can be manipulated through chemical modification, paving the way for potential applications in optoelectronic devices. The whole thesis revolved around the design of appropriate precursors for D-A ensembles, the development of synthetic methods, and a detailed investigation of their redox and optical properties. From the obtained results, we gain some insights into the relationship between structure and properties, which is of high importance for establishing chemical design principles for high-performance optoelectronic devices.

In the context of molecular electronics, appropriately functionalized N-heterocyclic molecules have been prepared and exploited for the formation of N-doped graphene nanoribbons on various surfaces. On the other hand, their electrical transport properties have been characterized through sandwiched single-molecule bilayer-graphene junctions *via* vdW interactions.

2. Chemically controlled charge flow in a compact TTF-fused dipyrrolylquinoxaline difluoroborate (QB)

This section is adapted to the following publication:

Chemical control of photoinduced charge-transfer direction in a tetrathiafulvalene-fused dipyrrolylquinoxaline difluoroborate dyad

Ping Zhou, *Ulrich Aschauer, Silvio Decurtins, Thomas Feurer, Robert Häner and Shi-Xia Liu*

Chem. Commun., 2020, **56**, 13421.

https://doi.org/10.1039/D0CC05736C

Contributions to this work

I successfully synthesized QB, PQ, TTF-PQ and TTF-QB and characterized them by ^{1}H NMR, Mass spectrometry and elemental analysis. I conducted and analyzed electrochemical experiments, UV-Vis spectra, fluroscence spectra, anion titration, oxidation, photostability measurements. Prof. Ulrich Aschauer, from our department, did the TD-DFT calculations and analyzed the data. The initial manuscript was written by me and revised by my supervisors.

2.1 Article

Chemical control of photoinduced charge-transfer direction in a tetrathiafulvalene-fused dipyrrolylquinoxaline difluoroborate dyad

ChemComm

ROYAL SOCIETY OF CHEMISTRY

COMMUNICATION

View Article Online
View Journal | View Issue

Cite this: *Chem. Commun.*, 2020, **56**, 13421

Received 24th August 2020,
Accepted 4th October 2020

DOI: 10.1039/d0cc05736c

rsc.li/chemcomm

Chemical control of photoinduced charge-transfer direction in a tetrathiafulvalene-fused dipyrrolylquinoxaline difluoroborate dyad†

Ping Zhou,[a] Ulrich Aschauer, *[a] Silvio Decurtins,[a] Thomas Feurer,[b] Robert Häner [a] and Shi-Xia Liu *[a]

A new approach for a compact annulation of tetrathiafulvalene (TTF) and dipyrrolylquinoxaline difluoroborate (QB) is presented, leading to strong electronic interactions between the TTF and QB units. Regulation of distinct photoinduced charge flows within this dyad is achieved by external stimuli, which is also verified by TD-DFT calculations.

Inspired by the unidirectionality of electron transfer evidenced in photosystem II, special attention has been devoted to efficient control of electron flow in π-conjugated ensembles consisting of electron donor (D) and acceptor (A) subunits.[1] However, regulating the direction of intramolecular charge transfer (ICT) over multiple pathways present in such D–A systems remains a big challenge.[2] An in-depth understanding of this key issue is a prerequisite for the successful implementation of organic molecules in photovoltaics, electronics and photonics.[3] Their intrinsic electronic properties are governed by the extent of communication between D and A units which can be fine-tuned by the meticulous choice and modification of the D–A architectures as well as external stimuli such as coordination,[4] protonation,[5] redox[6,7] and light.[8] Very recently, a fullerene–phenothiazine dyad was reported to show *in situ* switchable molecular photodiode-like behaviour by regulating the redox state of phenothiazine.[7] Our strategy involves a direct annulation of a redox-active π-electron donor TTF[9] (black part, Chart 1) and a strong chromophore dipyrrolylquinoxaline difluoroborate (QB, blue part, Chart 1) leading to the formation of the TTF–QB dyad. QB is analogous to BODIPY (boron dipyrromethene) with high extinction coefficient and fluorescence quantum yield and can act as a π-electron acceptor.[10] In stark contrast to the previously reported TTF–BODIPY ensembles,[11] TTF–QB absorbs strongly in the visible spectral region due to a strong effective ICT dominated by one-electron excitation from the HOMO localized on the TTF moiety to the LUMO on the QB core, indicative of largely enhanced electronic communication between them. On the other hand, TTF–QB featured with a peripheral pyrrolic NH unit, is envisaged to form a hydrogen bond with a fluoride, leading to an ICT from the HOMO mainly localized on the pyrrolylquinoxaline–fluoride adduct to the LUMO on the pyrrolylquinoxaline difluoroborate coordination moiety. Moreover, upon chemical oxidation of the TTF subunit to its radical cation $TTF^{\bullet+}$, a reverse ICT from the QB to the TTF moiety would occur. As a consequence, chemical regulation of photoinduced charge flow within this compact multicomponent dyad is fulfilled.

In the present contribution, the synthesis and electronic properties of TTF–QB in response to external stimuli including H-bonded fluoride adduct and chemical oxidation are discussed.

The target dyad TTF–QB was readily prepared in a yield of 60% *via* a reaction of a TTF-fused 2,3-di(1*H*-2-pyrrolyl)quinoxaline (TTF–PQ)[12] with BF_3OEt_2 using DBU as a base (Scheme S1, ESI†). A coplanar conformation of the

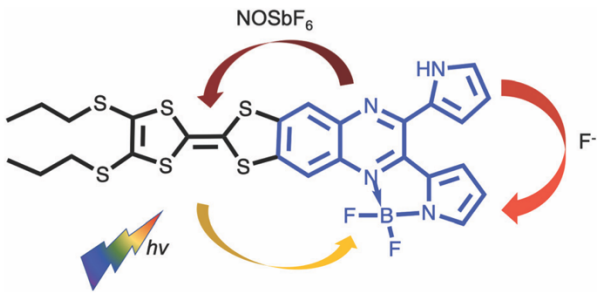

Chart 1 Chemical structure of the target dyad TTF–QB and chemical regulation of ICT direction in the presence of fluoride and oxidant $NOSbF_6$.

[a] *Department of Chemistry and Biochemistry, University of Bern, Freiestrasse 3, CH-3012 Bern, Switzerland. E-mail: ulrich.aschauer@dcb.unibe.ch, liu@dcb.unibe.ch*

[b] *Institute of Applied Physics, University of Bern, Sidlerstrasse 5, CH-3012 Bern, Switzerland*

† Electronic supplementary information (ESI) available. See DOI: 10.1039/d0cc05736c

resultant pyrrolide with the quinoxaline core renders a chelating ligand forming a stable five-membered ring with a boron atom, which leads to extended π-conjugation in the dyad TTF–QB. Purification by chromatographic separation on silica gel afforded the analytically pure product which was fully characterized. ^{1}H NMR and mass spectrometric data match well with its predicted molecular structure.

The electrochemical properties of TTF–QB, the free ligand TTF–PQ and the reference compounds dipyrrolylquinoxaline (PQ) or QB in CH_2Cl_2 were investigated by cyclic voltammetry (Fig. S1, S2 and Table S1, ESI†). TTF–QB undergoes two reversible oxidation processes at 0.78 and 1.10 V to the TTF radical cation and dication states and one reversible reduction process at −0.81 V, corresponding to the reduction of the QB subunit. Upon complexation of the PQ unit with one equivalent of BF_2, both oxidation and reduction potentials are positively shifted, indicative of the enhanced π-electron withdrawing ability of the quinoxaline core due to B–N bond formation between the nitrogen lone pair and the vacant p-orbital of the boron atom. It can therefore be deduced that the resultant QB subunit acts as a stronger π-electron acceptor than the quinoxaline unit itself. A separation between the onset oxidation and reduction potentials leads to an electrochemical HOMO–LUMO gap of 1.37 eV for TTF–QB, which is significantly reduced compared to that for TTF–PQ (1.91 eV).

The dark blue TTF–QB strongly absorbs over an extended range within the UV-Vis spectral region (Fig. 1). A strong and broad absorption band ($\varepsilon \approx 2.3 \times 10^4$ M^{-1} cm^{-1}) peaked at 610 nm is attributed to an ICT transition from the TTF unit to the QB fragment as confirmed theoretically (*vide infra*). A series of less-intense absorption bands is observed between 550 nm and 350 nm, followed by a very intense absorption band centered at 310 nm. These spectral features are in stark contrast with those of the free ligand TTF–PQ. On the one hand, its lowest energy absorption band is hypsochromically shifted by 120 nm, as evidenced by its purple-red colour. This observation is attributed to a weaker electron-withdrawing effect of the quinoxaline itself than the QB subunit. Consequently, the optical HOMO–LUMO gap of TTF–PQ (2.23 eV) is much larger than that of TTF–QB (1.69 eV). On the other hand, its absorption spectrum looks much simpler due to the decreased π-conjugation of the molecule induced by the non-planarity of two pyrrole rings with the quinoxaline core. In other words, BF_2 complexation leads to an extended π-conjugation, which renders a series of electronic transitions observable in the visible spectral region. This assumption is corroborated by the computational results (*vide infra*). All these spectroscopic results are in good agreement with the aforementioned electrochemical properties.

A successive addition of tetrabutylammonium fluoride trihydrate (TBAF) in CH_2Cl_2 leads to a profound change in the absorption spectrum of TTF–QB (Fig. 2). The occurrence of clearly defined isosbestic points at 345 nm, 530 nm and 655 nm indicates the conversion of TTF–QB to its corresponding H-bonded species with F^-. The low-energy ICT absorption band decreases at the benefit of a new ICT transition at 650 nm which is bathochromically shifted by 40 nm in good agreement with a significant colour change from blue to yellow-green. This behaviour is ascribed to the formation of N–H···F hydrogen bonds, as previously observed during the titration of the ligand TTF–PQ with the fluoride anion.[12] Concomitantly, the emergence of a strong absorption band at 410 nm occurs at the expense of the absorption band around 310 nm. Upon addition of 80 equiv. of TBAF, no further noticeable spectral changes are observed. The final spectrum resembles that of the reference QB in the presence of 80 equiv. TBAF, by exhibiting three distinct electronic transitions (Fig. S4, ESI†). As expected, all these transitions are bathochromically shifted and much stronger in TTF–QB than in QB, by virtue of the large extended π-conjugation that substantially lowers the energy level of the LUMO. In the following, quantum-chemical calculations demonstrate that the lowest energy transition of TTF–QB, when H-bonded to fluoride, corresponds to an ICT from the pyrrole···F^- unit to the QB moiety, suggesting that the direction of the ICT in TTF–QB can be regulated by adding F^-.

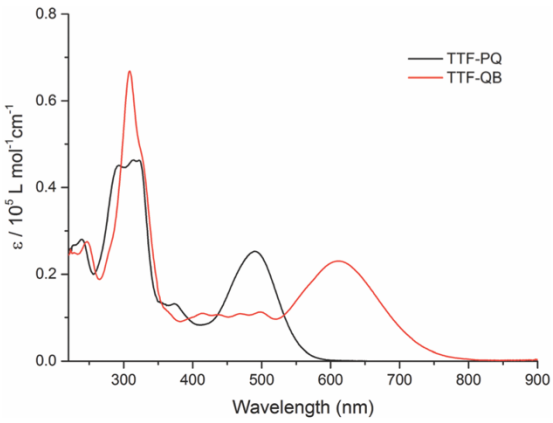

Fig. 1 The UV-Vis absorption spectra of TTF–PQ and TTF–QB (1.6×10^{-5} M) in CH_2Cl_2 at room temperature.

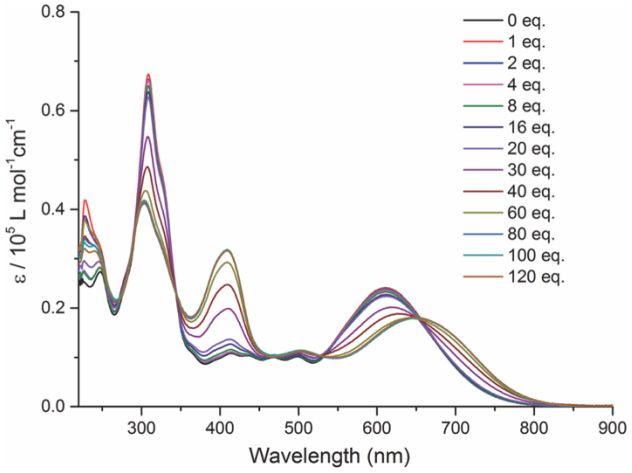

Fig. 2 Variation of UV-Vis absorption spectra of TTF–QB (1.5×10^{-5} M) in CH_2Cl_2 upon successive addition of aliquots of TBAF at room temperature.

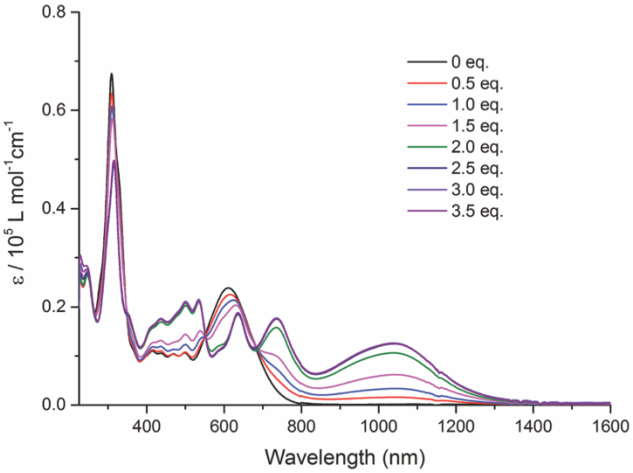

Fig. 3 Variation of UV-Vis-NIR absorption spectra of TTF–QB (1.5×10^{-5} M) in CH_2Cl_2 upon successive addition of aliquots of $NOSbF_6$ at room temperature.

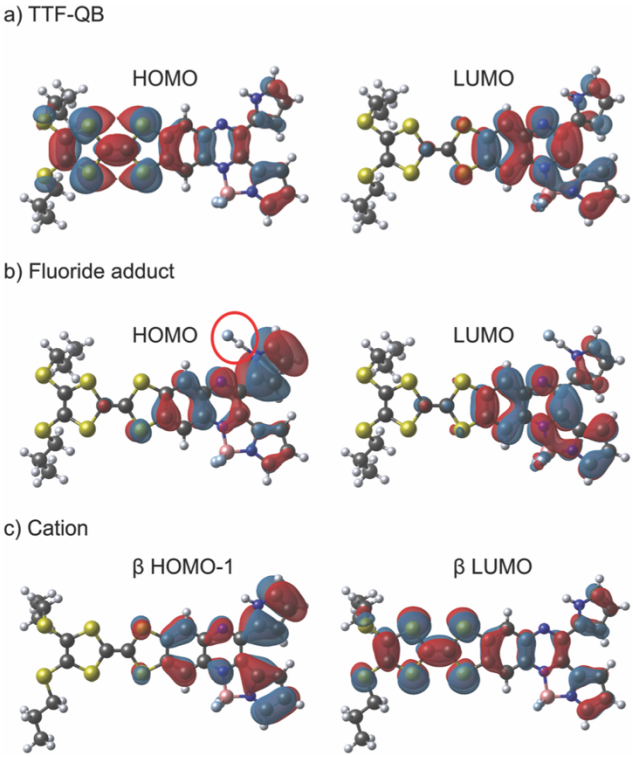

Fig. 4 Molecular orbitals of TTF–QB that are involved in the ICT transition, in the neutral state (a), in the presence of fluoride (b) and in the oxidised state (c). The red circle in (b) points to the H-bonded fluoride.

Intramolecular electronic interactions between the TTF and QB units in the TTF–QB dyad have further been explored by UV-Vis-NIR spectroscopy, whereby a chemical oxidation of TTF–QB was carried out by successive addition of $NOSbF_6$ aliquots at room temperature. As depicted in Fig. 3, a progressive reduction of the absorbance of both π–π* and ICT transitions at 310 nm and 610 nm, respectively, is accompanied with a concomitant emergence of new absorption bands at 736 nm and around 1040 nm which reach their maximum values upon addition of 2.5 equiv. of $NOSbF_6$. These new transitions are characteristic of the TTF radical cation species $TTF^{\bullet+}$ within a D–A ensemble.[13] We note that in previously reported studies on oxidised D–A compounds,[14] the lowest energy absorption band is assigned to the dimeric radical cation species arising from enforced intermolecular interactions. In the actual multicomponent molecule, however, the two lowest energy electronic transitions in the NIR around the asymmetric 1040 nm absorbance show a back CT character, which is corroborated by TD-DFT calculations in the following.

To characterise and verify the various electronic transitions, TD-DFT calculations were accomplished using the Gaussian 16[15] package at the B3LYP/6-31G(d,p) level of theory. After DFT relaxation to within default thresholds, TD-DFT calculations of the 40 lowest excited states were carried out and the absorption spectra extracted with GaussSum 3.0.[16] The predicted absorption spectra of TTF–QB, its fluoride adduct and its oxidised form are in fairly good agreement with experimental results (Tables S2–S7 and Fig. S11, ESI†). Compared to TTF–PQ, TTF–QB reveals in particular an absorption onset at a much larger wavelength. This lowest energy absorption band, peaked at 610 nm, is attributed to the $S_0 \rightarrow S_1$ excitation, almost exclusively (99%) dominated by the HOMO–LUMO transition that involves CT from the TTF to the QB moiety, as clearly shown by the associated molecular orbitals in Fig. 4a. This directionality of the longest wavelength ICT is a kind of standard for fused TTF–acceptor ensembles.[13] Similarly, also the calculated excitations at higher energy match well with the observed absorption spectrum. In the actual case of the fluoride adduct, however, the fluoride binding on the acceptor side destabilises the occupied MO localised on the QB site such that it represents now the HOMO of the dyad (Fig. 4b). Consequently, the corresponding HOMO–LUMO transition (96% of the calculated $S_0 \rightarrow S_1$ excitation) corresponds to a charge flow predominantly in an orthogonal direction and at longer wavelength compared to the former one, in full agreement with the observed bathochromic shift of the ICT band by 40 nm. The latter energy shift is well substantiated by the calculation. Also in the blue/UV spectral region, the calculated excitations represent closely the experimental absorption bands. Upon oxidation to the radical cation species $TTF^{\bullet+}$–QB, a broad and clearly asymmetric absorption feature emerges in the NIR region at wavelengths above 800 nm, which points to two new excitations. In accordance with it, the calculation of the open-shell molecule reveals two electronic transitions in the NIR part, $D_0 \rightarrow D_1$ (98% β-HOMO to β-LUMO) and $D_0 \rightarrow D_2$ (97% β-HOMO−1 to β-LUMO) at 1483 nm and 1075 nm, respectively. Importantly, both excitations reveal that upon photoexcitation, the charge flow is directed in the reverse direction, hence from the QB to the $TTF^{\bullet+}$ unit which is now the acceptor site (Fig. 4c, Tables S6 and S7, ESI†). Moreover, the calculated excitations $D_0 \rightarrow D_n$ ($n \geq 3$) cover well the experimental absorption features at wavelengths around 800 nm and lower.

In conclusion, the key finding is that, through external stimuli like fluoride binding or oxidation reaction, the

directionality of a photoinduced charge flow within a multichromophoric D–A system can be regulated. TD-DFT calculations allow the characterisation of the ground- and excited electronic states, which in turn reveals the different directions and locations of charge flow within the intricate but still compact molecule. These obtained results pave the way to manipulate photoinduced CT through various pathways by judicious design and chemical modification for potential applications in optoelectronic devices.

This work was financially supported by the Swiss NSF through the NCCR MUST "Molecular Ultrafast Science and Technology", the Swiss National Foundation (200020_188468), and SNF professorship grants (PP00P2_157615 and PP00P2_187185).

Conflicts of interest

There are no conflicts to declare.

Notes and references

1 A. Benniston, *Chem. Soc. Rev.*, 2004, **33**, 573; R. Kaur, F. Possanza, F. Limosani, S. Bauroth, R. Zanoni, T. Clark, G. Arrigoni, P. Tagliatesta and D. M. Guldi, *J. Am. Chem. Soc.*, 2020, **142**, 7898; A. Felouat, A. D'Aleo, A. Charaf-Eddin, D. Jacquemin, B. Le Guennic, E. Kim, K. J. Lee, J. H. Woo, J.-C. Ribierre, J. W. Wu and F. Fages, *J. Phys. Chem. A*, 2015, **119**, 6283; A. T. Turley, A. Danos, A. Prlj, A. P. Monkman, B. F. E. Curchod, P. R. McGonigal and M. K. Etherington, *Chem. Sci.*, 2020, **11**, 6990; M. R. Wasielewski, *Chem. Rev.*, 1992, **92**, 435; J. J. Bergkamp, S. Decurtins and S.-X. Liu, *Chem. Soc. Rev.*, 2015, **44**, 863.

2 J. E. Klare, G. S. Tulevski, K. Sugo, A. De Picciotto, K. A. White and C. Nuckolls, *J. Am. Chem. Soc.*, 2003, **125**, 6030; A. L. Kanibolotsky, I. F. Perepichka and P. J. Skabara, *Chem. Soc. Rev.*, 2010, **39**, 2695.

3 T. M. Clarke and J. R. Durrant, *Chem. Rev.*, 2010, **110**, 6736; W. Z. Yuan, Y. Gong, S. Chen, X. Y. Shen, J. W. Y. Lam, P. Lu, Y. Lu, Z. Wang, R. Hu, N. Xie, H. S. Kwok, Y. Zhang, J. Z. Sun and B. Z. Tang, *Chem. Mater.*, 2012, **24**, 1518; O. Inganas, *Adv. Mater.*, 2018, **30**, e1800388; S. Ullbrich, J. Benduhn, X. Jia, V. C. Nikolis, K. Tvingstedt, F. Piersimoni, S. Roland, Y. Liu, J. Wu, A. Fischer, D. Neher, S. Reineke, D. Spoltore and K. Vandewal, *Nat. Mater.*, 2019, **18**, 459; Y. Zhong, B. Kumar, S. Oh, M. T. Trinh, Y. Wu, K. Elbert, P. Li, X. Zhu, S. Xiao, F. Ng, M. L. Steigerwald and C. Nuckolls, *J. Am. Chem. Soc.*, 2014, **136**, 8122; C. Huang, S. Chen, K. B. Ornso, D. Reber, M. Baghernejad, Y. Fu, T. Wandlowski, S. Decurtins, W. Hong, K. S. Thygesen and S.-X. Liu, *Angew. Chem., Int. Ed.*, 2015, **54**, 14304; A. Amacher, C. Yi, J. Yang, M. P. Bircher, Y. Fu, M. Cascella, M. Graetzel, S. Decurtins and S.-X. Liu, *Chem. Commun.*, 2014, **50**, 6540.

4 S. Grunder, R. Huber, V. Horhoiu, M. T. González, C. Schönenberger, M. Calame and M. Mayor, *J. Org. Chem.*, 2007, **72**, 8337; X. Liu, X. Li, S. Sangtarash, H. Sadeghi, S. Decurtins, R. Haner, W. Hong, C. J. Lambert and S. X. Liu, *Nanoscale*, 2018, **10**, 18131; J. Chen and O. S. Wenger, *Chem. Sci.*, 2015, **6**, 3582; H. Pan, G.-L. Fu, Y.-H. Zhao and C.-H. Zhao, *Org. Lett.*, 2011, **13**, 4830.

5 J. Wu, N. Dupont, S.-X. Liu, A. Neels, A. Hauser and S. Decurtins, *Chem. – Asian J.*, 2009, **4**, 392.

6 Z. Li, H. Li, S. Chen, T. Froehlich, C. Yi, C. Schoenenberger, M. Calame, S. Decurtins, S.-X. Liu and E. Borguet, *J. Am. Chem. Soc.*, 2014, **136**, 8867.

7 Y. Chai, X. Liu, B. Wu, L. Liu, Z. Wang, Y. Weng and C. Wang, *J. Am. Chem. Soc.*, 2020, **142**, 4411.

8 D. Gust, T. A. Moore and A. L. Moore, *Chem. Commun.*, 2006, 1169.

9 M. R. Bryce, *Adv. Mater.*, 1999, **11**, 11.

10 C. Yu, E. Hao, T. Li, J. Wang, W. Sheng, Y. Wei, X. Mu and L. Jiao, *Dalton Trans.*, 2015, **44**, 13897.

11 K. Tsujimoto, R. Ogasawara, T. Nakagawa and H. Fujiwara, *Eur. J. Inorg. Chem.*, 2014, 3960; K. Tsujimoto, R. Ogasawara and H. Fujiwara, *Tetrahedron Lett.*, 2013, **54**, 1251; J. Xiong, L. Sun, Y. Liao, G.-N. Li, J.-L. Zuo and X.-Z. You, *Tetrahedron Lett.*, 2011, **52**, 6157; K.-L. Huang, N. Bellec, M. Guerro, F. Camerel, T. Roisnel and D. Lorcy, *Tetrahedron*, 2011, **67**, 8740.

12 H.-P. Jia, J. C. Forgie, S.-X. Liu, L. Sanguinet, E. Levillain, F. Le Derf, M. Salle, A. Neels, P. J. Skabara and S. Decurtins, *Tetrahedron*, 2012, **68**, 1590.

13 C. Jia, S.-X. Liu, C. Tanner, C. Leiggener, A. Neels, L. Sanguinet, E. Levillain, S. Leutwyler, A. Hauser and S. Decurtins, *Chem. – Eur. J.*, 2007, **13**, 3804; C. Jia, S. Liu, C. Tanner, C. Leiggener, L. Sanguinet, E. Levillain, S. Leutwyler, A. Hauser and S. Decurtins, *Chem. Commun.*, 2006, 1878.

14 W. Li, C. Jiao, X. Li, Y. Xie, K. Nakatani, H. Tian and W. Zhu, *Angew. Chem., Int. Ed.*, 2014, **53**, 4603; H.-P. Jia, J. Ding, Y.-F. Ran, S.-X. Liu, C. Blum, I. Petkova, A. Hauser and S. Decurtins, *Chem. – Asian J.*, 2011, **6**, 3312; J. M. Spruell, A. Coskun, D. C. Friedman, R. S. Forgan, A. A. Sarjeant, A. Trabolsi, A. C. Fahrenbach, G. Barin, W. F. Paxton, S. K. Dey, M. A. Olson, D. Benítez, E. Tkatchouk, M. T. Colvin, R. Carmielli, S. T. Caldwell, G. M. Rosair, S. G. Hewage, F. Duclairoir, J. L. Seymour, A. M. Z. Slawin, W. A. Goddard, M. R. Wasielewski, G. Cooke and J. F. Stoddart, *Nat. Chem.*, 2010, **2**, 870.

15 M. J. Frisch, G. W. Trucks, H. B. Schlegel, G. E. Scuseria, M. A. Robb, J. R. Cheeseman, G. Scalmani, V. Barone, G. A. Petersson, H. Nakatsuji, X. Li, M. Caricato, A. V. Marenich, J. Bloino, B. G. Janesko, R. Gomperts, B. Mennucci, H. P. Hratchian, J. V. Ortiz, A. F. Izmaylov, J. L. Sonnenberg, D. Williams-Young, F. Ding, F. Lipparini, F. Egidi, J. Goings, B. Peng, A. Petrone, T. Henderson, D. Ranasinghe, V. G. Zakrzewski, J. Gao, N. Rega, G. Zheng, W. Liang, M. Hada, M. Ehara, K. Toyota, R. Fukuda, J. Hasegawa, M. Ishida, T. Nakajima, Y. Honda, O. Kitao, H. Nakai, T. Vreven, K. Throssell, J. A. Montgomery Jr., J. E. Peralta, F. Ogliaro, M. J. Bearpark, J. J. Heyd, E. N. Brothers, K. N. Kudin, V. N. Staroverov, T. A. Keith, R. Kobayashi, J. Normand, K. Raghavachari, A. P. Rendell, J. C. Burant, S. S. Iyengar, J. Tomasi, M. Cossi, J. M. Millam, M. Klene, C. Adamo, R. Cammi, J. W. Ochterski, R. L. Martin, K. Morokuma, O. Farkas, J. B. Foresman and D. J. Fox, *Gaussian 16 Revision C.01*, Gaussian, Inc., Wallingford, CT, 2016.

16 N. M. O'Boyle, A. L. Tenderholt and K. M. Langner, *J. Comput. Chem.*, 2008, **29**, 839.

3. TAP-based donor-acceptor (D-A) systems

This section is partially adapted to the following publication:

a. Effect of *tert*-butyl groups on electronic communication between redox units in tetrathiafulvalene-tetraazapyrene triads

Ping Zhou, *Ulrich Aschauer, Silvio Decurtins, Thomas Feurer, Robert Häner and Shi-Xia Liu*

Chem. Commun., 2021, **57**, 12972.

https://doi.org/10.1039/D1CC05671A

b. Modulate lifetime of charge separation state

Ping Zhou, *Maryam Nazari Haghighi Pashaki, Ulrich Aschauer, Hans-Martin Frey, Silvio Decurtins, Andrea Cannizzo, Thomas Feurer, Robert Häner, and Shi-Xia Liu*

Manuscript in preparation

Contribution to the work

My contribution includes synthesis and characterization of target compounds by NMR and MS and a detailed study of their electronic properties by cyclic voltammetry and UV-Vis spectra in neutral and oxidized states. Importantly, an efficient protocol for the functionalization of the tetraazapyrene (TAP) core has been developed, which paves the way for the collaborative research on self-assembly and surface-assisted chemical reactions of TAP building blocks, as well as for designing new D-A molecules in the future. Prof. Ulrich Aschauer did the TD-DFT calculations and analyzed various transitions. Prof. Andrea Cannizzo and Dr. Maryam Nazari Haghighi Pashaki, from the institute of applied physics of Bern University, performed transient absorption measurements and analyzed these data. The initial manuscript was written by me and revised by my supervisors.

3.1 Electronic communication

3.1.1 Article

Effect of *tert*-butyl groups on electronic communication between redox units in tetrathiafulvalene-tetraazapyrene triads

ChemComm

COMMUNICATION

View Article Online
View Journal | View Issue

Cite this: *Chem. Commun.*, 2021, **57**, 12972

Received 7th October 2021,
Accepted 12th November 2021

DOI: 10.1039/d1cc05671a

rsc.li/chemcomm

Effect of *tert*-butyl groups on electronic communication between redox units in tetrathiafulvalene-tetraazapyrene triads†

Ping Zhou,[a] Ulrich Aschauer,[a] Silvio Decurtins,[a] Thomas Feurer,[b] Robert Häner[a] and Shi-Xia Liu *[a]

The electronic effect of *tert*-butyl groups on intramolecular through-bond interactions between redox units in tetrathiafulvalene-tetraazapyrene (TAP) triads is investigated. The insertion of *tert*-butyl groups raises the TAP-localised LUMO level by 0.21 eV, in fairly good agreement with 0.17 eV determined by DFT calculations.

Tetraazapyrene (TAP), a prototype of nitrogenated polycyclic aromatic hydrocarbons (N-PAHs), exhibits intrinsic optoelectronic and electrochemical properties as well as high thermal and chemical stability, which are important requirements for its diverse applications in the field of organic (opto)electronics.[1,2] However, reports on synthetic approaches to the TAP scaffold and its derivatization are quite limited in the literature.[3] In 2012, a series of 2,7-substituted TAP derivatives was prepared and tested as n-type semiconductors in organic field-effect transistors (OFETs).[1] It has been demonstrated that the electronic properties are significantly affected by the nature of substituents at the core positions. Inspired by these appealing results, we have embarked on the design and synthesis of tetrathiafulvalene (TTF)-functionalized TAPs to create triads (Scheme 1) with promising material properties.

Within the context of organic conductors, TTF acts as a strong π-electron donor and takes a prominent place in this class of materials.[4] By virtue of its unique redox properties, it has been incorporated into a variety of (supra)molecular architectures for the development of highly efficient (opto)electronic materials.[5] Among them, TTF-based electron donor–acceptor (D–A) ensembles have attracted a lot of attention with a special focus on redox modulation of intramolecular charge transfer (ICT) and chemical/optical control over multiple ICT pathways.[6,7] Herein, we report a facile and efficient synthetic protocol to 2,7-di-*tert*-butyl-1,3,6,8-tetraazapyrene (**2**) as well as the further derivatization by 4-fold core-bromination for subsequent nucleophilic substitutions with a cyanoethyl-protected TTF (**4**), leading to the formation of two triads **TTF-TAP** and **TTF-*t*-Bu-TAP** with a D–A–D architecture (Scheme 1).

It is well known that bulky *tert*-butyl groups have been widely incorporated into large N-PAH molecules for improved solubility because of suppressed aggregation.[8,9] Also, *tert*-butylation has been exploited to bias regioselectivity, *e.g.* insertion of *tert*-butyl groups into 2,7 positions of pyrene can avoid the reaction occurring at the electron-rich 1,3,6,8-carbons instead of the *K*-region (4,5,9,10-carbons).[10] This work aims to reveal the effects of *tert*-butyl groups[9,11] on the electronic characteristics of the triads. Redox and optical properties of **TTF-TAP** and **TTF-*t*-Bu-TAP** have been investigated in detail. The insertion of *tert*-butyl groups at positions 2 and 7 of the TAP core has indeed a very pronounced effect on the TAP-localised LUMO energy level.

As illustrated in Scheme 1, our synthetic approach to the 2,7-substituted TAP scaffold **2** involves a twofold cyclocondensation of naphthalene-1,4,5,8-tetraamine tin(II) salt (**1**)[12] with an excess of pivalic anhydride, followed by oxidation of the intermediate 1,8-dihydropyrimido[4,5,6-*gh*]perimidine. This reaction was performed at reflux in THF in the presence of catalytic amounts of triethylamine, affording **2** as a pale-yellow powder in a yield of 60%. The subsequent core-bromination was accomplished to yield **3** (70%) in concentrated sulfuric acid in the presence of Br_2 with catalytic amounts of iodine, similar to the synthetic procedure reported for **5**.[1] Both 4-fold core-brominated compounds **3** and **5** undergo nucleophilic substitution with **4** in the presence of CsOH/MeOH to produce the desired products **TTF-*t*-Bu-TAP** and **TTF-TAP** in a yield of 18% and 24%, respectively. These as-prepared compounds were unambiguously characterized by ^{1}H and ^{13}C NMR, cyclic voltammetry, UV-Vis-NIR spectroscopy and high-resolution mass spectrometry. All analytical data match well with their chemical structures.

The electrochemical properties of **TTF-TAP**, **TTF-*t*-Bu-TAP** and the reference compounds **2** and **4** were investigated by cyclic voltammetry and differential pulse voltammetry in CH_2Cl_2 (Fig. 1 and Table S1, Fig. S1, ESI†). **TTF-TAP** undergoes three distinct

[a] *Department of Chemistry, Biochemistry and Pharmaceutical Sciences, University of Bern, Freiestrasse 3, Bern CH-3012, Switzerland. E-mail: shi-xia.liu@unibe.ch*
[b] *Institute of Applied Physics, University of Bern, Sidlerstrasse 5, Bern CH-3012, Switzerland*

† Electronic supplementary information (ESI) available. See DOI: 10.1039/d1cc05671a

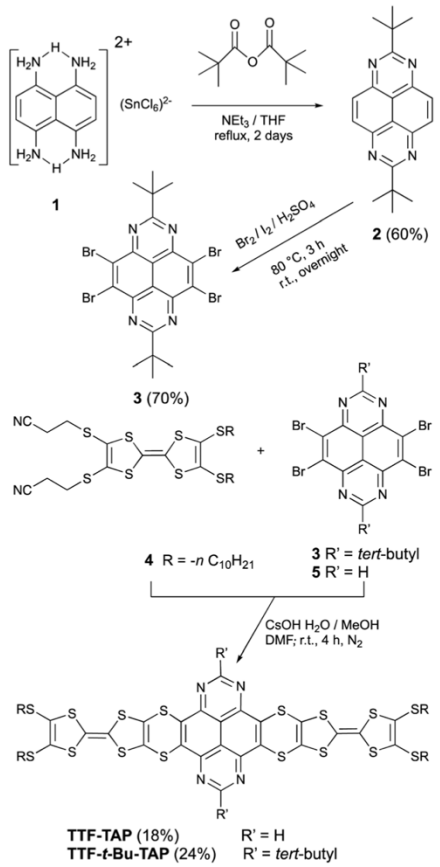

Scheme 1 Synthesis of a key precursor **3**, triads **TTF-TAP** and **TTF-*t*-Bu-TAP**.

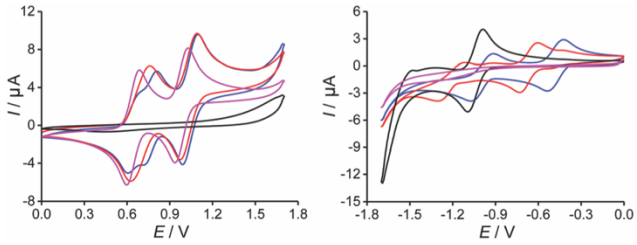

Fig. 1 Cyclic voltammograms of **TTF-TAP** (blue), **TTF-*t*-Bu-TAP** (red), *t*-Bu-TAP **2** (black) and TTF precursor **4** (pink) were measured in dichloromethane solution (c = 3 × 10^{-4} M), containing 0.1 M $TBAPF_6$ as the supporting electrolyte at room temperature, Pt working electrode, Ag/AgCl electrode as the reference electrode and the scan rate at 100 mV s^{-1}.

reversible oxidation processes at 0.63 V, 0.77 V and at 1.06 V (*vs.* Ag/AgCl), indicating that two TTF units are successively oxidized to TTF radical cation species and simultaneously to TTF dication species. This phenomenon remains even in a very diluted solution (Fig. S2, ESI†), indicating that the possibility of associations between TTF-TAP molecules is ruled out, which can further be verified by concentration-dependent UV-Vis spectra (Fig. S3, ESI†). The occurrence of step-wise oxidation processes for the generation of the radical cation species points to significant intramolecular through-bond interactions between two TTF units, as previously observed in analogous molecules.[13] In the negative potential window, two reversible reduction waves at −0.46 V and −0.98 V are observed, corresponding to the sequential addition of electrons to the TAP unit. Interestingly, the incorporation of *tert*-butyl group has an appreciable influence on the redox properties of TTF and TAP units. **TTF-*t*-Bu-TAP** shows only two reversible oxidation waves at 0.70 V and 1.03 V (Fig. S1, ESI†), suggesting that two TTF units are simultaneously oxidized to their radical cation and dication species, respectively. Similarly, it undergoes two reversible reductions at −0.67 V and −1.19 V, which, however, are negatively shifted compared to **TTF-TAP**. Consequently, the insertion of *tert*-butyl groups raises the LUMO level by 0.21 eV, very probably due to the hyperconjugation effect of the *tert*-butyl groups, but an electrostatic destabilization of the TAP-localized π* MO can also be invoked based on computed electrostatic potentials at nuclear positions (Table S2, ESI†). The first reduction potential values of both triads are positively shifted with respect to that of the TAP, ref. 2 indicative of the extended conjugation *via* four S atoms caused by the covalent linkage of two TTF units to the central TAP core. In stark contrast, their oxidation potentials are either shifted only slightly positively or remain almost unchanged compared to those of the TTF precursor **4**, most likely because of the lack of an effective electronic communication between the redox units. The latter is a consequence of nonplanar conformations of the triads, as shown by the corresponding calculated structures (Fig. S4, ESI†). As a result, both triads show pronouncedly lowered LUMO energies while maintaining similar HOMO energies with respect to the constituting moieties **2** and **4**, which matches well the UV-Vis spectroscopic results presented below.

TTF-TAP and **TTF-*t*-Bu-TAP** strongly absorb in the UV-Visible-NIR spectral region as evidenced by their yellow-green colour. Their absorption spectra in CH_2Cl_2 are depicted in Fig. 2.

In the UV and blue part of the optical spectra, the observed strong absorption bands are attributed to π–π* transitions localized on the TTF and TAP cores, similarly to the reference compounds **2** and **4**, only with bathochromic shifts owing to extended conjugation. By comparison of **TTF-*t*-Bu-TAP** (red) to **TTF-TAP** (blue), the insertion of the *tert*-butyl groups leads to

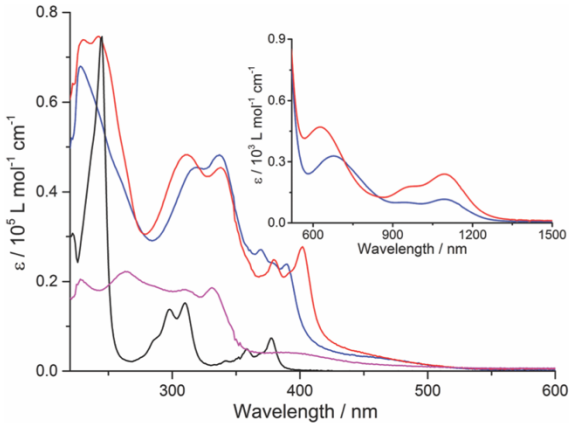

Fig. 2 UV-Vis absorption spectra of **TTF-TAP** (blue), **TTF-*t*-Bu-TAP** (red), *t*-Bu-TAP **2** (black) and TTF precursor **4** (pink) (c = 7 × 10^{-6} M) in CH_2Cl_2 at r.t. Inset: Vis-NIR absorption spectra of **TTF-TAP**, **TTF-*t*-Bu-TAP** (c = 7 × 10^{-4} M) in CH_2Cl_2 at r.t.

noticeable bathochromic shifts of the absorption bands in a range of 360 nm to 450 nm and a slight hypsochromic shift of the absorption band around 320 nm. As these transitions correspond mainly to π–π* excitations of the TAP core, the observed shifts can be accounted for by the fact that the presence of bulky *tert*-butyl groups at 2,7-positions of the TAP is unfavourable for possible *H*- and *J*-aggregation and impedes effective intermolecular interactions. More importantly, both triads exhibit two weak and broad absorption bands centered at 680 nm and 1100 nm for **TTF-TAP**, and 630 nm and 1100 nm for **TTF-*t*-Bu-TAP**, which are not observed, however, in solutions of the acceptor **2** and donor **4** components. Consequently, these absorptions reflect ICT transitions dominated by excitations from MOs localized on the TTF units to the LUMO localized on the TAP core. These assignments are corroborated by the computational results (see below). An attempt can be made to approach with some uncertainties the onsets of the very weak and broad absorption bands of both triads in the NIR region (Fig. 2) while extrapolating the linear portions on their red sides to the abscissa. Their optical bandgaps lie approximately between 1 eV and 0.92 eV, with the higher value assigned to the more steeply falling absorption edge of the **TTF-*t*-Bu-TAP** triad, a trend compliant with the electrochemical study.

In order to shed more light on the intramolecular electronic interactions between the TTF and TAP units in **TTF-TAP** and **TTF-*t*-Bu-TAP**, spectroelectrochemical measurements were carried out. Chemical oxidation of **TTF-TAP** and **TTF-*t*-Bu-TAP** was performed by successive addition of $NOSbF_6$ aliquots at room temperature. As shown in Fig. 3 for **TTF-TAP**, a progressive reduction of the absorbance of the high energy π–π* transitions is accompanied with a concomitant appearance of new absorption bands at 452 nm and 835 nm which reach their maximum values upon addition of 12 equiv. of $NOSbF_6$. The lowest energy absorption band is continuously blue-shifted during the oxidation process. These new transitions are characteristic of the newly formed cationic $TTF^{\bullet+}$ radical within a D–A–D triad.[13,14] In contrast, the initial oxidation of **TTF-*t*-Bu-TAP** leads to a broad absorption band which emerges at 905 nm and, after addition of 1.2 equiv., suddenly moves towards higher energy (830 nm) with increasing amounts of $NOSbF_6$ (Fig. 4). Again, it reaches its maximum value upon addition of 12 equiv. of $NOSbF_6$. In both cases, this broad and distinctly asymmetric absorption band in the NIR region is mainly attributed to electronic transitions localized on the $TTF^{\bullet+}$ unit with some back ICT character from the TAP unit to the radical species $TTF^{\bullet+}$, however to a much lesser extent than previously reported in TTF-fused D–A systems.[7,14,15] This result could be accounted for by their non-planar geometries (Fig. S4, ESI†). Moreover, the observed variance in the evolution of the absorption spectra in this spectral region is very probably due to different degrees of intermolecular π-dimerization of the $TTF^{\bullet+}$ radical cation imparted by sequential or simultaneous oxidation of two TTF cores in **TTF-TAP** and **TTF-*t*-Bu-TAP**, as corroborated by CV measurements.

To characterize and verify the various electronic transitions, TD-DFT calculations were performed using the Gaussian 16 package at the B3LYP/6-31G(d,p) level of theory.[16] The predicted absorption spectra of **TTF-TAP** and **TTF-*t*-Bu-TAP** (Fig. S5, ESI†) are in fairly good agreement with experimental results. Fig. 5 illustrates the frontier MOs of **TTF-TAP** which are involved in the ICT transitions. The HOMO and HOMO−1

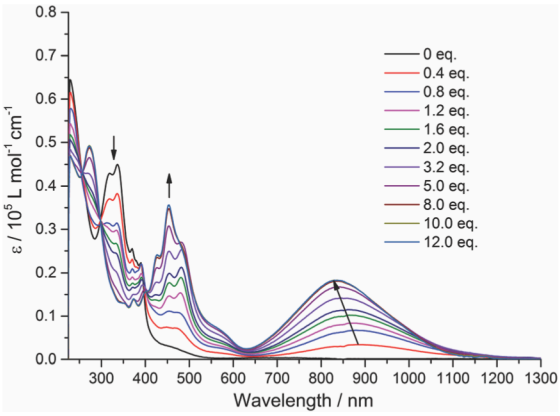

Fig. 3 Variation of UV-Vis-NIR absorption spectra of **TTF-TAP** (7×10^{-6} M) in CH_2Cl_2 upon successive addition of aliquots of $NOSbF_6$ at room temperature.

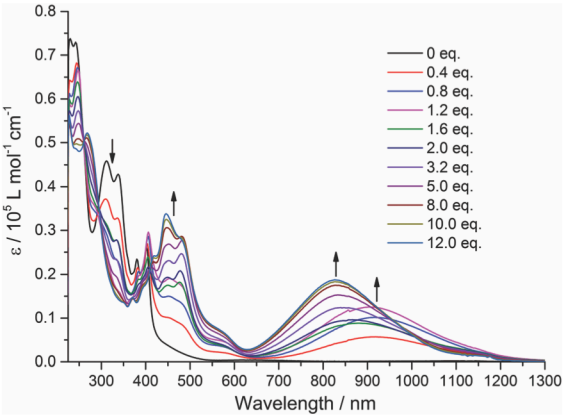

Fig. 4 Variation of UV-Vis-NIR absorption spectra of **TTF-*t*-Bu-TAP** (7×10^{-6} M) in CH_2Cl_2 upon successive addition of aliquots of $NOSbF_6$ at room temperature.

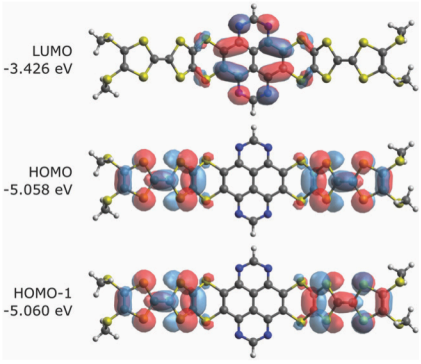

Fig. 5 Frontier molecular orbitals of **TTF-TAP** that are involved in the ICT transition.

represent the symmetric and asymmetric combinations of the two donor TTF MOs. Analogously, HOMO−2 and HOMO−3 combine both pending units, however, the TAP core is now partly involved in their electron densities (Fig. S6, ESI†). The LUMO is localized at the acceptor TAP core with some extension to the adjacent sulfur atoms. The frontier MOs of **TTF-*t*-Bu-TAP** (Fig. S6, ESI†) show the same characteristics. The calculated HOMO–LUMO gap amounts to 1.63 eV for **TTF-TAP** and 1.76 eV for **TTF-*t*-Bu-TAP**.

The predicted absorption spectra for both triads (Fig. S5, ESI†) show a manifold of π–π* transitions with high oscillator strengths at wavelength below 450 nm, in good agreement with the measured absorption spectra. The measured low intensity absorptions around 630–680 nm are well characterized by calculated HOMO−2/HOMO−3 → LUMO excitations, fairly close to that energy range and also with low oscillator strengths (Tables S3 and S4, ESI†). The same holds for the very weak longest wavelength absorptions which are now attributed to HOMO/HOMO−1 → LUMO excitations. Clearly, the orbital overlap among these MOs is little, which leads to a small transition dipole moment, hence low intensities for their transitions. To note, there is a distinct blue-shift for these calculated excitations for the **TTF-*t*-Bu-TAP** triad compared to **TTF-TAP**. Fig. S7 and Tables S5–S8 (ESI†) show the calculated transitions and the involved open-shell molecular orbitals (Fig. S8–S11, ESI†) for the +1 and +2 cationic states of both triads which by and large look similar. Upon oxidation of two TTF units to their radical states, the involved molecular orbitals of the NIR transitions reveal that the majority of charge remains on the TTF units.

In conclusion, the newly synthesized **TTF-TAP** and **TTF-*t*-Bu-TAP** absorb in the UV-Vis-NIR spectral region due to ICT excitations from TTF units to the central TAP core. Interestingly, the two TTF units of **TTF-TAP** are sequentially oxidized to the TTF radical cation species while this process occurs simultaneously in **TTF-*t*-Bu-TAP**. With respect to **TTF-TAP**, the LUMO level of **TTF-*t*-Bu-TAP** is raised by 0.21 eV. Also it is worthy of note that a modification at the TTF side would potentially be a tuning factor in the molecule as well.[17] Our findings represent a novel concept in the manipulation of the relative HOMO and LUMO energetic positions of organic donor–acceptor ensembles by chemical modification.

We greatly appreciate preliminary clarifications on these systems by Dirk Guldi. This work was financially supported by the Swiss NSF through the NCCR MUST "Molecular Ultrafast Science and Technology", the Swiss NSF (200020_188468 and 200021_204053), and the Swiss NSF professorship grants (PP00P2_157615 and PP00P2_187185). Computations were performed on Ubelix, the HPC cluster at the University of Bern.

Conflicts of interest

There are no conflicts to declare.

Notes and references

1 S. Geib, S. C. Martens, U. Zschieschang, F. Lombeck, H. Wadepohl, H. Klauk and L. H. Gade, *J. Org. Chem.*, 2012, **77**, 6107.
2 S. C. Martens, L. Hahn, F. Lombeck, A. Rybina, H. Wadepohl and L. H. Gade, *Eur. J. Org. Chem.*, 2013, 5295; M. J. Sienkowska, J. M. Farrar, F. Zhang, S. Kusuma, P. A. Heiney and P. Kaszynski, *J. Mater. Chem.*, 2007, **17**, 1399; Y.-R. Shi, H.-L. Wei and Y.-F. Liu, *New J. Chem.*, 2019, **43**, 5706.
3 A. V. Aksenov, D. S. Ovcharov, N. A. Aksenov, D. A. Aksenov, O. N. Nadein and M. Rubin, *RSC Adv.*, 2017, **7**, 29927; A. V. Aksenov, A. S. Lyakhovnenko, T. S. Perlova and I. V. Aksenova, *Chem. Heterocycl. Compd.*, 2011, **47**, 916.
4 D. Canevet, M. Salle, G. Zhang, D. Zhang and D. Zhu, *Chem. Commun.*, 2009, 2245; J. L. Segura and N. Martin, *Angew. Chem., Int. Ed.*, 2001, **40**, 1372; N. Martin, *Chem. Commun.*, 2013, **49**, 7025.
5 A. Jana, S. Bahring, M. Ishida, S. Goeb, D. Canevet, M. Salle, J. O. Jeppesen and J. L. Sessler, *Chem. Soc. Rev.*, 2018, **47**, 5614; Y. Wu, M. Frasconi, W. G. Liu, R. M. Young, W. A. Goddard, M. R. Wasielewski and J. F. Stoddart, *J. Am. Chem. Soc.*, 2020, **142**, 11835; L. Tan, Y. Guo, Y. Yang, G. Zhang, D. Zhang, G. Yu, W. Xu and Y. Liu, *Chem. Sci.*, 2012, **3**, 2530; J. Wu, N. Dupont, S.-X. Liu, A. Neels, A. Hauser and S. Decurtins, *Chem. – Asian J.*, 2009, **4**, 392; K. Herve, S.-X. Liu, O. Cador, S. Golhen, Y. Le Gal, A. Bousseksou, H. Stoeckli-Evans, S. Decurtins and L. Ouahab, *Eur. J. Inorg. Chem.*, 2006, 3498.
6 F. Pop and N. Avarvari, *Chem. Commun.*, 2016, **52**, 7906; J. J. Bergkamp, S. Decurtins and S.-X. Liu, *Chem. Soc. Rev.*, 2015, **44**, 863; E. J. Rohwer, Y. Geng, M. Akbarimoosavi, L. M. L. Daku, O. Aleveque, E. Levillain, J. Hauser, A. Cannizzo, R. Häner, S. Decurtins, R. J. Stanley, T. Feurer and S. X. Liu, *Chem. – Eur. J.*, 2021, **27**, 5399.
7 P. Zhou, U. Aschauer, S. Decurtins, T. Feurer, R. Häner and S. X. Liu, *Chem. Commun.*, 2020, **56**, 13421.
8 B. Gao, M. Wang, Y. Cheng, L. Wang, X. Jing and F. Wang, *J. Am. Chem. Soc.*, 2008, **130**, 8297; L. Zoephel, V. Enkelmann, R. Rieger and K. Muellen, *Org. Lett.*, 2011, **13**, 4506; N. Kulisic, S. More and A. Mateo-Alonso, *Chem. Commun.*, 2011, **47**, 514.
9 Z.-H. Wu, Z.-T. Huang, R.-X. Guo, C.-L. Sun, L.-C. Chen, B. Sun, Z.-F. Shi, X. Shao, H. Li and H.-L. Zhang, *Angew. Chem., Int. Ed.*, 2017, **56**, 13031.
10 H. Bock, D. Subervie, P. Mathey, A. Pradhan, P. Sarkar, P. Dechambenoit, E. A. Hillard and F. Durola, *Org. Lett.*, 2014, **16**, 1546; T. H. El-Assaad, K. N. Parida, M. F. Cesario and D. V. McGrath, *Green Chem.*, 2020, **22**, 5966.
11 J. Shao, J. Chang and C. Chi, *Org. Biomol. Chem.*, 2012, **10**, 7045.
12 V. Vitske, C. König, O. Hübner, E. Kaifer and H.-J. Himmel, *Eur. J. Inorg. Chem.*, 2010, 115.
13 H.-P. Jia, S.-X. Liu, L. Sanguinet, E. Levillain and S. Decurtins, *J. Org. Chem.*, 2009, **74**, 5727; C. Jia, S. Liu, C. Tanner, C. Leiggener, L. Sanguinet, E. Levillain, S. Leutwyler, A. Hauser and S. Decurtins, *Chem. Commun.*, 2006, 1878.
14 C. Jia, S.-X. Liu, C. Tanner, C. Leiggener, A. Neels, L. Sanguinet, E. Levillain, S. Leutwyler, A. Hauser and S. Decurtins, *Chem. – Eur. J.*, 2007, **13**, 3804.
15 M. Jaggi, C. Blum, B. S. Marti, S.-X. Liu, S. Leutwyler and S. Decurtins, *Org. Lett.*, 2010, **12**, 1344.
16 M. J. Frisch, G. W. Trucks, H. B. Schlegel, G. E. Scuseria, M. A. Robb, J. R. Cheeseman, G. Scalmani, V. Barone, G. A. Petersson, H. Nakatsuji, X. Li, M. Caricato, A. V. Marenich, J. Bloino, B. G. Janesko, R. Gomperts, B. Mennucci, H. P. Hratchian, J. V. Ortiz, A. F. Izmaylov, J. L. Sonnenberg, D. Williams-Young, F. Ding, F. Lipparini, F. Egidi, J. Goings, B. Peng, A. Petrone, T. Henderson, D. Ranasinghe, V. G. Zakrzewski, J. Gao, N. Rega, G. Zheng, W. Liang, M. Hada, M. Ehara, K. Toyota, R. Fukuda, J. Hasegawa, M. Ishida, T. Nakajima, Y. Honda, O. Kitao, H. Nakai, T. Vreven, K. Throssell, J. A. Montgomery Jr., J. E. Peralta, F. Ogliaro, M. J. Bearpark, J. J. Heyd, E. N. Brothers, K. N. Kudin, V. N. Staroverov, T. A. Keith, R. Kobayashi, J. Normand, K. Raghavachari, A. P. Rendell, J. C. Burant, S. S. Iyengar, J. Tomasi, M. Cossi, J. M. Millam, M. Klene, C. Adamo, R. Cammi, J. W. Ochterski, R. L. Martin, K. Morokuma, O. Farkas, J. B. Foresman and D. J. Fox, *Gaussian 16 Revision C.01*, Gaussian, Inc., Wallingford, CT, 2016.
17 P. J. Skabara and M. Sallé, *Beilstein J. Org. Chem.*, 2015, **11**, 1528; J. Sly, P. Kasák, E. Gomar-Nadal, C. Rovira, L. Górriz, P. Thordarson, D. B. Amabilino, A. E. Rowan and R. J. M. Nolte, *Chem. Commun.*, 2005, 1255; E. Gomar-Nadal, L. Mugica, J. Vidal-Gancedo, J. Casado, J. T. L. Navarrete, J. Veciana, C. Rovira and D. B. Amabilino, *Macromolecules*, 2007, **40**, 7521; A. M. Amacher, J. Puigmarti-Luis, Y. Geng, V. Lebedev, V. Laukhin, K. Kraemer, J. Hauser, D. B. Amabilino, S. Decurtins and S.-X. Liu, *Chem. Commun.*, 2015, **51**, 15063.

3.2 Modulate lifetime of charge separation state

3.2.1 Introduction

In the past two decades, TTF and its numerous derivatives are strong redox-active electron-donor molecules with unique electronic properties, and therefore have been widely used in the fields of solar cells, conductors,[77-79] electrochemical sensors,[80-82] and switches.[83] Nitrogenated polycyclic aromatic hydrocarbons (N-PAHs) have been invested recently because of their unique optoelectronic and electrochemical properties.[51, 84] TAP, as a new type of electron acceptor, is an interesting building block for the development of organic materials in the field of organic (opto) electronics.[14, 24, 85] Compared to pyrene, TAP is however, much less known due to the lack of efficient and convenient synthetic protocols to derivatization. To tackle this challenge, I have successfully synthesised symmetric non-fused 2TTF-TAP triads with or without *tert*-butyl groups at 2.7-positions of the TAP core. The electrochemical measurements by cyclic voltammetry demonstrate that they show good reversible oxidation and reduction waves. However, no strong ICT interactions between the TTF and TAP units occur.[85] To circumvent this problem, I have further embarked on the design and synthesis of TTF-TAP fused systems without, with one and two TTF units. A facile and efficient synthetic protocol to a key precursor, 2,7-di-t-butyl-4,5,9,10-tetraone-1,3,6,8-tetraazapyrene (**4**) has been developed. Schiff-base condensation of **4** with different equivalents of 5,6-diamino-2-(4,5-bis(propylthio)-1,3-dithio-2-ylidene)benzo[*d*]-1,3-dithiole (**TTF-2NH$_2$**) and 4,5-diaminophthalonitrile, respectively, led to the formation of **quinoxaline-TAP-TTF**, **TTF-TAP-TTF** and **diquinoxaline-TAP** (Scheme 1).

CT dynamics in D-A systems investigated by time-resolved transient spectroscopy demonstrated that electron-accepting strength governs whether electronic coupling dictates charge recombination (CR) rate: the strong and moderate-strength acceptors support more stable CS states with weaker coupling and longer lifetimes.[86] In a polar solvent, the CR rate increases substantially with strong acceptors, leading to a decrease in the lifetime of the CS state.[87] Therefore, this work aims to reveal the effect of spatial arrangement of D and A units in different architectures on ICT dynamics. Redox and optical properties of **quinoxaline-TAP-TTF**, **TTF-TAP-TTF** and **diquinoxaline-TAP** have been investigated in detail. It has been found that the symmetric **TTF-TAP-TTF** triad show the CS state with a longer lifetime,

namely, more than two orders of magnitude compared to the asymmetric **quinoxaline-TAP-TTF**.

3.2.2 Results and discussion

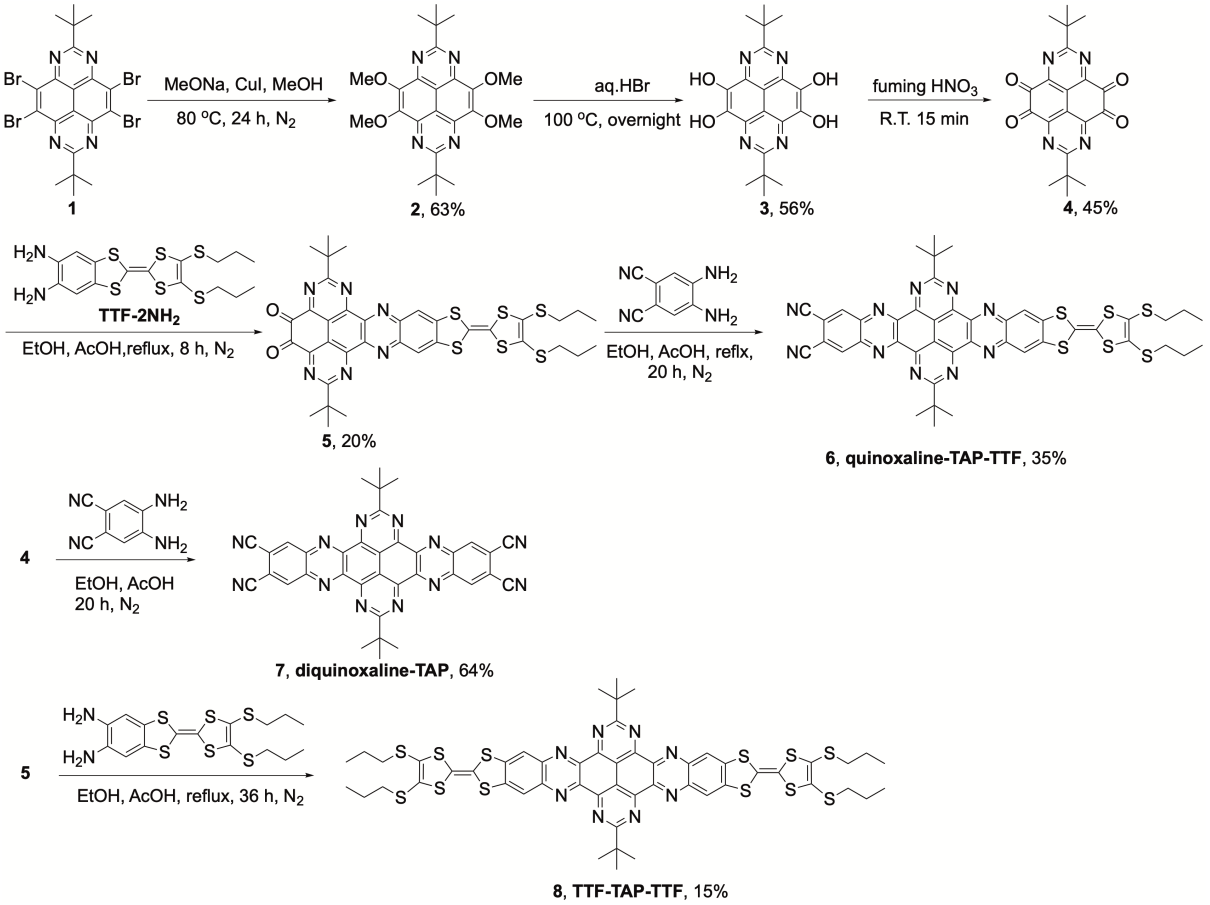

Scheme 1 Synthetic routes to asymmetric and symmetric donor-acceptor compounds.

As illustrated in **Scheme 1**, our synthetic approach to target compounds starts with the aromatic nucleophilic substitution (S_NAr) reaction of methoxy anions to 2,7-di-*t*-butyl-4,5,9,10-tetrabromo-1,3,6,8-tetraazapyrene (**1**) forming the 2,7-di-*t*-butyl-4,5,9,10-tetramethoxy-1,3,6,8-tetraazapyrene (**2**, yield 63%), following by acidic hydrolysis of **2** under HBr aq. to afford 2,7-di-*t*-butyl-4,5,9,10-tetrahydroxy-1,3,6,8-tetraazapyrene (**3**, yield 90%), and then oxidation of **3** in the presence of fuming nitric acid to obtain precursor 2,7-di-*t*-butyl-4,5,9,10-tetraone-1,3,6,8-tetraazapyrene (**4**) in a yield of 45%. The desired compounds **quinoxaline-TAP-TTF**, **diquinoxaline-TAP** and **TTF-TAP-TTF** were obtained *via* direct condensation of **TTF-2NH$_2$** and 4,5-diaminophthalonitrile with the precursor **4** in the presence of acetic acid/EtOH in 35%, 64% and 15% yields, respectively. Stable **quinoxaline-TAP-TTF**, **diquinoxaline-TAP** and **TTF-TAP-TTF** were obtained as a dark blue, yellow and dark blue

solid, respectively, and purified either by chromatographic separation or by filtration. These compounds have been unambiguously characterized by ^{1}H and ^{13}C NMR, cyclic voltammetry, UV-Vis-NIR spectroscopy as well as by high resolution mass spectrometry. All analytical data match well with their chemical structures.

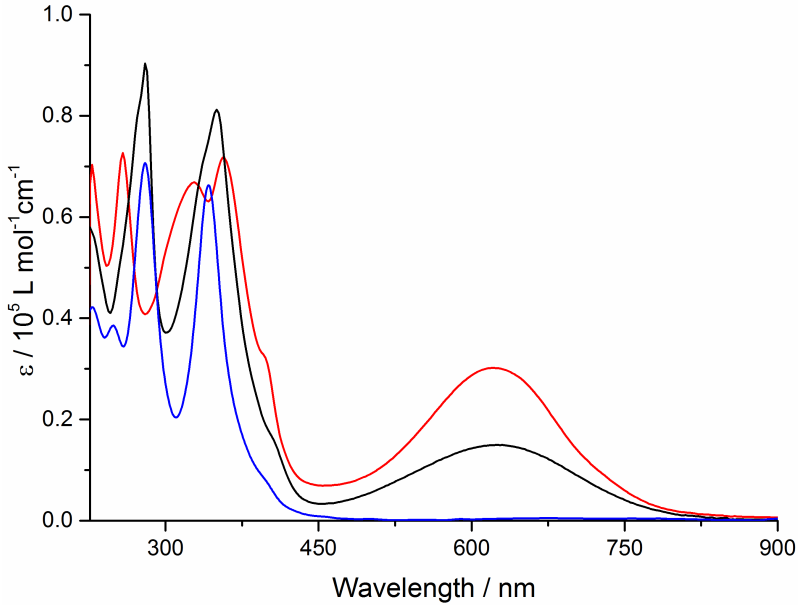

Figure 1 The UV-Vis absorption spectra of **quinoxaline-TAP-TTF** (black), **TTF-TAP-TTF** (red) and **diquinoxaline-TAP** (blue) (c = 5×10^{-6} M) in DCM r.t.

Both **quinoxaline-TAP-TTF** and **TTF-TAP-TTF** strongly absorb over an extended range in the UV-Vis spectral region ($c = 5\times10^{-6}$ M in DCM) (**Figure 1**). A strong and broad absorption band ($\varepsilon \approx 1.5\times10^{4}$ L mol^{-1} cm^{-1} and $\varepsilon \approx 3.0\times10^{4}$ L mol^{-1} cm^{-1}, respectively) peaked at 620 nm is attributed to an ICT transition from the TTF unit to the TAP-quinoxaline moiety as confirmed theoretically. This transition in both cases occurs at the same energy, but the amplitude increases with the number of TTF units, suggesting that one TTF unit does not affect the ICT from the other. In the UV and blue part of the optical spectra, a series of very intense absorption bands are observed between 400 nm and 230 nm, which is attributed to π–π* transitions localized on the TTF and TAP cores. These spectral features are in stark contrast with **diquinoxaline-TAP**. **TTF-TAP-TTF** shows a strong band around 320 nm, which is blue-shifted compared to **quinoxaline-TAP-TTF**, pointing to an interaction between the two TTF units, mediated by the TAP one. According to the onset of the lowest energy absorption band, the estimated optical HOMO-LOMO gaps of the **quinoxaline-TAP-TTF** and **TTF-TAP-TTF** are the same.

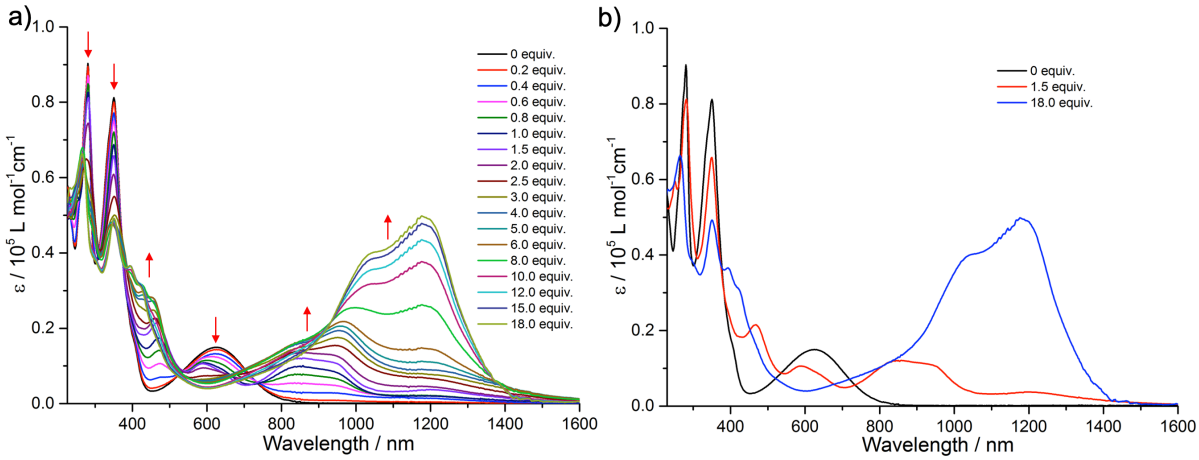

Figure 2 Variation of UV-Vis-NIR absorption spectra of **quinoxaline-TAP-TTF** (5×10^{-6} M) in DCM upon successive addition of aliquots of $NOSbF_6$ at r.t.

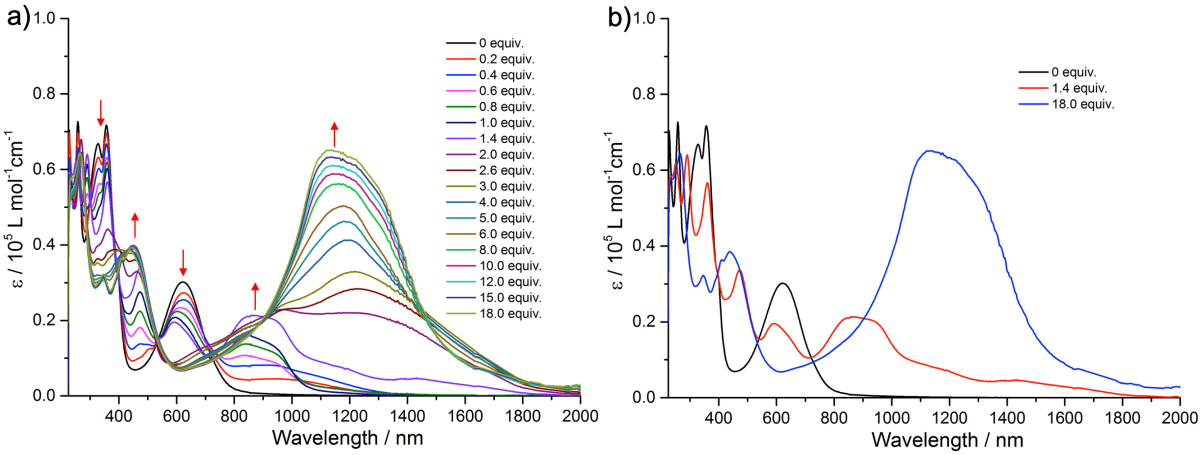

Figure 3 Variation of UV-Vis-NIR absorption spectra of **TTF-TAP-TTF** (5×10^{-6} M) in DCM upon successive addition of aliquots of $NOSbF_6$ at r.t.

In order to deeply understand the intramolecular electronic interactions between the TTF, TAP and quinoxaline units in the **quinoxaline-TAP-TTF** and **TTF-TAP-TTF** (c = 5×10^{-6} M in DCM), chemical oxidation of **quinoxaline-TAP-TTF** and **TTF-TAP-TTF** was explored by successive addition of $NOSbF_6$ aliquots at room temperature. As shown in **Figure 2** for **quinoxaline-TAP-TTF**, a progressive reduction of the absorbance of the high energy π-π* transition and ICT transition band at 320 nm and 620 nm, respectively, is accompanied with a concomitant emergence of absorption bands at 450 nm, 900 nm and 1200 nm which reach their maximum values upon addition of 18 equiv. of $NOSbF_6$. The appearance of new absorption bands around 450 nm and 900 nm is characteristic of the $TTF^{\bullet+}$ radical cation-related transitions within a D-A ensemble.[1, 88] Moreover, a new absorption band around 1300 nm could be assigned to the dimeric $TTF^{\bullet+}$ radical cation species arising from enforced intermolecular

interactions. Interestingly, for **TTF-TAP-TTF**, the initial oxidation leads to a broad absorption band which emerges around 900 nm, indicative of $TTF^{\bullet+}$ radical cation species. Gradually, a broad absorption band centered at 1400 nm appears, which is probably attributed to a mixed-valence charge transfer transition from neutral TTF to $TTF^{\bullet+}$ radical cation.[1, 83, 89, 90] During the oxidation process, this band is continuously blue-shifted to 1150 nm and reaches its maximum value upon addition of 18 equiv. of $NOSbF_6$. Having a close look at the band around 375 nm, the double-peak feature is distinct from the single peak at the same energy in **quinoxaline-TAP-TTF**, clearly due to the presence of two TTF units. It completely disappears upon addition of 1.4 equiv. of $NOSbF_6$. This points to two possible scenarios: the two TTF units are not equivalent, or there is some excitonic coupling between them. For the former case, the spectral change is due to the consecutive oxidation of two TTF units, the first TTF unit is much easily and more efficiently oxidized than the second. This scenario is inconsistent with cyclic voltammetry measurements reported in the following. As a result, the most probable explanation is related to the formation of an excitonic state involving the two TTF units.

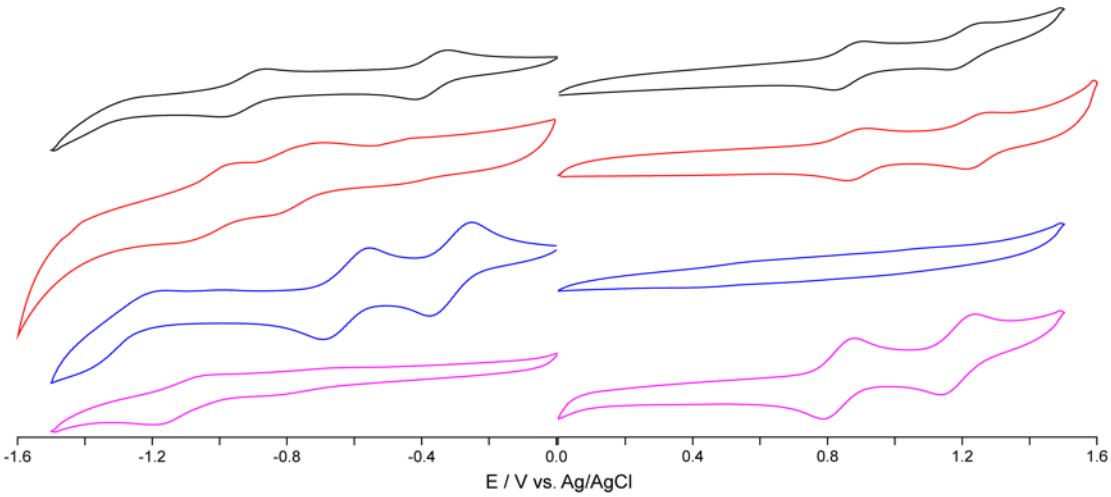

Figure 4 Cyclic voltammograms of **quinoxaline-TAP-TTF** (black), **TTF-TAP-TTF** (red), **diquinoxaline-TAP** (blue) and **5** (pink) were measured in DCM, containing 0.1 M $TBAPF_6$ as the supporting electrolyte at room temperature, a platinum electrode as a working electrode, Ag/AgCl electrode as the reference electrode and the scan rate at 500 mV s^{-1}.

The electrochemical properties of **quinoxaline-TAP-TTF**, **TTF-TAP-TTF**, **diquinoxaline-TAP** and the reference compounds **5** (**Figure 5**), **TTF-2NH$_2$** and ***t*-Bu-TAP** (**Figure 5**) were investigated by cyclic voltammetry in DCM (**Figure 4**). **Quinoxaline-TAP-TTF** undergoes two distinct reversible oxidation processes at 0.86 V and 1.22 V (*vs*. Ag/AgCl), indicating that TTF unit is successively oxidized to TTF radical cation and dication species.[91] In the negative

potential window, two reversible reduction waves at -0.37 and -0.92 V are observed, corresponding to the addition of electrons to the quinoxaline-extended TAP core (**Figure 6a**). The symmetric **TTF-TAP-TTF** shows two pairs of two-electron oxidation waves at 0.89 V and 1.24 V, suggesting that two TTF units are simultaneously oxidized to their radical cation and dication species, respectively. It can be therefore deduced that these two TTFs behave as independent redox centres without any electronic communication between them.[92-94] Also, the oxidation potentials are quite similar to those of **quinoxaline-TAP-TTF**, indicating that two TTF units are equally affected by the electron-withdrawing effect of the quinoxaline-extended TAP core. However, it undergoes three reductions at -0.42, -0.79 V and -1.02 V (**Figure 6b**, DPV results), which are negatively shifted compared to **quinoxaline-TAP-TTF** ascribing to the electron donating ability of the additional TTF. In addition, the symmetric **diquinoxaline-TAP** undergoes two reversible reduction processes at -0.31 and -0.63 V, which are attributed to reductions of the quinoxaline-extended TAP core. The extended π-conjugation in **diquinoxaline-TAP** significantly stabilize the LUMO with respect to ***t*-Bu-TAP**. As expected, oxidation potentials are positively shifted while reduction potentials are negatively shifted for **quinoxaline-TAP-TTF** and **TTF-TAP-TTF** compared to those of **TTF-2NH₂** (**Figure 5**) and **diquinoxaline-TAP**, due to electron withdrawing effect of the quinoxaline-extended TAP core and electron-donating ability of the TTF unit(s), respectively. Surprisingly, **5** undergoes only one reduction at -1.11 V, which is even negatively shifted with respect to ***t*-Bu-TAP**.

Table 1 Electrochemical data. Redox potentials [V] vs. Ag/AgCl in DCM.

Compounds	$E_{1/2}^{ox1}$ (V)	$E_{1/2}^{ox2}$ (V)	$E_{1/2}^{red1}$ (V)	$E_{1/2}^{red2}$ (V)	$E_{1/2}^{red3}$ (V)	HOMO (eV)	LUMO (eV)	*Eg* (eV)
quinoxaline-TAP-TTF	0.86	1.22	-0.37	-0.92		-5.07	-3.96	1.11
TTF-TAP-TTF	0.89	1.24	-0.42	-0.79	-1.02	-5.06	-3.90	1.16
diquinoxaline-TAP			-0.31	-0.63			-4.03	
5	0.83	1.19	-1.11			-5.03	-3.27	1.76
TTF-2NH₂	0.37	0.75				-4.62		
***t*-Bu-TAP**			-1.05				-3.31	

E_{LUMO} = -e ($E_{\mathrm{red}}^{\mathrm{onset}}$+ 4.27), E_{HOMO} = -e ($E_{\mathrm{ox}}^{\mathrm{onset}}$+ 4.27), $E_{\mathrm{red}}^{\mathrm{onset}}$ = the onset reduction potential, E_{ox}^{onset} = the onset oxidation potential, $E_{\mathrm{HOMO}} = E_{\mathrm{LUMO}} - E_{\mathrm{g}}$. Fc/Fc^{+} is 0.53 V relative to Ag/AgCl in DCM. (**TTF-2NH₂** stands of 5,6-diamino-2-(4,5-bis(propylthio)-1,3-dithio-2-ylidene)benzo[*d*]-1,3-dithiole and ***t*-Bu-TAP** is an abbreviation of 2,7-di-*tert*-butyl tetraazapyrene.)

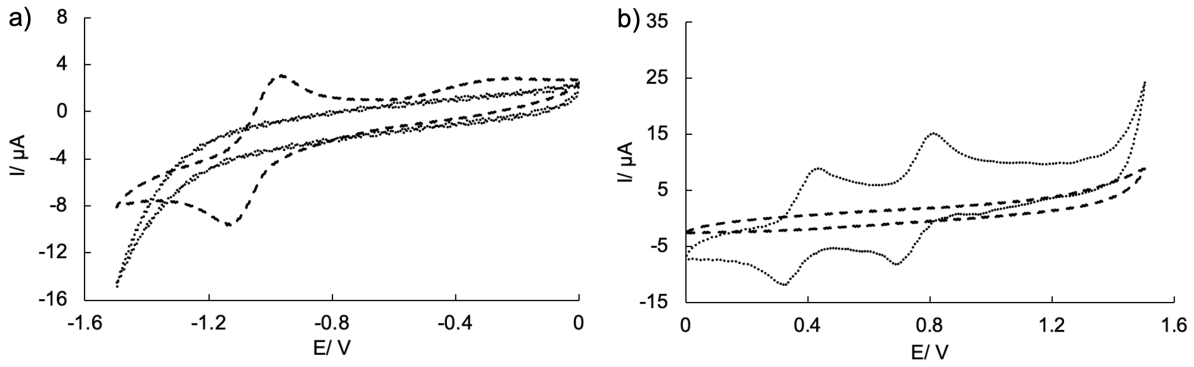

Figure 5 Cyclic voltammograms of **TTF-2NH$_2$** (dot) and ***t*-Bu-TAP** (line) were measured in dichloromethane solution, containing 0.1 M $TBAPF_6$ as the supporting electrolyte at room temperature, a platinum electrode as a working electrode, Ag/AgCl electrode as the reference electrode and the scan rate at 500 mV s^{-1}.

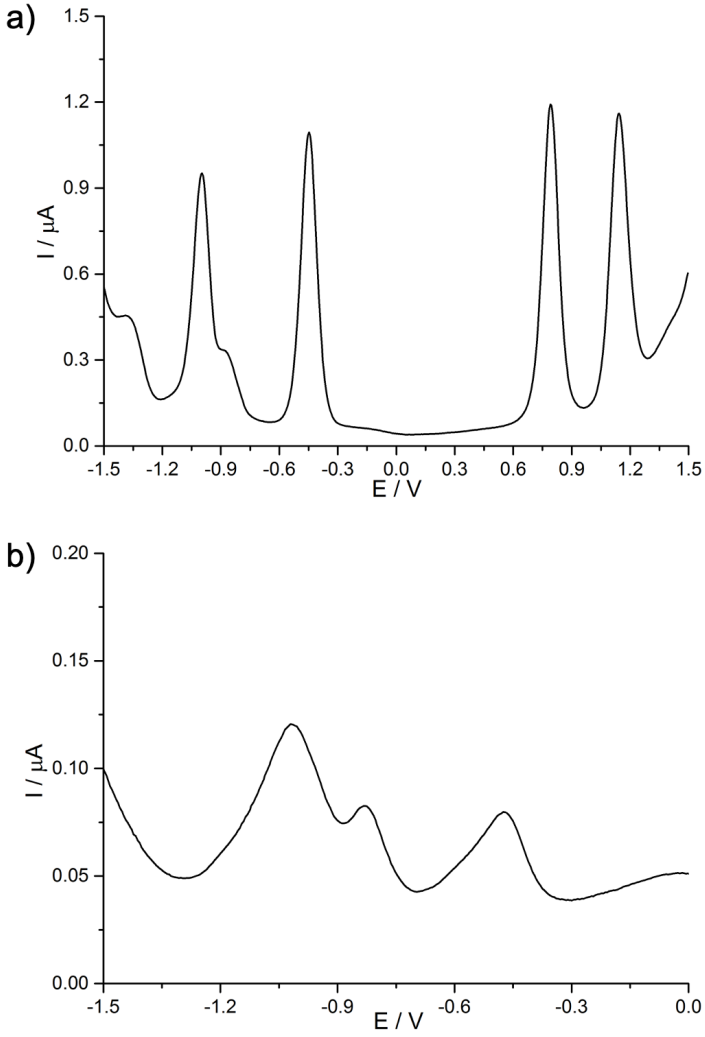

Figure 6 Differential pulse voltammogram of **quinoxaline-TAP-TTF** (a) and **TTF-TAP-TTF** (b) in DCM at r.t.

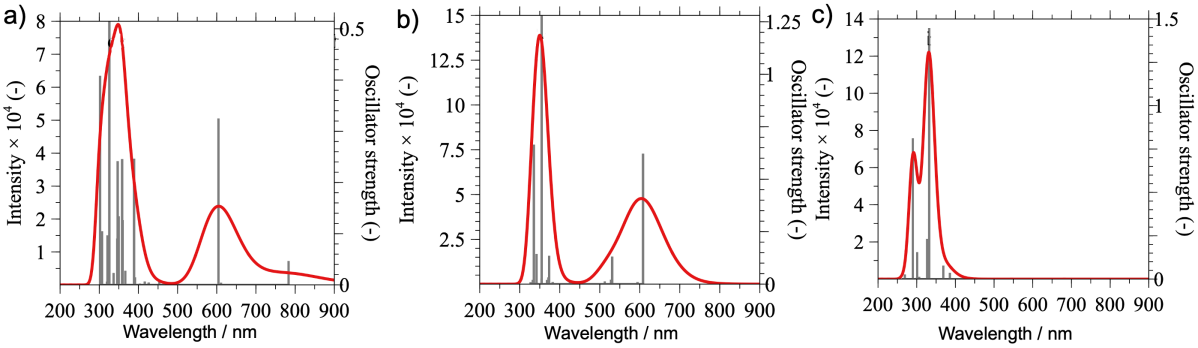

Figure 7 The Computed absorption spectra and oscillator strengths of the neutral a**) quinoxaline-TAP-TTF**, b) **TTF-TAP-TTF** and c) **diquinoxaline-TAP.**

To characterize and verify the various electronic transitions, TD-DFT calculations were accomplished using the Gaussian 16 package at the B3LYP/6-31G(d,p) level of theory. The predicted absorption spectra of **quinoxaline-TAP-TTF**, **TTF-TAP-TTF** and **diquinoxaline-TAP** are in fairly good agreement with experimental results (**Figure 7**). For **quinoxaline-TAP-TTF**, the HOMO orbital is mainly located on TTF unit and LUMO orbital distributes on TAP-quinoxaline-CN moiety. The lowest-energy absorption band peaked at 620 nm, is assigned to the HOMO → LUMO (100%) /LUMO+1 (99%) /LUMO+2 (99%) transitions that involve an ICT from the TTF unit to the quinoxaline-extended TAP core, as clearly shown by the associated molecular orbitals in the left column of **Figure 8**. Also, the calculated transitions at higher energies match well with the observed absorption spectrum. Similarly, the HOMO and HOMO-1of **TTF-TAP-TTF** are degenerated and localized on the TTF units while the LUMO is delocalized on the quinoxaline-extended TAP core. The lowest-energy absorption band is mainly ascribed to the HOMO → LUMO (79%) transition, thus has a clear ICT character. In addition, the LUMO distribution of **diquinoxaline-TAP** over the whole molecule is verified.

In order to deeply explore the intramolecular electronic interactions, we investigated their excited state population dynamics by femtosecond time-resolved TAS. We performed a comparative study of **quinoxaline-TAP-TTF** and **TTF-TAP-TTF** upon direct (at 580 and 605 nm, respectively) and indirect excitations (excitation at 355 nm) to their ICT states.

Data analysis of time-resolved spectra

We used the so-called Singular Value Decomposition and Global Fit (SVD-GF) analysis of the transient absorption data, $TA(\lambda, t)$, to separate noise, $\Xi(\lambda, t)$, from the spectral evolution of the

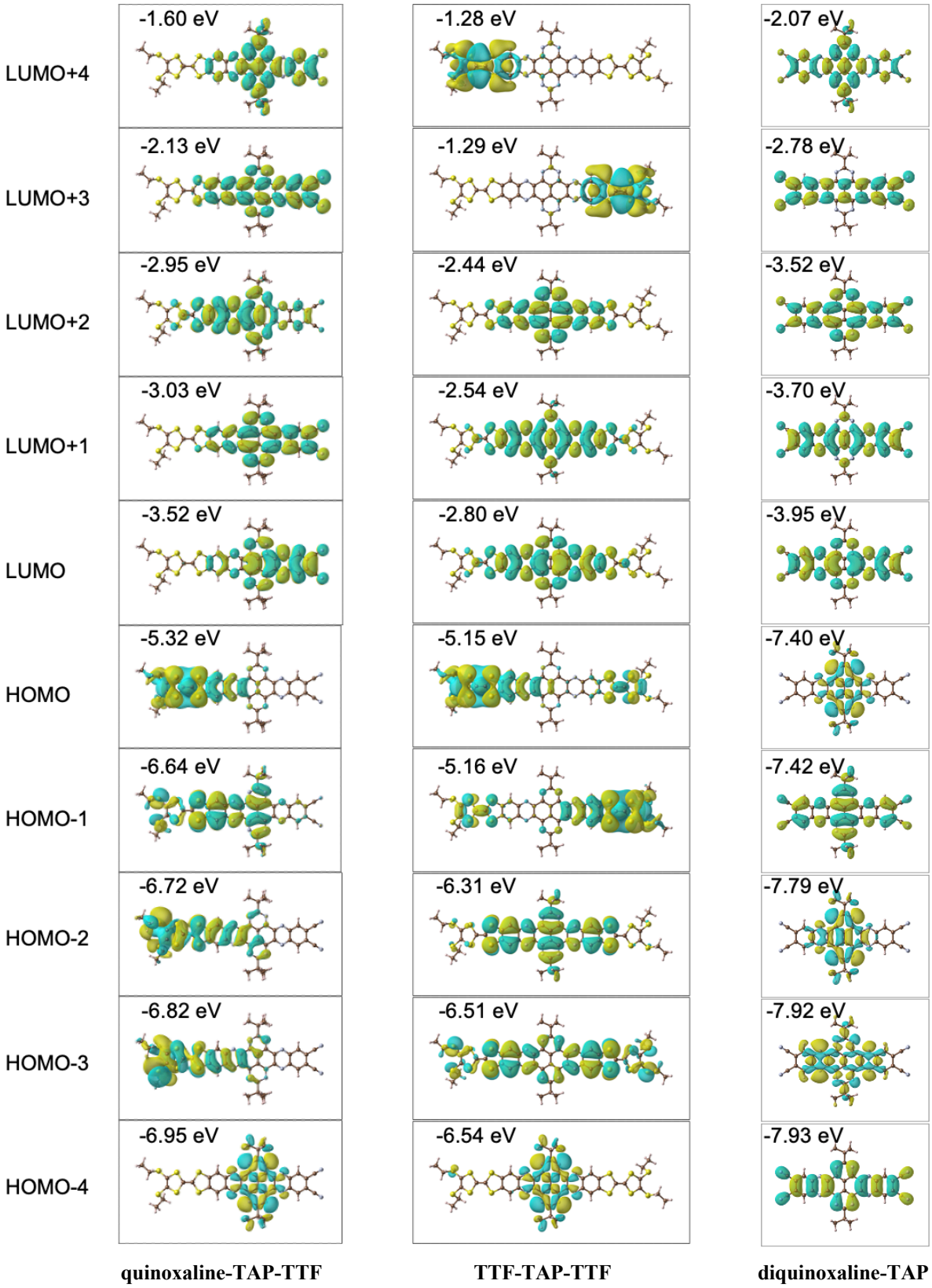

Figure 8 Frontier molecular orbitals of **quinoxaline-TAP-TTF** (left), **TTF-TAP-TTF** (middle) and **diquinoxaline-TAP** (right), respectively.

system, $\widehat{TA}(\lambda, t)$.

$$\mathrm{TA}(\lambda, t) = \widehat{TA}(\lambda, t) + \Xi(\lambda, t) \qquad \text{eq. 1}$$

Assuming that real dynamics can be described by exponential decays, the SVD-GF analysis allows to decompose $\widehat{TA}(\lambda, t)$ as an expansion of exponential decays with characteristic lifetimes (τ_k) and decay associated spectra, DASs:

$$\widehat{TA}(\lambda, t) = \sum_{k=1}^{k=p} DAS_k(\lambda)\, e_{t>0}^{-\frac{t}{t_k}} |_{IRF(K,t_0,t)} \qquad \text{eq. 2}$$

Where $e_{t>0}^{-t/\tau_k} |_{IRF(K,t_0,t)}$ represents an exponential decay with decay constant τ_k multiplied by the Heaviside step function $u_0(t)$ and convoluted with the instrument response function (IRF). The latter is assumed to be a Gaussian centred at t_0 and with a full width at half maximum of *K*.

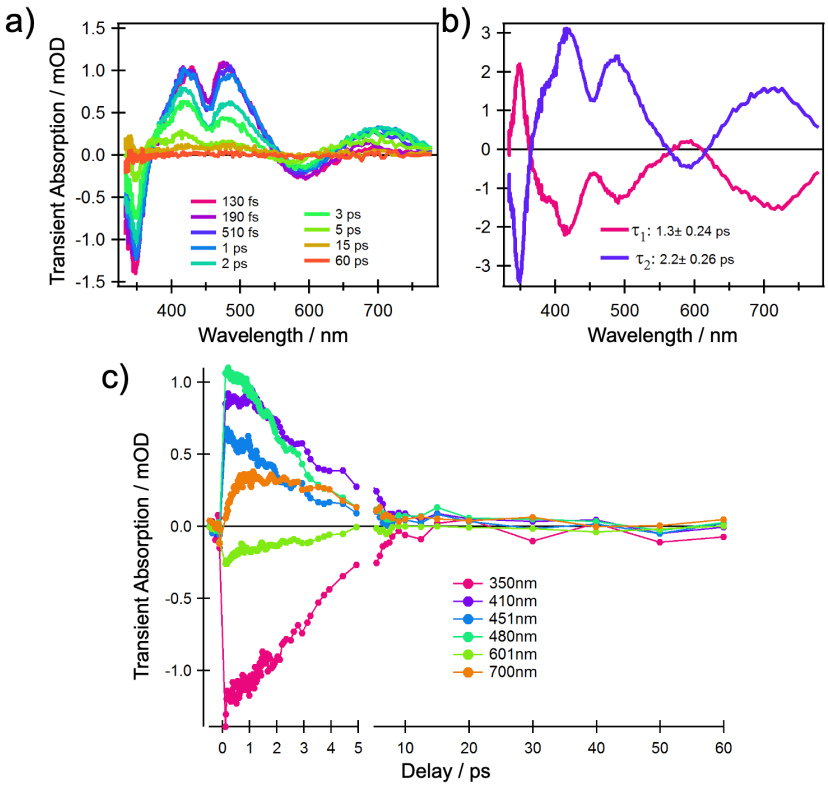

Figure 9 a) Selection of ultrafast transient absorption spectra of **quinoxaline-TAP-TTF** in THF solvent (λ_{ex}= 580 nm). b) Time-spectrum decomposition analysis: decay associated spectra (DAS) and relative decay time constants are shown. c) Selected kinetic traces from **quinoxaline-TAP-TTF** upon excitation at 580 nm.

The TA spectra show from the earliest spectrum (130 fs after excitation) an ICT ground state bleach (GSB) signal at 580 nm, accompanied by a GSB at 350 nm and three excited-state

absorption (ESA) peaks at 400 nm, 480 nm and 650-700 nm. These spectral changes upon excitation of the ICT state are in excellent agreements with the changes induced by chemical oxidation of **quinoxaline-TAP-TTF** (**Figure 2**): the rise of an absorption signal around at 450 nm and at $\lambda > 700$ nm, with a concomitant reduction of the ICT at 620 nm and π-π^* transition at 350 nm. This allows us to assign the GSB at 350 nm and the ESA bands to the oxidation of the TTF unit. Accordingly, the red shift from 660 nm to 700 nm of the red-most ESA band can be rationalized as the effect of solvation dynamics driving the stabilization of the ICT state in ca. 1ps. Concerning dynamics, data and kinetic traces in (**Figure 9**) allow us to estimate the lifetime of the excited molecule, and therefore the time constant of the back CT process, in ca. 2-2.5 ps.

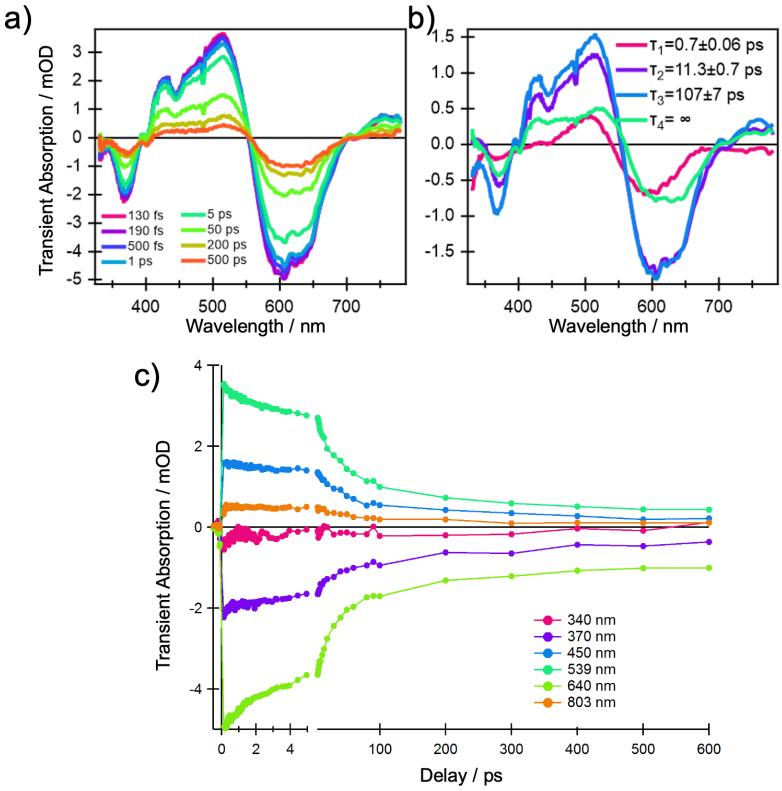

Figure 10 a) Selection of ultrafast transient absorption spectra of **TTF-TAP-TTF** in THF solvent (λ_{ex}= 605 nm). b) Time-spectrum decomposition analysis: decay associated spectra (DAS) and relative decay time constants are shown. c) Selected kinetic traces from **TTF-TAP-TTF** upon excitation at 605 nm.

As depicted in **Figure 10**, the TA spectra of **TTF-TAP-TTF** are overall very similar to those of **quinoxaline-TAP-TTF** with only small differences: a red-shift of the GSB at 350 nm to 375 nm, the appearance of additional GSB at $\lambda < 350$ nm and a broader ESA at $\lambda > 450$ nm. These spectral features are related to the $TTF^{\cdot+}$ radical cation which is in good agreement with

the spectroelectrochemical data shown in **Figure 3**. The result of SVD-GF analysis identifies four main dynamics: The 700 fs DAS describes a shift and appearance of a band mainly due to solvation and stabilization of the ICT state (in agreement with the qualitative discussion of the kinetics in **quinoxaline-TAP-TTF**). Since we detected at magic angle, all the three components at 11 ps, 107 ps and infinity (with respect to the measurement time window) describe population decays, energy redistribution and reorganization of the electron density. It is worth noting that all of them have a similar shape and a clear GSB band. This means that both components at 11 and 107 ps describe mainly a back CT of ~ 80% of molecules and the remaining 15% of population decays on time scale longer than few ns. These outcomes clearly indicate that the back CT rate in **TTF-TAP-TTF** is much slower than that in **quinoxaline-TAP-TTF**, which is not straightforward to rationalize.

3.2.3 Conclusions and outlook

The (a)symmetric TAP-based D-A fused triads have been successfully synthesized by direct condensation of precursor **4** with **TTF-2NH$_2$** and 4,5-diaminophthalonitrile, respectively. In both cases, the lowest-energy absorption band is assigned to an ICT from the TTF unit(s) to the quinoxaline-extended TAP core, as confirmed by cyclic voltammetry and DFT calculations. Interestingly, TAS measurements reveal that the symmetric **TTF-TAP-TTA** triad has a CS state with a lifetime of few ns, much longer than **quinoxaline-TAP-TTF**. These results demonstrate that the lifetime of the CS state can be modulated by variation of symmetry.

3.2.4 Experimental section

Set-up description of transient absorption experiment: We generated the excitation pulses in the visible region at 580 nm and 605 nm using a tuneable commercial non-collinear optical parametric amplifier (Topas White by Light conversion). UV pulses at 355 nm was generated by focusing the fundamental visible pulses (680 nm and 710 nm generated by Topas white) into a BBO crystal (250 μm thickness) and fulfilling frequency doubling condition by angle tuning to the right phase-matching angle. The residual visible radiation was filtered out by a harmonic separator and the excitation UV pulse was focused into a spot with ca. 60 μm diameter ($1/e^2$) and with ~ 18-20 nJ energy per pulse.

The probe pulse was a broadband continuum covering from 320 nm to 800 nm, generated by focusing a fraction of the Ti:Sapphire laser source into a 5 mm thick CaF_2 crystal mounted on

a motorized stage horizontally wobbling to avoid thermal damage. The probe beam was focused into a spot with ca. 45 μm diameter on the sample. The polarization of the pump with respect to the probe was at magic angle (54.7°) to measure only population dynamics and excluding rotational ones. A power dependence was regularly carried out to ensure that experiments are conducted in a linear absorption regime. More details on the set up and calculation of the TA signal in a single-shot detection scheme have been already published.[95] To allow a quantitative intercomparison of the signal amplitudes, we took special care to always have the same excitation intensity and optical density (all the other parameters, as spot size and overlap were constant). When small deviations from the standardized conditions (20 nJ/pulse and 0.1OD at the excitation wavelength, respectively) were observed, or it was not possible to match them perfectly, a normalization to the standardized values of excitation intensity and optical density were applied.

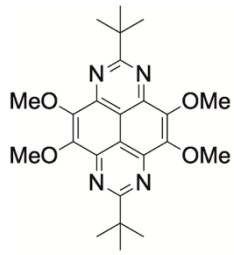

2,7-di-t-butyl-4,5,9,10-tetramethoxy-1,3,6,8-tetraazapyrene (2). 2,7-di-t-butyl-4,5,9,10-tetrabromo-1,3,6,8-tetraazapyrene (634 mg, 1 mmol), copper iodide (952 mg, 5 mmol), sodium methoxide solution (702 mg, 13 mmol), and methanol (50 mL) were put into a round-bottom flask (100 ml), and the resultant solution was stirred at 80 °C for 1 days under N_2. After cooling down to room temperature, the reaction was quenched by water (50 ml). The mixture was extracted by dichloromethane (50 mL) for three times. The combined organic phase was washed with an aqueous solution of ammonium chloride, and then the solvent was removed by a rotavapor. The crude product was purified by flash column chromatography (silica gel, DCM). As a result, 2,7-di-t-butyl-4,5,9,10-tetramethoxy-1,3,6,8-tetraazapyrene was isolated as a yellow solid (278 mg). Yield: 63%. ^{1}H NMR (300 MHz, $CDCl_3$) δ 4.48 (s, 12H), 1.67 (s, 18H). ^{13}C NMR (75 MHz, $CDCl_3$) δ 175.08, 150.31, 149.73, 107.32, 63.08, 40.92, 30.40. IR data (cm^{-1}): 2933, 2902, 2866, 2359, 1548, 1468, 1380, 1206, 990, 801, 471. HR-MS (ESI, positive): *m/z* calcd for $[C_{24}H_{30}N_4O_4+H]^+$: 439.2340; found: 439.2324.

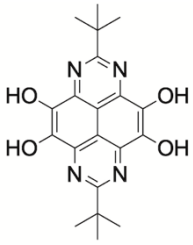

2,7-di-t-butyl-4,5,9,10-tetrahydroxy-1,3,6,8-tetraazapyrene (3). 2,7-di-t-butyl-4,5,9,10-tetramethoxy-1,3,6,8-tetraazapyrene (79 mg, 0.18 mmol) and 48% hydrobromic acid (10 mL) were put into a round-bottom flask (50 mL), and the reaction solution was stirred at 100 °C overnight under N_2. After the

temperature of the reaction mixture was cooled to room temperature, water (20 mL) was added, leading to some precipitation. After filtration, the collected solid was washed with water and dried *in vacuum*. 2,7-di-*t*-butyl-4,5,9,10-tetrahydroxy-1,3,6,8-tetraazapyrene was obtained as a dark-brown solid (61 mg). Yield: 90%. ^{1}H NMR (300 MHz, $CDCl_3$) δ 1.69 (s, 18H). ^{13}C NMR (101 MHz, DMSO) δ 173.33, 145.93, 140.87, 101.41, 30.26. IR data (cm^{-1}): 3363, 3188, 2956, 2921, 2857, 2361, 1736, 1477, 1302, 983, 836, 686, 497. HR-MS (ESI, positive): *m/z* calcd for $[C_{20}H_{22}N_4O_4+H]^+$: 383.1714; found: 383.1708.

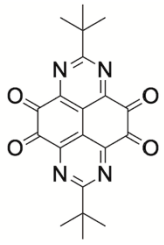

2,7-di-t-butyl-4,5,9,10-tetraone-1,3,6,8-tetraazapyrene (4). 2,7-di-t-butyl-4,5,9,10-tetrahydroxy-1,3,6,8-tetraazapyrene (57 mg, 0.15 mmol) and fuming nitric acid (10 mL) were put into a round-bottom flask (50 mL), and the reaction solution was stirred at room temperature for 15 minutes. Water (16 mL) was added, and then the resultant solution was concentrated. A yellow precipitate was formed and separated by filtration. The obtained yellow solid was redissolved in chlorobenzene (25 mL) and the resulting solution was stirred overnight under reflux. By cooling down to room temperature, the precipitate was formed, filtrated off and then dried *in vacuum*. 2,7-di-t-butyl-4,5,9,10-tetraone-1,3,6,8-tetraazapyrene was obtained as an orange solid (26 mg). Yield: 45%. ^{1}H NMR (300 MHz, DMSO) δ 1.47 (s, 18H). ^{13}C NMR (101 MHz, DMSO) δ 177.41, 174.95, 155.03, 121.11, 29.39. IR data (cm^{-1}): 2965, 2927, 2904, 2361, 2333, 1734, 1704, 1566, 1504, 1478, 1456, 1399, 1357, 1215, 1103, 842,429. HR-MS (ESI, positive): *m/z* calcd for $[C_{20}H_{18}N_4O_4+2H_2O+H]^+$415.1612, found 415.1604.

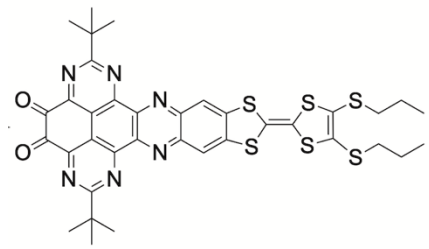

s-TTF-TAP (5). A mixture of 5,6-diamino-2-(4,5-bis(propylthio)-1,3-dithio-2-ylidene)benzo[d]-1,3-dithiole (195 mg, 0.45 mmol) and 2,7-di-t-butyl-4,5,9,10-tetraone-1,3,6,8-tetraazapyrene (189 mg, 0.5 mmol) in EtOH (50 mL) was refluxed for 8 h in the presence of a catalytical amount of acetic acid (5 mL). The resulting precipitate was filtered off, washed with EtOH and diethyl ether and dried *in vacuum*. The crude product was purified by flash column chromatography (silica gel, DCM:EtOAc, 20/1, v/v) to afford **5** as a blue solid (68 mg). Yield: 19.5%. ^{1}H NMR (300 MHz, $CDCl_3$) δ 8.34 (s, 2H), 2.84 (m, 4H), 2.35 (t, J = 6.8 Hz, 4H), 1.72 (s, 18H), 1.05 (t, J = 7.3 Hz, 6H). HR-MS (ESI, positive): *m/z* calcd for $C_{36}H_{34}N_6O_2S_6$:774.1067; found: 774.1078.

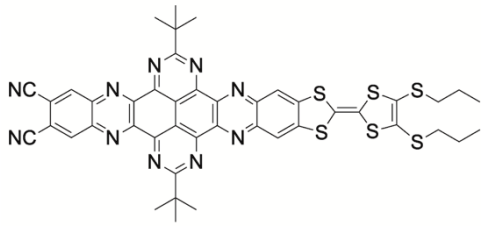

Quinoxaline-TPA-TTF (**6**)**.** A mixture of 4,5-diaminophthalonitrile (20 mg, 0.13 mmol) and **5** (48 mg, 0.06 mmol) in EtOH (15 mL) was refluxed for 20 h in the presence of a catalytical amount of acetic acid (2 mL). The resulting precipitate was filtered off, washed with EtOH and diethyl ether and dried *in vacuum.* The crude product was purified by flash column chromatography (silica gel, DCM:EtOAc, 20/1, v/v) to produce **quinoxaline-TAP-TTF** as a blue solid (19 mg). Yield: 35%. ^{1}H NMR (300 MHz, $CDCl_3$) δ 9.23 (d, J = 5.6 Hz, 2H), 8.26 (s, 2H), 2.89 - 2.84 (m, 4H), 1.89 (d, J = 2.6 Hz, 18H), 1.75-1.68(m, 4H) 1.09 - 1.03 (m, 6H). HR-MS (ESI, positive): *m/z* calcd for $C_{44}H_{36}N_{10}S_6$: 896.1449; found: 896.1445.

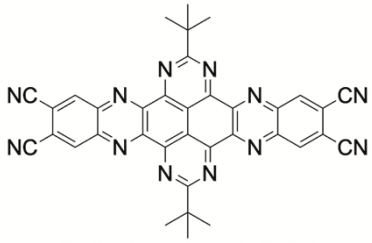

Diquinoxaline-TAP (**7**)**.** A mixture of 4,5-diaminophthalonitrile (95 mg, 0.6 mmol) and 2,7-di-t-butyl-4,5,9,10-tetraone-1,3,6,8-tetraazapyrene (76 mg, 0.2 mmol) in EtOH (10 mL) was refluxed for 20 h in the presence of a catalytical amount of acetic acid (2 mL). The resulting precipitate was filtered off, washed with EtOH and diethyl ether and dried *in vacuum* to afford **diquinoxaline-TAP** as a yellow solid (80 mg). Yield: 64%. ^{1}H NMR (300 MHz, DMSO) δ 9.59 (s, 4H), 1.81 (s, 18H). HR-MS (ESI, positive): *m/z* calcd for $[C_{36}H_{22}N_{12}+H]^+$: 623.2163; found: 623.2171.

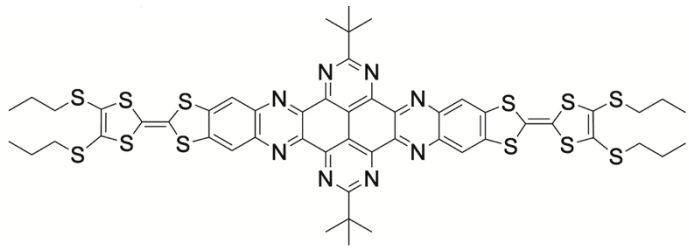

TTF-TAP-TTF (**8**)**.** A mixture of 5,6-diamino-2-(4,5-bis(propylthio)-1,3-dithio-2-ylidene)benzo[*d*]-1,3-di-thiole (80 mg, 0.19 mmol) and **5** (72 mg, 0.09 mmol) in EtOH (25 mL) was refluxed for 36 h in the presence of a catalytical amount of acetic acid (4 mL). The resulting precipitate was filtered off, washed with EtOH and diethyl ether and dried *in vacuum*. The crude product was purified by flash column chromatography (silica gel, DCM:EtOAc, 50/1, v/v) to afford **TTF-TAP-TTF** as a blue solid (16 mg). Yield: 15%. ^{1}H NMR (300 MHz, $CDCl_3$) δ 8.43 (s, 4H), 2.89 – 2.84 (m, 8H), 1.88 (s, 18H), 1.77 – 1.72 (m, 8H), 1.09 – 1.03 (m, 12H). MS (MALDI-TOF, DCTB as matrix, positive) calcd. for $[C_{52}H_{50}N_8S_{12}+H]^+$1171.0880, found 1171.09. HR-MS (ESI, positive): *m/z* calcd for $[C_{52}H_{50}N_8S_{12}+H]^+$1171.0880, found 1171.0872.

4. π-Extended perylene diimide (PDI)-based D-A conjugates

This section is partially adapted to the following publication:

a. Nanographene favors electronic interactions with an electron acceptor rather than an electron donor in a planar fused push–pull conjugate

Michel Volland, ***Ping Zhou****, Leonie Wibmer, Robert Häner, Silvio Decurtins, Shi-Xia Liu and Dirk M. Guldi*

Nanoscale, 2019, **11**, 1437.

https://doi.org/10.1039/C8NR06961A

b. Azulene-PDI triads

Ping Zhou*, Ulrich Aschauer, Silvio Decurtins, Thomas Feurer, Robert Häner, and Shi-Xia Liu*

Manuscript in preparation

Contribution to the work

I synthesized all target compounds including **TTF-fused PDI**, **2-A-PDI**, **2-A-fused PDI** and **6-A-PDI** and characterized them by ^{1}H NMR and MS spectra. I also conducted and analyzed UV-Vis absorption spectra, pH responsive measurements and electrochemical experiments. Dr. Michel Volland, from Friedrich-Alexander-Universität Erlangen-Nürnberg, performed transient absorption measurements, Raman spectra, transmission electron microscopy (TEM) imaging and atomic force microscopy (AFM) imaging. Prof. Ulrich Aschauer carried out the TD-DFT calculations and computed absorption spectra.

4.1 TTF-fused PDI

4.1.1 Article

Nanographene favors electronic interactions with an electron acceptor rather than an electron donor in a planar fused push–pull conjugate

Nanoscale

PAPER

View Article Online
View Journal | View Issue

Cite this: *Nanoscale*, 2019, **11**, 1437

Nanographene favors electronic interactions with an electron acceptor rather than an electron donor in a planar fused push–pull conjugate†

Michel Volland,*[a] Ping Zhou,[b] Leonie Wibmer,[a] Robert Häner,[b] Silvio Decurtins,[b] Shi-Xia Liu *[b] and Dirk M. Guldi *[a]

Received 28th August 2018,
Accepted 18th December 2018

DOI: 10.1039/c8nr06961a

rsc.li/nanoscale

A combination of a preexfoliated nanographene (NG) dispersion and fused electron donor–acceptor tetrathiafulvalene–perylenediimide (TTF–PDI) results in a noncovalent functionalization of NG. Such novel types of nanohybrids were characterized by complementary spectroscopic and microscopic techniques. The design strategy of the chromophoric and electroactive molecular conjugate renders a large and planar π-extended system with a distinct localization of electron-rich and electron-poor parts at either end of the molecular conjugate. Within the *in situ* formed nanohybrid, the conjugate was found to couple electronically with NG preferentially through the electron accepting PDI rather than the electron donating TTF and to form the one-electron reduced form of PDI, which corresponds to p-doping of graphene.

Introduction

Graphene films are potential candidates for their implementation in nanoelectronic devices, but require functionalization or doping of the graphene sheets – either at the atomic or molecular level.[1–7] Importantly, noncovalent functionalization of graphene, which does not disrupt the extended π-conjugation, unlike covalent functionalization,[8] is of high interest from an application point of view.[9–15] Various routes to fabricate graphene sheets have been explored and reported.[16,17] At the forefront are non-invasive wet chemical strategies, which are based on ultrasonic processing and stabilizing the resulting graphene sheets using suitable intercalators/surfactants.[18] Incorporation of intercalators in the form of redox- and/or photoactive building blocks enables the utilization of electron donor–acceptor (D–A) interactions. Accordingly, the noncovalent functionalization of nanographene (NG) or graphene sheets with either aromatic electron donors or acceptors, as demonstrated in the case of carbon nanotubes,[19–25] is widely exploited in contemporary research.[26–28] For example, the immobilization of electron donating phthalocyanines[29,30] and porphyrins[31,32] is governed by π–π and charge-transfer interactions and, in turn, leads to stable hybrid materials. The investigations of electron acceptors are focused on porphycenes,[33] pyridyl-phthalocyanines[34] and perylenediimides. In the case of a mono-bay substitution the latter may act in an electron-donating manner towards graphene.[35] A central question, which remains elusive to this date, is whether the basal plane of graphene prefers interactions with an electron donor or an electron acceptor.

Herein, we report the exfoliation of graphite through intercalation and immobilization of planar and extended π-conjugates onto its basal plane and the investigation of the electronic coupling by complementary spectroscopic and microscopic techniques. Importantly, the specific chromophoric and electroactive D–A of the actual study comprises a tetrathiafulvalene (TTF) which is annulated to a perylenediimide (PDI) (Scheme 1). On one hand, the TTF is known to be a ver-

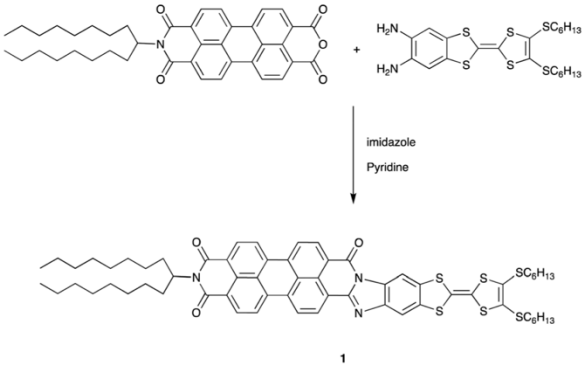

1

Scheme 1 Synthesis of TTF-fused PDI **1**.

[a]*Department of Chemistry and Pharmacy & Interdisciplinary Center for Molecular Materials (ICMM), Friedrich-Alexander-Universität Erlangen-Nürnberg, Egerlandstrasse 3, 91058 Erlangen, Germany. E-mail: dirk.guldi@fau.de*
[b]*Department of Chemistry and Biochemistry, University of Bern, Freiestrasse 3, CH-3012 Bern, Switzerland. E-mail: liu@dcb.unibe.ch*

†Electronic supplementary information (ESI) available. See DOI: 10.1039/c8nr06961a

satile electron donor, which plays a prominent role in the development of electrically conducting materials.[36,37] On the other hand, PDI type molecular building blocks give rise to good electron accepting ability and high optical absorption across the visible region.[38,39] Generally, the annulation of an electron donor and an electron acceptor into a compact and planar π-conjugate promotes intramolecular charge-transfer processes in the ground and excited states.[40,41] An integral part of such D–A systems is the location of an energetically high-lying molecular orbital (HOMO) on the electron donor and of a low-lying empty molecular orbital (LUMO) on the electron acceptor.[42] This leads to electrochemically amphoteric properties; in the case of combining the TTF with a bithienoquinoxaline acceptor the ΔE ($E_{ox} - E_{red}$) is as small as 0.52 V.[43] The TTF and PDI were fused together either on the bay-side of the PDI,[44,45] or along the imide side of the PDI, which affords, for example, the TTF–PDI **1**.[46,47] The planarity of fused D–A moieties is demonstrated from single crystal structure determination[46] and also atomic force (AFM) and scanning tunneling microscopy (STM) studies in the case of a TTF-dppz.

Results and discussion

As illustrated in Scheme 1, the preparation of TTF–PDI was accomplished *via* the direct condensation reaction of *N*-(1-octylnonyl)perylene-3,4,9,10-tetracarboxylic acid 3,4-anhydride-9,10-imide with 5,6-diamino-2-(4,5-bis(hexylthio)-1,3-dithio-2-ylidene)benzo[*d*]-1,3-dithiole according to a similar synthetic method for its analogue.[46] The crude product was purified by chromatographic separation on silica gel to afford analytically pure **1** in 43% yield. It was fully characterized from its spectroscopic data (NMR, MS, and IR; see the ESI†). Investigations of the electronic ground and excited states were performed in toluene, chloroform ($CHCl_3$), tetrahydrofuran (THF), and dichloromethane (Fig. S1†). In THF, for example, the PDI-related π–π* transitions are found at 497, 537, and 570 nm. In addition, the absorption in the region of 435 nm is assigned to a TTF-centered transition. Overall, a broadening of the absorption features is noted, when compared to a monomeric PDI reference. This hampers monitoring intramolecular charge-transfer (ICT) transitions at longer wavelengths. To this end, we varied the concentration of **1** from 5×10^{-7} to 1×10^{-5} M and found no appreciable changes. From the latter trend we conclude that **1** aggregates, regardless of its concentration. As a complement to the absorption data, PDI-related fluorescence emerges at 585, 631, and 695 nm in THF upon photoexcitation at 530 nm. In time-correlated single photon counting measurements following the same 530 nm excitation wavelength, fluorescence lifetimes of 2.14 and 6.26 ns were determined and they stem from the fluorescence of monomeric **1** and smaller aggregates of **1**, respectively. The quantum yields in THF, toluene, dichloromethane, and $CHCl_3$ are 16.3%, 19.2%, 18.3%, and 19.4%, respectively.

Subsequently, transient absorption spectra following a 550 nm femtosecond excitation of **1** in THF were recorded

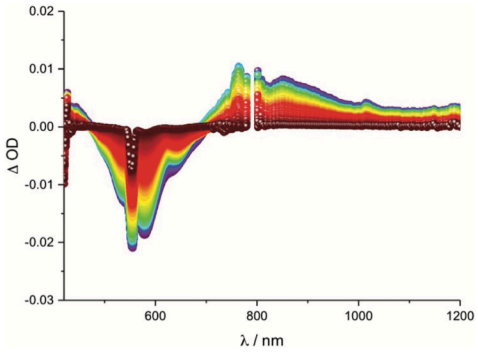

Fig. 1 Differential absorption spectra (vis and NIR) obtained upon femtosecond pump probe experiments (550 nm) of **1** in THF with time delays between 2.1 (blue) and 7500 ps (red).

(Fig. 1 and Fig. S2†). Directly after excitation, the differential absorption characteristics of the PDI-centred singlet excited state emerge in the form of minima in the 537 to 570 nm range. Furthermore, features in the 700 to 900 nm region are assigned to singlet–singlet transitions,[48] as well as to the fingerprint of the one-electron reduced form resulting from a charge transfer (CT). Independent confirmation for this assignment stems from transient absorption measurements with a 530 nm excitation wavelength (Fig. S3†). The markers of the one-electron reduced form at 735 and 825 nm are distinguishable from the broad singlet–singlet transitions. A comparison with non-push–pull PDIs, where the transient absorption spectra differ in peak positions as well as peak widths and shapes, further corroborates the charge-transfer character.[49]

To shed light on the deactivation mechanism and the corresponding kinetics we performed target analysis and fit the fs-TAS data – both vis and NIR – to a three species model shown in Fig. S4.† The first species is the PDI-centered singlet excited state, which transforms with a 3.56 ps lifetime into the second species, that is, the solvent relaxed singlet excited state. From there, a parallel decay to the CT state with a 62.4 ps lifetime and to the ground state with a 3.01 ns lifetime sets in. As such, the CT state is the third species and its lifetime of 536 ps relates to the recovery of the ground state.‡

In addition to the aforementioned spectroscopic characterization, **1** was characterized by spectroelectrochemical (SEC) means in THF. Applying a reductive potential of −0.8 V *vs.* Ag-wire leads to changes in the vis and NIR parts of the absorption spectrum, which are ascribed to the formation of the one-electron reduced form of **1**. Next to the bleaching of the characteristic PDI ground state absorption, new maxima evolve at 410, 735, 824, and 1006 nm in the differential absorption spectra. Upon applying an oxidative voltage of up to +1.2 V *vs.* Ag-wire, no notable changes were discernable in neither the vis nor the NIR parts of the absorption spectrum. Nevertheless, when recording the PDI-centred fluorescence,

‡Complementary fit of the ns-TAS – Fig. S5 confirmed the deactivation of the second and third species with lifetimes of 546 ps and 3.21 ns.

while applying an oxidative voltage, an appreciable increase in the fluorescence intensity (Fig. S6 and S7†) is noted. The latter relates to the electron donating and, in turn, the fluorescence quenching nature of the TTF in **1**. In short, oxidizing the TTF in **1** eliminates the fluorescence deactivating pathway.

Next, we turned our attention to the preparation and investigation of nanohybrid **2**. In particular, 1–2 mg of natural graphite were added to a 5×10^{-6} M solution of TTF–PDI in THF, ultrasonicated at a frequency of 37 kHz and 80% power for 30 minutes, and centrifuged at 2*g* for 30 minutes. The supernatant was then extracted and subjected to ultrasonication with newly added graphite. The cycle of ultrasonication and centrifugation was performed repeatedly to enrich the corresponding dispersions with well exfoliated **2**. To monitor the progress in enrichment, absorption and fluorescence spectra were recorded after each cycle. Overall, an increase in absorbance goes hand-in-hand with a decrease in fluorescence with equal contributions from the absorption and scattering of exfoliated graphite. As an alternative, mild hybrid preparation routes, lacking ultrasonication, were tested. First, preexfoliated NG dispersions in THF were titrated to a 5×10^{-6} M solution of TTF–PDI. The outcome is, however, identical to that based on ultrasonication in terms of absorption. Second, the fluorescence of **1** was monitored during its diffusion into preexfoliated NG dispersions in THF (Fig. S8†). An increase of the fluorescence intensity is discernible up to the point when formation of **2** sets in. Here, the fluorescence is once again quenched and, in turn, corroborates the formation of **2**.

In a reference experiment, decisive insight into the impact of **1** on the stability of the prepared dispersion was gathered. Two dispersions were prepared following the aforementioned procedures. A reference dispersion (**R**) was prepared in THF in the absence of **1** and a dispersion of **2** with **1** present. The dispersions were centrifuged at 11*g* for a time period of 20 minutes and investigated by means of steady state absorption measurements. Notably, the overall optical density after the centrifugation step was three times higher in the case of **2** compared to that of **R**. Therefore, we conclude better exfoliation when utilizing **1**. In addition, both dispersions were measured in intervals of one day during a total time period of fourteen days. This is summarized in Fig. S9,† where the optical density normalized to the starting value of **1** is plotted as a function of time. The two dispersions decrease similarly in intensity within the first six days before significant changes are discernible. Dispersions of **2** are significantly more stable than dispersions of **R**, and, in turn, highlights the stabilizing features of **1**.

To gain information about the nature of the nanohybrid, we first focused on Raman measurements after drop casting the dispersions onto a Si/SiO_2 wafer. Typical Raman spectra of graphene consist of the D-band at 1350 cm^{-1}, the region of the G-band at around 1580 cm^{-1}, and the region of the 2D-band centred between 2560 and 2700 cm^{-1}. Fig. 2 shows a selected Raman spectrum of **2** and the statistical data regarding the FWHM of the 2D band as well as the positions of the G- and the 2D-bands. All of the aforementioned are compared to **R**. FWHMs for both dispersions peak at the same value, namely 65 cm^{-1}, suggesting the presence of turbostratic graphite. By monitoring and comparing the positions of the G- and the 2D-bands of **2** with those of **R**, a clear upshift is observed. This is due to the electron accepting nature of PDI resulting in p-doping of the graphene sheets.[28]

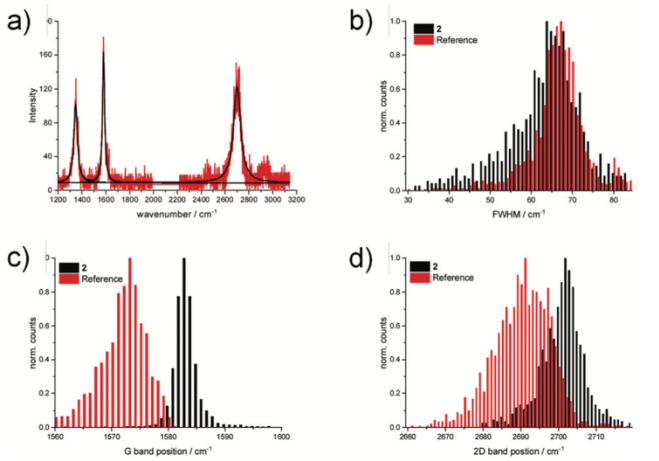

Fig. 2 (a) Selected Raman spectrum of **2**. (b) Histogram of the 2D-band FWHM of **2** and **R**. (c) Histogram of the G-band positions of **2** and **R**. (d) Histogram of the 2D-band positions of **2** and **R**.

These results go hand in hand with the characterization by transmission electron microscopy (TEM) (Fig. S10†). In particular, thin flakes are seen on top of bigger flakes and larger individual flakes with lateral sizes of up to 2 μm. They appear folded, intertwined, and rolled up to minimize the surface energy. AFM also revealed intertwined graphene sheets, on which smaller flakes and agglomeration of graphitic materials are found. Height profiles regarding flake sizes of up to 1 μm indicate heights around 3 nm, which are assignable to monolayer graphene flakes with absorbed water or stabilizer on top (Fig. S11†).

Next, the nature of electronic communications and interactions between NG and **1** in terms of either energy and/or electron transfer were probed by transient absorption experi-

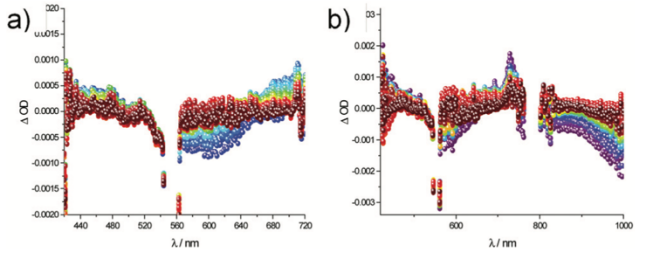

Fig. 3 (a) Differential absorption spectra (vis) obtained upon femtosecond pump probe experiments (550 nm) of **2** in THF with time delays between 1.3 (blue) and 20 ps (red). (b) Differential absorption spectra (vis and NIR) obtained upon femtosecond pump probe experiments (550 nm) of **2** in THF with improved white light settings with time delays between 2.2 (blue) and 9 ps (red).

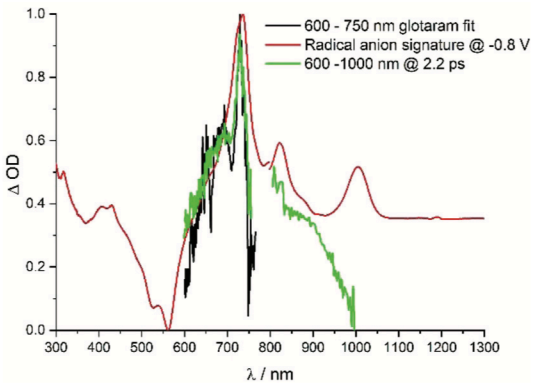

Fig. 4 Comparison of the differential absorption spectrum of **2** at 2.2 ps (green) with the differential absorption spectrum of the reduced form of **1** (red) derived from SEC and the charge separation global analysis fit (black).

ments. Within the first few picoseconds after 550 nm photoexcitation, broad minima evolve (Fig. 3 and Fig. S12†). These comprise PDI related ground-state-bleaching in the region of 500–600 nm as well as graphene related bleaching in the NIR region. Importantly, the new transient between 700 and 850 nm is attributed to the one-electron reduced form of PDI as a consequence of electron transfer from graphene to PDI.

This is in sound agreement with the global analysis and the SEC data as shown in Fig. 4 and Fig. S13.† Global analyses reveal two lifetimes (Fig. S14†): a short-lived component of 1.3 ± 0.2 ps, which represents the charge separation, and a long-lived component of 103 ± 14 ps, which correlates with the charge recombination.

Conclusions

In summary, planar and fused TTF–PDI push–pull **1** was synthesised to exfoliate graphite *via* intercalation and immobilization onto its basal plane. It is demonstrated that strong electronic communication is present within **1** which can only be disturbed *via* direct electronic intervention as was observed from SEC investigations. Furthermore, immobilization of **1** onto graphene is enabled by means of electronic coupling as corroborated from a series of titration and diffusion assays. From pump–probe spectroscopy, we conclude that the ground state charge transfer from the basal plane of graphene to the electron accepting PDI in **2** is the inception to a full charge separation in the excited state to afford the one-electron reduced form of PDI and p-doped graphene. TEM, Raman spectroscopy and AFM analyses revealed that after drop casting the dispersion onto a Si/SiO_2 wafer or a lacey carbon grid, the exfoliated graphene flakes tend to restack and, thus, minimize their surface energy by means of forming turbostratic graphite.

Conflicts of interest

There are no conflicts to declare.

Acknowledgements

This work was supported by the Swiss National Science Foundation and by the deutsche Forschungsgemeinschaft as part of the Excellence Cluster Engineering of Advanced Materials and funded by the Deutsche Forschungsgemeinschaft (DFG) – Projektnummer 182849149 – SFB 953 as well as by the Bavarian State Gonvernment as part of the Solar Technologies go Hybrid initiative. Financial support from the Marie Curie Initial Training Network "MOLESCO" (No. 606728) is gratefully acknowledged.

Notes and references

1 A. K. Geim, *science*, 2009, **324**, 1530–1534.
2 H. Park, J. A. Rowehl, K. K. Kim, V. Bulovic and J. Kong, *Nanotechnology*, 2010, **21**, 505204.
3 L. Gomez De Arco, Y. Zhang, C. W. Schlenker, K. Ryu, M. E. Thompson and C. Zhou, *ACS Nano*, 2010, **4**, 2865–2873.
4 X. Liang and S. Wi, *ACS Nano*, 2012, **6**, 9700–9710.
5 X. Wan, Y. Huang and Y. Chen, *Acc. Chem. Res.*, 2012, **45**, 598–607.
6 H. Wang, K. Kurata, T. Fukunaga, H. Ago, H. Takamatsu, X. Zhang, T. Ikuta, K. Takahashi, T. Nishiyama and Y. Takata, *Sens. Actuators, A*, 2016, **247**, 24–29.
7 P. Cui, J.-H. Choi, C. Zeng, Z. Li, J. Yang and Z. Zhang, *J. Am. Chem. Soc.*, 2017, **139**, 7196–7202.
8 S. P. Economopoulos and N. Tagmatarchis, *Chem. – Eur. J.*, 2013, **19**, 12930–12936.
9 A. Stergiou and N. Tagmatarchis, *ACS Appl. Mater. Interfaces*, 2016, **8**, 21576–21584.
10 T. Sreeprasad and V. Berry, *Small*, 2013, **9**, 341–350.
11 V. Georgakilas, M. Otyepka, A. B. Bourlinos, V. Chandra, N. Kim, K. C. Kemp, P. Hobza, R. Zboril and K. S. Kim, *Chem. Rev.*, 2012, **112**, 6156–6214.
12 B. Luo, S. Liu and L. Zhi, *Small*, 2012, **8**, 630–646.
13 W. Wang, Y. Zhang and Y.-B. Wang, *J. Chem. Phys.*, 2014, **140**, 094302.
14 A. Ghosh, K. V. Rao, S. J. George and C. Rao, *Chem. – Eur. J.*, 2010, **16**, 2700–2704.
15 B. Das, R. Voggu, C. S. Rout and C. Rao, *Chem. Commun.*, 2008, 5155–5157.
16 M. Bernal and E. M. Pérez, *Int. J. Mol. Sci.*, 2015, **16**, 10704–10714.
17 X. Van Heerden and H. Badenhorst, *Carbon*, 2015, **88**, 173–184.
18 J. N. Coleman, *Acc. Chem. Res.*, 2012, **46**, 14–22.
19 D. Tasis, N. Tagmatarchis, A. Bianco and M. Prato, *Chem. Rev.*, 2006, **106**, 1105–1136.
20 C. Ehli, C. Oelsner, D. M. Guldi, A. Mateo-Alonso, M. Prato, C. Schmidt, C. Backes, F. Hauke and A. Hirsch, *Nat. Chem.*, 2009, **1**, 214.
21 H.-J. Shin, S. M. Kim, S.-M. Yoon, A. Benayad, K. K. Kim, S. J. Kim, H. K. Park, J.-Y. Choi and Y. H. Lee, *J. Am. Chem. Soc.*, 2008, **130**, 2062–2066.

22 A. Star, T.-R. Han, J.-C. P. Gabriel, K. Bradley and G. Grüner, *Nano Lett.*, 2003, **3**, 1421–1423.
23 K. Dirian, S. Backes, C. Backes, V. Strauss, F. Rodler, F. Hauke, A. Hirsch and D. M. Guldi, *Chem. Sci.*, 2015, **6**, 6886–6895.
24 Y. Tsarfati, V. Strauss, S. Kuhri, E. Krieg, H. Weissman, E. Shimoni, J. Baram, D. M. Guldi and B. Rybtchinski, *J. Am. Chem. Soc.*, 2015, **137**, 7429–7440.
25 A. Stergiou, H. Gobeze, I. Petsalakis, S. Zhao, H. Shinohara, F. D'Souza and N. Tagmatarchis, *Nanoscale*, 2015, **7**, 15840–15851.
26 P. Samorí, N. Severin, C. D. Simpson, K. Müllen and J. P. Rabe, *J. Am. Chem. Soc.*, 2002, **124**, 9454–9457.
27 Q. Su, S. Pang, V. Alijani, C. Li, X. Feng and K. Müllen, *Adv. Mater.*, 2009, **21**, 3191–3195.
28 X. Dong, D. Fu, W. Fang, Y. Shi, P. Chen and L. J. Li, *Small*, 2009, **5**, 1422–1426.
29 J. Malig, N. Jux, D. Kiessling, J. J. Cid, P. Vázquez, T. Torres and D. M. Guldi, *Angew. Chem., Int. Ed.*, 2011, **50**, 3561–3565.
30 L. Brinkhaus, G. Katsukis, J. Malig, R. D. Costa, M. Garcia-Iglesias, P. Vázquez, T. Torres and D. M. Guldi, *Small*, 2013, **9**, 2348–2357.
31 J. Malig, A. W. I. Stephenson, P. Wagner, G. G. Wallace, D. L. Officer and D. M. Guldi, *Chem. Commun.*, 2012, **48**, 8745–8747.
32 D. Kiessling, R. D. Costa, G. Katsukis, J. Malig, F. Lodermeyer, S. Feihl, A. Roth, L. Wibmer, M. Kehrer, M. Volland, P. Wagner, G. G. Wallace, D. L. Officer and D. M. Guldi, *Chem. Sci.*, 2013, **4**, 3085–3098.
33 R. D. Costa, J. Malig, W. Brenner, N. Jux and D. M. Guldi, *Adv. Mater.*, 2013, **25**, 2600–2605.
34 L. Wibmer, L. M. O. Lourenco, A. Roth, G. Katsukis, M. G. P. M. S. Neves, J. A. S. Cavaleiro, J. P. C. Tome, T. Torres and D. M. Guldi, *Nanoscale*, 2015, **7**, 5674–5682.
35 L. Martin-Gomis, N. Karousis, F. Fernandez-Lazaro, I. D. Petsalakis, K. Ohkubo, S. Fukuzumi, N. Tagmatarchis and A. Sastre-Santos, *Photochem. Photobiol. Sci.*, 2017, **16**, 596–605.
36 N. Martin, *Chem. Commun.*, 2013, **49**, 7025–7027.
37 F. M. Raymo, *J. Am. Chem. Soc.*, 2005, **127**, 9309–9309.
38 Z. Chen, V. Stepanenko, V. Dehm, P. Prins, L. D. A. Siebbeles, J. Seibt, P. Marquetand, V. Engel and F. Würthner, *Chem. – Eur. J.*, 2007, **13**, 436–449.
39 C. Huang, S. Barlow and S. R. Marder, *J. Org. Chem.*, 2011, **76**, 2386–2407.
40 C. Goze, C. Leiggener, S.-X. Liu, L. Sanguinet, E. Levillain, A. Hauser and S. Decurtins, *ChemPhysChem*, 2007, **8**, 1504–1512.
41 A. Amacher, C. Yi, J. Yang, M. P. Bircher, Y. Fu, M. Cascella, M. Gratzel, S. Decurtins and S.-X. Liu, *Chem. Commun.*, 2014, **50**, 6540–6542.
42 J. J. Bergkamp, S. Decurtins and S.-X. Liu, *Chem. Soc. Rev.*, 2015, **44**, 863–874.
43 X. Guégano, A. L. Kanibolotsky, C. Blum, S. F. L. Mertens, S.-X. Liu, A. Neels, H. Hagemann, P. J. Skabara, S. Leutwyler, T. Wandlowski, A. Hauser and S. Decurtins, *Chem. – Eur. J.*, 2009, **15**, 63–66.
44 M. Jaggi, C. Blum, B. S. Marti, S.-X. Liu, S. Leutwyler and S. Decurtins, *Org. Lett.*, 2010, **12**, 1344–1347.
45 M. E. El-Khouly, M. Jaggi, B. Schmid, C. Blum, S.-X. Liu, S. Decurtins, K. Ohkubo and S. Fukuzumi, *J. Phys. Chem. C*, 2011, **115**, 8325–8334.
46 M. Jaggi, C. Blum, N. Dupont, J. Grilj, S.-X. Liu, J. Hauser, A. Hauser and S. Decurtins, *Org. Lett.*, 2009, **11**, 3096–3099.
47 R. Pfattner, E. Pavlica, M. Jaggi, S.-X. Liu, S. Decurtins, G. Bratina, J. Veciana, M. Mas-Torrent and C. Rovira, *J. Mater. Chem. C*, 2013, **1**, 3985–3988.
48 B. K. Kaletaş, R. Dobrawa, A. Sautter, F. Würthner, M. Zimine, L. De Cola and R. M. Williams, *J. Phys. Chem. A*, 2004, **108**, 1900–1909.
49 L. Feng, M. Rudolf, S. Wolfrum, A. Troeger, Z. Slanina, T. Akasaka, S. Nagase, N. Martín, T. Ameri, C. J. Brabec and D. M. Guldi, *J. Am. Chem. Soc.*, 2012, **134**, 12190–12197.

4.2 Azulene-PDI triads

4.2.1 Introduction

As aforementioned, azulene is a non-benzenoid aromatic hydrocarbon isomer of naphthalene, which consists of an electron-rich five-membered ring and an electron-deficient seven-membered ring.[96] It was demonstrated that some of azulene derivatives show unique acid-base responsive properties,[46, 97] which makes them possible for the sensor applications. In the past decade, little work has been done on azulene-based D-A systems, in which an azulene core is mostly functionalized at the 2-position and linked to an electron acceptor either directly or through a triple bond.[49, 50] Only in one report, azulene is incorporated to a naphthodithiophene diimide directly through the carbon at the 6-position of the azulene ring, leading to a typical n-channel behavior with the highest electron mobility up to 0.13 $cm^2 V^{-1} s^{-1}$.[51] The main reason for this is that synthetic procedures for the key precursor 6-azulenyl boronic acid ester (6-borylazulene) were quite tedious and frustrating.[49] Until last year, Yorimitsu group successfully synthesized 6-borylazulene in one step through sodium mediated borylation,[41] which gives us a hint to explore further functionalization of the azulene core at the 6-position. Given that PDI possesses excellent thermal, chemical and photochemical stabilities combined with its optical and redox properties,[11] we have decided to prepare π-extended PDI ensembles by introducing two azulene groups directly to the PDI core, either through the carbon atoms at 2- or 6-positions of azulene rings, respectively. In this section, the synthesis, characterization, electronic and acid-basic responsive properties will be discussed.

4.2.2 Results and discussion

Synthesis of azulene-functionalized PDI derivatives starts with borylation of azulene at 2- or 6-position, respectively (**Scheme 1**). On the one hand, azulene was reacted with bis(pinacolato)diboron in the presence of $[Ir(OMe)(cod)]_2$ catalyst to obtain 2-(2-azulenyl)-4,4,5,5-tetramethyl-1,3,2-dioxaborolane in a yield of 45% (2-borylazulene), while the 1-borylazulene was also obtained as a byproduct in 8% yield. On the other hand, 6-borylazulene was prepared with exclusive regioselectivity. The detailed process is that azulene was reduced under sodium dispersion and reacted with methoxypinacolborane in 1,2-dimethoxyethane at -

40 °C for 2 h, forming a diborylated intermediate. 2,2,6,6-Tetramethylpiperidine-1-oxyl (TEMPO) was then added as an oxidant to the reaction mixture at -40 °C and stirred about 0.5 h. This procedure successfully resulted in the selective oxidative monodeborylative dearomatization to produce 6-borylazulene as a dark blue solid in 60% yield.[41]

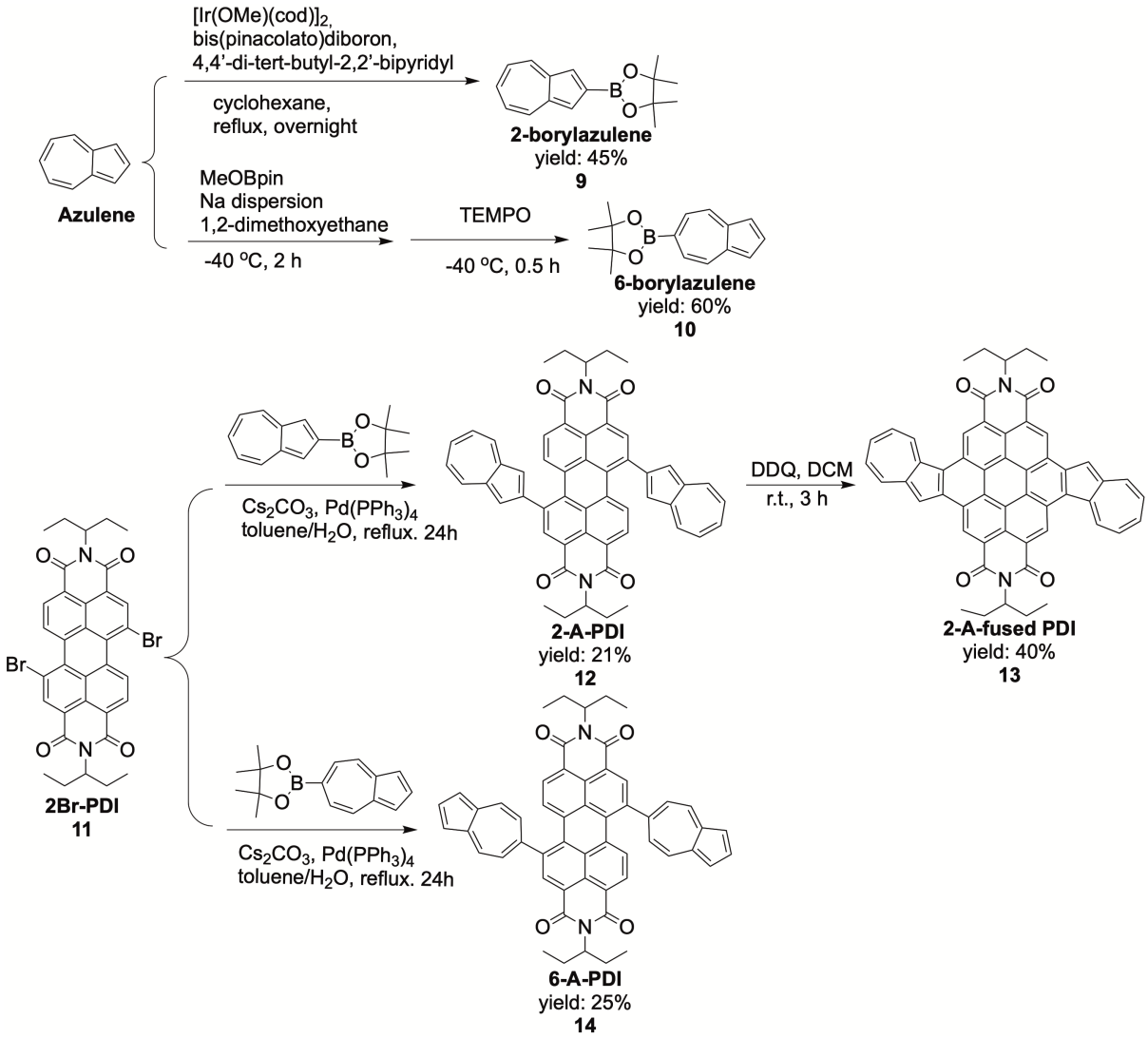

Scheme 1. Synthesis of azulene-functionalized PDI derivatives.

1,7-Dibromo-*N,N'*-bis-(1-ethylpropyl)-perylene-3,4,9,10-tetracarboxylic diimide (**2Br-PDI**) was synthesized by bromination of perylene bisanhydride.[98] Both of 1,7- and 1,6- regioisomers were formed and could not be separated by column chromatography. Analytically pure 1,7-dibromo-PDI was obtained by recrystallization in a mixture of DCM and methanol, at least repeated for three times. Its purity can be clearly checked by ^{1}H-NMR (**Figure 1**). For the targets, we adopted a synthetic strategy similar to that reported for the preparation of an

azulene-fused tetracene diimide system.[50] The Suzuki coupling reaction of **2Br-PDI** with 2-borylazulene in a toluene-water mixture in the presence of $Pd(PPh_3)_4$ catalyst and Cs_2CO_3 under reflux for 24 h afforded **2-A-PDI** in 21% yield. The subsequent oxidation of **2-A-PDI** with 2,3-dicyno-5,6-dichloro-1,4-benzoquinone (DDQ) at r.t. in DCM afforded **2-A-fused PDI** in a yield of 40%. Similarly, the Suzuki coupling of 6-borylazulene with **2Br-PDI** produced **6-A-PDI** in 25% yield. The oxidation process, however, failed to afford the desired target **6-A-fused PDI** despite many attempts (**Table 1**). It is very probably due to the fact that the 7-membered ring is electron-deficient which prevents an oxidative cyclization.

Table 1. The tested reaction conditions for cyclization of **6-A-PDI**.

	Oxidant	Solvent	Tem.	Acid
1	DDQ	DCM	-20 °C	
2	DDQ	DCM	0 °C	
3	DDQ	DCM	r.t.	
4	DDQ	DCM	reflux	
5	DDQ	DCM	r.t.	$BF_3.OEt_2$
6	TEMPO	DCM	r.t.	

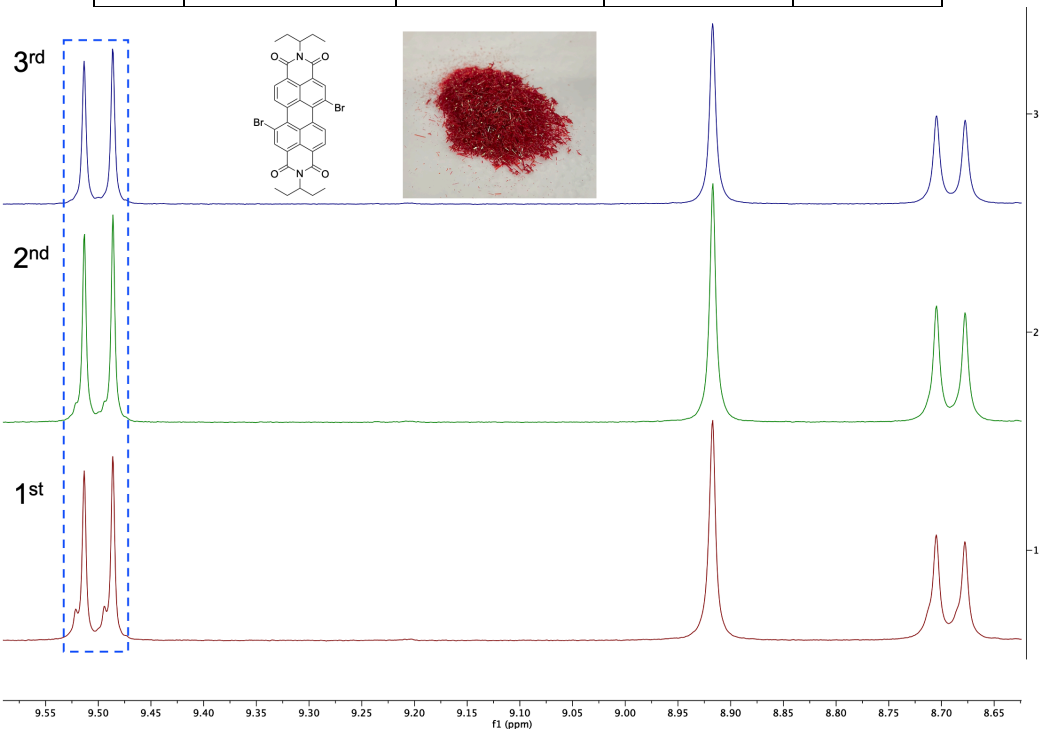

Figure 1 ^1H NMR spectra of 1,7-dibromo-PDI (**2Br-PDI, 11**) obtained after each recrystallization.

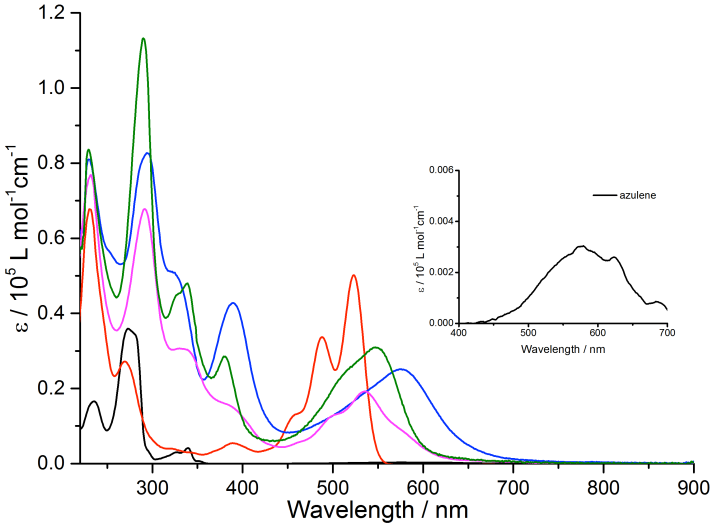

Figure 2 The UV-Vis spectra of **2-A-PDI** (blue), **2-A-fused PDI** (pink), **6-A-PDI** (green), **2Br-PDI** (red) and azulene (black) at the concentration of 10^{-5} M in DCM at r.t. The inset highlights the very broad peak by magnifying the region from 400 to 700 nm for azulene.

The optical properties of **2-A-PDI**, **2-A-fused PDI**, **6-A-PDI** and references azulene and **2Br-PDI** were investigated by UV-Vis absorption spectra in DCM at r.t. (**Figure 2**). Azulene shows a series of absorption bands in the whole UV region, in which the absorption band around 340 nm is attributed to the $S_0 \rightarrow S_2$ transition. A very weak absorption band peaked around 580 nm corresponds to the $S_0 \rightarrow S_1$ transition (**Figure 2**, inset).[99] **2Br-PDI** strongly absorbs at 485 nm and 525 nm. Compared to reference compounds, the neutral **2-A-PDI** exhibits a very broad absorption band peaked at 577 nm which is red-shifted. It is very likely due to a combination of an ICT from azulene to PDI units and the π-π* transition localized on the PDI core. Its fused counterpart **2-A-fused PDI** also shows a broad absorption band centered at 535 nm, which is blue-shifted compared to **2-A-PDI**. One possible reason is that the fused counterpart has an enlarged diazulenylcoronene diimide π-system which is distinct from the PDI itself as shown in the following theoretical part. In comparison with dinaphthocoronene diimide (**diN-PDI, Figure 3**),[100] **2-A-fused PDI** displays a significant bathochromic shift of the lowest-energy absorption band which extends to 675 nm, causing by different electronic properties of azulene and naphthalene.

Similarly, **6-A-PDI** shows a broad absorption band with a maximum peak at 548 nm (with a shoulder at 512 nm), which is blue-shifted with respect to **2-A-PDI**, probably caused by electronic interactions between the electron-deficient 7-membered ring of azulene and the PDI

core. This assumption is consistent with the CV results and also verified by TD-DFT calculations.

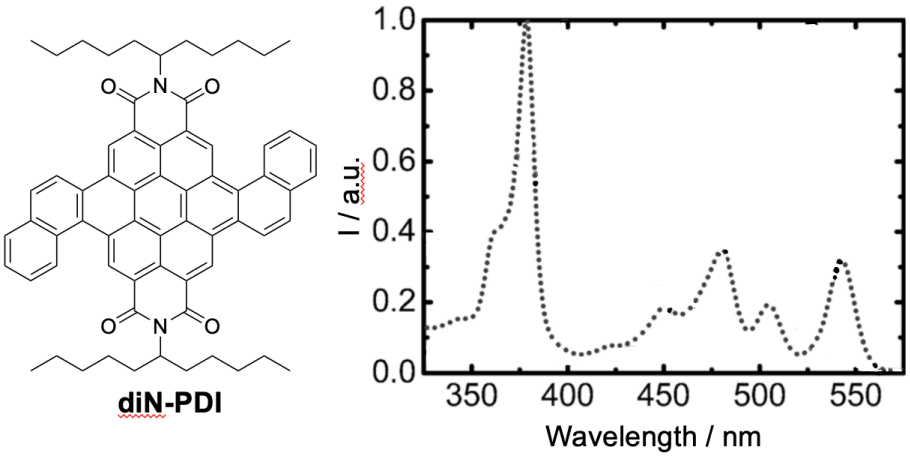

Figure 3 UV-Vis spectra of **diN-PDI** (dotted line) in DCM.

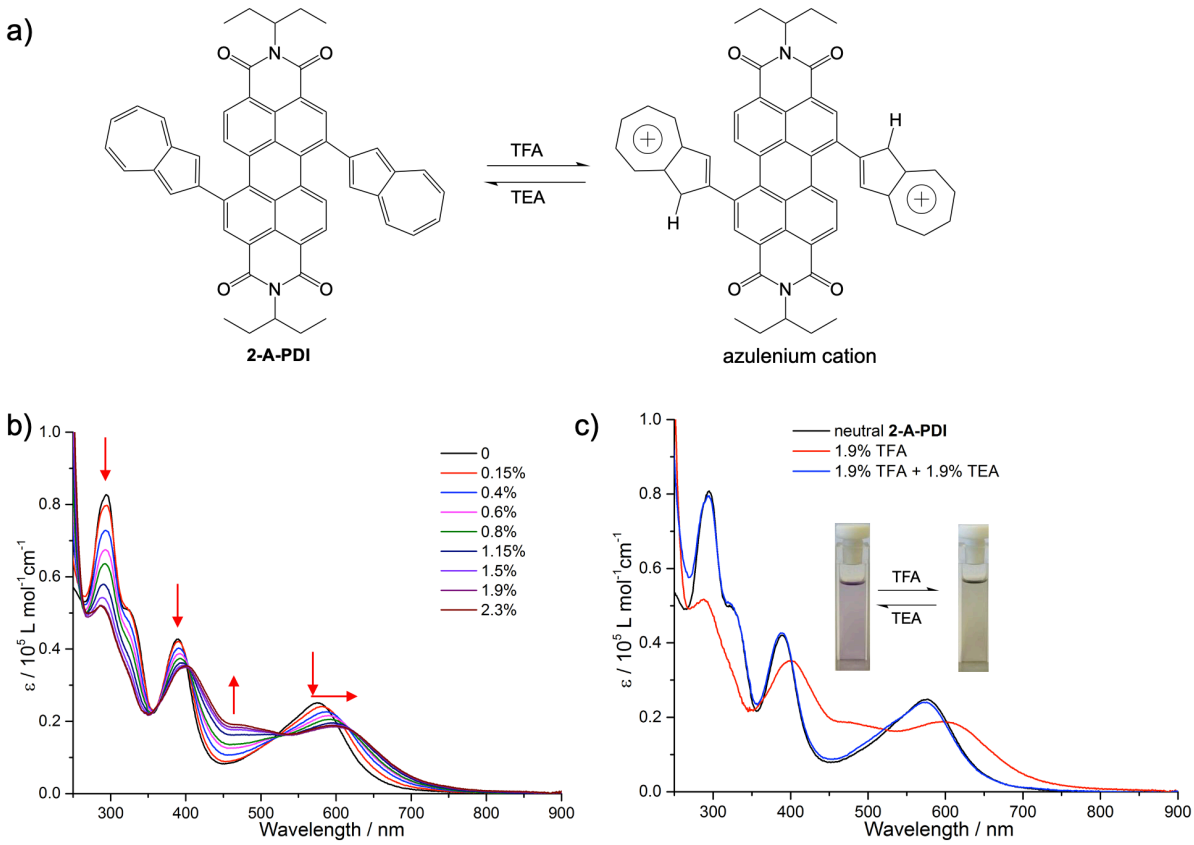

Figure 4 The spectral evolution of **2-A-PDI** at the concentration of 10^{-5} M in DCM in the presence of an acid (TFA) and a base (TEA).

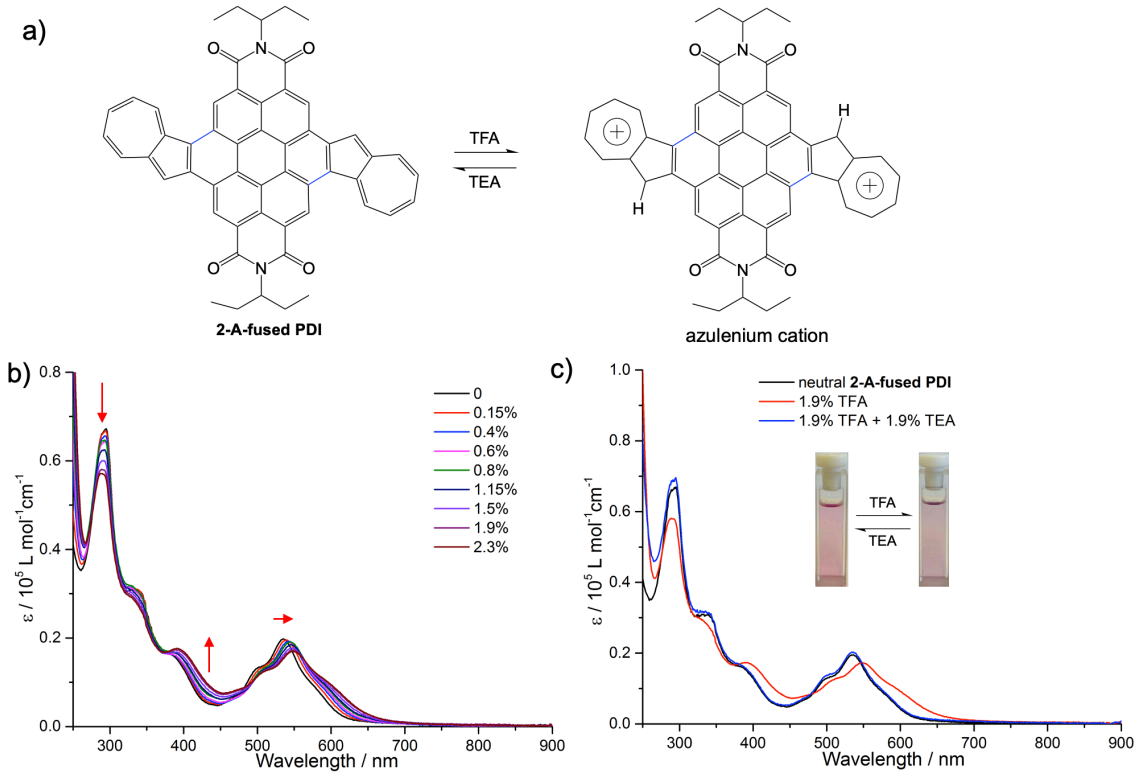

Figure 5 The spectral evolution of **2-A-fused PDI** at the concentration of 10^{-5} M in DCM in the presence of TFA and TEA.

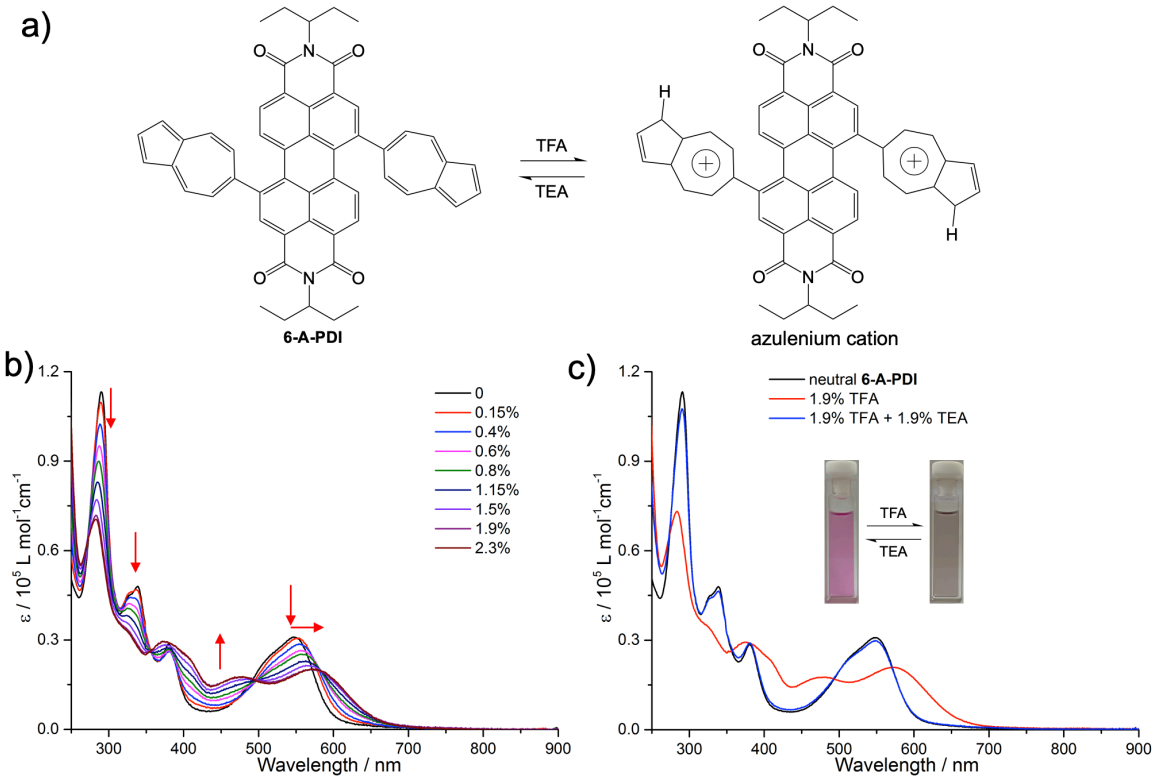

Figure 6 The spectral evolution of **6-A-PDI** at the concentration of 10^{-5} M in DCM in the presence of TFA and TEA.

It is known that azulene and most of its derivatives can be protonated at the electron-rich five-membered ring by trifluoroacetic acid (TFA) to form the corresponding azulenium. The optical properties of the protonated species were studied in DCM-TFA solution at r.t. As depicted in **Figure 4**, upon addition of TFA to **2-A-PDI** solution in DCM, a fast color change from violet to light-green was observed. With the increase in the concentration of TFA, the absorption intensities around 280 nm and 380 nm decrease gradually, accompanying with a red-shift of the absorption band from 380 nm to 390 nm. At the same time, an increase in the absorption between 400 nm and 520 nm occurs at the expense of the lowest energy absorption which is red-shifted to 600 nm. The absorption bands around 390 nm and 600 nm are attributed to the formation of azulenium cations.[47, 101] Notably, **2-A-PDI** is quite pH-sensitive as demonstrated by a drastic change in its absorption spectrum with adding a small amount of TFA (1.9%). Moreover, several isosbestic points are observed, suggesting that two interconverting optically different species are formed. No further noticeable spectral changes are detected upon the addition of 1.9% TFA (V/V) suggesting that the population of azulenium cation was saturated under this concentration (0.25 M). More interestingly, **2-A-PDI** displays a distinct reversible colorimetric pH-response. Neutralization of the acidic solution of **2-A-PDI** with 1.9% of TEA leads to a complete recovery of its original UV-Vis spectrum.

As illustrated in **Figure 5**, **2-A-fused PDI** exhibits a similar spectral evolution upon protonation, but less pronounced as **2-A-PDI**. This phenomenon was also observed in 1- and 3-substituted azulene-based polymers.[96, 101] This pH-response process is reversible as well. Moreover, **6-A-PDI** obviously shows a color change from pink to light-purple, consistent with a considerable spectral change in response to TFA (**Figure 6**). The colorimetric reversibility is independent on the connectivity between azulene and PDI which renders such systems appealing in the development of sensors.

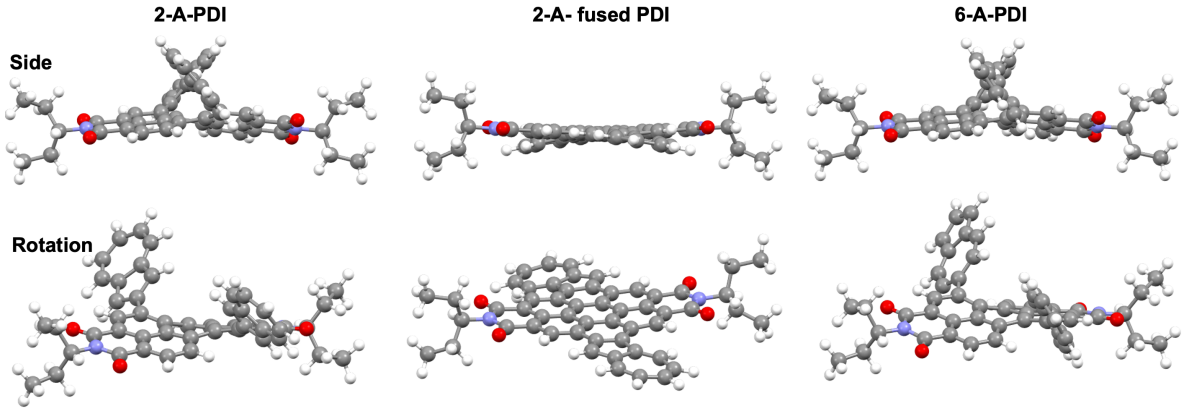

Figure 7 Structures of **2-A-PDI**, **2-A-fused PDI** and **6-A-PDI**.

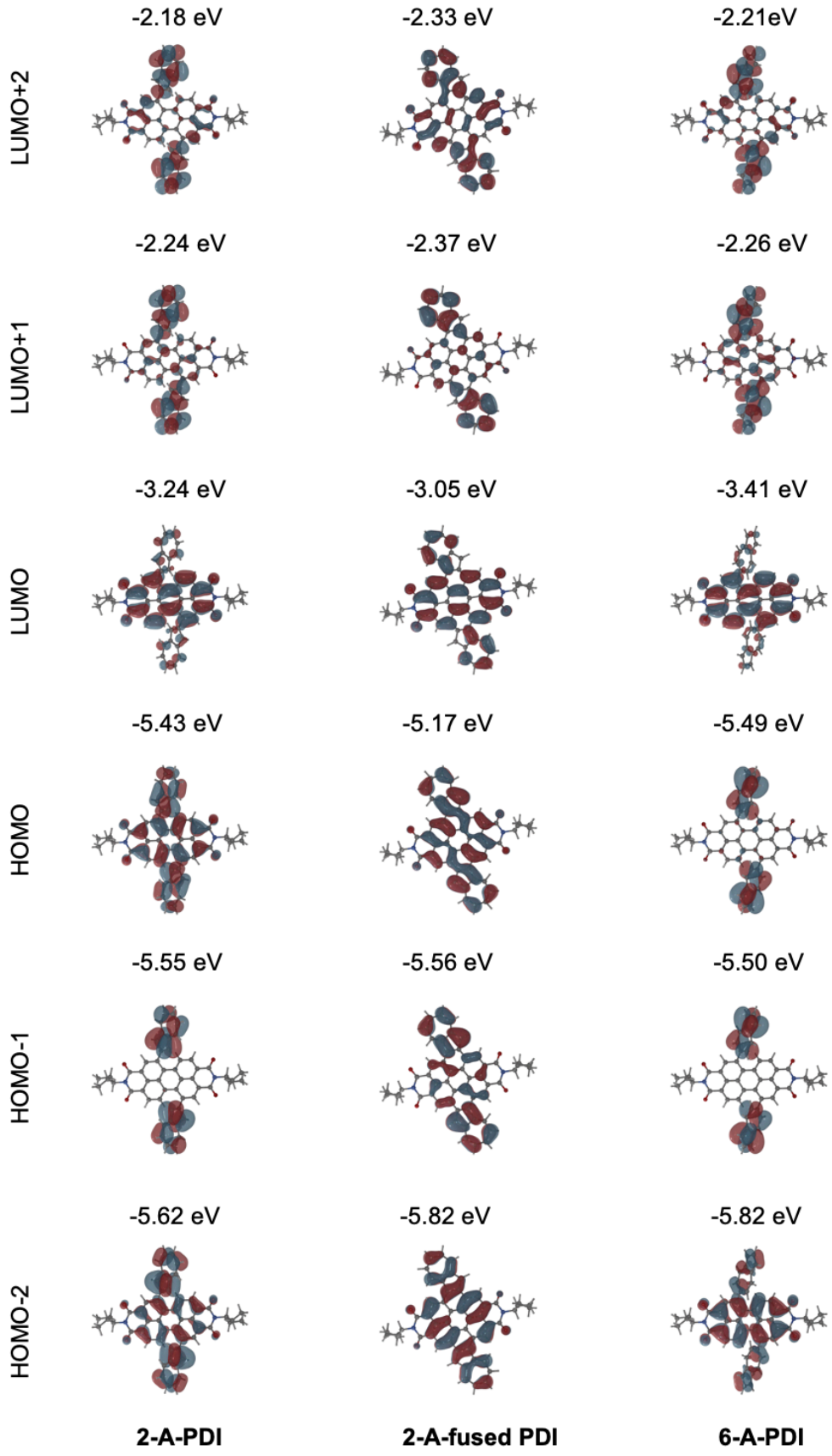

Figure 8 Frontier molecular orbitals of **2-A-PDI**, **2-A-fused PDI and 6-A-PDI**.

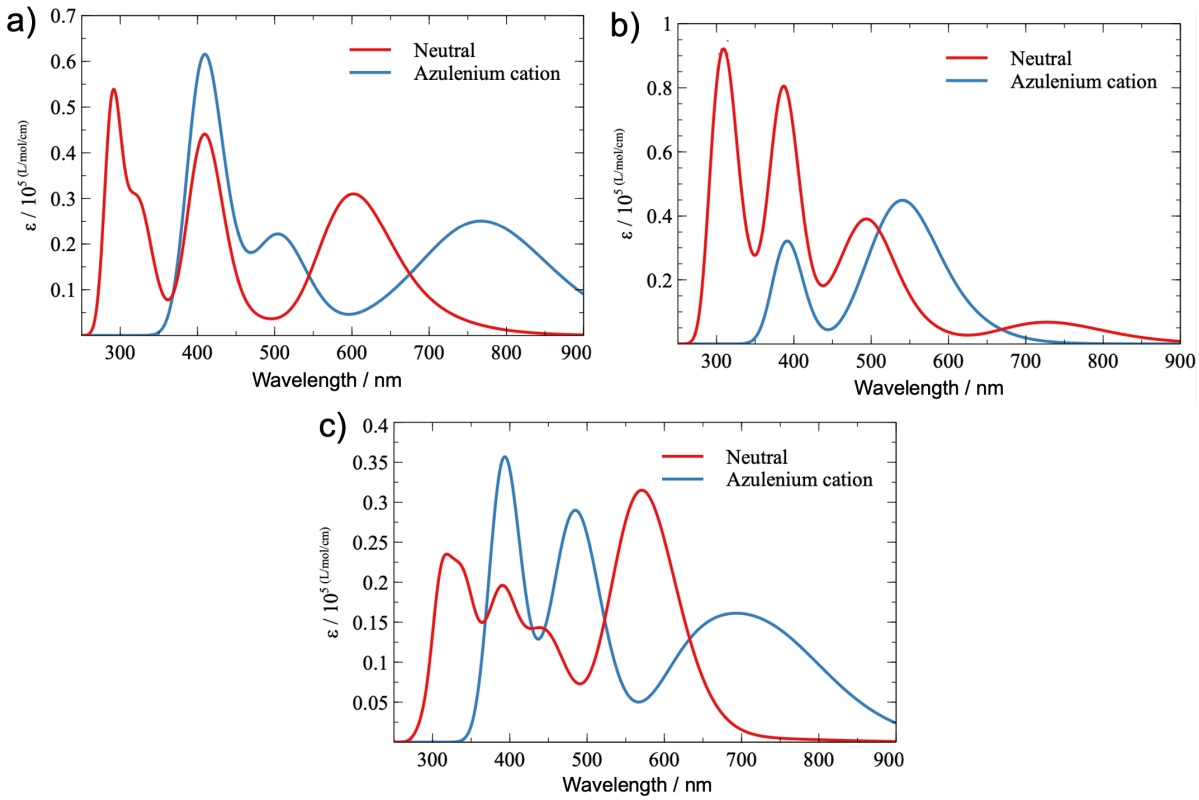

Figure 9 The computed absorption spectra of **2-A-PDI** (a), **2-A-fused PDI** (b) and **6-A-PDI** (c) before and after protonation

To characterize and verify the various electronic transitions, TD-DFT calculations were performed using the Gaussian 16 package at the B3LYP/6-31G(d,p) level of theory. As shown in **Figure 7**, the molecular structures of **2-A-PDI** and **6-A-PDI** are not planar while **2-A-fused PDI** is almost coplanar. **Figure 8** illustrates some frontier molecular orbitals (MOs) of **2-A-PDI**, **2-A-fused PDI** and **6-A-PDI**. On the one hand, the LUMO of **2-A-PDI** and **6-A-PDI** are mainly located on PDI core. The calculated E_{LUMO} is -3.24 eV for **2-A-PDI**, about 0.17 eV higher than **6-A-PDI** (-3.41 eV), which is in good agreement with the reported NDI-azulene systems, showing that the connection of 7-membered rings of azulene units to the NDI core leads to a lower LUMO than the counterpart with a connectivity *via* 5-membered rings of azulene.[49, 51] On the other hand, the HOMO of **2-A-PDI** is distributed over the azulene and PDI core while HOMO of **6-A-PDI** is only localized at terminal two azulene units. As for **2-A-fused PDI**, both LUMO and HOMO are completely delocalized over the entire π-extended aromatic skeleton.

The calculated vertical electronic transitions for **2-A-PDI**, **2-A-fused PDI** and **6-A-PDI** in neutral and protonated states are shown in **Figure 9**. For three compounds, the calculated

energies and oscillator strengths at wavelengths below 450 nm corresponding to π-π* transitions localized on PDI and azulene units compare well with their absorption spectra. In the low energy region, a transition with low oscillator strength is found around 700 nm which is attributed to the $S_0 \rightarrow S_1$ excitation dominated by electron transfer from HOMO → LUMO (76% for **2-A-PDI**, 93% for **2-A-fused PDI** and 98% for **6-A-PDI**). The next largest oscillator strength belongs to the transition at 600 nm for **2-A-PDI**, 500 nm for **2-A-fused PDI** and 570 nm for **6-A-PDI**, respectively. It is dominated by a one-electron HOMO-2 → LUMO promotion (75% for **2-A-PDI**, 59% for **2-A-fused PDI** and 97% for **6-A-PDI**). As a result, **2-A-PDI** exhibits an ICT character as electron density is moved from the azulene units to the PDI core, but not for **2-A-fused PDI** and **6-A-PDI**. The calculated energies and oscillator strengths of these transitions compare fairly well with the broad absorption band peaked at 577 nm for **2-A-PDI**, 535 nm for **2-A-fused PDI** and 548 nm for **6-A-PDI**. The calculated HOMO-LUMO gap amounts to 2.19 eV for **2-A-PDI**, 2.12 eV for **2-A-fused PDI** and 2.08 eV for **6-A-PDI**. After protonation, the calculated vertical electronic transitions for **2-A-PDI**, **2-A-fused PDI** and **6-A-PDI** are read-shifted compared to neutral states leading by the formation of azulenium cation.

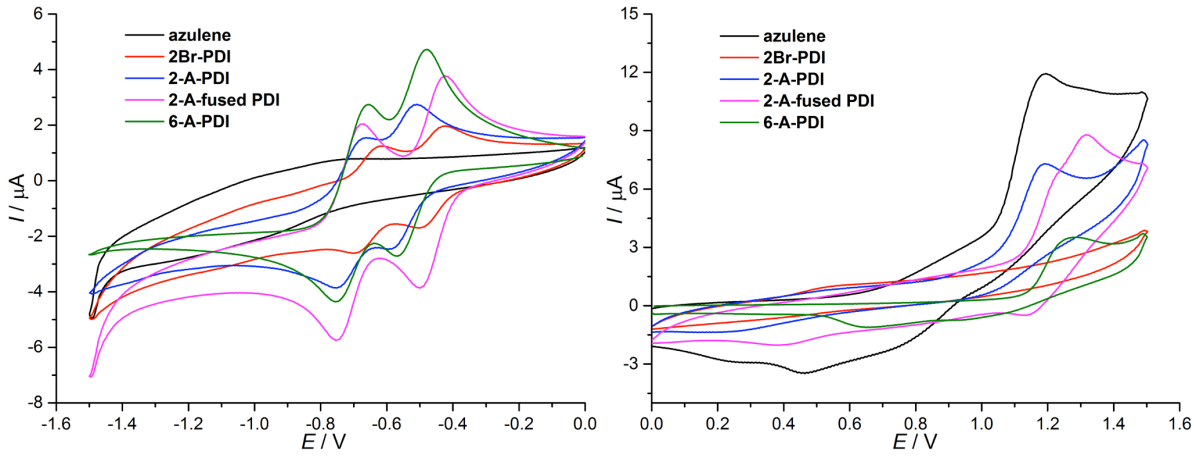

Figure 10 Cyclic voltammograms of azulene, PDI, **2-A-PDI**, **2-A-fused PDI** and **6-A-PDI** were measured in DCM, containing 0.1 M $TBAPF_6$ as the supporting electrolyte at r.t., Pt working electrode, Ag/AgCl reference electrode at the scan rate of 100 mV s^{-1}. E_{HOMO} = -e (E_{ox}^{onset} + 4.3), E_{LUMO} =-e (E_{red}^{onset} + 4.3), E_{ox}^{onset} = the onset oxidation potential, E_{red}^{onset} = the onset reduction potential, $E_{HOMO} = E_{LUMO} - E_g$, optical gap = $1240/\lambda_{onset}$. λ_{onset} represents the absorption edge wavelength obtained from the offset wavelength, derived and extrapolated from the lowest-energy absorption band.[102, 103] Fc/Fc^+ is 0.5 V relative to Ag/AgCl in DCM.

Table 2 Electrochemical data. Redox potentials [V] vs. Ag/AgCl in DCM.

Compounds	E^{ox} (V)	$E_{1/2}^{red1}$ (V)	$E_{1/2}^{red2}$ (V)	HOMO (eV)	LUMO (eV)	*Eg* (eV)	Optical gap(eV)
Azulene	1.19			-5.31			3.45
2Br-PDI		-0.47	-0.67		-3.90		2.27
2-A-PDI	1.19	-0.55	-0.72	-5.36	-3.81	1.55	1.90
2-A-fused PDI	1.32	-0.46	-0.71	-5.43	-3.90	1.53	2.00
6-A-PDI	1.26	-0.53	-0.71	-5.44	-3.84	1.60	2.07

The electrochemical properties of targets and references were investigated by the cyclic voltammetry at r.t. in DCM (**Figure 10**). The reference azulene underwent an oxidation process at 1.19 V while **2Br-PDI** experienced two reversible reductions at -0.47 V and -0.67 V, respectively. As expected, **2-A-PDI** has one anodic peak (1.19 V) for the oxidation of the azulene core and the two reversible reduction peaks (-0.55 V and -0.72 V) corresponding to the reduction processes of the PDI moiety. The reduction potentials are negatively shifted compared to those of **2Br-PDI** while they are slightly positive-shifted with respect to those of the PDI itself (-0.60V and -0.79 V).[104] These results are ascribed to stronger electron-withdrawing ability of bromo groups and extended π-conjugation between azulene and PDI core, respectively. **2-A-fused PDI** shows one oxidation wave at 1.32 V and two reversible reduction processes at -0.46 V and -0.71 V, respectively. In comparison to **2-A-PDI**, both oxidation and reduction potentials are positively shifted, indicative of an enhanced π-electron withdrawing ability of coronene core due to cyclization between 5-membered ring of azulene and PDI. Both HOMO and LUMO are stabilized by the π-extended conjugation through the coronene diimide and azulene units. Besides, **2-A-PDI** has a higher LUMO than **2Br-PDI** (-3.90 eV), which is attributed to the electron donating ability of azulene. **6-A-PDI** has one oxidation potential of 1.26 V and two reversible reduction potentials of -0.53 V and -0.71 V. In contrast to **2-A-PDI**, the oxidation potential is positively shifted due to an increased electron-withdrawing effect of 7-memberd ring of azulene caused by a direct connection to the electron-deficient PDI core. As expected, reduction potentials are negligibly dependent on connectivity due to nonplanarity between the PDI and azulene units that impedes the electronic interactions between them as previously reported in the literature. As a result, the LUMO energy level for **6-A-PDI** (-3.84 eV) is almost same as that for **2-A-PDI** (-3.81 eV). The trend is agreement with DFT calculations. The HOMO energy levels are -5.36 eV and -5.44 eV for **2-A-PDI** and **6-A-PDI**, respectively. Their electrochemical HOMO-LUMO band gap are 1.55 eV and 1.60

eV, respectively, which are in good agreement with their optical band gaps (1.90 eV and 2.07 eV). Additionally, **2-A-fused PDI** has a much lower HOMO-LUMO band gap (1.53 eV vs 2.18 eV) and a lower LUMO energy (-3.90 eV vs -3.72 eV) with respect to **diN-PDI**.[100]

4.2.3 Conclusions and outlook

A series of azulene-PDI conjugates through different connectivities have been synthesized successfully, namely **2-A-PDI**, **2-A fused PDI** and **6-A-PDI**. The UV-Vis spectra of **2-A-PDI** and **6-A-PDI** show sizable electronic interactions between the azulene and PDI as verified by TD-DFT calculations. The CV results show that **6-A-PDI** has a higher oxidation potential than **2-A-PDI** albeit similar reduction potentials. All these conjugates exhibit reversible colorimetric pH-response in the presence of an acid (TFA) and a base (TEA). The UV and CV results suggest that HOMO-LUMO gaps of azulene-PDI conjugates can be tuned by changing the connectivity between these two units which renders them promising in the field of organic transistors.

4.2.4 Experimental part

The related chemicals, solvents and the conditions of cyclic voltammetry are given in Appendix **A.1**.

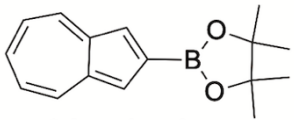

2-borylazulene (**9**). A dried flask was charged with $[Ir(OMe)(cod)]_2$ (33 mg, 50 μmol), 4,4'-di-*tert*-butyl-2,2'-bipyridyl (26.8 mg, 100 μmol), azulene (564 mg, 4.4 mmol), bis(pinacolato)diboron (508 mg, 2.0 mmol), and cyclohexane (6.0 mL). After stirring at 110 °C for 12 h, the solvent was removed under reduced pressure. The residue was subjected to column chromatography on silica gel with heptane/EtOAc (v/v = 20/1) as an eluent to afford the 2-(4,4,5,5-teramethyl-1,3,2-dioxaborolan-2-yl)azulene (229 mg, 45%) as a blue solid.. ^{1}H NMR (300 MHz, $CDCl_3$) δ 8.35 (d, J = 9.2 Hz, 2H), 7.76 (s, 2H), 7.58 (t, J = 9.9 Hz, 1H), 7.11 (t, J = 9.8 Hz, 2H), 1.40 (s, 12H). ^{13}C NMR (75 MHz, $CDCl_3$) δ 140.84, 138.90, 138.33, 125.23, 122.88, 83.89, 25.08.

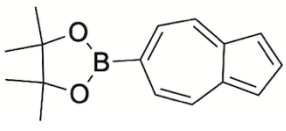

6-borylazulene (**10**). A 20-mL Schlenk tube was charged with azulene (0.13 g, 1.0 mmol), MeOBpin (1.0 mL, 6.0 mmol), and DME (4.0 mL). Na dispersion (0.25 mL, 2.5 mmol) was dropwise added over 30 s. The resulting solution was stirred at -40 °C for 2 h. TEMPO (0.39 g, 2.5 mmol) was added, and the reaction mixture was stirred for 30 min. After addition of saturated aqueous

NH_4Cl (0.5 mL) and H_2O (5 mL), the resulting biphasic solution was extracted with EtOAc (15 mL × 3). The combined organic layer was washed with brine, dried over Na_2SO_4, and concentrated under reduced pressure. The residue was purified by column chromatography on silica gel with an eluent (hexane/EtOAc = 100/1) to provide **6-Bpin-azulene** (0.18 g, 69%) as a dark blue solid. ^{1}H NMR (300 MHz, $CDCl_3$) δ 8.37 (d, J = 9.7 Hz, 2H), 7.97 (t, J = 3.7 Hz, 1H), 7.73 (d, J = 9.7 Hz, 2H), 7.39 (d, J = 3.7 Hz, 2H), 1.40 (s, 12H). ^{13}C NMR (75 MHz, $CDCl_3$) δ 141.48, 138.68, 135.72, 128.70, 117.70, 84.70, 25.08. HR-MS calcd for M 254.1478, found 254.1473.

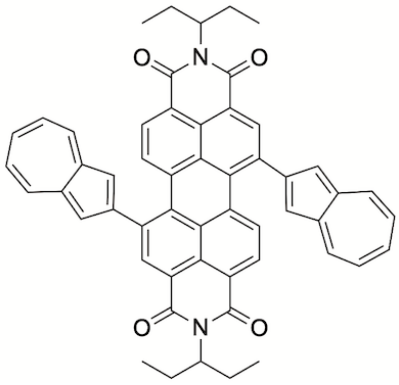

2-A-PDI (**12**). **2Br-PDI** (103 mg, 0.15 mmol), 2-(4,4,5,5-teramethyl-1,3,2-dioxaborolan-2-yl)azulene (114 mg, 0.45 mmol), Cs_2CO_3 (293 mg, 0.9 mmol), and $Pd(PPh_3)_4$ (69 mg, 0.06 mmol) were added to a three-necked flask (100 mL) and flushed with N_2. The toluene/H_2O (20 mL/10 mL) was added into the flask and refluxed under N_2 for 24h. The reaction was quenched with aqueous 2M HCl (0.6 mL), extracted with toluene, washed with water and brine, and dried over Na_2SO_4. The obtained crude product was purified by silica gel column chromatography (25 mg, 21%). ^{1}H NMR (300 MHz, CD_2Cl_2) δ 8.78 (s, 2H), 8.34 (d, J = 9.4 Hz, 4H), 7.97 (s, 4H), 7.64 (t, J = 10.1 Hz, 2H), 7.59 (s, 4H), 7.24 (t, J = 9.8 Hz, 4H), 5.06 – 4.95 (m, 2H), 2.31 – 2.14 (m, 4H), 1.96 – 1.81 (m, 4H), 0.89 (t, J = 7.4 Hz, 12H).HR- MS (ESI, positive): *m/z* calcd for $[M+H]^+$ 783.3217, found 783.3207.

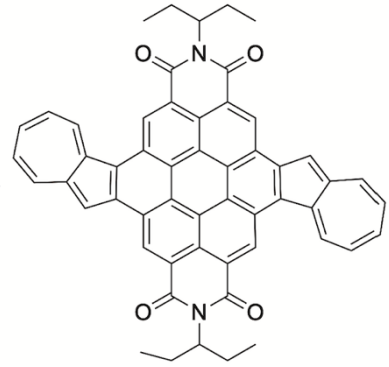

2-A-fused-PDI (**13**). 2,3-dicyano-5,6-dichloro-1,4-benzoquinone (DDQ, 36 mg, 0.16 mmol) was added into a solution of **2-A-PDI** (31 mg, 0.04 mmol) in DCM (20 mL) at r.t. and stirred for 3 h. The mixture was directly purified by column chromatography on neutral alumina with the eluent of DCM with a yield of 40% (12 mg). ^{1}H NMR (300 MHz, CD_2Cl_2) δ 8.76 (s, 1H), 8.68 (s, 1H), 8.56 (d, J = 9.6 Hz, 2H), 8.42 (t, J = 9.9 Hz, 2H), 8.13 (t, J = 7.9 Hz, 2H), 7.95 (s, 1H), 7.89 (s, 1H), 7.77 (t, J = 9.3 Hz, 2H), 7.36 (t, J = 9.8 Hz, 2H), 7.31 – 7.21 (m, 2H), 5.04 – 4.93 (m, 2H), 2.27 – 2.11 (m, 4H), 1.91 – 1.78 (m, 4H), 0.86 (t, J = 7.4 Hz, 12H). HR-MS (ESI, positive): *m/z* calcd for $[M+H]^+$ 779.2904, found 779.2888.

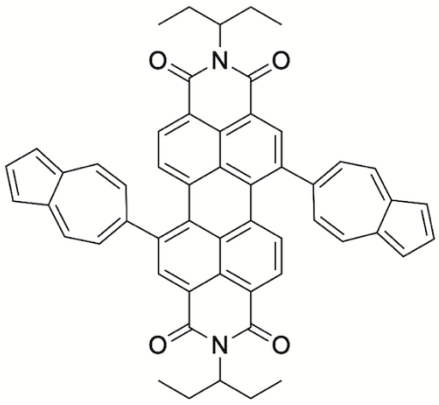

6-A-PDI (**14**). **2Br-PDI** (172 mg, 0.25 mmol), 2-(4,4,5,5-teramethyl-1,3,2-dioxaborolan-2-yl)azulene (254 mg,1 mmol), Cs_2CO_3 (489 mg, 1.5 mmol), and Pd $(PPh_3)_4$ (116 mg, 0.1 mmol) were added to a three-necked flask (100 mL) and flushed with N_2. The toluene/H_2O (34 mL/17 mL) was added into flask and heated at reflux under N_2 for 24 h. The reaction was quenched with aqueous 2M HCl (1 mL), extracted with toluene, washed with water and brine, and dried over Na_2SO_4. The obtained crude product was purified by column chromatography on silica gel with pure DCM as eluent (25 mg, 21%). ^{1}H NMR (300 MHz, CD_2Cl_2) δ 8.71 (s, 2H), 8.45 (d, J = 10.0 Hz, 4H), 8.05 – 7.99 (m, 4H), 7.90 (d, J = 8.2 Hz, 2H), 7.52 – 7.47 (m, 8H), 5.02 – 4.94 (m, 2H), 2.25 – 2.12 (m, 4H), 1.94 – 1.80 (m, 4H), 0.88 (t, J = 7.5 Hz, 12H). HR-MS (ESI, positive): *m/z* calcd for $[M+H]^+$ 783.3217, found 783.3203.

5. Through-space ICT in benzothiadiazole (BTD)-PCP-TTF conjugates

5.1 Introduction

As aforementioned, we have designed and investigated through-bond ICT interactions in both flexible and compact fused D-A ensembles. In this section, we will move on exploration of through-space ICT interactions. As we have already discussed in **Section 1**, [2,2]paracyclophane (PCP) consists of face-to-face stacked benzene rings with an average ring-to-ring distance of 3.09 Å and linking by diethylene groups, leading to a rigid structure and good conformational stability. Because of its special structure, PCP and its derivatives have been investigated in the optoelectronic devices. A limited number of PCP-based D-A molecules have been explored in recent years. Except for systems of Types A-C, other types of PCP-based ensembles have also been studied, including conjugated polymers,[105, 106] helical structures,[107, 108] molecular wires as a mimic of the DNA,[109] and so on.

Such D-A systems can exhibit through-space electronic interactions between a donor and an acceptor linked through a rigid PCP bridge and the lifetime of the resulting CS state can be modulated by the way how D and A units are connected to the PCP core.[110-112] Although an extensive investigation on through-bond ICT interactions in TTF-based D-A systems has been reported, none of examples of through-space ICT interactions have been discussed yet. Therefore, based on our experience on synthesis of TTF and 2,1,3-benzothiadizole (BTD), we have designed two TTF-PCP-BTD triads, in which TTF and BTD introduce into *pseudo-para* positions of PCP directly or by triple bonds, namely BTD-PCP-TTF-s and BTD-PCP-TTF-tri. In this section, we will discuss about their synthesis, characterization, optical and electrochemical properties, as well as about the effect of different linkers on CT dynamics by transient absorption spectroscopy.

5.2 Results and discussion

As illustrated in Scheme 1, our synthetic approach is divided to different sections. The first step is to synthesize **TTF** precursor (**15**) by a phosphite-mediated cross coupling reaction of 4,5-bis-(propylthio)-1,3-dithiole-2-one with 1,3-dithiole-2-thione.[113] Next, the precursor **15** was treated with perfluorohexyl iodide in the presence of *n*-BuLi to obtain **TTF-I** in a yield of 46% by using a convenient method for iodination.[114, 115] Suzuki cross-coupling of the *pseudo-para* dibromo[2,2]PCP and 4-(4,4,5,5-tetramethyl-1,3,2-dioxaborolan-2-yl)benzo[*c*][1,2,5]thiadiazole[116] in the presence of $Pd(dppf)Cl_2$ catalyst and base K_3PO_4

produced an intermediate **BTD-PCP-s** in 49% yield. It was further transformed to BTD-PCP-Bpin in a yield of 51% by the subsequent reaction with bis(pinacolato)diborane. A reaction of **TTF-I** with BTD-PCP-Bpin led to the formation of **BTD-PCP-TTF-s** as a light-yellow powder in 66% yield, in which the PCP core is substituted with a TTF as an electron D unit and a BTD as an electron A unit at the *pseudo-para* direction.

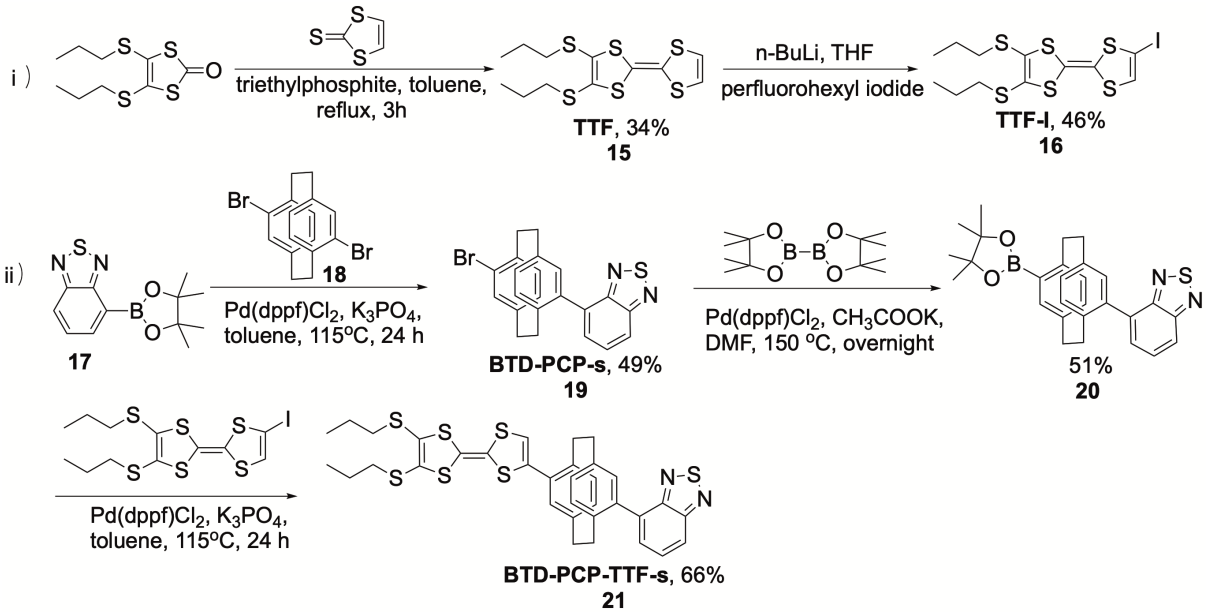

Scheme 1. Synthetic routes for the target compound **BTD-PCP-TTF-s** and the reference compounds **TTF** and **BTD-PCP-s**.

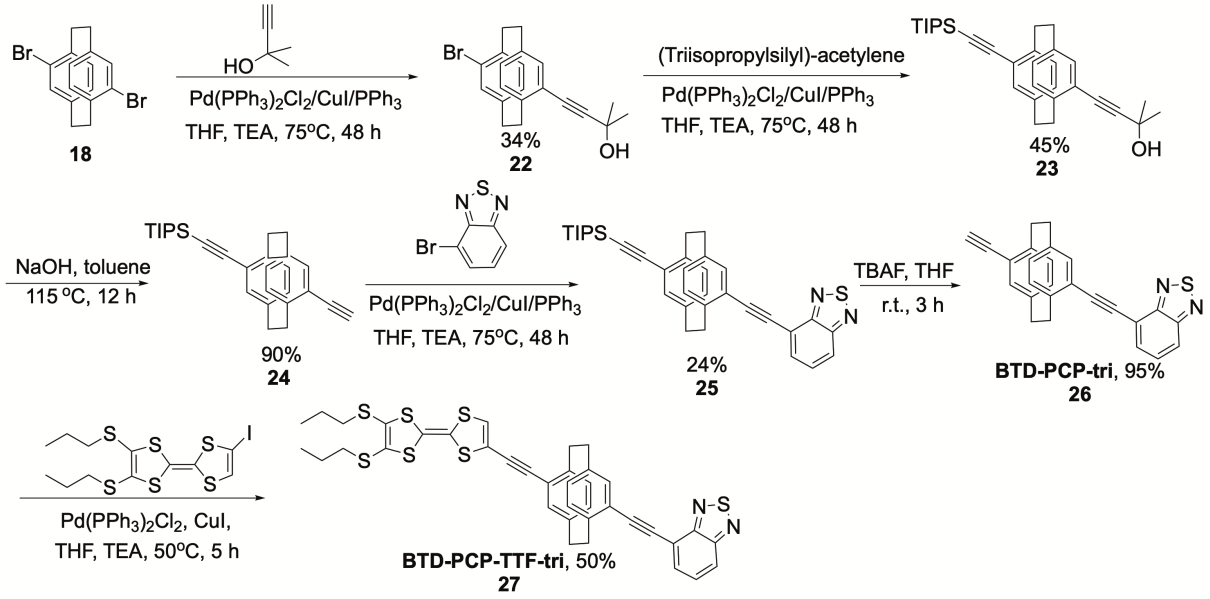

Scheme 2. Synthetic routes for **BTD-PCP-TTF-tri** and the reference compound **BTD-PCP-tri**.

In general, the synthesis of **BTD-PCP-TTF-tri** was based on Sonogashira coupling reaction as follows : $Pd(PPh_3)_2Cl_2$ as a catalyst, CuI as a co-catalyst, triethylamine as a base and THF as a solvent. Dibromo[2,2]paracyclophane was treated with 2-methyl-3-butyn-2-ol under reflux for 2 days to obtain Br-PCP-tri-OH (**22**) in 34% yield, which was reacted with (triisopropylsilyl)-acetylene to obtain TIPS-PCP-tri-OH (**23**). After deprotection of TIPS-PCP-tri-OH (**23**) under NaOH condition, TIPS-PCP-tri (**24**) was almost quantitatively obtained, which underwent the Sonogashira coupling with Br-BTD to obtain TIPS-PCP-BTD (**25**) in a yield of 24%. The subsequent desilylation in the presence of TBAF led to the formation of the **BTD-PCP-tri** in a quantitative yield. Sonogashira coupling of **TTF-I** with **BTD-PCP-tri** afforded the final product **BTD-PCP-TTF-tri** as a deep yellow powder in 50% yield.

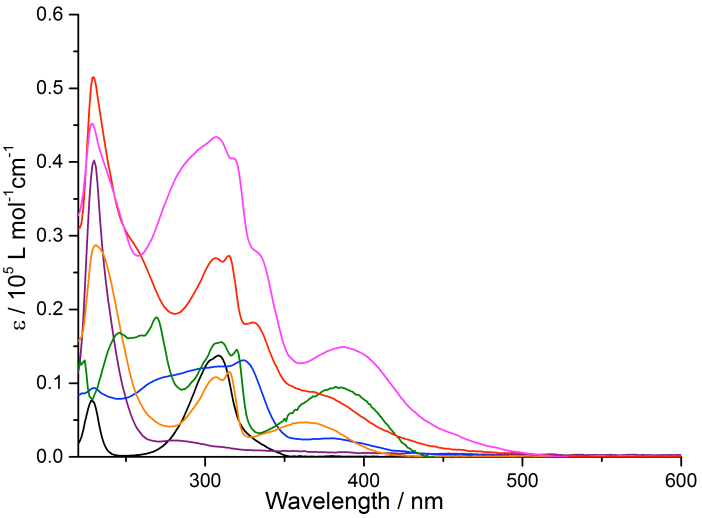

Figure 1 UV-Vis spectra of **BTD-PCP-TTF-s** (red), **BTD-PCP-TTF-tri** (pink) and reference compounds 2,1,3-benzothiadiazole (**BTD**, black), [2,2]paracyclophane (**PCP**, purple), **TTF** (blue), **BTD-PCP-s** (yellow) and **BTD-PCP-tri** (green) at r.t. in DCM ($c = 10^{-5}$ M).

The UV-Vis spectra of a series of molecules were investigated at the concentration of 10^{-5} M in DCM at r.t. (**Figure 1**). Compared to reference compounds **BTD**, **PCP** and **TTF**, **BTD-PCP-s** and **BTD-PCP-tri** show a new absorption band at 370 and 383 nm, respectively, corresponding to an ICT from the PCP unit to the BTD moiety. The red shift of this lowest-energy absorption band and the appearance of a strong band around 270 nm in **BTD-PCP-tri** with respect to **BTD-PCP-s** are attributed to the extended π-conjugation *via* triple bonds between PCP and BTD. For **BTD-PCP-TTF-s** and **BTD-PCP-TTF-tri**, there is a strong absorption around 230 nm caused by the PCP unit. The broad absorption bands ranging from 250 to 350 nm are mainly assigned to π-π* transitions localized on BTD and TTF units. Remarkably, the incorporation of a TTF unit to **BTD-PCP-s** and **BTD-PCP-tri** not only leads

to a significant red-shift of the lowest-energy absorption band with the maximum peak at 370 and 388 nm, respectively, but also with the enhanced absorption coefficients. These results are very likely because of a mixture of a through-space ICT from the TTF to the BTD units and a through-bond ICT from the PCP to the BTD units. It seems that the through-space interaction between the TTF and the BDT units is weak as it only contributes to a long tail of the lowest-energy absorption band with a relative low absorption coefficient.

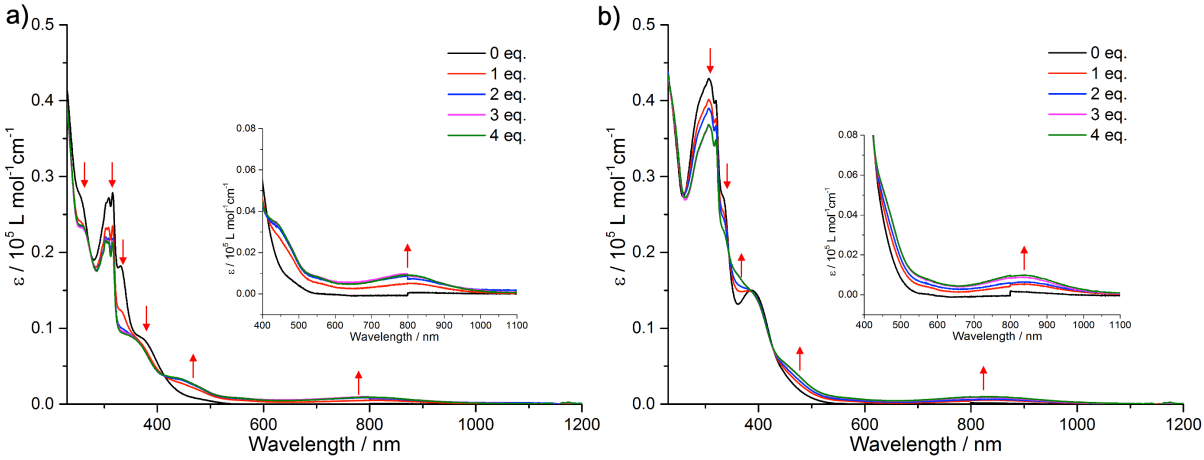

Figure 2 Variation of UV-Vis-NIR absorption spectra of **BTD-PCP-TTF-s** (a) and **BTD-PCP-TTF-tri (**b) in DCM upon successive addition of aliquots of $NOSbF_6$ at room temperature at the concentration of 10^{-5} M.

Intramolecular electronic interactions in **BTD-PCP-TTF-s** and **BTD-PCP-TTF-tri** have been explored by UV-Vis-NIR spectroscopy. A chemical oxidation of two compounds was carried out by successive addition of $NOSbF_6$ aliquots at room temperature in DCM. As depicted in **Figure 2**, in both cases, a progressive reduction of a series of absorption bands ranging from 200 nm to 415 nm is accompanied with a concomitant emergence of two new absorption bands around 460 nm and 800 nm which reach their maximum values upon addition of 4 equiv. of $NOSbF_6$. These new transitions are characteristic of the TTF radical cation species $TTF^{\bullet+}$. Several isosbestic points are observed, indicating that two interconverting optically different species are formed.

The fluorescence emission spectra of BTD-PCP-TTF systems together with the reference compounds were explored at 5×10^{-6} M at r.t. in DCM (**Figure 3a**). There is no emission of **TTF** and weak emissions of **PCP** and **BTD**. When **BTD-PCP-s** was excited at 370 nm, relatively broad CT emission was observed at 480 nm. When **BTD-PCP-tri** was excited at 383 nm, relatively strong CT emission was observed at 488 nm. This slight red-shift is very probably

due to the extended π-conjugation of **BTD-PCP-tri**. As expected, the **BTD-PCP-TTF-s** and **BTD-PCP-TTF-tri** are nonfluorescent due to the electron-donating effect of the TTF unit. These results clearly suggest that efficient through-bond CT occurs from the TTF to the PCP units in both cases. As shown in **Figure 3b**, upon addition of $NOSbF_6$ (4 eq.) the ICT emission of **BTD-PCP-TTF-tri** partially restored whereas there is negligible emission of **BTD-PCP-TTF-s**. This observation can be attributed to the better overlapping of the absorption band of $TTF^{\bullet+}$ with the ICT emission band of **BTD-PCP-s** related to **BTD-PCP-tri**.

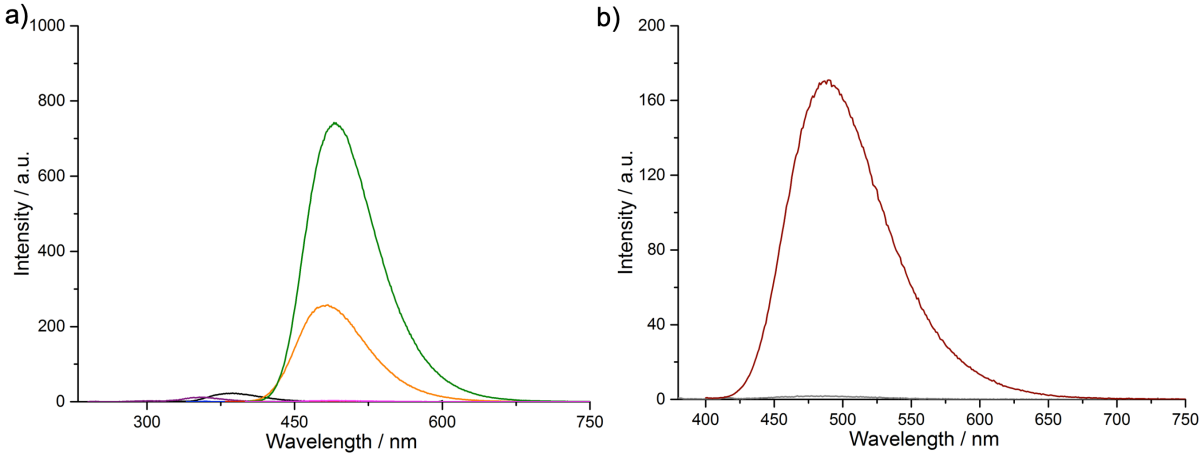

Figure 3 a) Fluorescent emission spectra of **BTD-PCP-TTF-s** (red, λ_{ex} = 370 nm), **BTD-PCP-TTF-tri** (pink, λ_{ex} = 388 nm) and reference compounds **BTD** (black, λ_{ex} = 305 nm); **PCP** (purple, λ_{ex} = 230 nm), **TTF** (blue, λ_{ex} = 325 nm), **BTD-PCP-s** (yellow, λ_{ex} = 365 nm) and **BTD-PCP-tri** (green, λ_{ex} = 383 nm) recorded in DCM at room temperature and concentrations are 5×10^{-6} M. b) Fluorescent emission spectra of **BTD-PCP-TTF-s** (grey, λ_{ex} = 370 nm) and **BTD-PCP-TTF-tri** (brown, λ_{ex} = 388 nm) upon addition of $NOSbF_6$ (4 eq.) at room temperature at the concentration of 5×10^{-6} M.

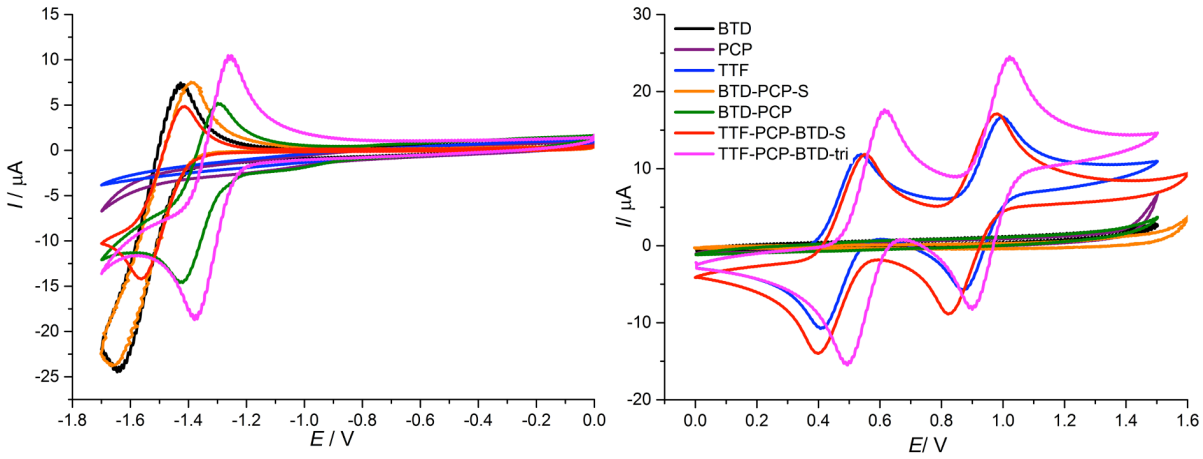

Figure 4 Cyclic voltammograms of **BTD-PCP-TTF-s** (red), **BTD-PCP-TTF-tri** (pink) and reference compounds **BTD** (black), **PCP** (purple), **TTF** (blue), **BTD-PCP-s** (yellow) and

BTD-PCP-tri (green) were measured in DCM, containing 0.1 M $TBAPF_6$ as the supporting electrolyte at r.t., Pt working electrode and Ag/AgCl reference electrode at the scan rate of 100 mV s^{-1}.

Table 1 Electrochemical data. Redox potentials [V] vs. Ag/AgCl in DCM.

Compounds	$E_{1/2}^{ox1}$ (V)	$E_{1/2}^{ox2}$ (V)	$E_{1/2}^{red1}$ (V)	HOMO (eV)	LUMO (eV)	Eg (eV)	Optical gap (eV)
BTD			-1.54		-2.85		3.62
PCP							3.22
TTF	0.47	0.93		-4.70			2.85
BTD-PCP-s			-1.52		-2.89		2.96
BTD-PCP-tri			-1.36		-3.01		2.87
BTD-PCP-TTF-s	0.48	0.91	-1.49	-4.71	-2.90	1.81	2.78
BTD-PCP-TTF-tri	0.56	0.96	-1.32	-4.78	-3.06	1.72	2.55

E_{LUMO} = -e ($E_{\mathrm{red}}^{\mathrm{onset}}$+ 4.3), E_{HOMO} = -e ($E_{\mathrm{ox}}^{\mathrm{onset}}$+ 4.3), $E_{\mathrm{red}}^{\mathrm{onset}}$ = the onset reduction potential, E_{ox}^{onset} = the onset oxidation potential, $E_{\mathrm{HOMO}} = E_{\mathrm{LUMO}} - E_{\mathrm{g}}$, Fc/Fc^{+} is 0.5 V relative to Ag/AgCl in DCM.

The electrochemical properties of **BTD-PCP-TTF-s**, **BTD-PCP-TTF-tri** and reference compounds **BTD**, **PCP**, **TTF**, **BTD-PCP-s** and **BTD-PCP-tri** were further investigated by cyclic voltammetry (**Figure 4** and **Table 1**). **BTD-PCP-s** has a reduction potential of -1.52 eV similar to the reference **BTD** (-1.54 V), indicative of a negligible electronic interaction between the PCP and the BTD units. **BTD-PCP-tri** shows one reversible wave at -1.36 V, which is positive-shifted compared to **BTD**, due to the electron-withdrawing effect of triple bonds. **TTF-PCP-BTD-s** undergoes two reversible oxidation processes at 0.48 and 0.91 V, which are assigned to TTF radical cation and dication states. It has one reduction process at -1.49 V, corresponding to the reduction of the BDT unit. All these redox potentials are comparable to those of reference compounds **TTF**, **BTD and BTD-PCP-s**. In contrast, **TTF-PCP-BTD-tri** has two oxidation potentials of 0.56 and 0.96 V that are positive-shifted with respect to the reference **TTF**, because of the electron-withdrawing effect of the triple bond. Its reduction potential of -1.32 V is however almost same as that of **BTD-PCP-tri**. Clearly, the through-space interactions between the TTF and the BTD units are much weaker than the through-bond interactions between the BTD and the PCP moieties, which is consistent with observations in UV-Vis spectroscopy measurements.

5.3 Conclusions and outlook

Two BTD-PCP-TTF molecules, namely **BTD-PCP-TTF-s** and **BTD-PCP-TTF-tri** have been synthesized successfully, in which the TTF and BTD units are introduced into *pseudo-para* positions of the PCP moiety directly or by triple bonds. In both cases, a strong through-bond ICT transition between the PCP and BTD moieties and a weak through-space ICT transition from the TTF to the BTD has been demonstrated by UV-Vis absorption spectra, fluorescence spectra and cyclic voltammetry. However, both of triads show shorter lifetime compared to fused TTF-BTD dyads. ICT dynamics will be discussed later in detail.

5.4 Experimental part

The related chemical, solvent, devices and the conditions of cyclic voltammetry can check Appendix **A.1**.

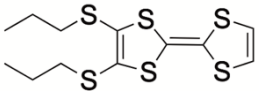

TTF (**15**). The literature procedure[113] was modified as follows. Triethylphosphite (30 mL) was added slowly to a solution of 4,5-bis(propylthio)-1,3-dithiole-2-one (1.33 g, 5 mmol) and vinylene trithiocarbonate (1.34 g, 10 mmol) in toluene (20 mL) under N_2. The mixture was heated to 120 °C and stirred for 3 h. After the solvent was removed under vacuum, the resulting oily red residue was subjected to chromatography (silica gel, heptan/EtOAc (10/1, v/v)) to give compound **TTF** precusor as a yellow oily liquid (600 mg, 34%). ^{1}H NMR (300 MHz, DMSO-d_6) δ 6.77 (s, 2H), 2.83 (t, J = 7.0 Hz, 4H), 1.64 – 1.52 (m, 4H), 0.96 (t, J = 7.3 Hz, 6H)

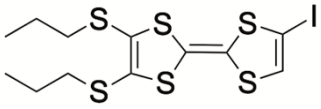

TTF-I (**16**). The literature procedure[117] was modified as follows. To a stirred solution of the TTF precursor (988 mg, 2.8 mmol) in dry argon-flushed THF (100 mL) kept at -78 °C, was dropwise added a solution of n-BuLi (1.35 mL, 3.36 mmol) in hexane over the course of 10 min. The resulting dark red reaction mixture was stirred at -78 °C for 3 h. A solution of perfluorohexyliodide (1.2 mL, 5.6 mmol) in THF (10 mL) was added dropwise over the course of 10 min. The resulting orange solution was stirred at -78 °C overnight and then allowed to slowly reach r.t. It was then diluted with diethyl ether (100 mL) and washed with water (50 mL) and brine (50 mL). The combined aqueous phase was extracted with diethyl ether (100

mL). The combined organic phase was collected, dried over $NaSO_4$, filtered and concentrated in vacuum. The resulting dark yellow residue was purified by column chromatography (SiO_2 pre-treated with a 2% solution of Et_3N, 5% DCM/ heptan), which gave **TTF-I** precursor (620 mg, 46%) as a dark orange oil. ^{1}H NMR (300 MHz, DMSO-d_6) δ 7.02 (s, 1H), 2.83 (t, J = 7.0 Hz, 4H), 1.63 – 1.51 (m, 4H), 0.98 - 0.93 (m, 6H).

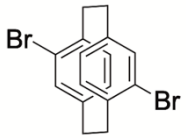

4,16-dibromo-[2,2]paracyclophane (**18**). To iron powder (24.2 mg, 0.43 mmol) was added a solution (5 mL) of bromine (1.03 mL, 3.2 g, 20 mmol) in DCM (8 mL). After stirring for 1 h, the reaction mixture was diluted with DCM (100 mL) and [2,2]paracyclophane (2.0 g, 9.6 mmol) were added. The mixture was stirred for further 30 min, followed by dropwise addition of the residual bromine solution over 5 h. The resultant mixture was stirred for 3 d. Then a sat. aqueous solution of Na_2SO_3 was added to the reaction mixture, which was stirred until decoloration occurred (1 h). The organic phase was filtered and evaporated to afford the product without further purification. The product (1.05 g, 28%) was obtained as a white solid. ^{1}H NMR (300 MHz, $CDCl_3$) δ 7.17 - 7.11 (m, 2H), 6.51 (d, J = 1.6 Hz, 2H), 6.44 (d, J = 7.8 Hz, 2H), 3.54 - 3.45 (m, 2H), 3.21 – 3.11 (m, 2H), 2.99 – 2.90 (m, 2H), 2.89 – 2.79 (m, 2H).

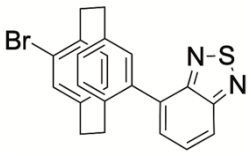

BTD-PCP-s (**19**). An oven-dried Schlenk tube containing a stir bar was charged with dibromo-paracyclophane (280 mg, 0.77 mmol), 4-(4,4,5,5-tetramethyl-1,3,2-dioxaborolan-2-yl)benzo[*c*][1,2,5] thiadiazole (BTD-Bpin) (300 mg, 1.15 mmol), $Pd(dppf)Cl_2$ (22.5 mg, 0.031 mmol) and K_3PO_4 (490 mg, 2.31 mmol). After degassing for 30 min with nitrogen, freshly distilled toluene (10 mL) was injected. The reaction mixture was vigorously stirred at 115 °C for 24 h. After cooling down to r.t., toluene (10 mL) was added and the mixture was hydrolyzed with NaOH (1M, 10 mL). This was followed by phase separation and extraction of the aqueous phase with EtOAc (3 × 25 mL). The collected organic layer was dried over $MgSO_4$ and concentrated *in vacuo*. The crude product was purified by flash chromatography on silica gel using a mixture of DCM and heptan (1/1) as an eluent to afford a light-yellow solid product (159 mg, 49%). ^{1}H NMR (300 MHz, CD_2Cl_2) δ 8.05 – 8.02 (m, 1H), 7.82 – 7.72 (m, 2H), 7.25 – 7.21 (m, 1H), 6.88 (d, J = 1.9 Hz, 1H), 6.75 – 6.64 (m, 3H), 6.58 - 6.54 (m, 1H), 3.60 - 3.51 (m, 1H), 3.34 – 3.25 (m, 1H), 3.15 – 2.94 (m, 3H), 2.89 – 2.61 (m, 3H). ^{13}C NMR (101 MHz, CD_2Cl_2) δ 155.94, 154.47, 142.67, 140.10, 139.62, 139.57, 137.97, 137.78, 135.55, 135.10, 135.08, 133.22, 130.25, 130.14, 129.87, 129.51, 126.94, 120.94, 36.11, 34.97, 34.90, 33.81, 30.26.

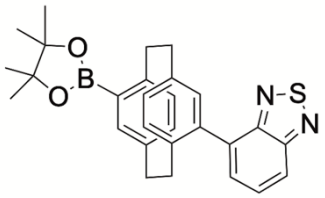

BTD-PCP-Bpin (**20**). To a round-bottom flask (50 mL) were added **BTD-PCP-s** (166 mg, 0.4 mmol), bis(pinacolato)diboron (304 mg, 1.2 mmol), anhydrous KOAc (196 mg, 2 mmol), $Pd(dppf)Cl_2$ (30 mg, 0.04 mmol) and dry DMF (15 mL, degassed for 15 min). The flask was sealed and heated at 150 °C for 36 hours. After the solvent was removed under reduced pressure, the residue was purified by column chromatography on silica gel with hexane/DCMas an eluent (v/v, 1:2) to give pure **BTD-PCP-Bpin** (96 mg, 51%) with a light-yellow color. ^{1}H NMR (300 MHz, $CDCl_3$) δ 8.05 - 8.02 (m, 1H), 7.81 – 7.73 (m, 2H), 7.16 (d, J = 2.0 Hz, 1H), 6.83 (d, J = 1.9 Hz, 1H), 6.72 – 6.62 (m, 3H), 6.50 – 6.46 (m, 1H), 4.08 – 4.00 (m, 1H), 3.18 – 2.96 (m, 4H), 2.87 – 2.69 (m, 3H), 1.43 (d, J = 3.8 Hz, 12H). ^{13}C NMR (75 MHz, $CDCl_3$) δ 155.37, 154.13, 147.50, 140.70, 140.07, 139.35, 138.72, 136.89, 135.60, 134.80, 134.10, 133.49, 132.27, 132.01, 129.84, 129.15, 120.45, 83.43, 39.12, 35.90, 35.59, 35.57, 35.11, 34.58, 34.27, 32.86, 32.03, 29.85, 29.64, 29.17, 28.10, 26.58, 26.47, 25.32, 25.16, 24.92, 23.11, 23.05, 22.84, 22.80, 20.30, 19.31, 14.55, 14.25, 11.54, 11.09. HR-MS (ESI, positive): *m/z* calcd for $[C_{28}H_{29}O_2N_2BS+H]^+$: 469.2116; found: 469.2121.

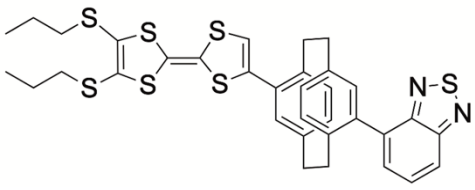

BTD-PCP-TTF-s (**21**). To a round-bottom flask (250 mL) was added **BTD-PCP-Bpin** (47 mg, 0.1 mmol), THF (80 mL) and H_2O (8 mL), and then potassium hydrate (73 mg, 1.3 mmol) and $Pd(PPh_3)_4$ (18 mg, 0.015 mmol). Compound **TTF-I** (96 mg, 0.2 mmol) was dropwise added over 30 min. The reaction mixture was stirred at 75 °C for 36 hours under N_2. After cooling to r.t., all solvents were removed under vacuum and the residue was purified by column chromatography on silica gel with hexane/DCM(v/v, 1:2) as an eluent to give pure **BTD-PCP-TTF-S** (46 mg, 66%) with a yellow powder.^{1}H NMR (300 MHz, CD_2Cl_2) δ 8.06 – 8.03 (m, 1H), 7.83 – 7.73 (m, 2H), 6.95 (d, J = 1.9 Hz, 1H), 6.84 – 6.77 (m, 2H), 6.65 – 6.56 (m, 3H), 6.33 (s, 1H), 3.73 – 3.67 (m, 1H), 3.20 – 3.02 (m, 4H), 2.94 – 2.81 (m, 5H), 2.79 – 2.73 (m, 1H), 2.70 – 2.61 (m, 1H), 1.76 – 1.63 (m, 4H), 1.04 (t, J = 7.3 Hz, 6H). ^{13}C NMR (101 MHz, CD_2Cl_2) δ 156.00, 154.51, 141.16, 140.19, 139.70, 138.68, 137.80, 136.56, 136.00, 135.46, 135.00, 133.47, 133.32, 133.19, 131.74, 131.34, 130.27, 129.91, 128.62, 128.51, 120.97, 115.95, 114.80, 106.78, 38.82, 35.36, 35.05, 34.85, 34.57, 30.26, 23.78, 13.49. HR-MS (ESI, positive): *m/z* calcd for $[C_{34}H_{32}N_2S_7]$: 692.0605; found: 692.0614.

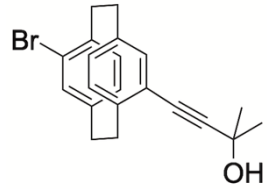

22. A mixture of 4,16-dibromo[2,2]paracyclophane (1.6 g, 4.4 mmol), 2-methyl-3-butyn-2-ol (0.82 mL), $Pd(PPh_3)_2Cl_2$ (0.31 g, 0.44 mmol), PPh_3 (0.23 g, 0.88 mmol), and CuI (0.09 g, 0.44 mmol) in THF-NEt_3 (49 mL, v/v = 5:2) was stirred at 75 °C for 3 days under a nitrogen atmosphere. The resulting precipitate was filtered off and the filtrate was evaporated under vacuum. The residue was subjected to column chromatography (silica gel, heptan/EtOAc (4/1, v/v)) to give compound **2** (0.55 g, 34%) as a light-yellow powder.

^{1}H NMR (300 MHz, $CDCl_3$) δ 7.17 – 7.12 (m, 1H), 7.00 – 6.93 (m, 1H), 6.55 – 6.40 (m, 4H), 3.61 – 3.43 (m, 2H), 3.22 – 3.10 (m, 2H), 3.04 – 2.91 (m, 2H), 2.91 – 2.79 (m, 2H), 1.72 (d, J = 2.8 Hz, 6H). ^{13}C NMR (75 MHz, $CDCl_3$) δ 141.91, 141.44, 139.34, 138.91, 137.50, 137.34, 134.44, 133.04, 129.34, 129.13, 126.82, 124.40, 97.46, 82.46, 65.97, 35.54, 34.10, 33.65, 33.20, 31.89, 31.84.

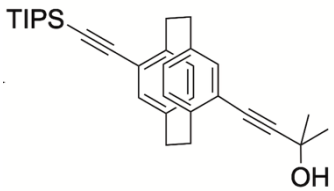

23. A mixture of **2** (150 mg, 0.41 mmol), triisopropylsilyl-acetylene (0.37 mL, 1.64 mmol), $Pd(PPh_3)_2Cl_2$ (29 mg, 0.041 mmol), PPh_3 (222 mg, 0.082 mmol), and CuI (8 mg, 0.041 mmol) in THF-NEt_3 (21 mL, v/v = 5:2) was stirred at 75 °C for 2 days under a nitrogen atmosphere. The resulting precipitate was filtered off, and the filtrate was evaporated under vacuum. The residue was subjected to column chromatography (silica gel, heptan/EtOAc (4/1, v/v)) to give compound **3** (87 mg, 45%) as a light-yellow powder. ^{1}H NMR (300 MHz, $CDCl_3$) δ 7.06 – 7.01 (m, 1H), 6.97 – 6.92 (m, 1H), 6.52 (d, J = 1.7 Hz, 1H), 6.47 – 6.38 (m, 3H), 3.71 – 3.44 (m, 2H), 3.22 – 2.78 (m, 6H), 1.71 (d, J = 3.0 Hz, 6H), 1.20 (s, 21H). ^{13}C NMR (75 MHz, $CDCl_3$) δ 142.50, 142.19, 139.52, 139.44, 138.06, 137.42, 133.22, 133.09, 130.23, 130.16, 125.21, 124.17, 107.48, 97.37, 93.81, 82.56, 65.96, 34.18, 34.14, 33.84, 33.81, 31.89, 31.84, 18.96, 18.94, 11.65.

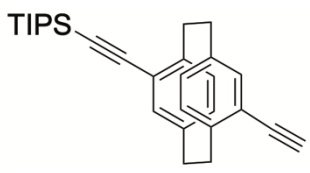

24. A standard Schlenk line was set up with compound **3** (94 mg, 0.2 mmol) and powder NaOH (56 mg, 1.4 mmol). After the addition of toluene (20 mL), the mixture was stirred at 115 °C overnight. Water was added to quench the reaction. The aqueous layer was extracted with DCM and the organic phase was washed by water. The combined organic phase was collected, and the solvents were removed under reduced pressure, and dried in vacuo to give **4** (79 mg, 90%). ^{1}H NMR (300 MHz, $CDCl_3$) δ 7.01 – 6.96 (m, 1H), 6.93 – 6.87 (m, 1H), 6.49 – 6.43 (m, 2H), 6.39 – 6.31 (m, 2H), 3.62 – 3.43 (m, 2H), 3.19 (s, 1H), 3.16

– 3.05 (m, 2H), 2.96 – 2.71 (m, 4H), 1.12 (s, 21H). ^{13}C NMR (75 MHz, $CDCl_3$) δ 142.82, 142.50, 139.62, 139.56, 138.08, 138.03, 133.29, 133.23, 130.70, 130.34, 125.17, 123.66, 107.48, 93.81, 84.08, 80.34, 34.17, 33.97, 33.79, 18.97, 18.95, 11.66.

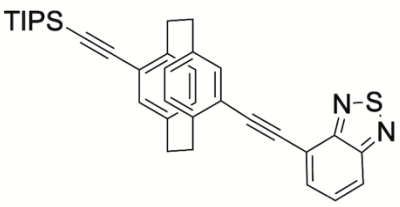

25. A mixture of **4** (50 mg, 0.12 mmol), 4-bromobenzo[*c*][1,2,5]thiadiazole (77 mg, 0.36 mmol), $Pd(PPh_3)_2Cl_2$ (8.4 mg, 0.012 mmol), PPh_3 (6.3 mg, 0.024 mmol), and CuI (2.3 mg, 0.012 mmol) in THF NEt_3 (16 mL, v/v = 5:2) was stirred at 75 °C for 24 h under a nitrogen atmosphere. The mixture was filtered off, and the filtrate was evaporated under vacuum. The residue was subjected to column chromatography (silica gel, heptan/EtOAc (2/1, v/v)) to give compound **5** (80 mg, 24%) as a bright yellow powder. ^{1}H NMR (300 MHz, $CDCl_3$) δ 8.05 – 7.98 (m, 1H), 7.84 – 7.77 (m, 1H), 7.67 – 7.58 (m, 1H), 7.17 – 7.09 (m, 2H), 6.69 (d, J = 1.7 Hz, 1H), 6.58 (d, J = 1.8 Hz, 1H), 6.53 – 6.48 (m, 2H), 3.95 – 3.84 (m, 1H), 3.72 – 3.61 (m, 1H), 3.47 – 3.34 (m, 1H), 3.29 – 3.17 (m, 1H), 3.10 – 2.84 (m, 4H), 1.21 (s, 21H). ^{13}C NMR (75 MHz, $CDCl_3$) δ 155.19, 154.91, 143.17, 142.49, 139.77, 139.74, 138.17, 137.56, 133.44, 133.20, 131.92, 130.91, 130.75, 129.42, 125.19, 124.28, 121.64, 117.96, 107.58, 96.57, 93.83, 88.90, 34.41, 34.21, 33.93, 33.86, 18.98, 18.96, 11.67. HR-MS (ESI, positive): *m/z* calcd for $[C_{35}H_{38}N_2SSi+H]^+$: 547.2598; found: 547.2580; calcd for $[C_{35}H_{38}N_2SSi+Na]^+$: 569.2417; found: 569.2405

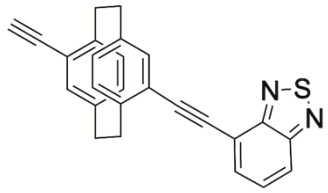

BTD-PCP-tri (**26**). To a solution of **5** (275 mg, 0.5 mmol) in dry THF (35 mL) was added TBAF (0.6 mL, 1.0 M solution in THF). The reaction mixture was stirred at r.t. for 5 h under a nitrogen atmosphere. The solution was evaporated under vacuum, and the residue was subjected to column chromatography (silica gel, heptan/EtOAc (4/1, v/v)) to give **BTD-PCP-tri** (186 mg, 95%) as a bright yellow powder. ^{1}H NMR (300 MHz, $CDCl_3$) δ 8.04 – 8.00 (m, 1H), 7.82 – 7.80 (m, 1H), 7.66 – 7.60 (m, 1H), 7.19 – 7.16 (m, 1H), 7.08 – 7.05 (m, 1H), 6.71 (d, J = 1.9 Hz, 1H), 6.61 (d, J = 1.9 Hz, 1H), 6.55 – 6.51 (m, 2H), 3.93 – 3.85 (m, 1H), 3.66 – 3.58 (m, 1H), 3.46 – 3.37 (m, 1H), 3.30 (s, 1H), 3.27 – 3.19 (m, 1H), 3.12 – 2.87 (m, 4H). ^{13}C NMR (101 MHz, $CDCl_3$) δ 155.17, 154.90, 143.12, 142.78, 139.87, 139.79, 138.05, 137.50, 133.54, 133.36, 131.93, 131.15, 130.96, 129.41, 124.33, 123.72, 121.66, 117.91, 96.50, 88.94, 84.12, 80.41, 34.37, 33.97, 33.94, 33.88. MALDI-TOF-MS (*m/z*): calcd for $[C_{26}H_{18}N_2S]$ 390.12; found: 390.36.

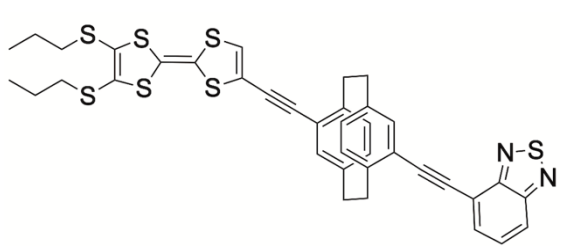

BTD-PCP-TTF-tri (**27**). A mixture of **TTF-I** precursor (96 mg, 0.2 mmol), **BTD-PCP-tri** (58 mg, 0.15 mmol), $Pd(PPh_3)_2Cl_2$ (10 mg, 0.015 mmol), and CuI (3 mg, 0.015 mmol) in THF-NEt_3 (16 mL, v/v = 5:3) was stirred at 50 °C for 5 h under a nitrogen atmosphere. The solvent was evaporated under vacuum. The residue was subjected to column chromatography (silica gel, heptan/EtOAc (9/1, v/v)) to give compound **7** (56 mg, 50%) as a yellow powder. ^{1}H NMR (300 MHz, CD_2Cl_2) δ 8.05 – 8.01 (m, 1H), 7.85 – 7.83 (m, 1H), 7.68 – 7.63 (m, 1H), 7.20 – 7.17 (m, 1H), 7.02 – 6.99 (m, 1H), 6.70 (d, J = 2.0 Hz, 1H), 6.65 (s, 1H), 6.57 – 6.56 (m, 2H), 6.54 (d, J = 3.0 Hz, 1H), 3.92 – 3.84 (m, 1H), 3.56 – 3.48 (m, 1H), 3.45 – 3.36 (m, 1H), 3.25 – 2.89 (m, 5H), 2.86 – 2.80 (m, 4H), 1.74 – 1.61 (m, 4H), 1.05 – 1.00 (m, 6H). ^{13}C NMR (101 MHz, $CDCl_3$) δ 155.20, 154.91, 143.16, 139.60, 137.54, 133.43, 131.95, 131.06, 129.41, 124.44, 121.72, 117.88, 96.44, 89.09, 34.33, 34.19, 33.98, 13.35. HR-MS (ESI, positive): *m/z* calcd for [$C_{38}H_{32}N_2S_7$]: 740.0610; found: 740.0590.

6. Molecular electronics

This section is partially adapted to the following manuscript:

a. Atomically Well-defined Nitrogen Doping in the Cross-plane Transport through Graphene Heterojunctions

Hewei Zhang, ***Ping Zhou****, Abdalghani Daaoub, Sara Sangtarash, Shiqiang Zhao, Zixian Yang, Yu Zhou, Yuling Zou, Silvio Decurtins, Robert Häner, Yang Yang, Hatef Sadeghi, Shi-Xia Liu, Wenjing Hong*

b. Self-assembly and on-surface polymerization

Contribution to the work

My contribution includes synthesis of 5,12-diazatetracene (2N-PAH4), 1,3,6,8-tetraazapyrene (4N-PAH4') and 6,13-diazapentacene (2N-PAH5) and a detailed study of their electronic properties by UV-Vis spectra and CV measurements. The group of Prof. Hong from Xiamen University, the group of Prof. Meyer from Basel University and the group of Prof. Fasel from Empa carried out charge transport through graphene heterojunctions, on-surface self-assembly and chemical reactions as well as analyzed the data. Abdalghani Daaoub and Sara Sangtarash from University of Warwick carried out theory on charge transport through molecular junctions.

6.1 Atomically well-defined nitrogen doping in the cross-plane transport through graphene heterojunctions

6.1.1 Manuscript

Atomically Well-defined Nitrogen Doping in the Cross-plane Transport through Graphene Heterojunctions

Hewei Zhang,[1,4] Ping Zhou,[2,4] Abdalghani Daaoub,[3,4] Sara Sangtarash,[3] Shiqiang Zhao,[1] Zixian Yang,[1] Yu Zhou,[1] Yuling Zou,[1] Silvio Decurtins,[2] Robert Häner,[2] Yang Yang,[1] Hatef Sadeghi,[3] Shi-Xia Liu,[2] Wenjing Hong[1]

[1]State Key Laboratory of Physical Chemistry of Solid Surfaces, College of Chemistry and Chemical Engineering & Pen-Tung Sah Institute of Micro-Nano Science and Technology, Xiamen University, 361005 Xiamen, China.
[2]Department of Chemistry, Biochemistry and Pharmaceutical Sciences, University of Bern, Freiestrasse 3, 3012 Bern, Switzerland
[3]Device Modelling Group, School of Engineering, University of Warwick, Coventry CV4 7AL, United Kingdom
[4]These authors contributed equally to this work

Abstract

The nitrogen doping of graphene leads to graphene heterojunctions with a tunable bandgap, suitable for electronics, electrochemical, and detector applications. However, the microscopic nature and charge transport properties of atomic-level nitrogen-doped graphene are still unknown, mainly due to the multiple doping sites with topological diversities. In this work, we fabricated the atomically well-defined N-doped graphene heterojunctions and investigated the cross-plane transport through these heterojunctions to reveal the effects of doping on their electronic properties. We found that different doping number of nitrogen atoms leads to a conductance difference of up to ~288%, and the conductance of graphene heterojunctions with nitrogen-doping at different positions in the conjugated framework can also lead to a conductance difference of ~170%. Combined ultraviolet photoelectron spectroscopy measurements and theoretical calculations reveal that the insertion of nitrogen atoms into the conjugation framework significantly stabilizes the frontier molecular orbitals, leading to a

change in the relative positions of HOMO and LUMO to the Fermi level of the electrodes. Our work provides a unique insight into the role of nitrogen doping on the charge transport through graphene heterojunctions and materials at the single atomic level.

Keywords: single-molecule conductance, molecular junction, cross-plane charge transport, graphene heterojunction

Introduction

The two-dimensional(2D) heterostructured materials not only retains the original advantages[1-3] but also show unique charge transport[4,5], catalytic activity[6,7], mechanical strength[8], and photoelectric property[9] beyond the classic two-dimensional (2D) materials. For instance, the doping of graphene leads to the fabrication of graphene heterojunctions with potential applications in electronics[10-14], sensing[15,16], photocatalytic[17-19] and other aspects by converting the zero bandgaps of graphene to tunable bandgaps[20]. Nitrogen is widely used for doping graphene materials and devices[15,19,21-23], and there are various nitrogen-doping approaches developed, including chemical vapor deposition[24], arc discharge[25], ion irradiation[26] and post treatment[27]. However, the microscopic nature and charge transport properties of atomic-level nitrogen-doped graphene remained unclear due to the complexity of the nitrogen sites and bonding topology within the carbon lattice during the doping process[20,26,28]. Along this line, recent advances in the investigation through single- molecule junctions offer a unique insight to reveal the role of N-doping with atomically well-defined doping sites.

To tackle this challenge, the single-molecule junctions with gold-molecule-gold configurations offer the opportunity to investigate the role of N-doping in the charge transport through molecular junctions with atomic precision. When nitrogen doping occurs in the aromatic cores of molecules, differences in the substitution positions can tune the quantum interference effects[29-31] and demonstrate the different gating efficiency[32] in a phenyl ring with meta connectivity. When nitrogen atoms are employed as an anchor group to form Au-N bonds, the different numbers and sites of nitrogen atoms provide different conductance pathways at molecular junctions, resulting in different conductance[33-35]. However, all the above studies investigated the charge transport through the molecular skeleton using gold electrodes but not the cross-plane transport as presented in the graphene heterojunctions. Recent advances in the fabrication of cross-plane heterojunctions can be considered as a microscopic model[36] to investigate the role of nitrogen doping on the charge transport with different numbers of

nitrogen atoms at different positions of the conjugated framework in nitrogen-containing polycyclic aromatic hydrocarbons (N-PAHs).

Herein, we investigated the charge transport through nitrogen-doped graphene heterojunctions where N-PAHs are embedded between graphene electrodes by using the cross-plane break junction technique and density functional theory transport calculations. Comparing the conductance values of the corresponding polycyclic aromatic hydrocarbons (PAHs), we find that the conductance decreases with the introduction of nitrogen atoms. We further investigated the conductance of heterojunctions with nitrogen atoms at different N- PAH framework sites and observed a clear site dependence in their conductance. In conjunction with transition voltage spectroscopy (TVS), ultraviolet photoelectron spectroscopy (UPS), and theoretical calculations, it is supposed that the insertion of nitrogen atoms alters the energy level alignment between the frontier molecular orbitals and the Fermi level of graphene electrodes, thereby regulating the electrical properties.

Results

Charge Transport Properties of nitrogen-containing polycyclic aromatic hydrocarbons

We investigate the cross-plane charge transport through the N-PAHs using the customized scanning tunneling microscopy break junction (STM-BJ) setup as shown in Figure 1A left and Figure S1 in the Supporting Information (SI). A U-shaped Cu wire with single-layer graphene and a Cu foil with single-layer graphene is chosen as substrates, and the tip is in soft contact with the substrate using with the lab-developed control program[37,38]. A push-pull process of the tip forms nanoscale gaps of varying sizes, and the molecule can be trapped in the nanogap between the graphene electrode pair and form a graphene-molecule-graphene van der Waals (vdW) heterojunction. The charge transport occurs in a cross-plane way due to the vdW interaction (Figure 1A right). We have synthesized four N-PAH molecules as probe molecules [39-43], whose structures are shown in Figure 1B.

The conductance of the graphene-based single-molecule junctions with a bias voltage of 0.1 V ranged from $10^{-6.5}$ G_0 (~24.5 pS; $G_0=2e_2/h$, quantum conductance) to $10^{-2.5}$ G_0 (~245.4 nS) at room temperature. Direct tunneling traces were obtained in pure decane as a solvent and showed neither a discernible peak in the one-dimensional (1D) conductance histogram nor a plateau in the 2D conductance histogram.

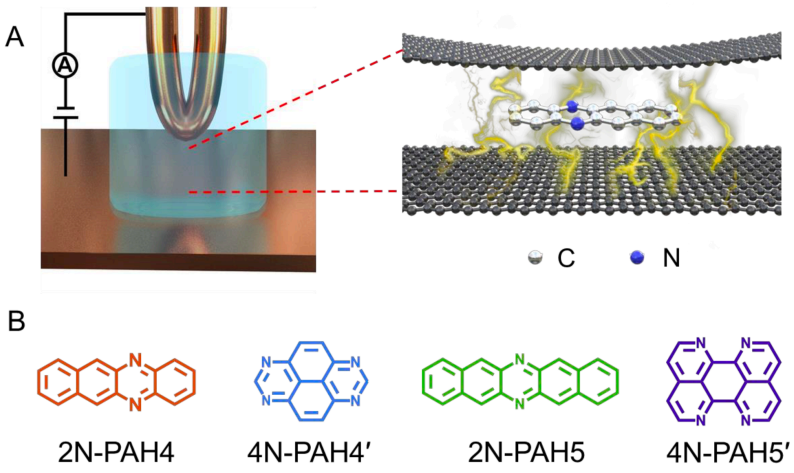

Figure 1 Schematic diagrams and molecular structures. (A) Schematic diagrams of the cross-plane break junction (XPBJ) setup based on STM-BJ setup (left) and the structures of sandwiched molecular junctions with a N-PAH (right). (B) Chemical structures of N-PAHs, including 5,12-diazatetracene (2N-PAH4), 1,3,6,8-tetraazapyrene (4N-PAH4'), 6,13 diazapentacene (2N-PAH5), 1,6,7,12-tetraazaperylene (4N-PAH5').

Typical individual conductance–displacement traces are shown in Figure 2A in the inset. For all four molecules, there are distinct conductance plateaus ranging from 10^{-5} G_0 (~775 pS) to 10^{-4} G_0 (~7.75 nS); over 1000 individual conductance–distance traces are overlayed for statistical analysis. Distinct peaks were observed in the 1D conductance histogram (Figure 2A), indicating that the molecular junctions of four N-PAHs were successfully constructed. The conductance of 2N-PAH4 and 4N-PAH4' are $10^{-4.81}$ G_0 (~1.20 nS) and $10^{-4.69}$ G_0 (~1.58 nS) by Gaussian fitting of the peaks, respectively. Interestingly, 2N-PAH5 and 4N-PAH5' have conductance of $10^{-4.41}$ G_0 (~3.02 nS) and $10^{-4.28}$ G_0 (~4.07 nS), respectively, which are much higher than those of the former two counterparts. The relationship between the conductance and the structures of the molecules is shown in Figure 2B, and the conductance of N-PAHs increase with the number of benzene rings, which is consistent with the conductance of PAHs[37]. The cross-plane area is an essential factor affecting the conductance. The conductance of 2N-PAH5 decreases most significantly, falling down to 46.8% of that of PAH5 ($10^{-4.08}$ G_0, 6.45 nS[37]), whereas the conductance of 4N-PAH4' increases most manifestly up to 135% of that of PAH4' ($10^{-4.82}$ G_0, 1.17 nS[37]), which is about ~288% of the former decrease. Compared to their PAH counterparts[37], both 2N-PAH4 and 2N-PAH5 show a decrease in conductance by 63.1% and 46.8%, respectively, indicating that the former decrease is about ~135% of the latter one. With the increase of the number of nitrogen atoms to four, the conductance of 4N-PAH5'

slightly decreases by 79.4%, while that of 4N-PAH4' actually increases by 135%, which is about ~170% of the former decrease (see Table S1 in the SI). Such a bipolar change can be accounted for by the fact that the insertion of nitrogen atoms stabilizes both the highest occupied molecular orbital (HOMO) and the lowest unoccupied molecular orbital (LUMO), leading to a change in the relative positions of HOMO and LUMO to the Fermi level of the electrodes. For a detailed explanation, see the section on the theoretical calculations.

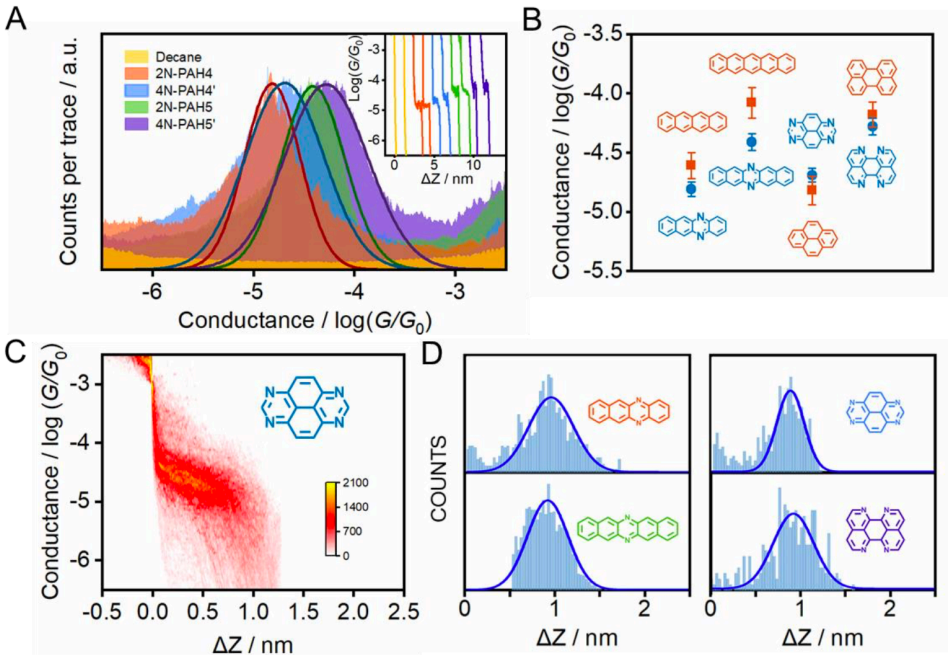

Figure 2 Electrical properties with XPBJ technique. (A) 1D conductance histograms were obtained from ~1000 conductance–displacement traces of the pure decane solvent (yellow) and the N-PAHs using graphene electrodes. The typical individual conductance–displacement traces are shown in the inset. (B) Comparison of conductance between N-PAHs and PAHs. The data of PAH conductance comes from our previous work.[37] (C) 2D conductance-distance histograms of 4N-PAH4'. (D) The plateau length histograms of 2N-PAH4, 2N-PAH5, 4N-PAH4', and 4N-PAH5'.

The 2D conductance-distance histograms of N-PAHs are constructed by superimposing conductance-displacement traces to investigate the junction configurations. As shown in Figure 2C, there are corresponding apparent intensity clouds in the range of conductance demonstrated in the 1D conductance histogram, indicating the successful construction of graphene-molecule-graphene junctions. Based on the plateau length of direct tunneling at 0.27 nm determined in pure solvent[37,38], the corrected plateau lengths of 2N-PAH4, 2N- PAH5, 4N-PAH4', and 4N-

PAH5' are determined to be 0.96 nm, 0.92 nm, 0.90 nm, and 0.93 nm, respectively (Figure 2D). They match the distance between the graphene sheet incorporated with N-PAHs, meaning the sandwiched graphene-N-PAHs-graphene junctions are successfully fabricated. Due to the absence of anchoring groups, PAHs do not show a conductance signal when gold electrodes are used. On the contrary, N-PAHs form molecular junctions through N-Au coordination bonds (see Figure S11 in the SI). In remarkable contrast to graphene-molecule-graphene van der Waals heterojunctions, Au-N-PAHs-Au junctions do not seem to be able to accurately assess the influence of nitrogen atoms on charge transport through PAHs due to N-Au coordination bonds.

To further investigate the change of HOMO and LUMO energy levels, UPS and ultraviolet-visible (UV-Vis) spectra were used to evaluate the energy level alignment of these junctions. UPS measurements were performed using a He I light source ($h\nu$ = 21.22 eV) to gauge the electronic states of monolayers on graphene[44]. At an applied bias of -5 V, all the binding energy spectra are shown in Figure S5 in the SI. We find that the insertion of nitrogen atoms gives rise to an increase in the energy offset ($E_F - E_{HOMO}$) as predicted by DFT calculations (Figure 3A). The ultraviolet-visible (UV-Vis) spectra show that the HOMO-LUMO gaps of N-PAHs also decrease or remain almost unchanged compared to their PAH counterparts (see Figure S6 in the SI). From the UPS and UV-Vis results, it can be deduced that the LUMO energy levels of N-PAHs decrease more rapidly than the HOMO energy levels, and notably, 4N-PAH4' shows the most pronounced drop in the LUMO energy.

To further determine energy level alignment in the heterojunctions, we measured TVS to obtain the transition voltage (Vtrans). After the I-V measurements of all molecules, Fowler- Nordheim diagrams (describing the relationship between ln(I/V2) and 1/V) were obtained using a specific mathematical analysis method called TVS (Figure 3C). Two trends corresponding to two different charge-transport mechanisms can be seen in the plots. The boundary between these two trends, the minimum value in the F-N plot, is defined as the transition voltage. The value of Vtrans is proportional to the energy offset between the Fermi energy (E_F) of the electrodes and the energy of the frontier molecular orbital (EFMO, HOMO or LUMO)[45-47]. The Vtrans values of N-PAHs and PAHs are linear with the absolute values of the theoretical E_F-E_{FMO} (Figure 3B). At the same time, the Vtrans values of N-PAHs and PAHs are compared (Figure 3C). The Vtrans values of 2N-PAH5 and PAH5 are 0.396 V and 0.289 V, and the Vtrans values of 2N-PAH4 and PAH4 are 0.463 V and 0.342 V, suggesting that Vtrans increases after the

insertion of nitrogen atoms. The results show that the E_F-E_{HOMO} increases and E_{HOMO} decreases due to the presence of nitrogen atoms, which is consistent with the theoretical calculations.

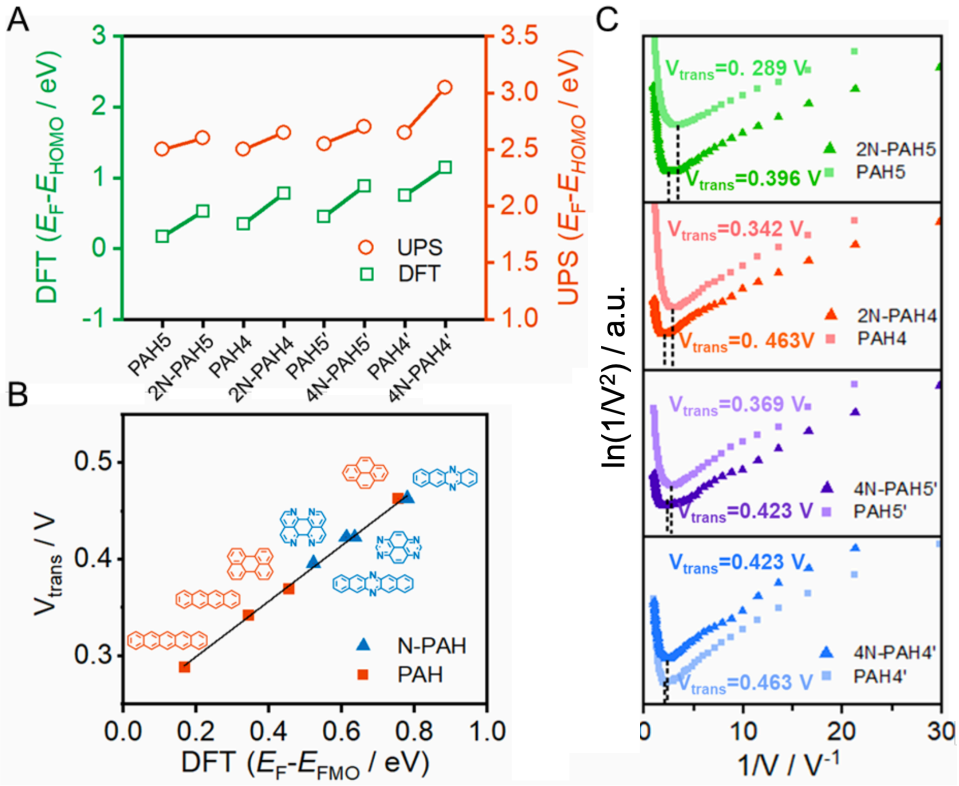

Figure 3 Ultraviolet photoelectron spectroscopy and transition voltage spectroscopy. (A) Comparison of $E_F - E_{HOMO}$ by UPS with $E_F - E_{FMO}$ by DFT theoretical calculation. (B) Vtrans versus $E_F - E_{FMO}$ by DFT theoretical calculation difference. (C) The transition voltage (ln(I/V2) vs1/V) spectra were obtained by over 500 I–V traces of 2N-PAH5, PAH5, 2N-PAH4, PAH4, 4N-PAH5', PAH5', 4N-PAH4', PAH4'.

In stark contrast, the frontier molecular orbital shifts from HOMO to LUMO when the number of nitrogen atoms is increased to four. The Vtrans values of 4N-PAH5' and PAH5' are 0.423 V and 0.369 V, respectively. And the Vtrans value of 4N-PAH4' (0.423V) is slightly smaller than that of PAH4' (0.463 V), indicative of a significantly reduced LUMO. This observation is corroborated by the UPS results mentioned earlier. It follows that 4N-PAH4' and 4N-PAH5' show a LUMO-dominated charge-transport mechanism that is distinct from the HOMO-dominated charge-transport through other N-PAHs and their PAH counterparts. It becomes clear that an interplay between the number of nitrogen atoms and the topology variation is applied to fine-tune the energy levels between the frontier orbitals and the Fermi level of the graphene electrodes, thereby regulating the charge-transport properties of the PAHs.

Theoretical Calculations

To understand the charge-transport properties of N-PAH and PAH molecules between graphene electrodes (Figure 4A), we calculated the ground-state geometries and electronic structures of gas phase molecules using SIESTA48 implementation of density functional theory (DFT) firstly as discussed in the method section in the SI. We find that HOMO and LUMO energy levels for each molecule move down in energy with the insertion of nitrogen atoms (see Table S4 in the SI). Next, we calculated ground-state geometries and electronic structures of molecules between two graphene electrodes (see methods). The calculated average optimum distance between the graphene sheet and molecules is between 3.42 to 3.46 Å depending on the type of N-PAHs and PAHs molecules (see Table S5 in the SI). The smallest vdW distance (3.42 Å) is for 4N-PAH4'. The graphene electrodes are periodic in the y and x directions with multiple k-points (Figure 4A) to resemble graphene sheets. We found that the ground state distance between graphene sheets is 3.36 Å in the transport direction (*z*).

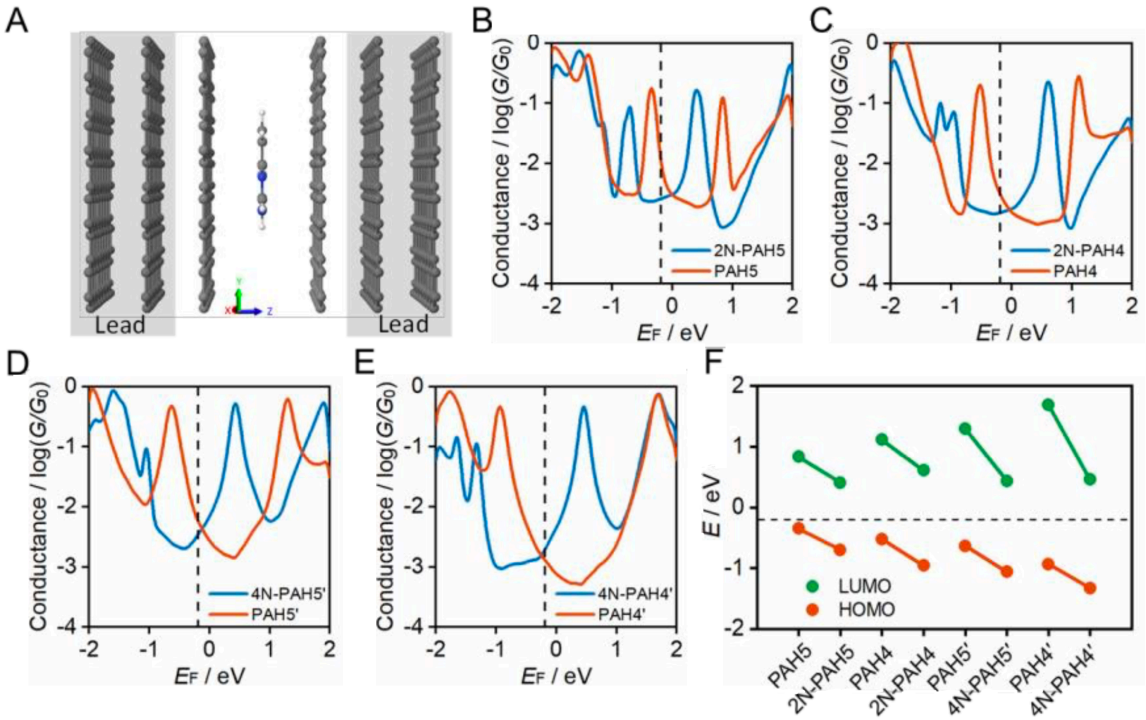

Figure 4 Electrical conductance properties of graphene-molecule-graphene van der Waals heterojunctions. (A) Structure of sandwiched molecular junctions with a 4N-PAH4' molecule. (B-D) The electrical conductance of N-PAHs and PAHs molecules as a function of the Fermi energy. The black dashed line (EF = -0.18 eV) shows the Fermi energy that agrees with the experiment results. (F) Energetic positions of HOMO and LUMO resonances of graphene-

molecule-graphene junctions obtained from Figure B-E. The black dashed line shows E_F = -0.18 eV.

To calculate cross-plane conductance through graphene-based single-molecule junctions, we obtain the mean-field Hamiltonian from density functional theory (DFT) and use the Gollum[49,50] quantum transport code (see theoretical methods) to calculate transmission coefficients of electrons of energy E passing from one electrode to the other. We then used the Landauer formula to calculate the electrical conductance (see theoretical methods). Since the molecules can interact with graphene electrodes in different stacking configurations, three different structures of AB, AA and a mixture of AA and AB stacking are considered. Figure 4B-E show the calculated ensemble average conductance of 3 different configurations (from AB to AA stacking) of N-PAHs and PAHs molecules between graphene electrodes with multiple k-points (5×5) perpendicular to the transport direction.

Figure 4E shows the calculated average conductance of PAH4' (red line) and 4N-PAH4' (blue line) as a function of the Fermi energy E_F. The HOMO resonance for 4N-PAH4' has shifted to the left far away from the Fermi energy by ~0.39 eV, while the LUMO resonance has shifted to the left by ~1.23 eV and is closer to E_F. This large shift of the LUMO resonance toward E_F combined with its slightly smaller vdW distance increases the electrical conductance. The black dashed line at E_F = -0.18 eV in Figure 4B-E shows the Fermi energy that gives the best agreement with experiments for all molecules (see Figure S8 in the SI). The LUMO resonances of 2N-PAH4 and 2N-PAH5 are also shifted downward in energy, as depicted in Figure 4C, B, but not as much as for 4N-PAH4'. Consequently, the electrical conductance values of 2N-PAHs are lower than those of the corresponding PAHs at E_F (-0.18 eV). As shown in Figure 4D, the same holds true for 4N-PAH5' (blue line), which has a lower conductance than PAH5'. We also performed calculations with a different graphene electrode configuration, as shown in Figure S9, S10 in the SI, and found similar results.

As shown in Figure 4F, we obtain the positions of HOMO (red circles) and LUMO (green circles) resonances relative to the Fermi energy of electrodes for each molecular junction from Figure 4B-D. Our calculation shows that in N-PAHs molecules, HOMO and LUMO energy levels move downward in energy, and the shift of LUMO energy level is larger for molecules with a higher number of nitrogen atoms, such as 4N-PAH4' and 4N-PAH5'. The largest shift of the LUMO energy happens to be in 4N-PAH4'. It is worth mentioning that electron transport in PAHs occurs close to HOMO, in agreement with the previous reports[37]. However, electron

transport in N-PAHs happens to move from HOMO to LUMO because the molecular orbitals move downward in energy and the FMOs change due to the higher number of nitrogen atoms. Our calculations also indicate that the conductance order between different PAHs and N-PAHs is sensitive to the choice of E_F, so gating by a third electrode could lead to different orders.

Conclusions

In summary, we fabricated the atomically well-defined N-doped graphene heterojunctions and investigated the cross-plane transport through these heterojunctions to reveal the effect of doping on their electronic properties. We found that the electronic cloud distribution *via* vdW interactions between N-PAHs and graphene electrodes plays an essential role in their conductance, and the presence of nitrogen atoms has a pronounced effect on the alignment of the energy levels of HOMO and LUMO with respect to the Fermi level of the electrodes. Given a HOMO-dominated charge transport through PAHs and N-PAHs, the insertion of nitrogen atoms significantly stabilizes the HOMO, leading to a decrease in the conductance of N-PAH compared to that of its PAH counterpart. As the number of nitrogen atoms increases, the LUMO becomes more stabilized than the HOMO. Together with a variation in the topology and the number of the phenyl rings of N-PAHs, the LUMO-dominated charge transport occurs, leading to a slight decrease (4N-PAH5') and an increase (4N-PAH4') in the conductance of N-PAH compared with that of its PAH counterpart. Our work represented a solid step for the actual application of the graphene device *via* cross-plane transport and demonstrated the essential role of heteroatoms in two-dimensional heterojunctions.

Experimental procedures

Materials

The Cu wires and Cu foils with single-layer graphene were purchased from 6 Carbon Technology (Shenzhen, China). 2N-PAH4[42], 2N-PAH5[42], 4N-PAH4'[40,43], and 4N-PAH5'[39,41] were prepared according to literature procedures.

Single-molecule conductance measurements

We used XPBJ technique modified from a home-built STM-BJ setup to perform single-molecule conductance measurements. A 0.1 V bias voltage was applied at room temperature. See more details in Section S2, and the previous work[37].

Transition voltage spectroscopy

Conductance measurements were performed with an applied bias of 0.1 V. When a conductance plateau appeared from 10^{-5} G_0 (~775 pS) to 10^{-4} G_0 (~7.75 nS), the movement of the piezo was paused and the tip was stationary. The bias voltage was scanned between -1 V and 1 V and the I-V curves were recorded during the process. More than 1000 curves were collected for statistical analysis. The fitting curve was obtained from the 2D I-V histogram, and the transition voltage spectrum was plotted based on the previous works[45-47].

Ultraviolet photoelectron spectroscopy

UPS measurements were performed to estimate the electronic structure of N-PAHs and PAHs on graphene. The binding energy spectra were obtained using a HeIlight source ($h\nu$ = 21.22 eV) at an applied bias of -5 V. More details are included in S25.

Theoretical Calculations

The optimized geometries with ground-state Hamiltonian and overlap matrix elements for gas phase molecules and molecules between graphene electrodes were obtained using density functional theory (DFT). These results were then combined with the Green function method to calculate the phase-coherent, elastic-scattering properties of the system, consisting of two graphene electrodes and the molecule as the scattering region. From the calculated transmission functions, the electrical conductance was calculated using the Landauer formula. See the Supporting Information for details of computational methods.

Supplemental information

Supplemental information PDF includes Figures S1-S11, and Table S1-S5.

Acknowlwdges

This work was supported by the National Natural Science Foundation of China (Nos. 21973079, 22032004), Natural Science Foundation of Fujian Province (2021J06008), National Key R&D Program of China (2017YFA0204902), the UKRI Future Leaders Fellowship (No. MR/S015329/2), the Leverhulme Trust Early Career Fellowship (No. ECF-2018-375), the

Swiss NSF through the NCCR MUST ‘‘Molecular Ultrafast Science and Technology’’ and the Swiss NSF (200020_188468 and 200021_204053).

Author contributions

W. H., Y. Y., H. S., and S. L. co-supervised the project. H. Z., P. Z. and A. D. prepared the manuscript with input from all authors H. Z., S. Z., Z. Y., Y. Z. and Y. Z. carried out experiments and analyzed the data. P. Z., S. D. and R. H. synthesized molecules. A. D. and S. S. carried out theoretical calculations. All authors have approved the final version of the manuscript.

Declaration of interest

The authors declare no competing interests.

References

1. Zhang, Y., Tan, Y.-W., Stormer, H.L., and Kim, P . Experimental Observation of the Quantum Hall Effect and Berry's Phase in Graphene. *Nature*, 2005, 438, 201-204.
2. Novoselov, K.S., Mishchenko, A., Carvalho, A., and Neto, A.H.C. 2D Materials and Van der Waals Heterostructures. *Science*, 2016, 353, aac9439.
3. Xu, X., Lou, Z., Cheng, S., Chow, P.C.Y., Koch, N., and Cheng, H.-M. Van der Waals Organic/Inorganic Heterostructures in the Two-Dimensional Limit. *Chem*., 2021, 7, 2989-3026.
4. Liu, Y., Zeng, C., Yu, J., Zhong, J., Li, B., Zhang, Z., Liu, Z., Wang, Z.M., Pan, A., and Duan, X. (2021). Moiré Superlattices and Related Moiré Excitons in Twisted Van der Waals Heterostructures. *Chem. Soc. Rev*., 50, 6401-6422.
5. Wang, S., Zhao, S., Guo, X., and Wang, G. 2D Material- Based Heterostructures for Rechargeable Batteries. *Adv. Energy Mater*., 2022, 12, 2100864.
6. Peng, J., Chen, X., Ong, W.-J., Zhao, X., and Li, N. Surface and Heterointerface Engineering of 2D MXenes and Their Nanocomposites: Insights into Electro- and Photocatalysis. *Chem*., 2019, 5, 18-50.
7. Deng, D., Novoselov, K.S., Fu, Q., Zheng, N., Tian, Z., and Bao, X. Catalysis with two-dimensional materials and their heterostructures. *Nat. Nanotechnol*., 2016, 11, 218-230.

8. El Abbassi, M., Sangtarash, S., Liu, X., Perrin, M.L., Braun, O., Lambert, C., van der Zant, H.S.J., Yitzchaik, S., Decurtins, S., Liu, S.- X., et al. Robust Graphene- Based Molecular Devices. *Nat. Nanotechnol*., 2019, 14, 957-961.
9. Geim, A.K., and Grigorieva, I.V. Van der Waals Heterostructures. *Nature*, 2013, 499, 419- 425.
10. Cai, J., Pignedoli, C.A., Talirz, L., Ruffieux, P ., Söde, H., Liang, L., Meunier, V., Berger, R., Li, R., Feng, X., et al. Graphene Nanoribbon Heterojunctions. *Nat. Nanotechnol*., 2014, 9, 896-900.
11. Ju, L., Velasco, J., Huang, E., Kahn, S., Nosiglia, C., Tsai, H.-Z., Yang, W., Taniguchi, T., Watanabe, K., Zhang, Y., et al. Photoinduced doping in Heterostructures of Graphene and Boron Nitride. *Nat. Nanotechnol*., 2014, 9, 348-352.
12. Han, J., Wang, J., Yang, M., Kong, X., Chen, X., Huang, Z., Guo, H., Gou, J., Tao, S., Liu, Z., et al. Graphene/Organic Semiconductor Heterojunction Phototransistors with Broadband and Bi-directional Photoresponse. *Adv. Mater.*, 2018, 30, 1804020.
13. Pan, F., Sun, C., Li, Y., Tang, D., Zou, Y., Li, X., Bai, S., Wei, X., Lv, M., Chen, X., and Li, Y. Solution-Processable n-Doped Graphene-Containing Cathode Interfacial Materials for High-Performance Organic Solar Cells. *Energy Environ. Sci*., 2019, 12, 3400-3411.
14. Montenegro, A., Dutta, C., Mammetkuliev, M., Shi, H., Hou, B., Bhattacharyya, D., Zhao, B., Cronin, S.B., and Benderskii, A.V. Asymmetric Response of Interfacial Water to Applied Electric Fields. *Nature*, 2021, 594, 62-65.
15. Tanguy, N.R., Arjmand, M., and Yan, N. Nanocomposite of Nitrogen-Doped Graphene/Polyaniline for Enhanced Ammonia Gas Detection. *Adv. Mater. Interfaces*, 2019, 6, 1900552.
16. Yoo, T.J., Kim, S.-Y., Kwon, M.G., Kim, C., Chang, K.E., Hwang, H.J., and Lee, B.H. A Facile Method for Improving Detectivity of Graphene/p-Type Silicon Heterojunction Photodetector. *Laser Photonics Rev.*, 2021, 15, 2000557.
17. Li, C., Xiao, Y., Zhang, L., Li, Y., Delaunay, J.-J., and Zhu, H. Efficient Photoelectrochemical Water Oxidation Enabled by an Amorphous Metal Oxide-Catalyzed Graphene/Silicon Heterojunction Photoanode. *Sustain. Energy Fuels*, 2018, 2, 663-672.
18. Yan, Y., Zhai, D., Liu, Y., Gong, J., Chen, J., Zan, P., Zeng, Z., Li, S., Huang, W., and Chen, P. van der Waals Heterojunction between a Bottom-Up Grown Doped Graphene

Quantum Dot and Graphene for Photoelectrochemical Water Splitting. *ACS Nano*, 2020, 14, 1185-1195.

19. Li, Y., Xu, X., Liu, X., Li, B., Han, Y., Zheng, Y., Chen, D.-f., Yeung, K.W.K., Cui, Z., Li, Z., et al. Photoelectrons Mediating Angiogenesis and Immunotherapy through Heterojunction Film for Noninvasive Disinfection. *Adv. Sci.*, 2020, 7, 2000023.
20. Kawai, S., Nakatsuka, S., Hatakeyama, T., Pawlak, R., Meier, T., Tracey, J., Meyer, E., and Foster, A.S. Multiple heteroatom substitution to graphene nanoribbon. *Sci. Adv.*, 2018, 4, eaar7181.
21. Taqieddin, A., and Aluru, N.R. Electronic Structure and Transport in Graphene Nanoribbon Heterojunctions under Uniaxial Strain: Implications for Flexible Electronics. *ACS Applied Nano Materials*, 2021, 4, 5816-5824.
22. Rizzo, D.J., Wu, M., Tsai, H.-Z., Marangoni, T., Durr, R.A., Omrani, A.A., Liou, F., Bronner, C., Joshi, T., Nguyen, G.D., et al. Length-Dependent Evolution of Type II Heterojunctions in Bottom- Up-Synthesized Graphene Nanoribbons. *Nano Lett.*, 2019, 19, 3221- 3228.
23. Bie, C., Zhu, B., Xu, F., Zhang, L., and Yu, J. In Situ Grown Monolayer N-Doped Graphene on CdS Hollow Spheres with Seamless Contact for Photocatalytic CO_2 Reduction. *Adv. Mater.*, 2019, 31, 1902868.
24. Guo, B., Liu, Q., Chen, E., Zhu, H., Fang, L., and Gong, J.R. Controllable N-Doping of Graphene. *Nano Lett.*, 2010, 10, 4975- 4980.
25. Li, N., Wang, Z., Zhao, K., Shi, Z., Gu, Z., and Xu, S. Large Scale Synthesis of N-Doped Multilayered Graphene Sheets by Simple Arc-Discharge Method. *Carbon*, 2010, 48, 255-259.
26. Sala, A., Zamborlini, G., Menteş, T.O., and Locatelli, A. Fabrication of 2D Heterojunction in Graphene via Low Energy N^{2+} Irradiation. *Small*, 2010, 11, 5927-5931.
27. Zhang, C., Fu, L., Liu, N., Liu, M., Wang, Y., and Liu, Z. Synthesis of Nitrogen-Doped Graphene Using Embedded Carbon and Nitrogen Sources. *Adv. Mater.*, 2011, 23, 1020-1024.
28. Wang, H., Maiyalagan, T., and Wang, X. Review on Recent Progress in Nitrogen-Doped Graphene: Synthesis, Characterization, and Its Potential Applications. *ACS Catal.*, 2012, 2, 781- 794.
29. Yang, Y., Gantenbein, M., Alqorashi, A., Wei, J., Sangtarash, S., Hu, D., Sadeghi, H., Zhang, R., Pi, J., Chen, L., et al. Heteroatom-Induced Molecular Asymmetry Tunes

Quantum Interference in Charge Transport through Single-Molecule Junctions. *J. Phys. Chem. C*, 2018, 122, 14965-14970.

30. Wang, L., Zhao, Z., Shinde, D.B., Lai, Z., and Wang, D. Modulation of Destructive Quantum Interference by Bridge Groups in Truxene-Based Single-Molecule Junctions. *Chem. Commun.*, 2021, 57, 667-670.
31. Liu, X., Sangtarash, S., Reber, D., Zhang, D., Sadeghi, H., Shi, J., Xiao, Z.-Y., Hong, W., Lambert, C.J., and Liu, S.-X. Gating of Quantum Interference in Molecular Junctions by Heteroatom Substitution. *Angew. Chem. Int. Ed.*, 2017, 56, 173-176.
32. Tang, C., Huang, L., Sangtarash, S., Noori, M., Sadeghi, H., Xia, H., and Hong, W. Reversible Switching between Destructive and Constructive Quantum Interference Using Atomically Precise Chemical Gating of Single- Molecule Junctions. *J. Am. Chem. Soc.*, 2021, 143, 9385-9392.
33. Miguel, D., Álvarez de Cienfuegos, L., Martín-Lasanta, A., Morcillo, S.P., Zotti, L.A., Leary, E., Bürkle, M., Asai, Y., Jurado, R., Cárdenas, D.J., et al. Toward Multiple Conductance Pathways with Heterocycle-Based Oligo(phenyleneethynylene) Derivatives. *J. Am. Chem. Soc.*, 2015, 137, 13818-13826.
34. Quek, S.Y., Kamenetska, M., Steigerwald, M.L., Choi, H.J., Louie, S.G., Hybertsen, M.S., Neaton, J.B., and Venkataraman, L. Mechanically Controlled Binary Conductance Switching of a Single-Molecule Junction. *Nat. Nanotechnol.*, 2009, 4, 230-234.
35. Kamenetska, M., Quek, S.Y., Whalley, A.C., Steigerwald, M.L., Choi, H.J., Louie, S.G., Nuckolls, C., Hybertsen, M.S., Neaton, J.B., and Venkataraman, L. Conductance and Geometry of Pyridine-Linked Single-Molecule Junctions. *J. Am. Chem. Soc.*, 2010, 132, 6817-6821.
36. Wang, X.-Y., Yao, X., and Müllen, K. Polycyclic Aromatic Hydrocarbons in the Graphene Era. *Sci. China Chem.*, 2019, 62, 1099-1144.
37. Zhao, S., Wu, Q., Pi, J., Liu, J., Zheng, J., Hou, S., Wei, J., Li, R., Sadeghi, H., Yang, Y., et al. Cross-Plane Transport in a Single-Molecule Two-Dimensional Van der Waals Heterojunction. *Sci. Adv.*, 2020, 6, eaba6714.
38. Zhao, S., Deng, Z.-Y., Albalawi, S., Wu, Q., Chen, L., Zhang, H., Zhao, X.-J., Hou, H., Hou, S., Dong, G., et al. Charge Transport Through Single-Molecule Bilayer- Graphene Junctions with Atomic Thickness. *Chem. Sci.,* 2022, DOI: 10.1039/D1SC07024J.

39. Brietzke, T., Mickler, W., Kelling, A., and Holdt, H.-J. Mono- and Dinuclear Ruthenium(ii) 1,6,7,12-Tetraazaperylene Complexes. *Dalton Trans.*, 2012, 41, 2788-2797.

40. Geib, S., Martens, S.C., Zschieschang, U., Lombeck, F., Wadepohl, H., Klauk, H., and Gade, L.H. 1,3,6,8- Tetraazapyrenes: Synthesis, Solid- State Structures, and Properties as Redox-Active Materials. *J. Org. Chem.*, 2012, 77, 6107-6116.

41. Kocić, N., Weiderer, P., Keller, S., Decurtins, S., Liu, S.X., and Repp, J. Periodic Charging of Individual Molecules Coupled to the Motion of an Atomic Force Microscopy Tip. *Nano Lett.*, 2015, 15, 4406-4411.

42. Kouno, H., Kawashima, Y., Tateishi, K., Uesaka, T., Kimizuka, N., and Yanai, N. Nonpentacene Polarizing Agents with Improved Air Stability for Triplet Dynamic Nuclear Polarization at Room Temperature. *J. Phys. Chem. Lett.*, 2019, 10, 2208-2213.

43. Zhou, P., Aschauer, U., Decurtins, S., Feurer, T., Häner, R., and Liu, S.-X. Effect of *tert*-butyl Groups on Electronic Communication between Redox Units in Tetrathiafulvalene-Tetraazapyrene Triads. *Chem. Commun.*, 2021, 57, 12972-12975.

44. Kim, Beebe, J.M., Jun, Y., Zhu, X.Y., and Frisbie, C.D. Correlation between HOMO Alignment and Contact Resistance in Molecular Junctions: Aromatic Thiols versus Aromatic Isocyanides. *J. Am. Chem. Soc.*, 2006, 128, 4970-4971.

45. Beebe, J.M., Kim, B., Gadzuk, J.W., Daniel Frisbie, C., and Kushmerick, J.G. Transition from Direct Tunneling to Field Emission in Metal-Molecule-Metal Junctions. *Phys. Rev. Lett.,* 2006, 97, 026801.

46. Beebe, J.M., Kim, B., Frisbie, C.D., and Kushmerick, J.G. Measuring Relative Barrier Heights in Molecular Electronic Junctions with Transition Voltage Spectroscopy. *ACS Nano*, 2008, 2, 827- 832.

47. Yang, Y., Liu, J., Feng, S., Wen, H., Tian, J., Zheng, J., Schöllhorn, B., Amatore, C., Chen, Z., and Tian, Z. Unexpected Current-Voltage Characteristics of Mechanically Modulated Atomic Contacts with the Presence of Molecular Junctions in an Electrochemically Assisted–MCBJ. *Nano Res.*, 2016, 9, 560-570.

48. Soler, J.M., Artacho, E., Gale, J.D., García, A., Junquera, J., Ordejón, P., and Sánchez-Portal, D. The SIESTA Method Forab Initioorder-Nmaterials Simulation. *J. Phys. Condens. Matter*., 2002, 14, 2745- 2779.

49. Ferrer, J., Lambert, C.J., García- Suárez, V.M., Manrique, D.Z., Visontai, D., Oroszlany, L., Rodríguez-Ferradás, R., Grace, I., Bailey, S.W.D., Gillemot, K., et al. GOLLUM: a

Next-Generation Simulation Tool for Electron, Thermal and Spin Transport. *New J. Phys.*, 2014, 16, 093029.

50. Sadeghi, H. Theory of Electron, Phonon and Spin Transport in Nanoscale Quantum Devices. *Nanotechnology*, 2018, 29, 373001.

6.1.2 Supporting information

Atomically Well-defined Nitrogen Doping in the Cross-plane Transport through Graphene Heterojunctions

Hewei Zhang,[1,4] Ping Zhou,[2,4] Abdalghani Daaoub,[3,4] Sara Sangtarash,[3] Shiqiang Zhao,[1] Zixian Yang,[1] Yu Zhou,[1] Yuling Zou,[1] Silvio Decurtins,[2] Robert Häner,[2] Yang Yang,[1] Hatef Sadeghi,[3] Shi-Xia Liu,[2] Wenjing Hong[1]

[1]State Key Laboratory of Physical Chemistry of Solid Surfaces, College of Chemistry and Chemical Engineering & Pen-Tung Sah Institute of Micro-Nano Science and Technology, Xiamen University, 361005 Xiamen, China.
[2]Department of Chemistry, Biochemistry and Pharmaceutical Sciences, University of Bern, Freiestrasse 3, 3012 Bern, Switzerland
[3]Device Modelling Group, School of Engineering, University of Warwick, Coventry CV4 7AL, United Kingdom
[4]These authors contributed equally to this work

Content

1. Cross-plane break junction (XPBJ) setup

2. Graphene-based single-molecule junction measurement

3. Transition voltage spectrum

4. Ultraviolet photoelectron spectrum

5. UV-Vis spectrum

6. Computational methods

7. Supplementary computational figures, tables and discussion

8. Gold-based single-molecule junction measurement

1. Cross-plane break junction (XPBJ) setup

In order to fabricate Gr-molecule-Gr single-molecule junctions, we modified the scanning tunneling microscopy break junction (STM-BJ) setup used for gold electrode testing in the group to obtain the cross-plane break junction (XPBJ) setup. The Au tip was replaced with Cu wire with high-quality graphene on the surface made by chemical vapor deposition (CVD), and the Au substrate was replaced with Cu foil with graphene. Photos of the specific XPBJ setup are shown in Figure S1.

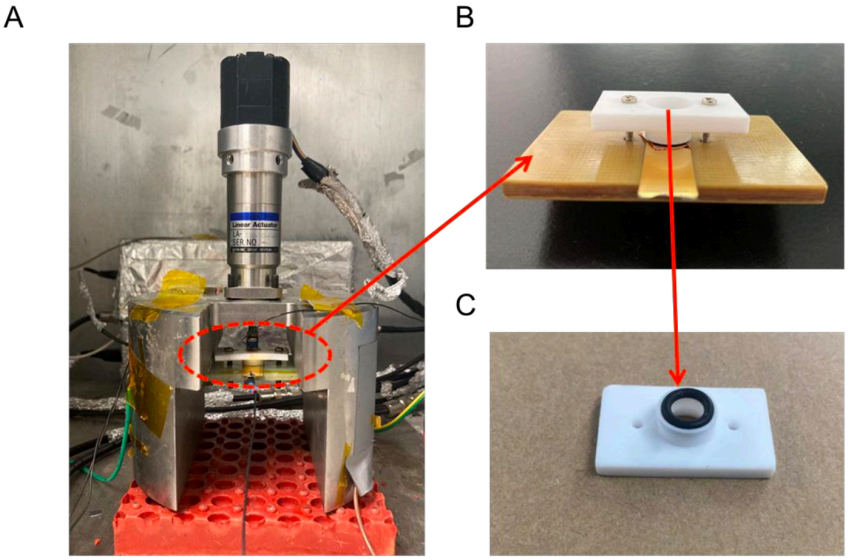

Figure S1 The photos of the home-built XPBJ setup. (A) The photos of the whole installation. (B) The liquid cell installation. (C) The O ring and liquid cell.

We used the O-ring and liquid cell made of acid-resistant materials in order to fix the position of Cu foil, ensure its flatness and alleviate the volatilization of solvent. The Cu wire is bent into an O shape and loaded into the syringe as a tip and fixed onto the piezo stack. The stepper motor above the piezo enables the tip to move quickly over a wide range. A large number of nanogaps with different intervals can be rapidly fabricated between the tip and the substrate by piezo, and the adjustment range is 0~10 V. The copper/graphene composites involved in the tip and substrate were purchased from Six- Carbon Technology Shenzhen. 30~40 μL of solution were dripped in the liquid cell. The liquid cell was connected to the skeleton through magnets, making the tip to dip into the solution. A current amplifier and a controller were connected to the tip and the substrate, and the measurement is completed through our own

developed program. During the break junction processes, a bias voltage of 100 mV was applied, and the current and voltage were recorded in real time at a sampling frequency of 20 kHz.

2. Graphene-based single-molecule junction measurement

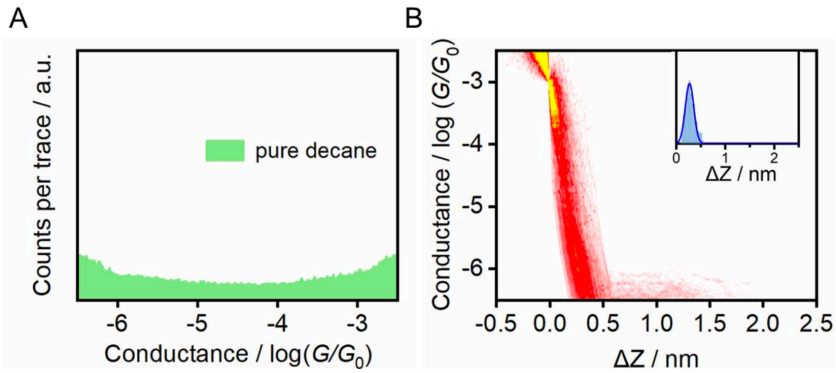

Figure S2 Pure solvent measurement. (A) 1D conductance histogram and (B) 2D conductance versus plateau length histogram of the pure decane.

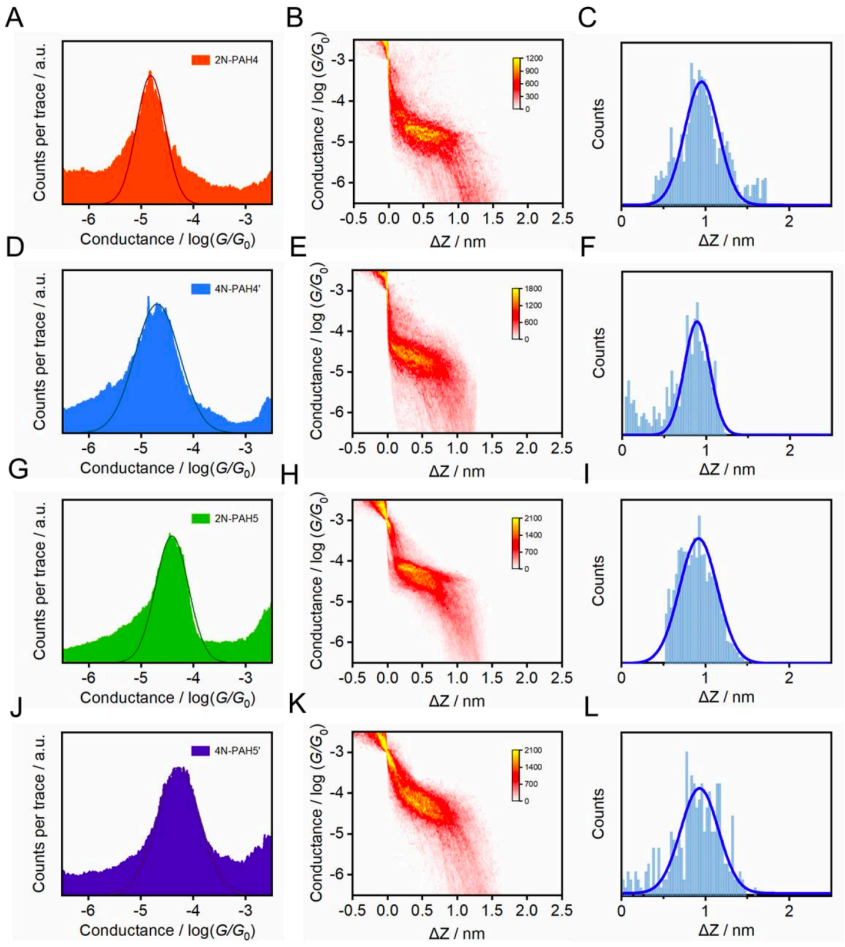

Figure S3 Results of single-molecule conductance by XPBJ measurement. 1D conductance histograms of 2N-PAH4 (A), 2N-PAH5 (D), 4N-PAH4′ (G), 4N-PAH5′ (J). 2D conductance-distance histograms of 2N-PAH4 (B), 2N-PAH5 (E), 4N-PAH4′ (H), 4N-PAH5′ (K). The plateau length histograms of 2N-PAH4 (C), 2N-PAH5 (F), 4N-PAH4′ (I), 4N-PAH5′ (L).

More than 1000 conductance traces were recorded during the measurement. When the conductance value is $10^{-3.0}$ G_0, the individual traces are considered to reach zero[1,2]. We measured the electrical properties of the pure solvent decane, as shown in Figure S2. Conductance-displacement traces plummeted, 1D conductance histograms showed no pronounced peak, and 2D conductance-distance histograms showed no apparent plateau.

Direct tunneling in the pure solvent is proved. The plateau length histograms were carried out for the conductance data from $10^{-3.0}$ G_0 to $10^{-6.0}$ G_0, and it was found that the plateau length of pure solvent decane was 0.27 nm[2,3], which was consistent with the previous work report. The plateau lengths of other molecules were corrected on this basis.

Supplementary Table S1 *C*onductance difference –

Molecule	G / nS	G (N-PAH)/ G(PAH)
2N-PAH5	3.02	0.468
PAH5	6.45	
2N-PAH4	1.20	0.631
PAH4	1.90	
4N-PAH5'	4.07	0.794
PAH5'	5.12	
4N-PAH4'	1.58	1.35
PAH4'	1.17	

The biggest conductance difference due to different doping number of nitrogen atoms:

$$1.35 \div 0.468 = 288\%$$

The conductance difference due to nitrogen-doping at different positions in the conjugated framework:

$$1.35 \div 0.794 = 170\%$$

$$0.631 \div 0.468 = 135\%$$

3. Transition voltage spectrum

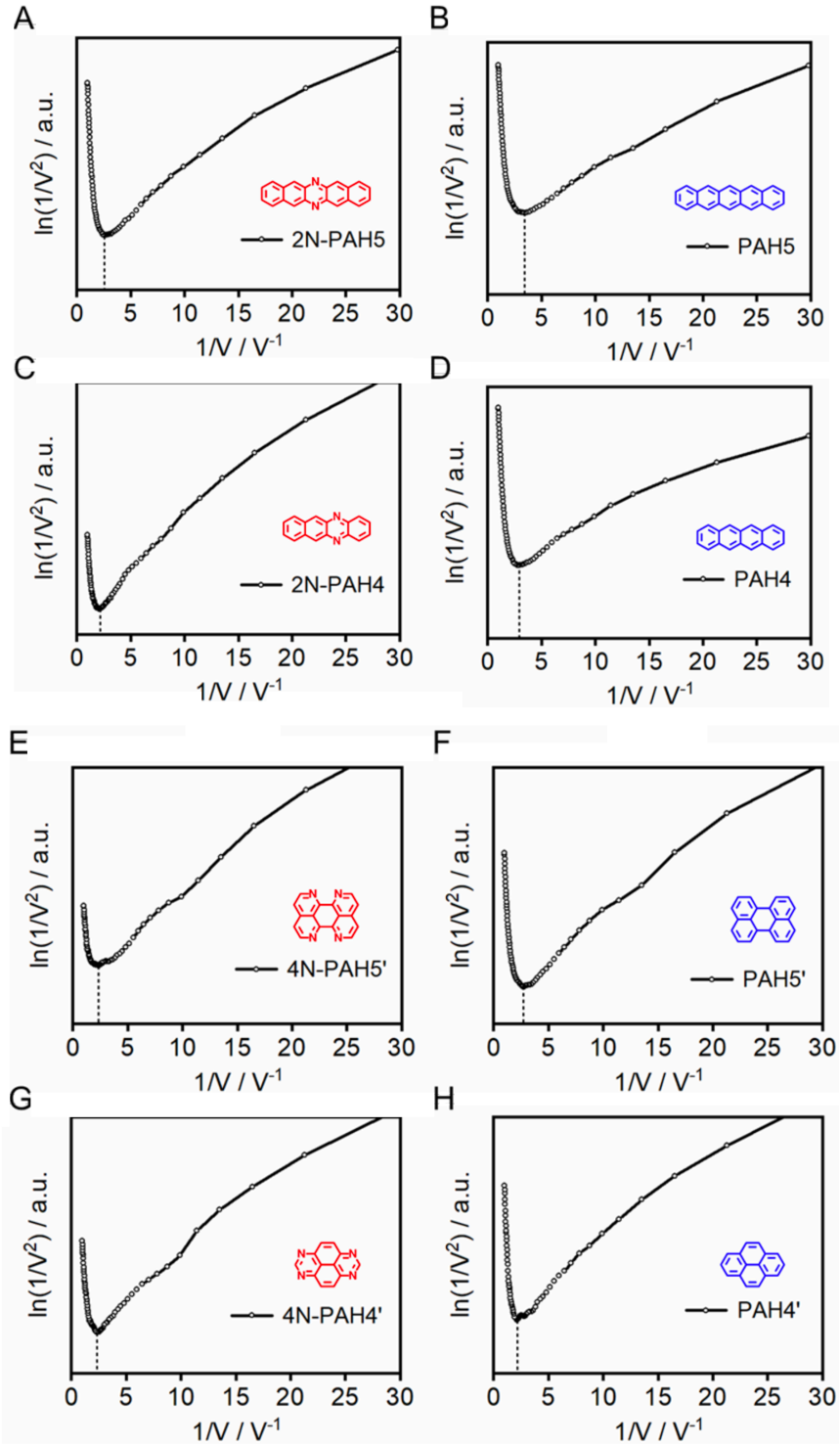

Figure S4 Transition voltage (ln(I/V2) vs1/V) spectra obtained from ~1000 I~V traces of 2N-PAH5 (A), PAH5 (B) ,2N-PAH4 (C), PAH4 (D), 4N-PAH5′ (E), PAH5′ (F), 4N-PAH4′ (G) and PAH4′ (H).

4. Ultraviolet photoelectron spectrum

The electronic structure of N-PAHs and PAHs on copper foil with single-layer graphene was measured by UPS. All data were obtained using a HeI light source (hν = 21.22 eV) with a bias of -5 V applied to the sample. The Fermi energy level of the electrode was corrected with the gold electrode on the same bench, and the intensity was normalized.

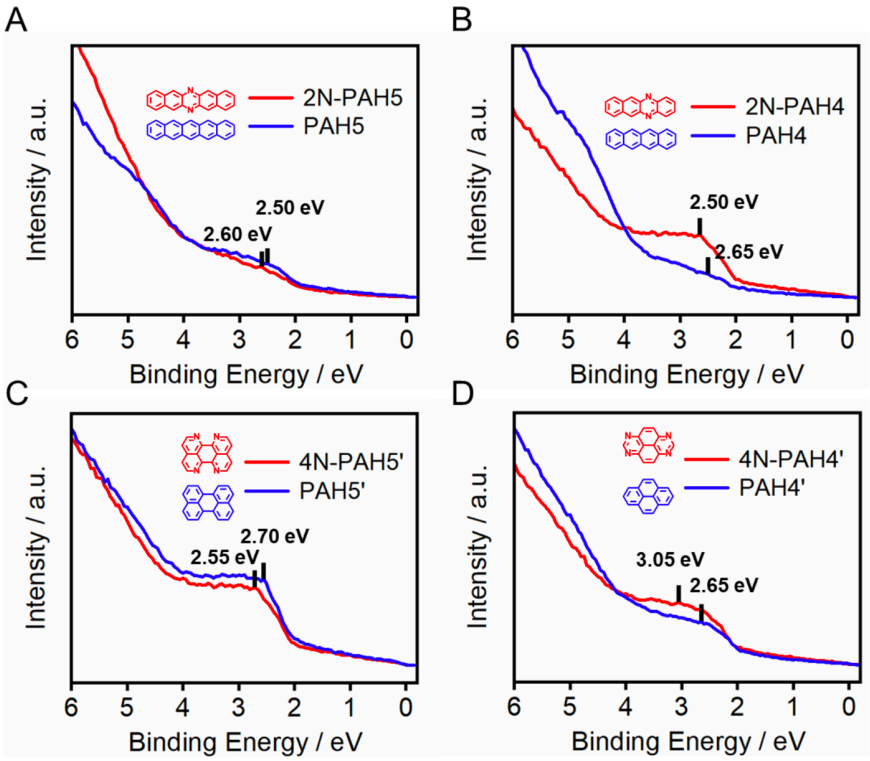

Figure S5 Ultraviolet photoelectron spectra of 2N-PAH5 and PAH5 (A), 2N-PAH4 and PAH4 (B), 4N-PAH5′ and PAH5′ (C), 4N-PAH4′ and PAH4′ (D).

Supplementary Table S2 E_F-E_{HOMO} of N-PAHs and PAHs by UPS

N-PAH	2N-PAH5	2N-PAH4	4N-PAH5′	4N-PAH4′
E_F-E_{HOMO} / eV	2.60	2.65	2.70	3.05

PAH	PAH5	PAH4	PAH5′	PAH4′
E_F-E_{HOMO} / eV	2.50	2.50	2.55	2.65

5. UV-Vis spectrum

According to an empirical formula:

$$E_g = 1240/\lambda_{abs}$$

E_g estimated from the UV-Vis spectrum onset of the lowest energy absorption band.

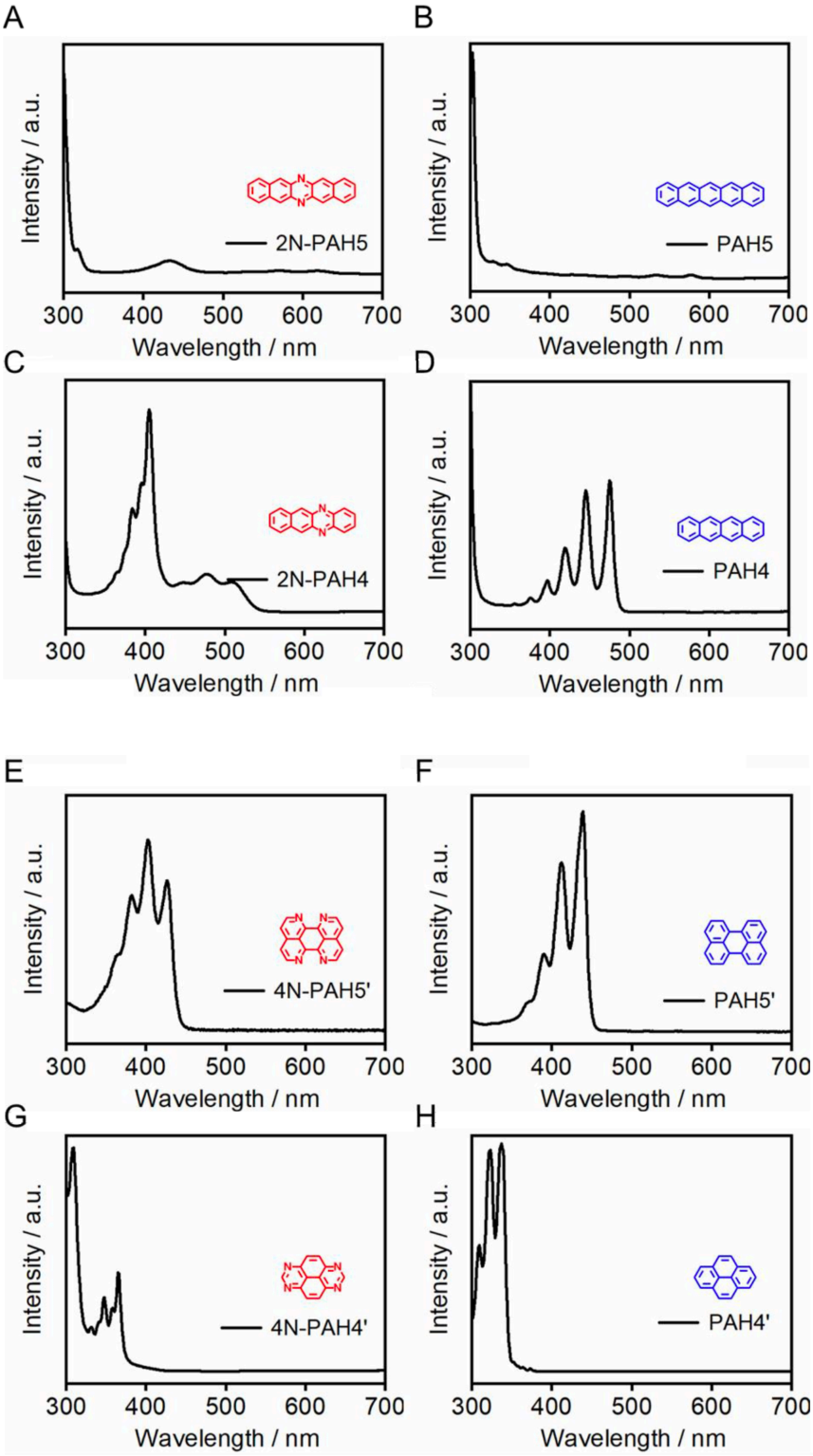

Figure S6 UV-Vis spectra of 2N-PAH5 (A), PAH5 (B) ,2N-PAH4 (C), PAH4 (D), 4N-PAH5′ (E), PAH5′ (F), 4N-PAH4′ (G) and PAH4′ (H) in chloroform.

Supplementary Table S3 Energy gap of N-PAHs and PAHs by UV-Vis

N-PAH	2N-PAH5	2N-PAH4	4N-PAH5′	4N-PAH4′
*E*g / eV	1.91	2.25	2.71	2.93

PAH	PAH5	PAH4	PAH5′	PAH4′
*E*g / eV	2.08	2.51	2.70	3.35

6. Computational methods

The optimized geometry and ground state Hamiltonian and overlap matrix elements of each structure studied in this paper was self-consistently obtained using the SIESTA implementation[4] of density functional theory (DFT). SIESTA employs norm-conserving pseudo-potentials to account for the core electrons and linear combinations of atomic orbitals to construct the valence states. The generalized gradient approximation (GGA) of the exchange and correlation functional is used with the Perdew-Burke-Ernzerhof parameterization (ca) a double-ζ (DZ) basis set, a real-space grid defined with an equivalent energy cut-off of 150 Ry. The geometry optimization for each structure is performed to the forces smaller than 20 meV/Å.

The mean-field Hamiltonian obtained from the converged DFT calculation was combined with Gollum[5,6] implementation of the non-equilibrium Green's function method6 to calculate the phase-coherent, elastic scattering properties of each system consist of left graphene (source) and right graphene (drain) leads and the scattering region. The transmission coefficient T(E) for electrons of energy E (passing from the source to the drain) is calculated *via* the relation: $T(E) = Trace(\Gamma_R(E)G^R(E)\Gamma_L(E)G^{R\dagger}(E))$. In this expression, $\Gamma_{L,R}(E) = i\,(\sum_{L,R}(E) - \sum_{L,R}{}^{\dagger}(E))$ describe the level broadening due to the coupling between left (L) and right (R) electrodes and the central scattering region, $\sum_{L,R}(E)$ are the retarded self-energies associated with this coupling and $G^R = (ES - H - \sum_L - \sum_R)^{-1}$ is the retarded Green's function.

The electrical conductance is then calculated using the Landauer formula $G(E_F,T) = G_0 \int^{+\infty} dE\ T(E)(-\partial f(E,\ T,\ E_F)/\partial E)$, where $f = (e^{(E-E_F)/k_BT} + 1)^{-1}$ is the Fermi-Dirac probability distribution function, T is the temperature, E_F is the Fermi energy, $G_0 = 2e^2/h$ is the conductance quantum, e is the electron charge, and h is the Planck's constant.

7. Supplementary computational figures, tables and discussion

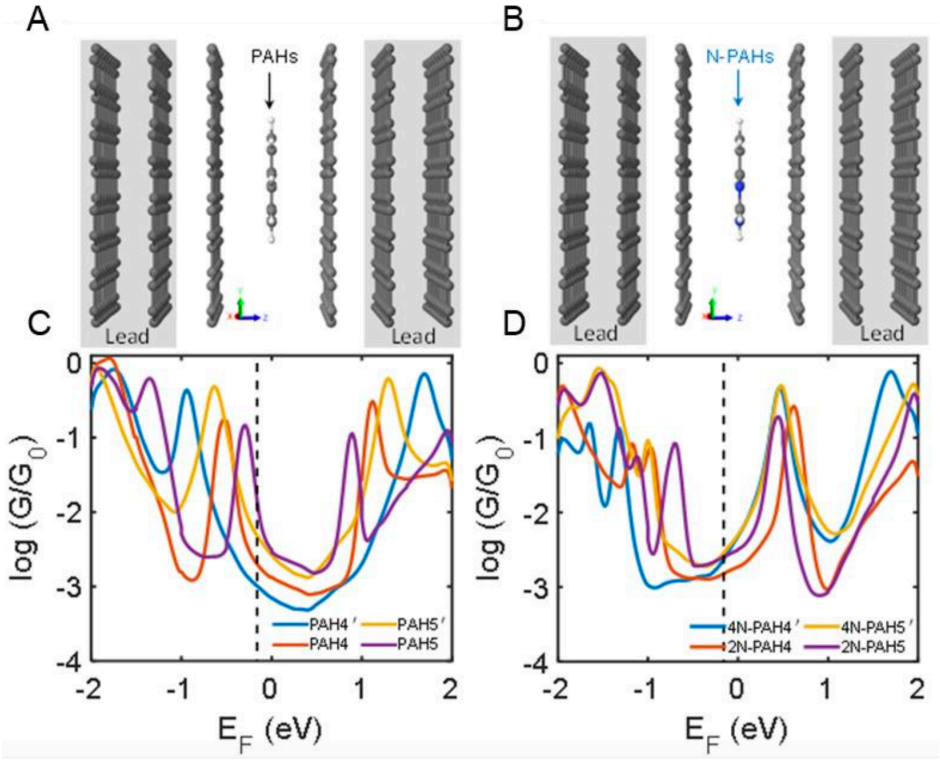

Figure S7 (A, C) Structure of sandwiched molecular junctions with PAH and N-PAH molecules between two graphene electrodes, respectively. (B, D) calculated ensemble average conductance of 3 different configurations (from AB to AA stacking) of N-PAH and PAH molecules between graphene electrodes with multiple k-points perpendicular to the z direction.

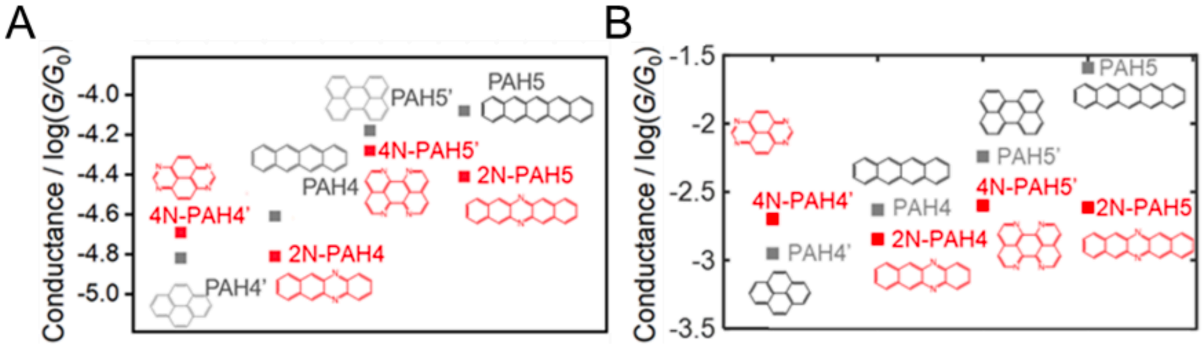

Figure S8 Measured (A) and calculated (B) electrical conductance of PAHs (gray) and N-PAHs (red), respectively. In (b), calculated ensemble average conductance is obtained at E_F = 0.18 eV in Figure S27 (b,d).

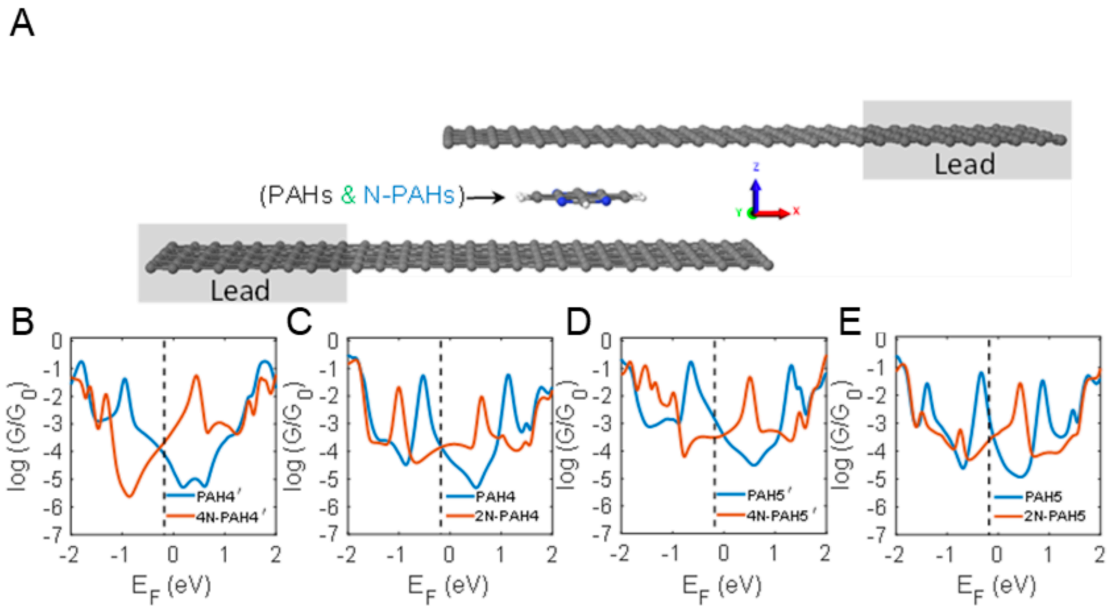

Figure S9 (A) Structure of sandwiched molecular junctions with PAH and N-PAH molecules between two graphene electrodes. (B, C, D, E) Boltzmann-weighted average conductance of 5 different configurations (from AB to AA stacking) of N- PAH and PAH molecules between graphene electrodes with multiple k-points (20) perpendicular to the z direction.

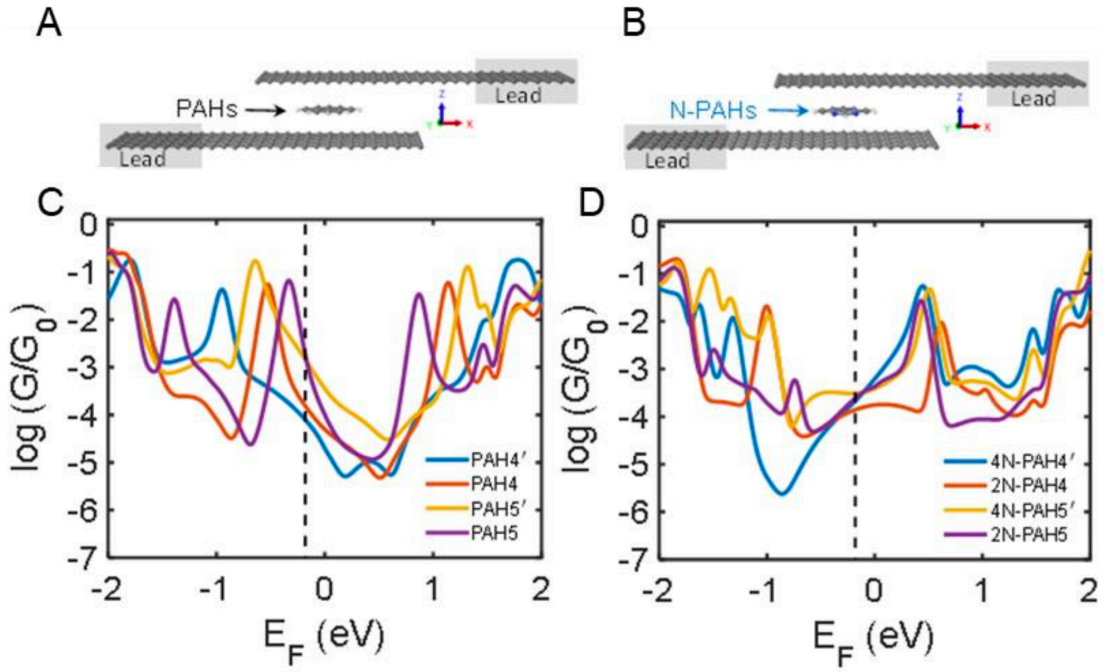

Figure S10 (A, C) Structure of sandwiched molecular junctions with PAH and N- PAH molecules between two graphene electrodes, respectively. (B, D) Boltzmann- weighted average conductance of 5 different configurations (from AB to AA stacking) of N-PAH and PAH molecules between graphene electrodes with multiple k-points (20) perpendicular to the z direction.

Supplementary Table S4 Frontier orbitals of relaxed structures of PAHs and N-PAHs molecules from HOMO-3 to LUMO+3 orbitals in (eV) energy unit.

Molecule	HOMO-3	HOMO-2	HOMO-1	HOMO	H-L Gap (eV)	LUMO	LUMO+1	LUMO+2	LUMO+3
	-6.50	-6.00	-5.50	-4.66	2.72	-1.94	-1.03	-0.53	0.12
	-6.35	-6.35	-5.54	-5.21	1.75	-3.46	-2.17	-1.46	-1.21
	-6.53	-5.72	-5.50	-4.21	1.72	-2.49	-0.98	-0.75	0.21
	-6.09	-5.92	-4.86	-4.77	1.67	-3.10	-1.34	-1.12	-0.24
	-5.95	-5.92	-5.78	-4.31	2.01	-2.30	-0.83	-0.61	-0.48
	-5.37	-5.32	-5.10	-4.73	1.43	-3.30	-1.69	-1.37	-1.24
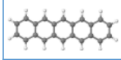	-6.08	-5.71	-5.11	-3.99	1.23	-2.76	-1.46	-0.79	-0.31
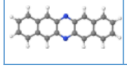	-6.02	-5.35	-4.82	-4.50	1.20	-3.30	-1.68	-1.10	-0.86

Supplementary Table S5 vdW distance between graphene and molecules in the relaxed ground state configuration

	PAH4'	4N-PAH4'	PAH4	2N-PAH4	PAH5'	4N-PAH5'	PAH5	2N-PAH5
vdW distance	3.460	3.420	3.432	3.428	3.460	3.425	3.430	3.460

8. Gold-based single-molecule junction measurement

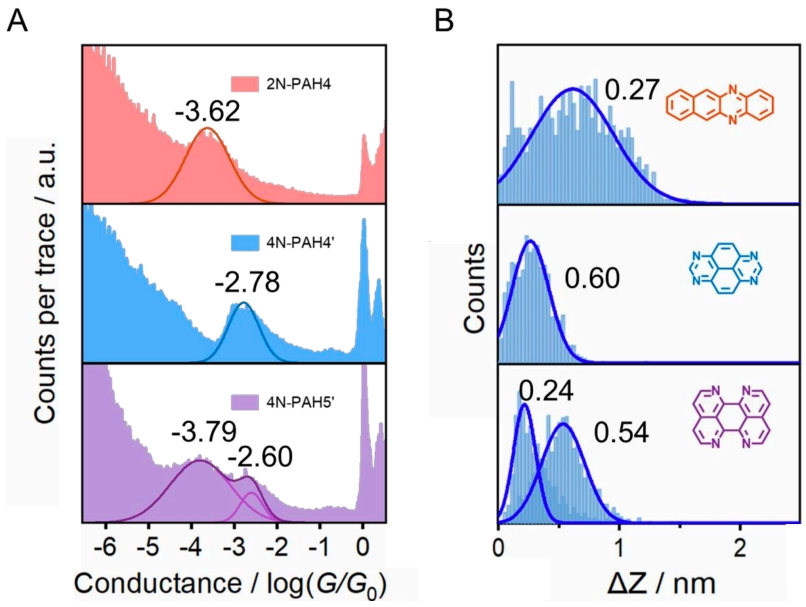

Figure S11 Electrical properties using gold electrodes with STM-BJ technique. (A) 1D conductance histograms obtained from ~1000 conductance–displacement traces of 2N-PAH4, 4N-PAH4′ and 4N-PAH5′. (B) The plateau length histograms of 2N-PAH4, 4N-PAH4′, and 4N-PAH5′.

Supplementary references

1. Caneva, S., Gehring, P., García-Suárez, V.M., García-Fuente, A., Stefani, D., Olavarria- Contreras, I.J., Ferrer, J., Dekker, C., and van der Zant, H.S.J. Mechanically Controlled Quantum Interference in Graphene Break Junctions. *Nat.Nanotechnol.*, 2018, 13, 1126-1131.
2. Zhao, S., Wu, Q., Pi, J., Liu, J., Zheng, J., Hou, S., Wei, J., Li, R., Sadeghi, H., Yang, Y., et al. Cross-plane Transport in a Single-Molecule Two-Dimensional Van der Waals Heterojunction. *Sci. Adv.*, 2020, 6, eaba6714.
3. Zhao, S., Deng, Z.-Y., Albalawi, S., Wu, Q., Chen, L., Zhang, H., Zhao, X.-J., Hou, H., Hou, S., Dong, G., et al. Charge Transport Through Single-Molecule Bilayer-Graphene Junctions with Atomic Thickness. *Chem. Sci.*, 2022, DOI: 10.1039/D1SC07024J.
4. Soler, J.M., Artacho, E., Gale, J.D., García, A., Junquera, J., Ordejón, P., and Sánchez-Portal, D. The SIESTA Method Forab Initioorder-Nmaterials Simulation. J. Phys. Condens. Matter, 2002, 14, 2745-2779.
5. Ferrer, J., Lambert, C.J., García-Suárez, V.M., Manrique, D.Z., Visontai, D., Oroszlany, L., Rodríguez-Ferradás, R., Grace, I., Bailey, S.W.D., Gillemot, K., et al. GOLLUM: a

Next-generation Simulation Tool for Electron, Thermal and Spin Transport. *New J. Phys*., 2014, 16, 093029.

6. Sadeghi, H. Theory of Electron, Phonon and Spin Transport in Nanoscale Quantum Devices. *Nanotechnology*, 2018, 29, 373001.

6.2 Self-assembly and on-surface polymerization

Given that polycyclic aromatic hydrocarbons (PAHs) are planar and thermally stable, the ease of halogenation allows to synthesize various building blocks (**Figure 1**) either for surface-assisted Ullmann coupling under ultra-high vacuum condition or for creating self-assembled nanostructures on different surfaces. All these projects are currently under investigation in collaboration with Prof. Ernst Meyer (University of Basel) and Prof. Roman Fasel (Empa). Some preliminary results are discussed below.

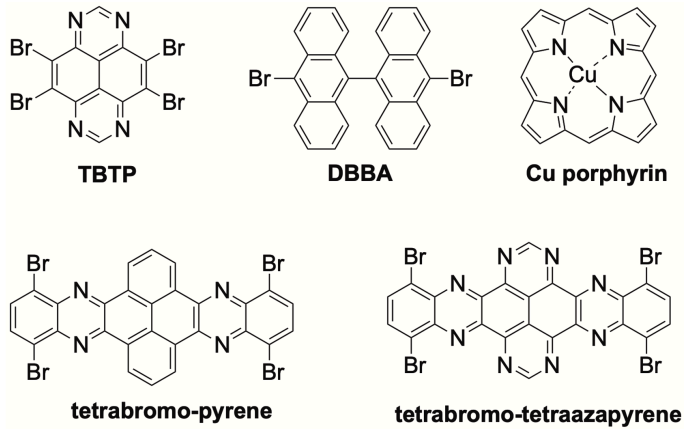

Figure 1 The chemical structures of the studied molecules.

6.2.1 Self-assembly of tetrabromotetraazapyrene (TBTP) on Ag(111)

Both discharging molecules on the surfaces and observations of electron-vibration coupling in molecules have been widely reported. Up to now, real-space imaging of electron-vibration coupling in molecules is still highly challenging due to the sub-molecular resolution and short lifetime of electron transfer in interface configurations. To address this issue, self-assembly of TBTP on Ag(111) has been carried out.

TBTP molecules were sublimated on Ag(111) at a sample temperature of 100 K. High-resolution STM and NC-AFM images (**Figure 2**) show the orientational glassy phase of self-assembled TBTP molecules.

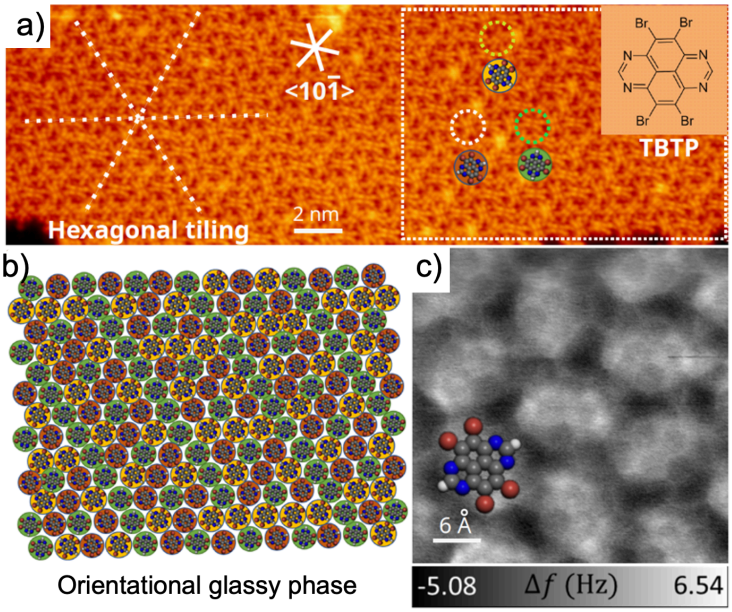

Figure 2 Self-assembly of TBTP molecules on Ag(111). a) Molecular islands of TBTP molecules. The inset in the right corner shows the chemical structure of TBTP molecules. Threefold symmetry dotted white lines cross each center of molecules and show a hexagonal tiling arrangement. Three different orientations of TBTP molecules are marked with red, green and yellow dotted circles, and their related structural models are located at the bottom of each circle. b) The orientational glassy phase of a molecule pattern is made up of three different molecular models. The pattern is a result of molecules in the white dotted rectangle in (a). c) Constant height Δf image of TBTP recorded with a CO tip.

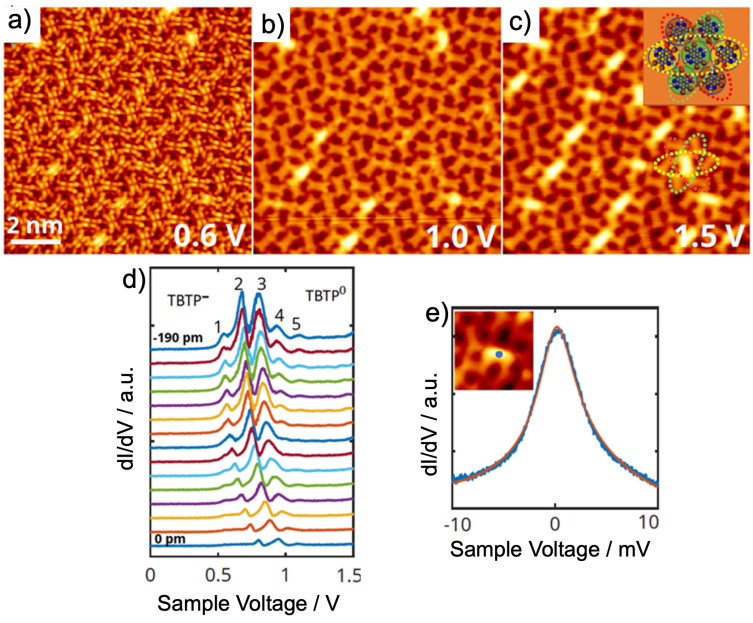

Figure 3 Electronic and vibronic structure of TBTP. (a-c) STM images of the same molecules with different sample voltages. When the sample voltage is increased, some molecules become

much brighter than others. An inset illustrates the structure of this kind of molecules. The molecule is surrounded by a uniform distribution of six molecules arranged in three orientations. (d) dI/dV spectra recorded at a molecule at different electric field by changing the tip-molecule distances. (e) STS of Kondo resonance in TBTP.

Scanning tunneling spectroscopy (STS) on molecules shows strong electron-vibration coupling due to the Franck-Condon blockade effect (**Figure 3**). To visualize the vibration features in real-space, dI/dV mapping images are used (**Figure 3d**). As shown in **Figure 3e**, there is a resonance peak around the Fermi energy which depicts the Kondo effect in molecules.

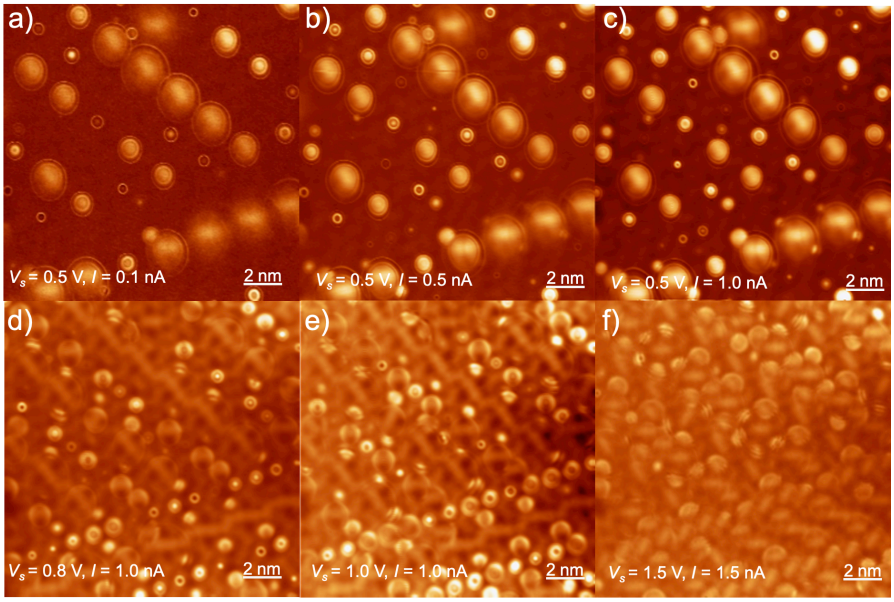

Figure 4 Real-space imaging of the electron-vibration coupling in TBTP. (a-f) Constant height dI/dV maps show the evolution of electron-vibration rings with increasing electric fields: V_s = 0.5 V and I = 0.1 nA (a), V_s = 0.5 V and I = 0.5 nA (b), V_s = 0.5 V and I = 1.0 nA (c), V_s = 0.8 V and I = 1.0 nA (d), V_s = 1.0 V and I = 1.0 nA (e), V_s = 1.5 V and I = 1.5 nA (f). The concentric rings expand and previous absent rings appear with increased electric fields.

Moreover, a series of constant height dI/dV maps recorded at different sample voltages are presented in **Figure 4**. As the sample voltages were increased from 0.5 V to 0.8 V, 1.0 V and 1.5 V, nearly all the molecules show the feature of concentric rings, indicating that electron vibrations are being coupled in TBTP at the discharging stage.

6.2.2 Self-assembly of TBTP on superconducting Pb(111)

To develop quantum materials hosting topological superconductivity and Majorana zero modes, a full control over exchange couplings between spins and conduction electrons of a superconductor is of high importance. As a consequence, self-assembly of TBTP upon sublimation in ultra-high vacuum on Pb(111) kept at room temperature, has been explored. As illustrated in **Figure 5**, a supramolecular TBTP assembly shows the coexistence of neutral (T) and radical anionic (S) molecules in the ground state, where electrons are ordered into a long-range superlattice. The molecules in S and T rows are stabilized by a combination of halogen bonds between neighboring Br atoms or between Br and the pyrimidine units (C–N···Br–C). For the T molecule, the LUMO lies at 0.75 mV and the HOMO is at -0.25 V. For the S molecule, we observe at positive bias voltage of V = 1 V a strong resonance peak, denoted D, which is absent in T molecule's spectra (**Figure 5f**). This is assigned as a fingerprint of a charge-state switching from an anionic state $TBTP^{\bullet-}$ to a neutral state $TBTP^{0}$ induced by the local electric field of the voltage applied to the tip.

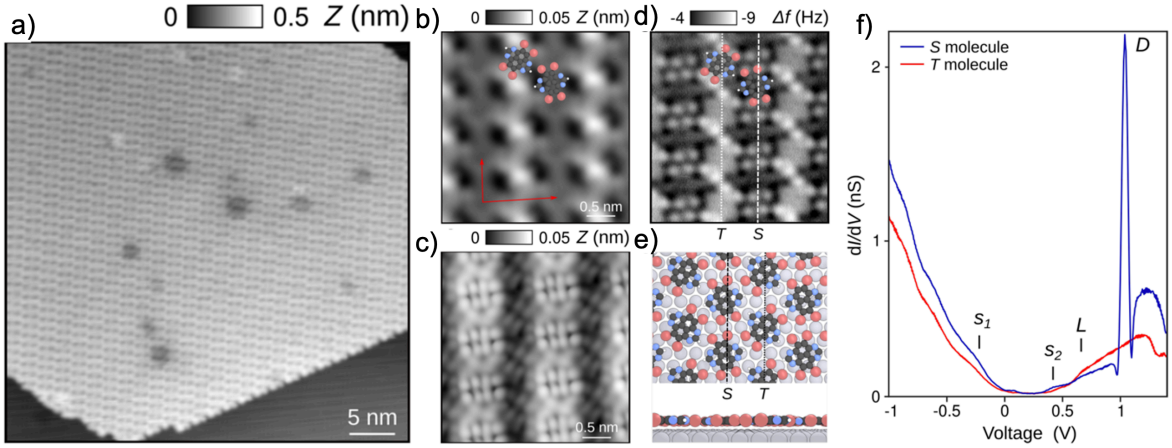

Figure 5 Self-assembly of TBTP molecules on Pb(111). a) STM overview of Pb(111) upon self-assembly of TBTP molecules (V = 1.0 V, I_t = 1 pA). b) Close-up STM image of the molecular lattice (V = 0.8 V, I_t = 0.8 pA). The unit cell of the TBTP layer is marked with red arrows. c) STM image of the same area for V = 80 mV. d) Corresponding constant-height AFM image acquired with a Br-tip showing the molecular arrangement within rows of straight (S) and tilted (T) molecules, partially overlaid with ball-and-stick structure models of TBTP molecules. e) Top and side views of the TBTP assembly on Pb(111) optimized by DFT calculations. Red, blue, black and gray colors correspond to bromide, nitrogen, carbon and lead atoms. f) dI/dV(V) point-spectra acquired above S (blue) and T (red) molecules.

$TBTP^{\bullet-}$ anions show characteristic quantum dot behavior, implying that tip gating allows removal of a single-electron at an appropriate threshold voltage (**Figure 6**, left), and

localization of electrons only in molecules of the S rows is also confirmed (**Figure 6**, right). The differential conductance, dI/dV, shows a pair of in-gap Yu-Shiba-Rusinov resonances for $TBTP^{\bullet-}$ attributed to the spin-1/2 of the confined electron in the molecule (**Figure 7**).

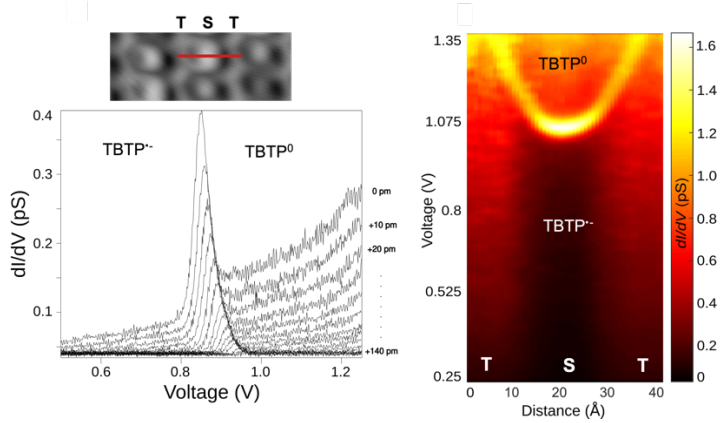

Figure 6 (left) dI/dV(V,z) point-spectra acquired above a single $TBTP^{\bullet-}$ molecule while increasing the tip-sample separation z. (right) dI/dV(V,x) cross-section across T-S-T rows (red line) in the top-left.

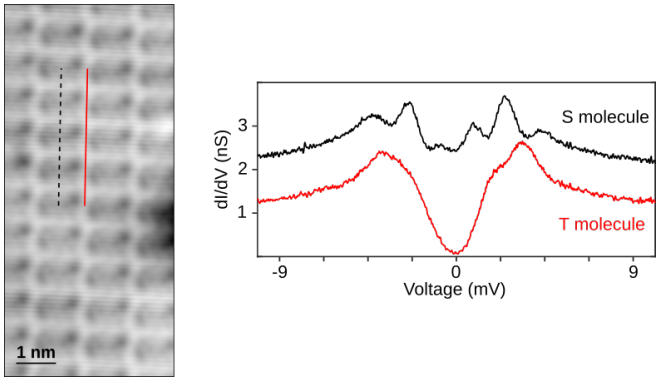

Figure 7 (left) STM topographic image of the supra-molecular assembly (V = -0.3V, I_t = 1 pA). Plain and dashed lines are aligned along T and S rows, respectively. (right) dI/dV(V) point-spectra measured with a superconducting STM tip above a single molecule of a S (black) and T (red) row, respectively. The spectra are shifted by 1 nS for clarity.

6.2.3 On-surface chemical reactions

6.2.3.1 Proximity-induced superconductivity in atomically precise nanographene

Proximity-Induced Superconductivity in Atomically Precise Nanographene

Jung-Ching Liu,*,† Rémy Pawlak,† Xing Wang,‡ Hongyan Chen,¶ Philipp D'Astolfo,† Carl Drechsel,† Ping Zhou,‡ Robert Häner,‡ Silvio Decurtins,‡ Ulrich Aschauer,‡ Shi-Xia Liu,‡ Wulf Wulfhekel,¶ and Ernst Meyer*,†

†*Department of Physics, University of Basel, Klingelbergstrasse 82, 4056 Basel, Switzerland*

‡*Department of Chemistry, Biochemistry and Pharmaceutical Sciences, University of Bern, Freiestrasse 3, 3012 Bern, Switzerland*

¶*Physikalisches Institut, Karlsruhe Institute of Technology, Wolfgang-Gaede-Str. 1, 76131 Karlsruhe, Germany*

E-mail: jungching.liu@unibas.ch; ernst.meyer@unibas.ch

Abstract

Obtaining a robust superconducting state in atomically precise nanographene (NG) structures by proximity to a superconductor could foster the discovery of topological superconductivity in graphene. On-surface synthesis of such NGs has been achieved on noble metals and metal oxides, however, it is still absent on superconductors. Here, we present a synthetic method to induce superconductivity to polymeric chains and NGs adsorbed on the superconducting Nb(110) substrate covered by thin Ag films. Using atomic force microscopy at low-temperature, we characterize the chemical structure of each sub-product formed on the superconducting Ag layer. Scanning tunneling spectroscopy further allows us to elucidate electronic properties of these nanostructures, which consistently show a superconducting gap. We foresee our approach to

become a promising platform for exploring the interplay between carbon magnetism and superconductivity at the fundamental level.

Keywords: scanning tunneling microscopy, atomic force microscopy, on-surface chemistry, nanographene, graphene nanoribbon, proximity-induced superconductivity

Introduction

Topological superconductors are currently of particular interest in the condensed matter physics due to their potential as building blocks for topological quantum computation.[1,2] Topological superconductivity (TS) is elusive in nature, but it can be engineered in hybrid heterostructures by coupling an electron gas with spin-momentum locking to a conventional superconductor.[3–5] As previously demonstrated in ferromagnetic atomic chains[6–8] or islands[9] proximitized with a *s*-wave superconductor, fingerprints of TS are Majorana quasiparticle excitations, so-called Majorana zero modes (MZMs). MZMs can be identified by scanning tunneling spectroscopy (STS) as zero-energy conductance peaks located at system boundaries which also mark the system topology.[10]

With the bottom-up synthesis through on-surface reactions, atomically-precise nanographenes (NGs) and graphene nanoribbons (GNRs)[11,12] can host Dirac fermions, topological electronic properties,[13–15] magnetic edge states,[12,16] and coupled spins.[17,18] Despite considerable efforts to engineer their structures and electronic properties on surfaces, observing the interaction of a superconducting state with graphene local magnetism is scarce in literature.[19] Interestingly, this interaction can lead to further application from strong spin-orbit coupled materials to novel graphene-based topological superconductors[20], which opens a new era for implementing Majorana-based *qubits* in topological quantum computation.

The fabrication of NGs is based on a bottom-up approach in which predefined organic precursors are deposited in ultra-high vacuum (UHV) onto crystalline substrates, and then undergo thermally triggered reactions. However, these reactions are so far restricted

to noble metals (Au, Ag or Cu)[11,21] or metal oxides (TiO_2),[22] where surface diffusion of molecules, dehalogenation and cyclodehydrogenation processes are possible by thermal treatment. In contrast, most conventional superconductors are unable to host these reactions due to their low melting points (Pb, In) or high reactivity (Nb, Re). Extending the on-surface chemistry toolbox to superconducting surfaces thus represents a crucial step in the study of the subtle interplay between carbon magnetism and superconductivity.

To date, proximity-induced superconductivity in epitaxial graphene has been achieved by top superconducting electrodes,[23] by proximity to co-adsorbed Pb islands,[19] or by synthesizing graphene on a superconducting substrate such as Re(0001).[24] Although the last approach offers the cleanest alternative as it prevents the contamination of graphene during the fabrication process, the strong hybridization of graphene π bands with 5*d* Re orbitals was found to prevent Dirac-like electronic dispersion close to the Fermi level.[24] Later, this issue was circumvented by intercalating an Au buffer layer between graphene and the superconductor,[25] which restores the intrinsic electronic properties similar to the ones encountered on bulk Au. In our context, such normal metal-superconductor heterostructures are interesting not only for the ability to preserve graphene electronic properties, but also for the capability of hosting surface-assisted reactions.

Inspired by the seminal work of Tomanic *et al.*,[26] this work targets Nb(110) substrates covered with thin Ag buffer layers grown in UHV as a reliable superconducting platform.[26] Using scanning tunneling microscopy (STM) and atomic force microscopy (AFM) at 4.7 K, we investigate Ullmann polymerization of 10,10′-dibromo-9,9′-bianthracene (DBBA) precursors. We characterize the synthesized nanostructures by AFM with CO-terminated tips and confirm proximity-induced superconductivity. We believe our results open a new route towards the study of topological superconductivity in atomically-precise NGs.

Results and Discussion

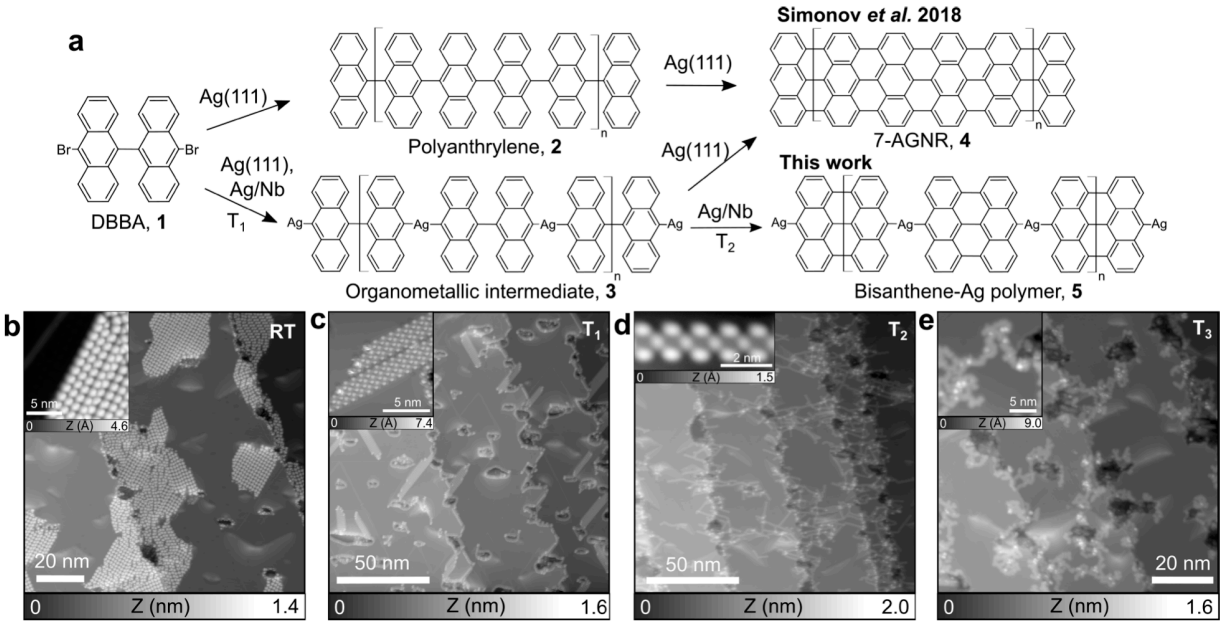

Figure 1: **Bottom-up synthesis of NGs on the superconducting Ag/Nb(110) substrate.** **a,** Hierarchical Ullmann polymerization leading to bisanthene-Ag chains as compared to literature. **b-e,** Series of STM images showing the evolution of surface morphology as a function of substrate temperature. **b,** Sublimating DBBA molecules (**1**) on Ag/Nb(110) leads to extended two-dimensional self-assemblies (I_T= 1 pA, V = 1.8 V. Inset: I_T= 1 pA, V= -1.5 V). **c,** Upon annealing to T_1= 75 °C, molecular domains evolve to one-dimensional stacks of compounds **3** (I_T = 1 pA, V= -1.5 V. Inset: I_T= 1 pA, V= 900 mV). **d,** Annealing to T_2= 300 °C leads to bisanthene-Ag chains **5** (I_T= 1 pA, V= 1.8 V. Inset: I_T= 1 pA, V= 900 mV). **e,** The final thermal treatment to T_3= 390 °C results in small NG domains (I_T = 1 pA, V = 1.9 V. Inset: I_T= 1 pA, V= 2 V).

Our aim is to reproduce Ullmann polymerization of DBBA precursors (compound **1** in Fig. 1a), which leads to 7-carbon-wide armchair GNRs (7-AGNRs) on Ag(111),[21,27] on the superconducting Ag/Nb(110) substrate. To achieve this, we first investigate by STM the growth of Ag thin films on Nb(110) with thicknesses ranging from 0.2 to 5 monolayers (ML) (see Methods in Supplementary Information and Figs. S2, S3). Precursor **1** is then sublimated to the Ag/Nb(110) substrate kept at room temperature, resulting in 2D self-assembled domains located mostly at step edges and defects (Fig. 1b). Upon annealing to T_1 = 75 °C, dehalogenation of **1** is initiated, forming bundles of chains (Fig. 1c). Increasing

the sample temperature to T_2 = 300 °C then results in single polymeric chains (Fig. 1d) while for T_3 = 390 °C, molecular structures appear more curved and fused. The close-up STM image of each sub-product is shown in the insets of Figs. 1b-e. We found the formation of these sub-products are independent of the Ag thickness explored so far.

To better understand the reaction steps, we elucidate the chemical structure of each sub-product using AFM imaging with CO-functionalized tips.[28] Figures 2a and b display AFM images of zigzag and armchair chains respectively (see Figs. S4b and c for corresponding STM images). Both chain configurations are found as intermediates towards 7-AGNRs on noble metal surfaces.[11,21] In our study, we assign both buckled structures to the formation of organometallic (OM) intermediates **3**, which are composed of bianthracene radicals and Ag surface adatoms. Due to the steric hindrance between anthracene moieties, only the topmost phenyl rings can be resolved by AFM (bold lines in the superimposed Kékulé structures of Figs. 2a and b). Our assignment is different from the previous study on Ag(111) using the same precursor,[21] in which the zigzag pattern was confirmed as polyanthrylene **2** after successful dehalogenation of **1** and formation of C-C bonds. We attribute the two different buckling patterns of **3** on Ag/Nb(110) to the accommodation to the distorted lattice of thin (2.5 ML) Ag films.

To enforce cyclodehydrogenation towards GNRs, we further annealed the sample to T_2 = 300 °C. Exemplary STM/AFM images of the resulting product are shown in the inset of Fig. 1d and Fig. 2c. Surprisingly, cyclodehydrogenation only occurs within each bianthracene moiety, but not between adjacent bisanthene monomers (Fig. 2c). By extracting the distance between adjacent bisanthenes, we find the interlinking bond length about 2.51$\pm$0.07 Å, which is too long to be a single C-C bond. Moreover, bright protrusions located at the interlinking position in the STM image (inset of Fig. 1d) indicate conducting species conjugated in between. Based on these observations, we assign the synthesized structure of Fig. 2c to the bisanthene-Ag polymer **5** even though Ag atoms are not clearly resolved by AFM.[29] According to the relaxed structure of **5** on Ag(111) optimized by

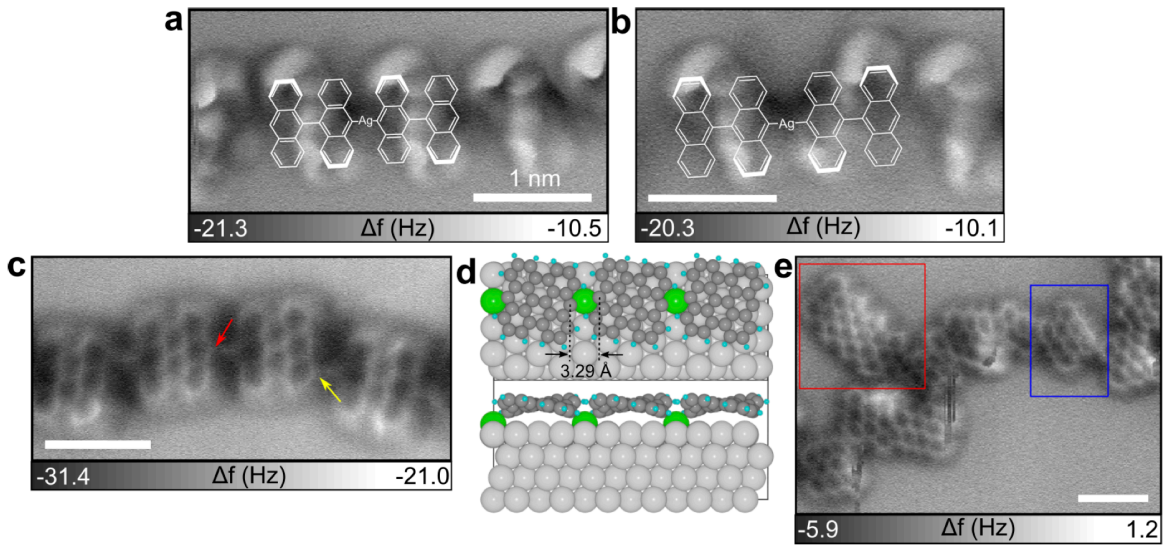

Figure 2: **Structural characterization of reaction sub-products. a,** AFM image of OM intermediates **3** showing a zigzag pattern. **b,** AFM image of the OM intermediates **3** which have an armchair pattern fingerprint in AFM. Bold bonds in the corresponding Kékulé structures of **a** and **b** represent the most protruding part of the chain. Two buckling patterns of **3** might result from the Ag lattice-modulated effect. **c,** AFM image of a bisanthene-Ag chain **5** where each monomer is linked by C-Ag-C bond. **d,** Relaxed structure of the OM intermediate on Ag(111) optimized by DFT. The DFT simulation result shows the distance of 3.29 Å between bisanthene moieties. **e,** AFM image of the irregularly fused bisanthenes (blue) leading to small 7-GNR segments (red) as well as irregular structures. All scale bars are 1 nm.

density function theory (DFT) (Fig. 2d), surface Ag atoms are pulled out, yielding a distance of 3.29 Å between middle peripheral carbons of adjacent bisanthene monomers. This distance is still much larger than our measured bond length (2.51 Å), which might be explained by different lattice configurations of thin Ag films and Ag(111). Besides, the shorter bond length may be caused by intrinsic limits of the AFM technique, such as the tilted CO molecule at the tip apex[30] and slight drift during the slow scan.

With the confirmation of **5**, we stress that intermediate **2** is unlikely to be synthesized at this step of the reaction, since breaking a strong C-C bond between anthracene moieties and forming a much weaker OM (C-Ag) bond is not energetically favorable. Furthermore, bisanthenes are interlinked not only from the middle of the bisanthene edge (red arrow in Fig. 2c) but also from the peripheral carbons (yellow arrow). This observation allows us to

conclude that surface Ag atoms of Ag/Nb(110) are involved in the reaction, causing the Ullmann-type reaction competes with surface-assisted dehydrogenative coupling (non-Ullmann). Noteworthy is the synthesis of **5** from DBBA precursors on Ag/Nb(110), which is novel comparing to previous studies on Ag(111), suggesting that these two substrates do not share the identical catalytic reactivity.[21,27]

Annealing the sample to T_3 = 390 °C promotes a cyclodehydrogenation reaction between neighboring bisanthene monomers, leading to dendritic structures (Fig. 1e) instead of straight GNRs. These structures are irregularly-fused bisanthenes or short GNR segments according to AFM imaging (Fig. 2e), which are similar to those obtained using chlorinated precursors on Au(111).[31] We suggest that the Ag coordination between bisanthene monomers prevents the conventional Ullmann reaction (Fig. 1a) and promotes alternative cyclodehydrogenation processes. Note that we are aware that kinetic factors such as annealing temperature of the substrate[21] or heating rate[27] are key parameters that can influence the reaction towards ordered GNRs. To overcome this, we thus explored various preparation procedures but no significant improvements of Ullmann reaction sub-products have been observed on top of 5 ML Ag. However, on the thicker Ag buffer layer ($\geq$ 5 monolayer), premises of GNR reaction has been obtained with slow annealing rate (Supplementary Information Fig. S8). Despite the large involvement of the substrate, short segments of 7-AGNRs on the thin Ag layer can be occasionally found as marked by the red rectangle in Fig. 2e.

Next, we performed scanning tunneling spectroscopy (STS) on **5** and fused NGs to gain an in-depth understanding of their electronic properties in combination with DFT calculations (see Methods). The proximity-induced superconducting states of **5** was confirmed at 1.3 K (Fig. 3a) as shown by the Bardeen-Cooper-Schrieffer (BCS) fit. In addition, a series of differential conductance ($\mathrm{d}I/\mathrm{d}V$) spectra and $\mathrm{d}I/\mathrm{d}V$ mapping were acquired along the central of **5** (Supplementary Information Fig. S5b) and across a bisanthene monomer (Supplementary Information Fig. S5c). Fig. 3b shows three representative $\mathrm{d}I/\mathrm{d}V$ spectra

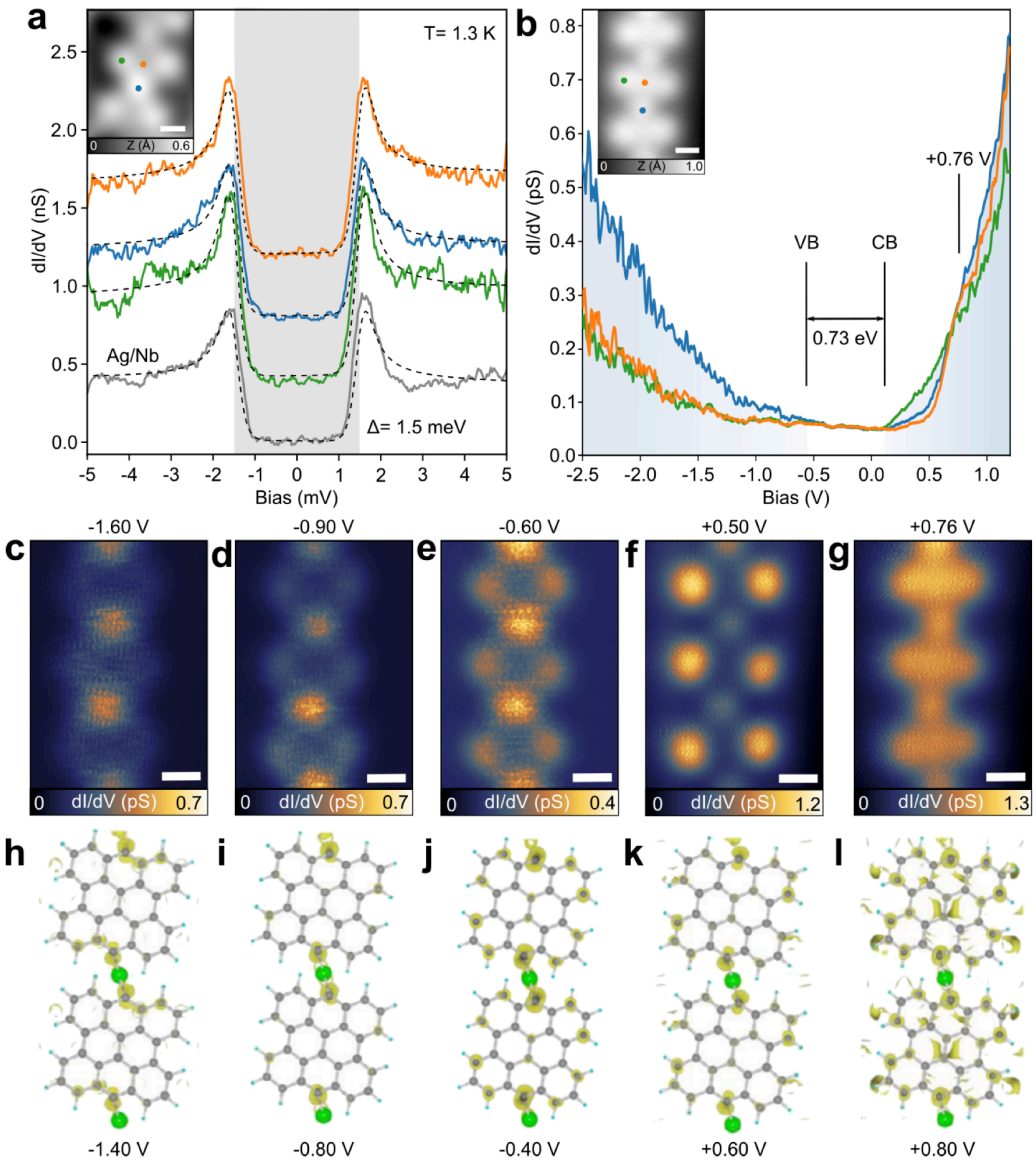

Figure 3: **Experimental and simulated electronic properties of bisanthene-Ag chains 5. a,** Proximity-induced superconductivity on **5** (V= 10 mV, A_{mod}= 50 µV. Inset: I_{t}= 20 pA, V= 760 mV). Shaded area marks the fitted width of the superconducting gap. Spectra are vertically shifted for clarity. **b,** dI/dV spectra measured at three representative positions of the bisanthene chain. Shaded areas refers to the onsets of CB and VB (V= 900 mV, A_{mod}= 20 mV. Inset: I_{t}= 1 pA, V= 900 mV). **c-g,** Series of dI/dV maps at indicated bias. Scale bars of all the images are 5 Å. **h-l,** Simulated DOS of **5** at different energy levels shows consistency with the experimental results in **c-g**.

acquired at positions marked in the inset. Along the chain axis, a shoulder at +0.76 eV is found on bisanthene monomers (orange) and Ag atomic sites (blue) which is absent at

the bisanthene armchair edge (green). The latter has a resonance at +0.13 eV attributed to the conduction band (CB) onset. The frontier resonance of the valence band (VB) onset is assigned to -0.60 eV, allowing to extract an energy gap of about 0.73 eV. In comparison, DFT calculations of the OM structure in gas phase reveal a gap of 1.05 eV in relative agreement with experimental data. Note that the band gap value extracted from STS measurements is typically reduced by an additional electron screening from the underlying metallic surface with respect to the band gap of the gas-phase polymer obtained by DFT.[32]

The $\mathrm{d}I/\mathrm{d}V$ map acquired at +0.50 eV (Fig. 3f) shows an increased density of states (DOS) over bisanthene edges and at Ag atomic sites while centers of bisanthene units are extinguished. The $\mathrm{d}I/\mathrm{d}V$ map above the VB edge (Fig. 3c) shows maxima at Ag atoms and lateral termini of the bisanthene moiety, while the $\mathrm{d}I/\mathrm{d}V$ map acquired at +0.76 eV (Fig. 3g) shows a continuous DOS over the entire chain. Despite the fact that DFT calculations cannot predict correctly the magnitude of the intrinsic band-gap of the polymeric chain, we find that the measured DOS of **5** on Ag/Nb(110) has a similar trend to the calculated frontier orbitals of **5** on Ag(111) for the VB and CB band edges (see Figs. 3h-l and Supplementary Information Fig. S6a), validating the character of the frontier orbitals predicted by DFT.

We last discuss the electronic properties of irregularly fused NGs. $\mathrm{d}I/\mathrm{d}V$ spectra acquired at different positions share almost identical line-shape (Fig. 4a), allowing a gap estimation of 1.58-1.68 eV. We also carry out STS measurements at 560 mK with a metallic tip of the superconducting gap within the NG structure to compare local variations of the proximitized superconducting state (Fig. 4b). Systematic gaps were observed at various positions, which indicate the robustness of the proximity-induced superconductivity. Based on this observation, we also expect to observe the interaction with localized spins at exposed zigzag edges, which may give rise to Yu-Shiba-Rusinov (YSR) states as pairwise peaks within the superconducting gap.[19] From the red and blue spectra in Fig. 4b, asymmetric coherence peaks give some evidence for weak YSR states. Although the emergence

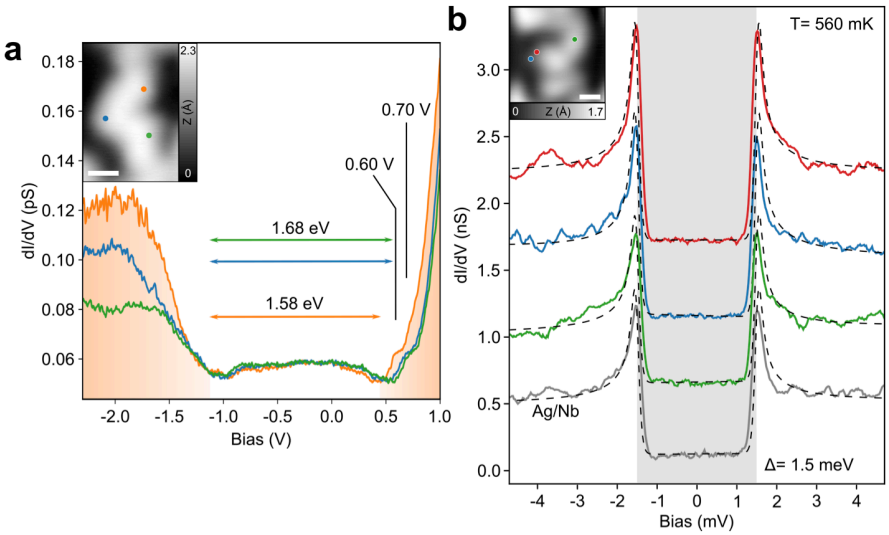

Figure 4: **Proximity-induced superconductivity in fused NG. a,** $\mathrm{d}I/\mathrm{d}V$ spectra showing VB and CB onsets of a NG segment (V= 1.8 V, A_{mod}= 20 mV). The STM image of the target NG is shown in the inset (I_{t}= 1 pA, V= 1.8 V). Green, orange and blue dots in the inset refer to positions of $\mathrm{d}I/\mathrm{d}V$ spectra. **b,** Superconducting gap measurement at different positions of NG in the inset and on Ag/Nb as the comparison (V= 10 mV, A_{mod}= 50 µV. Inset: I_{t}= 50 pA, V= 1.5 V). The estimated widths of superconducting gaps are highlighted by the shaded area, indicating a robust proximity-induced superconductivity on the NG. Curves are vertically shifted for clarity. Scale bars of the insets are 1 nm.

of YSR states on irregularly fused NGs remain uncertain from our experiments, we believe our approach paves the way to introducing superconductivity to atomically-precise nanographene structures.

Conclusion

In conclusion, we fabricated a metal-superconductor heterostructure consisting of a Nb(110) substrate covered by thin Ag films, and find robust proximity-induced superconductivity on the Ag layer.[26] In contrast to the reactive Nb surface, we demonstrated by STM/AFM at low temperature that the Ag buffer layer is compatible with thermal-triggered on-surface reactions, including surface diffusion of molecules, dehalogenation, formation of C-C intra-monomer bonds as well as cyclodehydrogenation. The presence of surface Ag adatoms however alters the reaction pathway as compared to pristine Ag(111)

and can lead to unexpected NG structures such as bisanthene-Ag polymeric chains or fused nanographene. Nevertheless, our results demonstrate an exciting starting point towards the general exploration of exotic electronic states in extended atomically precise NGs or metal-organic frameworks proximitized to a *s*-wave superconductor. This may open new routes towards the emergence of topological superconductivity in carbon-based nanostructures.

Supporting Information

Supporting information: experimental methods, additional results and DFT calculation (PDF).

Acknowledgement

Financial support from the Swiss National Science Foundation (SNSF grant 200021_204053), NCCR SPIN program, and the Swiss Nanoscience Institute (SNI) is gratefully acknowledged. We also thank the European Research Council (ERC) under the European Union's Horizon 2020 research and innovation programme (ULTRADISS Grant Agreement No. 834402). This project is under the scope of the QUSTEC program, which has received funding from the European Union's Horizon 2020 research and innovation program under the Marie Skłodowska-Curie grant number 847471. DFT calculations were financially supported by the SNSF Professorship PP00P2_187185 and performed on UBELIX (http://www.id.unibe.ch/hpc), the HPC cluster at the University of Bern.

Author Contributions

E.M., R.P. and W.W. designed the experiments. P.Z., S.-X.L., R.H. and S.D. synthesized the molecule. J.-C.L. performed STM/AFM experiments and analyzed the data. W.W.

provided the dilution STM and H.C. assisted the measurement. X.W. and U.A. performed the DFT calculations. J.-C.L. wrote the manuscript with the help of R.P. All authors discussed the results and revised the manuscript.

References

(1) Stern, A.; Lindner, N. H. Topological Quantum Computation–From Basic Concepts to First Experiments. *Science* **2013**, *339*, 1179–1184.

(2) Sarma, S. D.; Freedman, M.; Nayak, C. Majorana zero modes and topological quantum computation. *npj Quantum Inf.* **2015**, *1*, 15001.

(3) Fu, L.; Kane, C. L. Superconducting Proximity Effect and Majorana Fermions at the Surface of a Topological Insulator. *Phys. Rev. Lett.* **2008**, *100*, 096407.

(4) Sato, M.; Ando, Y. Topological superconductors: a review. *Rep. Prog. Phys.* **2017**, *80*, 076501.

(5) Lutchyn, R. M.; Bakkers, E. P. a. M.; Kouwenhoven, L. P.; Krogstrup, P.; Marcus, C. M.; Oreg, Y. Majorana zero modes in superconductor–semiconductor heterostructures. *Nature Reviews Materials* **2018**, *3*, 52–68.

(6) Nadj-Perge, S.; Drozdov, I. K.; Li, J.; Chen, H.; Jeon, S.; Seo, J.; MacDonald, A. H.; Bernevig, B. A.; Yazdani, A. Observation of Majorana fermions in ferromagnetic atomic chains on a superconductor. *Science* **2014**, *346*, 602–607.

(7) Ruby, M.; Pientka, F.; Peng, Y.; von Oppen, F.; Heinrich, B. W.; Franke, K. J. End States and Subgap Structure in Proximity-Coupled Chains of Magnetic Adatoms. *Physical Review Letters* **2015**, *115*, 197204.

(8) Pawlak, R.; Kisiel, M.; Klinovaja, J.; Meier, T.; Kawai, S.; Glatzel, T.; Loss, D.; Meyer, E.

Probing atomic structure and Majorana wavefunctions in mono-atomic Fe chains on superconducting Pb surface. *npj Quantum Inf.* **2016**, *2*, 16035.

(9) Kezilebieke, S.; Huda, M. N.; Vaňo, V.; Aapro, M.; Ganguli, S. C.; Silveira, O. J.; Głodzik, S.; Foster, A. S.; Ojanen, T.; Liljeroth, P. Topological superconductivity in a van der Waals heterostructure. *Nature* **2020**, *588*, 424–428.

(10) Jäck, B.; Xie, Y.; Yazdani, A. Detecting and distinguishing Majorana zero modes with the scanning tunnelling microscope. *Nature Reviews Physics* **2021**, *3*, 541–554.

(11) Cai, J.; Ruffieux, P.; Jaafar, R.; Bieri, M.; Braun, T.; Blankenburg, S.; Muoth, M.; Seitsonen, A. P.; Saleh, M.; Feng, X.; Müllen, K.; Fasel, R. Atomically precise bottom-up fabrication of graphene nanoribbons. *Nature* **2010**, *466*, 470–473.

(12) Ruffieux, P.; Wang, S.; Yang, B.; Sánchez-Sánchez, C.; Liu, J.; Dienel, T.; Talirz, L.; Shinde, P.; Pignedoli, C. A.; Passerone, D.; Dumslaff, T.; Feng, X.; Müllen, K.; Fasel, R. On-surface synthesis of graphene nanoribbons with zigzag edge topology. *Nature* **2016**, *531*, 489–492.

(13) Gröning, O.; Wang, S.; Yao, X.; Pignedoli, C. A.; Barin, G. B.; Daniels, C.; Cupo, A.; Meunier, V.; Feng, X.; Narita, A.; Müllen, K.; Ruffieux, P.; Fasel, R. Engineering of robust topological quantum phases in graphene nanoribbons. *Nature* **2018**, *560*, 209–213.

(14) Rizzo, D. J.; Veber, G.; Cao, T.; Bronner, C.; Chen, T.; Zhao, F.; Rodriguez, H.; Louie, S. G.; Crommie, M. F.; Fischer, F. R. Topological band engineering of graphene nanoribbons. *Nature* **2018**, *560*, 204–208.

(15) Rizzo, D. J.; Veber, G.; Jiang, J.; McCurdy, R.; Cao, T.; Bronner, C.; Chen, T.; Louie, S. G.; Fischer, F. R.; Crommie, M. F. Inducing metallicity in graphene nanoribbons via zero-mode superlattices. *Science* **2020**, *369*, 1597–1603.

(16) Mishra, S.; Beyer, D.; Berger, R.; Liu, J.; Gröning, O.; Urgel, J. I.; Müllen, K.; Ruffieux, P.; Feng, X.; Fasel, R. Topological Defect-Induced Magnetism in a Nanographene. *Journal of the American Chemical Society* **2020**, *142*, 1147–1152.

(17) Li, J.; Sanz, S.; Corso, M.; Choi, D. J.; Peña, D.; Frederiksen, T.; Pascual, J. I. Single spin localization and manipulation in graphene open-shell nanostructures. *Nature Communications* **2019**, *10*, 200.

(18) Mishra, S.; Catarina, G.; Wu, F.; Ortiz, R.; Jacob, D.; Eimre, K.; Ma, J.; Pignedoli, C. A.; Feng, X.; Ruffieux, P.; Fernández-Rossier, J.; Fasel, R. Observation of fractional edge excitations in nanographene spin chains. *Nature* **2021**, *598*, 287–292.

(19) Río, E. C.-d.; Lado, J. L.; Cherkez, V.; Mallet, P.; Veuillen, J.-Y.; Cuevas, J. C.; Gómez-Rodríguez, J. M.; Fernández-Rossier, J.; Brihuega, I. Observation of Yu–Shiba–Rusinov States in Superconducting Graphene. *Advanced Materials* **2021**, *33*, 2008113.

(20) Högl, P.; Frank, T.; Kochan, D.; Gmitra, M.; Fabian, J. Chiral Majorana fermions in graphene from proximity-induced superconductivity. *Physical Review B* **2020**, *101*, 245441.

(21) Simonov, K. A.; Generalov, A. V.; Vinogradov, A. S.; Svirskiy, G. I.; Cafolla, A. A.; McGuinness, C.; Taketsugu, T.; Lyalin, A.; Mårtensson, N.; Preobrajenski, A. B. Synthesis of armchair graphene nanoribbons from the 10,10′-dibromo-9,9′-bianthracene molecules on Ag(111): the role of organometallic intermediates. *Sci. Rep.* **2018**, *8*, 3506.

(22) Kolmer, M.; Steiner, A.-K.; Izydorczyk, I.; Ko, W.; Engelund, M.; Szymonski, M.; Li, A.-P.; Amsharov, K. Rational synthesis of atomically precise graphene nanoribbons directly on metal oxide surfaces. *Science* **2020**, *369*, 571–575.

(23) Natterer, F. D.; Ha, J.; Baek, H.; Zhang, D.; Cullen, W. G.; Zhitenev, N. B.; Kuk, Y.; Stroscio, J. A. Scanning tunneling spectroscopy of proximity superconductivity in epitaxial multilayer graphene. *Physical Review B* **2016**, *93*, 045406.

(24) Tonnoir, C.; Kimouche, A.; Coraux, J.; Magaud, L.; Delsol, B.; Gilles, B.; Chapelier, C. Induced Superconductivity in Graphene Grown on Rhenium. *PRL* **2013**, *111*, 246805.

(25) Mazaleyrat, E.; Vlaic, S.; Artaud, A.; Magaud, L.; Vincent, T.; Gómez-Herrero, A. C.; Lisi, S.; Singh, P.; Bendiab, N.; Guisset, V.; David, P.; Pons, S.; Roditchev, D.; Chapelier, C.; Coraux, J. How to induce superconductivity in epitaxial graphene via remote proximity effect through an intercalated gold layer. *2D Materials* **2020**, *8*, 015002.

(26) Tomanic, T.; Schackert, M.; Wulfhekel, W.; Sürgers, C.; v. Löhneysen, H. Two-band superconductivity of bulk and surface states in Ag thin films on Nb. *Phys. Rev. B* **2016**, *94*, 220503.

(27) Jacobse, P. H.; Simonov, K. A.; Mangnus, M. J. J.; Svirskiy, G. I.; Generalov, A. V.; Vinogradov, A. S.; Sandell, A.; Mårtensson, N.; Preobrajenski, A. B.; Swart, I. One Precursor but Two Types of Graphene Nanoribbons: On-Surface Transformations of 10,10′-Dichloro-9,9′-bianthryl on Ag(111). *J. Phys. Chem. C* **2019**, *123*, 8892–8901.

(28) Gross, L.; Mohn, F.; Moll, N.; Liljeroth, P.; Meyer, G. The Chemical Structure of a Molecule Resolved by Atomic Force Microscopy. *Science* **2009**, *325*, 1110–1114.

(29) Schulz, F.; Jacobse, P. H.; Canova, F. F.; van der Lit, J.; Gao, D. Z.; van den Hoogenband, A.; Han, P.; Gebbink, R. J. K.; Moret, M.-E.; Joensuu, P. M.; Swart, I.; Liljeroth, P. Precursor Geometry Determines the Growth Mechanism in Graphene Nanoribbons. *J. Phys. Chem. C* **2017**, *121*, 2896–2904.

(30) Gross, L.; Mohn, F.; Moll, N.; Schuler, B.; Criado, A.; Guitián, E.; Peña, D.; Gourdon, A.; Meyer, G. Bond-Order Discrimination by Atomic Force Microscopy. *Science* **2012**, *337*, 1326–1329.

(31) Jacobse, P. H.; van den Hoogenband, A.; Moret, M.-E.; Klein Gebbink, R. J. M.; Swart, I. Aryl Radical Geometry Determines Nanographene Formation on Au(111). *Angew. Chem. Int. Ed.* **2016**, *55*, 13052–13055.

(32) Neaton, J. B.; Hybertsen, M. S.; Louie, S. G. Renormalization of Molecular Electronic Levels at Metal-Molecule Interfaces. *Phys. Rev. Lett.* **2006**, *97*.

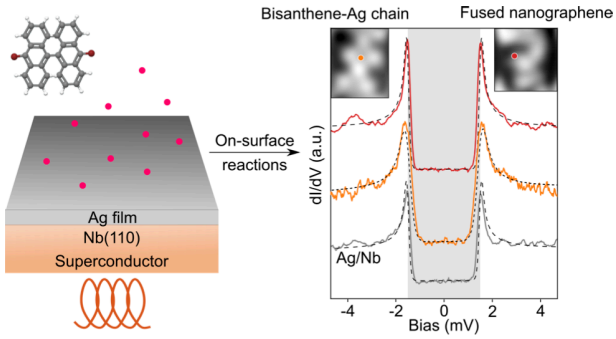

Figure 5: **For Table of Contents Only**

6.2.3.2 Synthesis of a covalently linked 2D porphyrin network

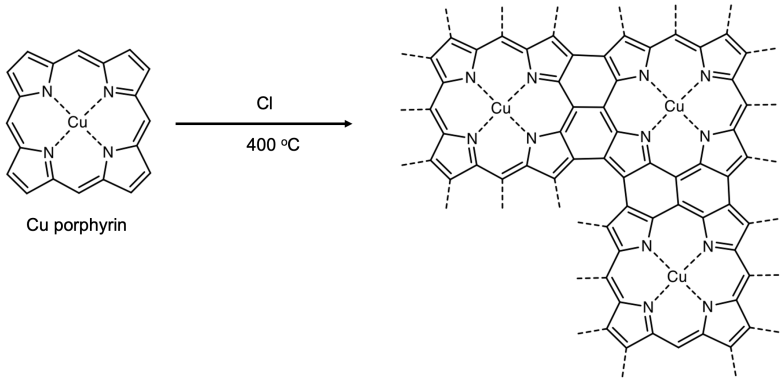

Scheme 1 Hydrogen elimination of Cu-porphyrin

The surfaces of coinage metal single crystals under ultra-high vacuum (UHV) conditions allow for unique chemical reactions to occur.[118] One such reaction seen on Au(111) surface is the chlorine-induced hydrogen elimination from planar aromatic molecules.[119] Here, the Cl atoms can be used to facilitate the cleavage of the C-H bonds at the edges of the aromatic molecules and due to the UHV conditions, the resulting loss of hydrogen atoms is irreversible. This leads to the formation of σ-radicals along the edges of the molecules.

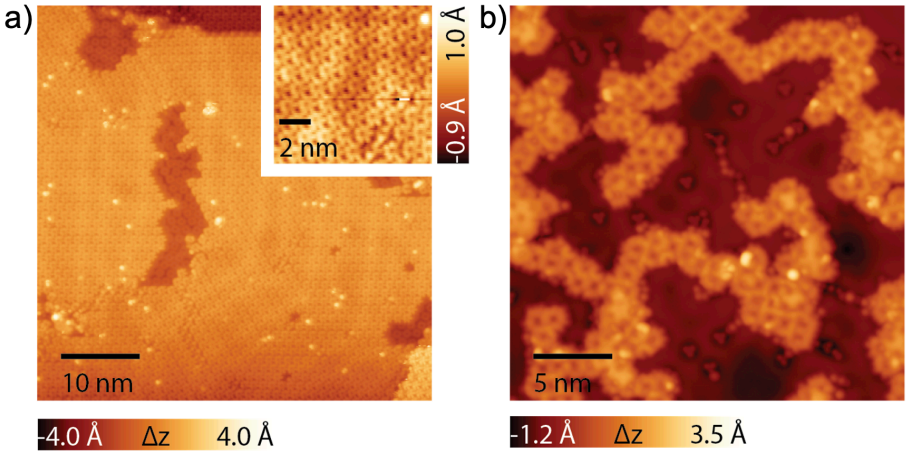

Figure 1 a) STM image of a bilayer of Cu-P molecules on Au(111) surface. (Tunneling parameters: 1.5 V, 20 pA). Inset: Higher magnification of the self-assembly of the top layer of the Cu-P molecules (1.5 V, 20 pA). **b**) Exposing the Cu-P molecules on Au(111) at 400 °C to a flux of chlorine leads to the elimination of hydrogen from their edges and their fusion to form a covalently linked network. (0.5 V, 50 pA).

Here we deposit a bilayer of Cu (II) porphyrin (Cu-P) on to a cleaned Au(111) surface. The surface is then imaged using a scanning tunneling microscope (STM) operating at 4.5 K, revealing the self-assembled Cu-P molecules (**Figure 1a**). Hydrogen elimination is achieved

by annealing the surface to 400 °C and exposing it to a flux of chlorine (generated by sublimating AuCl). This strips the hydrogen atoms from the Cu-P and the resulting σ-radicals are found passivated by the formation of organo-metallic bonds with the gold substrate, by the formation of C-Cl bonds with any present Cl on the surface, or by inter-molecular coupling reactions (**Figure 1b**). Controlled fusion of the Cu-P molecules could be used to generate a 2-D network of porphyrins. Due to the spin-spin interaction between Cu atoms mediated by the porphyrin network, such a 2D material may have interesting magnetic properties.

6.2.3.3 Synthesis of a Cu porphyrin-fused zigzag graphene nanoribbon

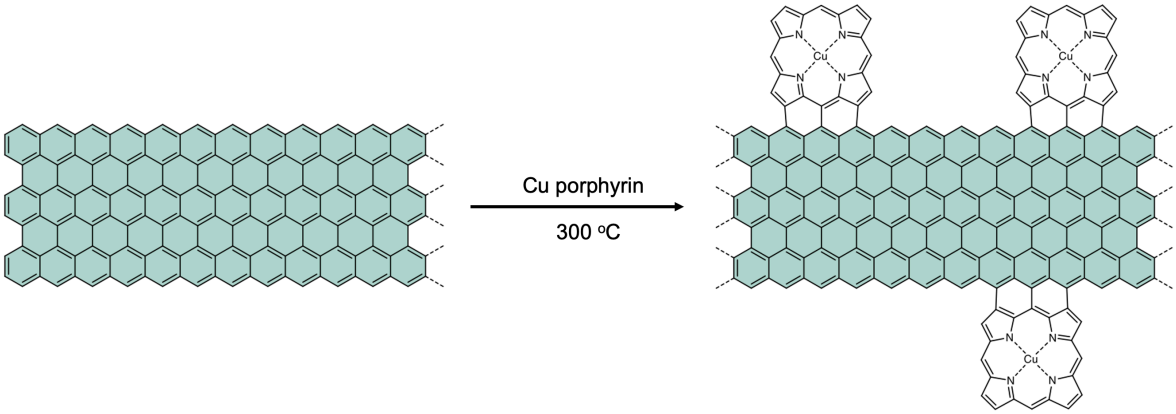

Scheme 2: Synthesis of a Cu-P-fused 6-ZGNR.

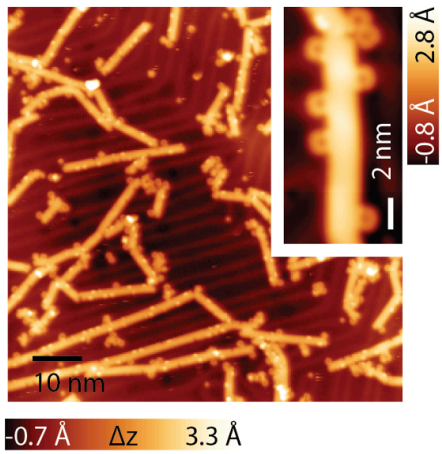

Figure 2 STM images of Cu-P-fused 6-ZGNRs. (-1.5 V, 100 pA inset: -0.9 V, 100 pA)

The atomically precise synthesis of graphene nanoribbons[120] (GNRs) and in particular the synthesis of 6-atom wide zigzag-edged GNR[121] (6-ZGNR) are keystone achievements of on-surface synthesis. ZGNRs pose spin-polarized edge states[122] which can mediate interactions between spins. Here, 6-ZGNRs are synthesized on Au(111). Cu-P is then deposited on the

surface, and the surface is then annealed to 300 °C. This leads to the fusion of the porphyrin with the ZGNR. However, the fusion is not site-specific along the ZGNR. This yields structures with a random positioning of the porphyrins along the zigzag edges (**Figure 2**).

6.2.3.4 The surface-assisted polymerization of TBTP and its counterpart tetrabromo-pyrene

This work is currently under investigation.

Bibliography

1. Brolos, L.; Kilde, M. D.; Hammerich, O.; Nielsen, M. B., Toward Redox-Active Indenofluorene-Extended Tetrathiafulvalene Oligomers-Synthesis and Studies of Dimeric Scaffolds. *J. Org. Chem.*, **2020**, *85* (5), 3277-3286.

2. Jana, A.; Ishida, M.; Park, J. S.; Bahring, S.; Jeppesen, J. O.; Sessler, J. L., Tetrathiafulvalene- (TTF-) Derived Oligopyrrolic Macrocycles. *Chem. Rev.*, **2017**, *117* (4), 2641-2710.

3. Bergkamp, J. J.; Decurtins, S.; Liu, S. X., Current Advances in Fused Tetrathiafulvalene Donor-Acceptor Systems. *Chem. Soc. Rev.*, **2015**, *44* (4), 863-874.

4. Rivadehi, S.; Reid, E. F.; Hogan, C. F.; Bhosale, S. V.; Langford, S. J., Fluoride-Selective Optical Sensor Based on the Dipyrrolyl-Tetrathiafulvalene Chromophore. *Org. Biomol. Chem.*, **2012**, *10* (4), 705-709.

5. Jia, H. P.; Forgie, J. C.; Liu, S. X.; Sanguinet, L.; Levillain, E.; Le Derf, F.; Salle, M.; Neels, A.; Skabara, P. J.; Decurtins, S., Tetrathiafulvalene-Annulated Dipyrrolylquinoxaline: the Effect of Fluoride on its Optical and Electrochemical Behaviors. *Tetrahedron*, **2012**, *68* (5), 1590-1594.

6. Jia, C.; Liu, S. X.; Tanner, C.; Leiggener, C.; Sanguinet, L.; Levillain, E.; Leutwyler, S.; Hauser, A.; Decurtins, S., A Redox-Active Tri-star Molecule: Merging of TTF and HAT Chemistry. *Chem. Commun.*, **2006**, (17), 1878-1880.

7. Jia, H. P.; Liu, S. X.; Sanguinet, L.; Levillain, E.; Decurtins, S., Star-shaped Tetrathiafulvalene-Fused Coronene with Large π-Extended Conjugation. *J. Org. Chem.*, **2009**, *74* (15), 5727-5729.

8. Liu, B.; Bockmann, M.; Jiang, W.; Doltsinis, N. L.; Wang, Z., Perylene Diimide-Embedded Double [8]Helicenes. *J. Am. Chem. Soc.*, **2020**, *142* (15), 7092-7099.

9. Bhosale, S. V.; Al Kobaisi, M.; Jadhav, R. W.; Morajkar, P. P.; Jones, L. A.; George, S., Naphthalene Diimides: Perspectives and Promise. *Chem. Soc. Rev.*, **2021**, *50* (17), 9845-9998.

10. Tan, L. X.; Guo, Y. L.; Yang, Y.; Zhang, G. X.; Zhang, D. Q.; Yu, G.; Xu, W.; Liu, Y. Q., New Tetrathiafulvalene Fused-Naphthalene Diimides for Solution-Processible and Air-Stable p-Type and Ambipolar Organic Semiconductors. *Chem. Sci.*, **2012**, *3* (8), 2530-2541.

11. Jaggi, M.; Blum, C.; Dupont, N.; Grilj, J.; Liu, S. X.; Hauser, J.; Hauser, A.; Decurtins, S., A Compactly Fused π-Conjugated Tetrathiafulvalene-Perylenediimide Donor-Acceptor Dyad. *Org. Lett.*, **2009**, *11* (14), 3096-3099.

12. Pfattner, R.; Pavlica, E.; Jaggi, M.; Liu, S.-X.; Decurtins, S.; Bratina, G.; Veciana, J.; Mas-Torrent, M.; Rovira, C., Photo-Induced Intramolecular Charge Transfer in an Ambipolar Field-Effect Transistor Based on a π-Conjugated Donor-Acceptor Dyad. *J. Mater. Chem. C*, **2013**, *1* (25), 3985–3988.

13. Jaggi, M.; Blum, C.; Marti, B. S.; Liu, S. X.; Leutwyler, S.; Decurtins, S., Annulation of Tetrathiafulvalene to the Bay Region of Perylenediimide. *Org. Lett.*, **2010**, *12* (6), 1344-1347.

14. Geib, S.; Martens, S. C.; Zschieschang, U.; Lombeck, F.; Wadepohl, H.; Klauk, H.; Gade, L. H., 1,3,6,8-Tetraazapyrenes: Synthesis, Solid-State Structures, and Properties as Redox-Active Materials. *J. Org. Chem.*, **2012**, *77* (14), 6107-6116.

15. Martens, S. C.; Hahn, L.; Lombeck, F.; Rybina, A.; Wadepohl, H.;Gade, L. H., Annulated Heterocyclic Derivatives of 1,3,6,8-Tetraazapyrene. *Eur. J. Org. Chem.*, **2013**, *2013* (24), 5295-5302.

16. Sienkowska, M. J.; Farrar, J. M.; Zhang, F.; Kusuma, S.; Heiney, P. A.; Kaszynski, P., Liquid Crystalline Behavior of Tetraaryl Derivatives of Benzo[c]cinnoline, Tetraazapyrene, Phenanthrene, and Pyrene: the Effect of Heteroatom and Substitution Pattern on Phase Stability. *J. Mater. Chem.*, **2007**, *17* (14), 1399-1411.

17. Shi, Y. R.; Wei, H. L.; Liu, Y. F., The Role of Electron-Attracting Substituents and Molecular Stacking Motifs in the Charge Transport of Tetraazapyrene Derivatives. *New J. Chem.*, **2019**, *43* (15), 5706-5718.

18. Otsuka,Y.; Hojo, N.; Yoshida, J. I.; Nokami,T.; Shimizu, A. Electrode Active Material for Power Storage Device. **2015**. Pub. No.: US 2015/0295244 A1.

19. Otto Dimroth, H. R., Das Naphtazarin und das 5,6-Dioxy-l,4-Naphtochinon. *Liebigs Ann. Chem.*, **1927**, *456*, 177-192.

20. Gerson, F., Die ESR.-Spektren der Radikal-Ionen des 1,3,6,8-Tetraazapyrens. *Helvetica Chimica Acta*., **1964**, *47*, 1484-1496.

21. Dawans, F.; Marvel, C. S.;Reichel, B., 2,7-Disubstituted 1,3,6,8-Tetraazopyrene and Related Polymers. *J Polym Sci A*, **1964**, *2*, 5005-5016.

22. Vitske, V.; König, C.; Hübner, O.; Kaifer, E.; Himmel, H. J., Syntheses of the First Coordination Compounds of the New Strong Molecular Electron Donor and Double Proton

Sponge 1,4,5,8-Tetrakis(tetramethylguanidino)naphthalene. *Eur. J. Inorg. Chem.*, **2009**, *2010* (1), 115-126.

23. Langis-Barsetti, S.; Maris, T.; Wuest, J. D., Synthesis of Salts of 1,2,5,6- and 1,4,5,8-Naphthalenetetramine. *ACS Omega*, **2017**, *2* (9), 6023-6030.

24. Aksenov, A. V.; Ovcharov, D. S.; Aksenov, N. A.; Aksenov, D. A.; Nadein, O. N.; Rubin, M., Dual Role of Polyphosphoric Acid-Activated Nitroalkanes in Oxidative Peri-Annulations: Efficient Synthesis of 1,3,6,8-Tetraazapyrenes. *RSC Adv.*, **2017**, *7* (48), 29927-29932.

25. Beer, M.; Longuethiggins, H. C., Anomalous Light Emission of Azulene. *J. Chem. Phys.,* **1955**, *23* (8), 1390-1391.

26. Shevyakov, S. V.; Li, H. R.; Muthyala, R.; Asato, A. E.; Croney, J. C.; Jameson, D. M.; Liu, R. S. H., Orbital Control of the Color and Excited State Properties of Formylated and Fluorinated Derivatives of Azulene. *J. Phys. Chem. A*, **2003**, *107* (18), 3295-3299.

27. Cowper, P.; Pockett, A.; Kociok-Köhn, G.; Cameron, P. J.; Lewis, S. E., Azulene - Thiophene - Cyanoacrylic Acid Dyes with Donor-π-Acceptor Sructures. Synthesis, Characterisation and Evaluation in Dye-Sensitized Solar Cells. *Tetrahedron*, **2018**, *74* (22), 2775-2786.

28. Ziegler, K.; Hafner, K., Eine Rationelle Synthese Des Azulens. *Angew. Chem. Int. Ed.*, **1955**, *67* (11), 301-301.

29. Yang, PW.; Yasunami, M.; Takase, K., The Formation of Azulene Derivatives by the Reaction of 2H-Cyclohepta[b]furan-2-Ones with Enamines. *Tetrahedron Lett.*, **1971**, *12* (45), 4275-4278.

30. Amir, E.; Amir, R. J.; Campos, L. M.; Hawker, C. J., Stimuli-Responsive Azulene-Based Conjugated Oligomers with Polyaniline-like Properties. *J. Am. Chem. Soc.*, **2011**, *133* (26), 10046-10049.

31. Kurotobi, K.; Tabata, H.; Miyauchi, M.; Murafuji, T.; Sugihara, Y., Coupling Reaction of Azulenyl-4,4,5,5-Tetramethyl-1,3,2-Dioxaborolanes with Haloazulenes. *Sci. Synth.*, **2002**, (8), 1013-1016.

32. Cowper, P.; Jin, Y.; Turton, M. D.; Kociok-Kohn, G.; Lewis, S. E., Azulenesulfonium Salts: Accessible, Stable, and Versatile Reagents for Cross-Coupling. *Angew. Chem. Int. Ed.*, **2016**, *55* (7), 2564-2568.

33. Dyker, G.; Borowski, S.; Heiermann, J.; Korning, J.; Opwis, K.; Henkel, G.; Kockerling, M., First Intermolecular Palladium Catalyzed Arylation of an Unfunctionalized Aromatic Hydrocarbon. *J. Organomet. Chem.,* **2000**, *606* (2), 108-111.

34. Ho, T. I.; Ku, C. K.; Liu, S. H., Preparation of 1-Arylazulenes through Regioselective Photoarylation of Azulene with Aryl Iodides. *Tetrahedron Lett.*, **2001**, *42* (4), 715-717.

35. Nozoe, T.; Seto, S.; Matsumura, S., Synthesis of 2-Substituted Azulenes by Nucleophilic Substitution Reactions of 2-Haloazulene Derivatives. *Bull. Chem. Soc. Jpn.*, **1962**, *35* (12), 1990-1998.

36. Kurotobi, K.; Tabata, H.; Miyauchi, M.; Mustafizur, R. A. F. M.; Migita, K.; Murafuji, T.; Sugihara, Y.; Shimoyama, H.; Fujimori, K., The First Generation of Azulenyl-Lithium and - Magnesium: A Novel, Versatile Method of Introducing a Substituent at the 2-Position of an Azulene Skeleton. *Synthesis-Stuttgart*, **2003**, (1), 30-34.

37. Kurotobi, K.; Miyauchi, M.; Takakura, K.; Murafuji, T.; Sugihara, Y., Direct Introduction of a Boryl Substituent into the 2-Position of Azulene: Application of the Miyaura and Smith Methods to Azulene. *Eur. J. Org. Chem.*, **2003**, *2003* (18), 3663-3665.

38. Murai, M.; Takami, K.; Takeshima, H.; Takai, K., Iridium-Catalyzed Dehydrogenative Silylation of Azulenes Based on Regioselective C-H Bond Activation. *Org. Lett.*, **2015**, *17* (7), 1798-801.

39. Fujinaga, M.; Murafuji, T.; Kurotobi, K.; Sugihara, Y., Polyborylation of Azulenes. *Tetrahedron*, **2009**, *65* (34), 7115-7121.

40. Ito, S.; Kubo, T.; Morita, N.; Matsui, Y.; Watanabe, T.; Ohta, A.; Fujimori, K.; Murafuji, T.; Sugihara, Y.; Tajiri, A., Preparation of Azulenyllithium and Magnesium Reagents Utilizing Halogen-Metal Exchange Reaction of Several Iodoazulenes with Organolithium or Magnesium ate Complex. *Tetrahedron Lett.*, **2004**, *45* (14), 2891-2894.

41. Fukazawa, M.; Takahashi, F.; Yorimitsu, H., Sodium-Promoted Borylation of Polycyclic Aromatic Hydrocarbons. *Org. Lett.*, **2021**, *23* (12), 4613-4617.

42. Zimmerman, H. E., A Mechanistic Analysis of the Birch Reduction. *Acc. Chem. Res.*, **2012**, *45* (2), 164-170.

43. Shibuya, Y.; Aonuma, K.; Kimura, T.; Kaneko, T.; Fujiwara, W.; Yamaguchi, Y.; Kumaki, D.; Tokito, S.; Katagiri, H., Linear Biazulene Isomers: Effects of Molecular and Packing Structure on Optoelectronic and Charge-Transport Properties. *J. Phys. Chem. C*, **2020**, *124* (8), 4738-4746.

44. Yamaguchi, Y.; Takubo, M.; Ogawa, K.; Nakayama, K.; Koganezawa, T.; Katagiri, H., Terazulene Isomers: Polarity Change of OFETs through Molecular Orbital Distribution Contrast. *J. Am. Chem. Soc.*, **2016**, *138* (35), 11335-11343.

45. Yamaguchi, Y.; Ogawa, K.; Nakayama, K.; Ohba, Y.; Katagiri, H., Terazulene: a High-Performance n-Type Organic Field-Effect Transistor Based on Molecular Orbital Distribution Control. *J. Am. Chem. Soc.*, **2013**, *135* (51), 19095-19098.

46. Murai, M.; Iba, S.; Ota, H.; Takai, K., Azulene-Fused Linear Polycyclic Aromatic Hydrocarbons with Small Bandgap, High Stability, and Reversible Stimuli Responsiveness. *Org. Lett.*, **2017**, *19* (20), 5585-5588.

47. Murai, M.; Amir, E.; Amir, R. J.; Hawker, C. J., Azulene-Based Conjugated Polymers: Unique Seven-Membered Ring Connectivity Leading to Stimuli-Responsiveness. *Chem. Sci.*, **2012**, *3* (9), 2721-2725.

48. Xin, H.; Ge, C.; Yang, X.; Gao, H.; Yang, X.; Gao, X., Biazulene Diimides: a New Building Block for Organic Electronic Materials. *Chem. Sci.*, **2016**, *7* (11), 6701-6705.

49. Xin, H. S.; Ge, C. W.; Fu, L. N.; Yang, X. D.; Gao, X. K., Naphthalene Diimides Endcapped with Ethynylazulene: Molecular Design, Synthesis and Properties. *Chin. J. Org. Chem.*, **2017**, *37* (3), 711-719.

50. Koide, T.; Takesue, M.; Murafuji, T.; Satomi, K.; Suzuki, Y.; Kawamata, J.; Terai, K.; Suzuki, M.; Yamada, H.; Shiota, Y.; Yoshizawa,K.; Tani,F.; An Azulene-Fused Tetracene Diimide with a Small HOMO–LUMO Gap. *ChemPlusChem*, **2017**, *82*, 1010-1014.

51. Ran, H.; Duan, X.; Zheng, R.; Xie, F.; Chen, L.; Zhao, Z.; Han, R.; Lei, Z.; Hu, J. Y., Two Isomeric Azulene-Decorated Naphthodithiophene Diimide-Based Triads: Molecular Orbital Distribution Controls Polarity Change of OFETs Through Connection Position. *ACS Appl. Mater. Interfaces*, **2020**, *12* (20), 23225-23235.

52. Yao, J. J.; Cai, Z. X.; Liu, Z. T.; Yu, C. M.; Luo, H. W.; Yang, Y.; Yang, S. F.; Zhang, G. X.; Zhang, D. Q., Tuning the Semiconducting Behaviors of New Alternating Dithienyldiketopyrrolopyrrole-Azulene Conjugated Polymers by Varying the Linking Positions of Azulene. *Macromolecules*, **2015**, *48* (7), 2039-2047.

53. Horrocks, D. L.; Brown, W. G., Solution Fluorescence Spectrum of Highly Purified Fluorene. *Chem. Phys. Lett.*, **1970**, *5* (2), 117-119.

54. Wang, X. B.; Ng, J. K. P.; Jia, P. T.; Lin, T. T.; Cho, C. M.; Xu, J. W.; Lu, X. H.; He, C. B., Synthesis, Electronic, and Emission Spectroscopy, and Electrochromic Characterization of Azulene-Fluorene Conjugated Oligomers and Polymers. *Macromolecules*, **2009**, *42* (15), 5534-5544.

55. Tsurui, K.; Murai, M.; Ku, S. Y.; Hawker, C. J.; Robb, M. J., Modulating the Properties of Azulene-Containing Polymers through Controlled Incorporation of Regioisomers. *Adv. Funct. Mater.*, **2014**, *24* (46), 7338-7347.

56. Tang, T.; Lin, T.; Wang, F.; He, C., Azulene-Based Conjugated Polymers with Tuneable Near-IR Absorption up to 2.5 μm. *Polym. Chem.*, **2014**, *5* (8), 2980-2989.

57. Brown, C. J.; Farthing, A. C., Preparation and Structure of Di-P-Xylylene. *Nature*, **1949**, *164* (4178), 915-916.

58. Hassan, Z.; Spuling, E.; Knoll, D. M.; Brase, S., Regioselective Functionalization of [2,2]Paracyclophanes: Recent Synthetic Progress and Perspectives. *Angew. Chem. Int. Ed.*, **2020**, *59* (6), 2156-2170.

59. Elacqua, E.; MacGillivray, L. R., From the Decks to the Bridges: Optoelectronics in [2,2]Paracyclophane Chemistry. *Eur. J. Org. Chem.*, **2010**, *2010* (36), 6883-6894.

60. Tatemitsu, H.; Natsume, B.; Yoshida, M.; Sakata, Y.; Misumi, S., Double-Layered and Triple-Layered Charge-Transfer Cyclophanes Containing Tetracyanoquinodimethane and Dimethoxybenzene Groups. *Tetrahedron Lett.*, **1978**, (37), 3459-3462.

61. Watanabe, M.; Goto, K.; Shibahara, M.; Shinmyozu, T., Synthesis, Structure, and Electronic and Photophysical Properties of Two-and Three-Layered [3,3]Paracyclophane-Based Donor-Acceptor Systems. *J. Org. Chem.*, **2010**, *75* (18), 6104-6114.

62. Sako, K.; Hasegawa, T.; Onda, H.; Shiotsuka, M.; Watanabe, M.; Shinmyozu, T.; Tojo, S.; Fujitsuka, M.; Majima, T.; Hirao, Y.; Kubo, T.; Iwanaga, T.; Toyota, S.; Takemura, H., Donor-Donor'-Acceptor Triads Based on [3,3]Paracyclophane with a 1,4-Dithiafulvene Donor and a Cyanomethylene Acceptor: Synthesis, Structure, and Electrochemical and Photophysical Properties. *Chem. Eur. J.*, **2018**, *24* (44), 11407-11416.

63. Miyazaki, T.; Shibahara, M.; Fujishige, J.; Watanabe, M.; Goto, K.; Shinmyozu, T., Synthesis and Electronic and Photophysical Properties of [2,2]- and [3,3]Paracyclophane-Based Donor-Donor'-Acceptor Triads. *J. Org. Chem.*, **2014**, *79* (23), 11440-11453.

64. Huang, C. H.; Chang, Y. J., Dyes for Sensitized Solar Cells by Using [2,2]Paracyclophane as a Bridging Unit. *Tetrahedron Lett.*, **2014**, *55* (35), 4938-4942.

65. Spuling, E.; Sharma, N.; Samuel, I. D. W.; Zysman-Colman, E.; Brase, S., (Deep) Blue through-Space Conjugated TADF Emitters based on [2,2]Paracyclophanes. *Chem. Commun.*, **2018**, *54* (67), 9278-9281.

66. Chang, Y. J.; Watanabe, M.; Chou, P. T.; Chow, T. J., [2,2]Paracyclophane as a Bridging Unit in the Design of Organic Dyes for Sensitized Solar Cells. *Chem. Commun.*, **2012**, *48* (5), 726-728.

67. Hirayama, F., Intramolecular Excimer Formation. I. Diphenyl and Triphenyl Alkanes. *The J. Chem. Phys.*, **1965**, *42* (9), 3163-3171.

68. Fujitsuka, M.; Miyazaki, T.; Lu, C.; Shinmyozu, T.; Majima, T., Multistep Electron Transfer Systems Containing [2,2]- or [3,3]Paracyclophane. *J. Phys. Chem. A*, **2016**, *120* (8), 1184-1189.

69. Kaiser, C.; Schmiedel, A.; Holzapfel, M.; Lambert, C., Long-Lived Singlet and Triplet Charge Separated States in Small Cyclophane-Bridged Triarylamine-Naphthalene Diimide Dyads. *J. Phys. Chem. C*, **2012**, *116* (29), 15265-15280.

70. Wang, T.; Zhu, J. F., Confined on-Surface Organic Synthesis: Strategies and Mechanisms. *Surf. Sci. Rep.*, **2019**, *74* (2), 97-140.

71. Cai, J.; Ruffieux, P.; Jaafar, R.; Bieri, M.; Braun, T.; Blankenburg, S.; Muoth, M.; Seitsonen, A. P.; Saleh, M.; Feng, X.; Mullen, K.; Fasel, R., Atomically Precise Bottom-up Fabrication of Graphene Nanoribbons. *Nature*, **2010**, *466* (7305), 470-473.

72. Sanchez-Sanchez, C.; Dienel, T.; Deniz, O.; Ruffieux, P.; Berger, R.; Feng, X.; Mullen, K.; Fasel, R., Purely Armchair or Partially Chiral: Noncontact Atomic Force Microscopy Characterization of Dibromo-Bianthryl-Based Graphene Nanoribbons Grown on Cu(111). *ACS nano*, **2016**, *10* (8), 8006-8011.

73. Gao, H. Y.; Franke, J. H.; Wagner, H.; Zhong, D. Y.; Held, P. A.; Studer, A.; Fuchs, H., Effect of Metal Surfaces in On-Surface Glaser Coupling. *J. Phys. Chem. C*, **2013**, *117* (36), 18595-18602.

74. Eichhorn, J.; Heckl, W. M.; Lackinger, M., On-surface Polymerization of 1,4-Diethynylbenzene on Cu(111). *Chem. Commun.*, **2013**, *49* (28), 2900-2902.

75. Pawlak, R.; Liu, X.; Ninova, S.; D'Astolfo, P.; Drechsel, C.; Sangtarash, S.; Häner, R.; Decurtins, S.; Sadeghi, H.; Lambert, C. J.; Aschauer, U.; Liu, S. X.; Meyer, E., Bottom-up Synthesis of Nitrogen-Doped Porous Graphene Nanoribbons. *J. Am. Chem. Soc.*, **2020**, *142* (29), 12568-12573.

76. Pawlak, R.; Liu, X.; Ninova, S.; D'Astolfo, P.; Drechsel, C.; Liu, J. C.; Häner, R.; Decurtins, S.; Aschauer, U.; Liu, S. X.; Meyer, E., On-Surface Synthesis of Nitrogen-Doped Kagome Graphene. *Angew. Chem. Int. Ed.*, **2021**, *60* (15), 8370-8375.

77. Kaneko, R.; Chowdhury, T. H.; Sugawa, K.; Lee, J.-J.; Otsuki, J.; Islam, A., Electro-Active Nanofibers of a Tetrathiafulvalene Derivative with Amide Hydrogen Bonds as a Dopant-free Hole Transport Material for Perovskite Solar Cells. *Sol. Energy*, **2019**, *194*, 248-253.

78. Zhou, Y.; Yu, F.; Su, J.; Kurmoo, M.; Zuo, J. L., Tuning Electrical- and Photo-Conductivity by Cation Exchange within a Redox-Active Tetrathiafulvalene-Based Metal-Organic Framework. *Angew. Chem. Int. Ed.*, **2020**, *59* (42), 18763-18767.

79. Li, H.; Chang, J.; Li, S.; Guan, X.; Li, D.; Li, C.; Tang, L.; Xue, M.; Yan, Y.; Valtchev, V.; Qiu, S.; Fang, Q., Three-Dimensional Tetrathiafulvalene-Based Covalent Organic Frameworks for Tunable Electrical Conductivity. *J. Am. Chem. Soc.*, **2019**, *141* (34), 13324-13329.

80. Zheng, Z.; Feng, Q.; Zhu, M.; Shang, J.; Li, M.; Li, C.; Kou, L.; Zheng, J.; Wang, C., Electrochemical Sensor for the Discrimination of Bilirubin in Real Human Blood Based on Au Nanoparticles/Tetrathiafulvalene - Carboxylate Functionalized Reduced Graphene Oxide 0D-2D Heterojunction. *Anal. Chim. Acta.*, **2019**, *1072*, 46-53.

81. Huang, X.; Zhang, J.; Zhang, L.; Su, H.; Liu, X.; Liu, J., A Sensitive H_2O_2 Biosensor based on Carbon Nanotubes/Tetrathiafulvalene and its Application in Detecting NADH. *Anal. Biochem.*, **2020**, *589*, 113493.

82. Zhou, Y.; Hu, Q.; Yu, F.; Ran, G. Y.; Wang, H. Y.; Shepherd, N. D.; D'Alessandro, D. M.; Kurmoo, M.; Zuo, J. L., A Metal-Organic Framework Based on a Nickel Bis(dithiolene) Connector: Synthesis, Crystal Structure, and Application as an Electrochemical Glucose Sensor. *J. Am. Chem. Soc.*, **2020**, *142* (48), 20313–20317.

83. Jung, J.; Liu, W.; Kim, S.; Lee, D., Redox-Driven Folding, Unfolding, and Refolding of Bis(tetrathiafulvalene) Molecular Switch. *J. Org. Chem.*, **2019**, *84* (10), 6258-6269.

84. Mishra, R.; Regar, R.; Singh, V.; Panini, P.; Singhal, R.; Keshtov, M. L.; Sharma, G. D.; Sankar, J., Modulation of the Power Conversion Efficiency of Organic Solar Cells via Architectural Variation of a Promising Non-Fullerene Acceptor. *J. Mater. Chem. A*, **2018**, *6* (2), 574-582.

85. Zhou, P.; Aschauer, U.; Decurtins, S.; Feurer, T.; Häner, R.; Liu, S. X., Effect of Tert-butyl Groups on Electronic Communication between Redox Units in Tetrathiafulvalene-Tetraazapyrene Triads. *Chem. Commun.*, **2021**, *57* (96), 12972-12975.

86. Barrett, B. J.; Jimenez, D.; Klausen, R. S.; Bragg, A. E., Intramolecular Photoinduced Charge Transfer and Recombination Dynamics in Vinylarene Terminated Organosilanes. *J. Phys. Chem. B*, **2021**, *125* (30), 8460-8471.

87. Akbarimoosavi, M.; Rohwer, E.; Rondi, A.; Hankache, J.; Geng, Y.; Decurtins, S.; Hauser, A.; Liu, S. X.; Feurer, T.; Cannizzo, A., Tunable Lifetimes of Intramolecular Charge-Separated States in Molecular Donor-Acceptor Dyads. *J. Phys. Chem. C*, **2019**, *123* (14), 8500-8511.

88. Schroder, H. V.; Stein, F.; Wollschlager, J. M.; Sobottka, S.; Gaedke, M.; Sarkar, B.; Schalley, C. A., Accordion-Like Motion in Electrochemically Switchable Crown Ether/Ammonium Oligorotaxanes. *Angew. Chem. Int. Ed.*, **2019**, *58* (11), 3496-3500.

89. Ahn, Y.; Koo, J. Y.; Choi, H. C., Morphology-Retained Conversion of Neutral to Mixed Valence Tetrathiafulvalene Crystals through a Spontaneous Redox Reaction. *ACS Appl. Electron. Mater.*, **2020**, *2* (12), 3831-3836.

90. Schroder, H. V.; Witte, F.; Gaedke, M.; Sobottka, S.; Suntrup, L.; Hupatz, H.; Valkonen, A.; Paulus, B.; Rissanen, K.; Sarkar, B.; Schalley, C. A., An Aryl-fused Redox-Active Tetrathiafulvalene with Enhanced Mixed-Valence and Radical-cation Dimer Stabilities. *Org. Biomol. Chem.*, **2018**, *16* (15), 2741-2747.

91. Shiina, Y.; Kage, Y.; Furukawa, K.; Wang, H.; Yoshikawa, H.; Furuta, H.; Kobayashi, N.; Shimizu, S., TTF-Annulated Silicon Phthalocyanine Oligomers and Their External-Stimuli-Responsive Orientational Ordering. *Angew. Chem. Int. Ed.*, **2020**, *59* (50), 22721-22730.

92. Jiang, H.; Mazzanti, V.; Parker, C. R.; Broman, S. L.; Wallberg, J. H.; Luspai, K.; Brincko, A.; Kjaergaard, H. G.; Kadziola, A.; Rapta, P.; Hammerich, O.; Nielsen, M. B., Interactions between Tetrathiafulvalene Units in Dimeric Structures - the Influence of Cyclic Cores. *Beilstein J. Org. Chem.*, **2015**, *11*, 930-948.

93. Ogi, D.; Fujita, Y.; Mori, S.; Shirahata, T.; Misaki, Y., Bis- and Tris-Fused Tetrathiafulvalenes Extended with Anthracene-9,10-Diylidene. *Org. Lett.*, **2016**, *18* (22), 5868-5871.

94. Lahlil, K.; Moradpour, A.; Merienne, C.; Bowlas, C., Pyrazine-Fused Bis(Tetrathiafulvalenes). *J. Org. Chem.*, **1994**, *59* (26), 8030-8033.

95. Nazari Haghighi Pashaki, M.; Mosimann-Schönbächler, N.; Riede, A.; Gazzetto, M.; Rondi, A.; Cannizzo, A., Two-Dimensional Ultrafast Transient Absorption Spectrograph Covering Deep-Ultraviolet to Visible Spectral Region Optimized for Biomolecules. *J. Phys. Photonics*, **2021**, *3*, 034014.

96. Xin, H.; Hou, B.; Gao, X., Azulene-Based π-Functional Materials: Design, Synthesis, and Applications. *Acc. Chem. Res.*, **2021**, *54* (7), 1737-1753.

97. Zeng, H. N.; Png, Z. M.; Xu, J., Azulene in Polymers and Their Properties. *Chem Asian J.*, **2020**, *15* (13), 1904-1915.

98. Hendsbee, A. D.; McAfee, S. M.; Sun, J.-P.; McCormick, T. M.; Hill, I. G.; Welch, G. C., Phthalimide-Based π-Conjugated Small Molecules with Tailored Electronic Energy Levels for Use as Acceptors in Organic Solar Cells. *J. Mater. Chem. C*, **2015**, *3* (34), 8904-8915.

99. Huang, J. Q.; Huang, S. H.; Zhao, Y. Z.; Feng, B. X.; Jiang, K. Y.; Sun, S.; Ke, C. C.; Kymakis, E.; Zhuang, X. D., Azulene-Based Molecules, Polymers, and Frameworks for Optoelectronic and Energy Applications. *Small Methods*, **2020**, *4*, 2000628.

100. Vollbrecht, J.; Bock, H.; Wiebeler, C.; Schumacher, S.; Kitzerow, H., Polycyclic Aromatic Hydrocarbons Obtained by Lateral Core Extension of Mesogenic Perylenes: Absorption and Optoelectronic Properties. *Chemistry*, **2014**, *20* (38), 12026-12031.

101. Gao, H.; Ge, C.; Hou, B.; Xin, H.; Gao, X., Incorporation of 1,3-Free-2,6-Connected Azulene Units into the Backbone of Conjugated Polymers: Improving Proton Responsiveness and Electrical Conductivity. *ACS Macro Lett.*, **2019**, *8* (10), 1360-1364.

102. Adeniyi, A. A.; Ngake, T. L.; Conradie, J., Cyclic Voltammetric Study of 2-Hydroxybenzophenone (HBP) Derivatives and the Correspondent Change in the Orbital Energy Levels in Different Solvents. *Electroanalysis*, **2020**, *32* (12), 2659-2668.

103. Leonat, L.; Sbarcea, G., Cyclic Voltammetry for Energy Levels Estimation of Organic Materials. *U.P.B. Sci. Bull., Series B*, **2013**, *75*, 111-118.

104. Mahmood, Z.; Sukhanov, A. A.; Rehmat, N.; Hu, M.; Elmali, A.; Xiao, Y.; Zhao, J.; Karatay, A.; Dick, B.; Voronkova, V. K., Intersystem Crossing and Triplet-State Property of Anthryl- and Carbazole-[1,12]fused Perylenebisimide Derivatives with a Twisted π-Conjugation Framework. *J. Phys. Chem. B*, **2021**, *125* (32), 9317-9332.

105. Lin, L.; Morisaki, Y.; Chujo, Y., New Type of Donor-Acceptor Through-Space Conjugated Polymer. *Int. J. Polym. Sci.*, **2010**, *2010*, 1-9.

106. Morisaki, Y.; Kawakami, N.; Nakano, T.; Chujo, Y., Energy-Transfer Properties of a [2,2]Paracyclophane-Based Through-Space Dimer. *Chemistry*, **2013**, *19* (52), 17715-17718.

107. Weiland, K. J.; Gallego, A.;Mayor, M., Beyond Simple Substitution Patterns - Symmetrically Tetrasubstituted [2,2]Paracyclophanes as 3D Functional Materials. *Eur. J. Org. Chem.*, **2019**, *2019* (20), 3073-3085.

108. Weiland, K. J.; Brandl, T.; Atz, K.; Prescimone, A.; Haussinger, D.; Solomek, T.; Mayor, M., Mechanical Stabilization of Helical Chirality in a Macrocyclic Oligothiophene. *J. Am. Chem. Soc.*, **2019**, *141* (5), 2104-2110.

109. Henderson, W. R.; Zhu, Y.; Fagnani, D. E.; Liu, G.; Abboud, K. A.; Castellano, R. K., Self-Assembling [n.n]Paracyclophanes: A Structure-Property Relationship Study. *J. Org. Chem.*, **2020**, *85* (2), 1158-1167.

110. Zafra, J. L.; Molina Ontoria, A.; Mayorga Burrezo, P.; Pena-Alvarez, M.; Samoc, M.; Szeremeta, J.; Ramirez, F. J.; Lovander, M. D.; Droske, C. J.; Pappenfus, T. M.; Echegoyen, L.; Lopez Navarrete, J. T.; Martin, N.; Casado, J., Fingerprints of Through-Bond and Through-Space Exciton and Charge π-Electron Delocalization in Linearly Extended [2,2]Paracyclophanes. *J. Am. Chem. Soc.*, **2017**, *139* (8), 3095-3105.

111. Zyss, J.; Ledoux, I.; Volkov, S.; Chernyak, V.; Mukamel, S.; Bartholomew, G. P.; Bazan, G. C., Through-Space Charge Transfer and Nonlinear Optical Properties of Substituted Paracyclophane. *J. Am. Chem. Soc.*, **2000**, *122* (48), 11956-11962.

112. Molina-Ontoria, A.; Wielopolski, M.; Gebhardt, J.; Gouloumis, A.; Clark, T.; Guldi, D. M.; Martin, N., [2,2']Paracyclophane-Based π-Conjugated Molecular Wires Reveal Molecular-Junction Behavior. *J. Am. Chem. Soc.*, **2011**, *133* (8), 2370-2373.

113. Jia, C.; Liu, S. X.; Tanner, C.; Leiggener, C.; Neels, A.; Sanguinet, L.; Levillain, E.; Leutwyler, S.; Hauser, A.; Decurtins, S., An Experimental and Computational Study on Intramolecular Charge Transfer: a Tetrathiafulvalene-Fused Dipyridophenazine Molecule. *Chemistry*, **2007**, *13* (13), 3804-3812.

114. Hasegawa, M.; Enozawa, H.; Kawabata, Y.; Iyoda, M., Hexagonally Ordered Nanostructures Comprised of a Flexible Disk-like Molecule with High Self-Assembling Properties at Neutral and Cationic States. *J. Am. Chem. Soc.*, **2007**, *129* (11), 3072-3073.

115. Wang, C. S.; Ellern, A.; Khodorkovsky, V.; Bernstein, J.; Becker, J., New Direct Iodination of Tetrathiafulvalene (TTF): Mono- and Di-iodo-TTF and their X-Ray Crystal Structures. *Journal of the Chemical Society, Chem. Commun.*, **1994**, 983-984.

116. Ni, Z.; Wang, H.; Dong, H.; Dang, Y.; Zhao, Q.; Zhang, X.; Hu, W., Mesopolymer Synthesis by Ligand-Modulated Direct Arylation Polycondensation Towards n-Type and Ambipolar Conjugated Systems. *Nat. Chem.*, **2019**, *11* (3), 271-277.

117. Broman, S. L.; Andersen, C. L.; Jevric, M.; Tortzen, C. G.; Hammerich, O.; Nielsen, M. B., Metal Cation Binding to Acetylenic Tetrathiafulvalene-Pyridine Conjugates: Affinity Tuned by Preorganization and Cavity Size. *Tetrahedron,* **2016**, *72* (39), 5831-5842.

118. Grill, L. & Hecht, S., Covalent on-Surface Polymerization. *Nat. Chem*., **2020**, *12*, 115–130.

119. Kinikar, A., New Polymerization and Post-Synthesis Strategies in on-Surface Synthesis. (ETH ZUR-ICH).

120. Koen Houtsma, R. S.; Rie, J. de la.; Stöhr, M., Atomically Precise Graphene Nanoribbons: Interplay of Structural and Electronic Properties. *Chem. Soc. Rev*., **2021**, *50*, 6541–6568.

121. Ruffieux, P.; Wang, S.; Yang, B.; Sánchez-Sánchez1, C.; Liu, J.; Dienel, T.; Talirz, L.; Shinde, P.; Pignedoli, C. A.; Passerone, D.; Dumslaff, T.; Feng, X.; Müllen, K.; Fasel, R., On-Surface Synthesis of Graphene Nanoribbons with Zigzag Edge Topology. *Nature*, **2016**, *531*, 489.

122. Wakabayashi, K.; Fujita, M.; Kusakabe, K.; Nakada, K., Magnetic Structure of Graphite Ribbon. *Czech J Phys*., **1996**, *46*, 1865–1866.

Appendix

A.1 General methods

Air- and/or water-sensitive reactions were conducted under nitrogen and dry, freshly distilled solvents were used. Chemicals used for synthesis compounds were purchased from commercial suppliers (Sigma-Aldrich, TCI or Alfa Aesar). UV-Vis-NIR absorption spectra were recorded on a Perkin Elmer Lambda 900 UV/Vis/NIR spectrometer and UV-Vis absorption spectra on Varian Cary-100 Bio-UV/VIS. ^{1}H NMR spectra were recorded on a Bruker Avance 300 (300 MHz) spectrometer. FT-IR data were collected on a FT/IR-4700 FTIR Spectrometer from JASCO. Chemical shifts are reported in parts per million (ppm) and are referenced to the residual solvent peak ($CDCl_3$, δ ^{1}H = 7.26 ppm and DMSO-d_6, δ ^{1}H = 2.50 ppm).

Cyclic voltammetry (CV) was performed in a three-electrode cell equipped with a Pt working electrode, a glassy carbon counter-electrode, and Ag/AgCl reference electrode. The electrochemical experiments were carried out under an oxygen-free atmosphere in dichloromethane with $TBAPF_6$ (0.1 M) as a supporting electrolyte.

A.2 NMR and MS spectra

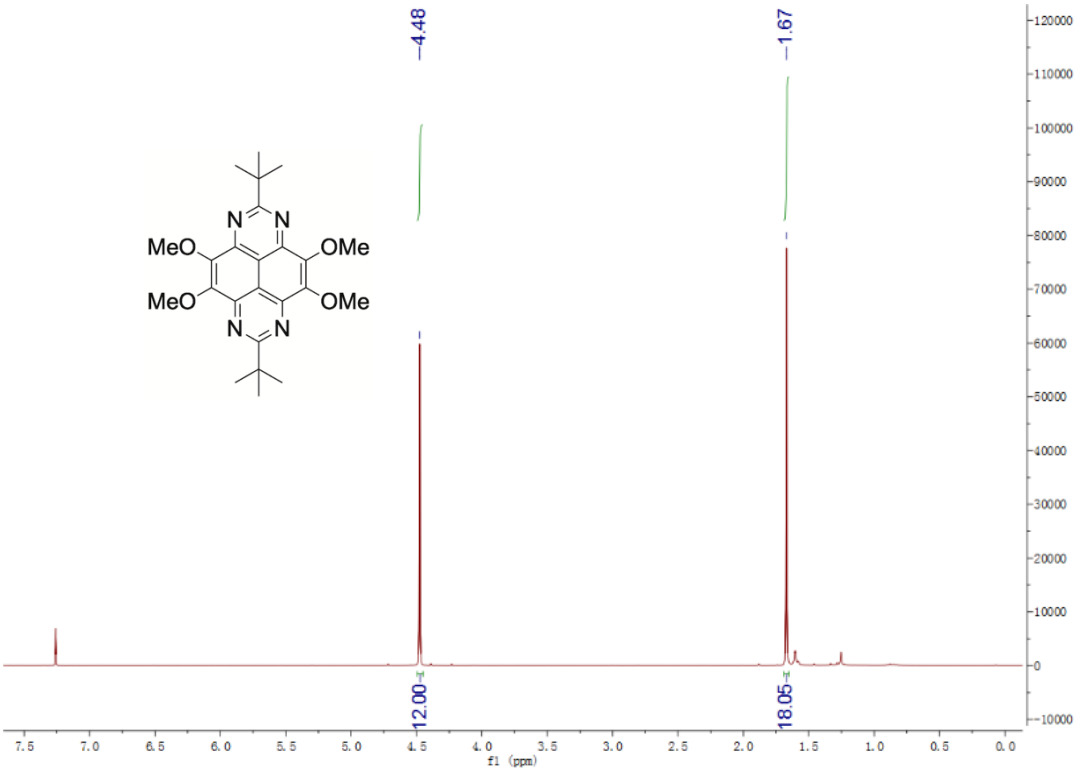

A 2. 1 ^{1}H NMR of compound **2** in $CDCl_3$.

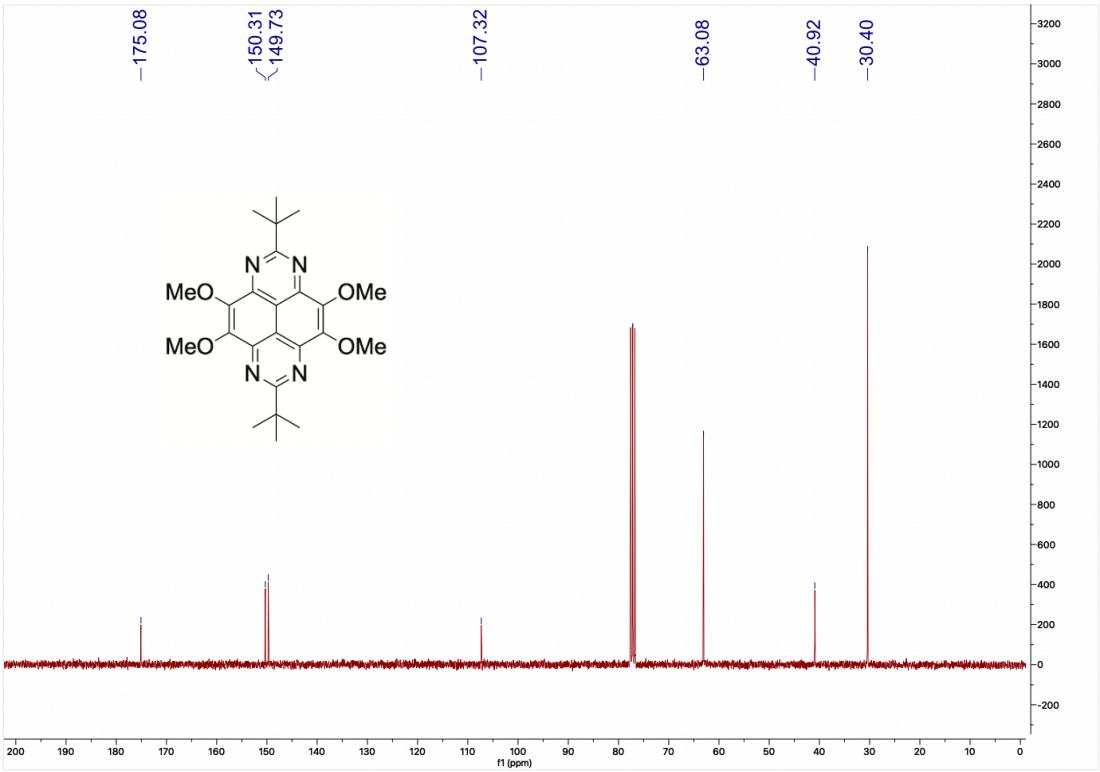

A 2. 2 ^{13} C of compound **2** in $CDCl_3$.

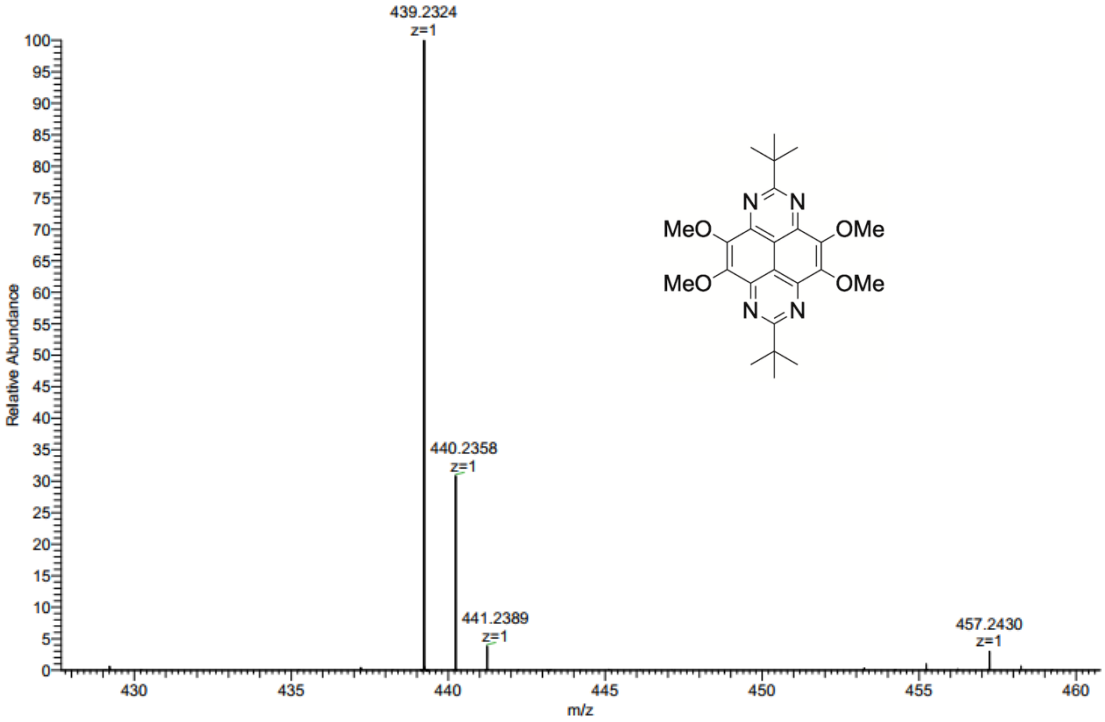

A 2. 3 HR-MS of compound **2**.

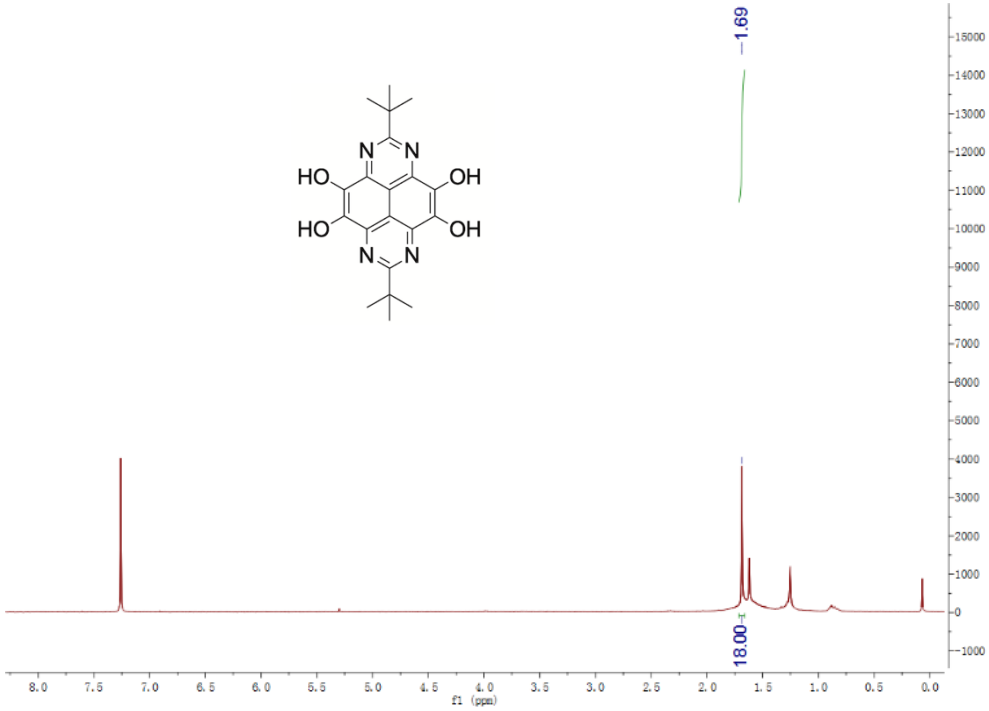

A 2. 4 ^{1}H NMR of compound **3** in $CDCl_3$.

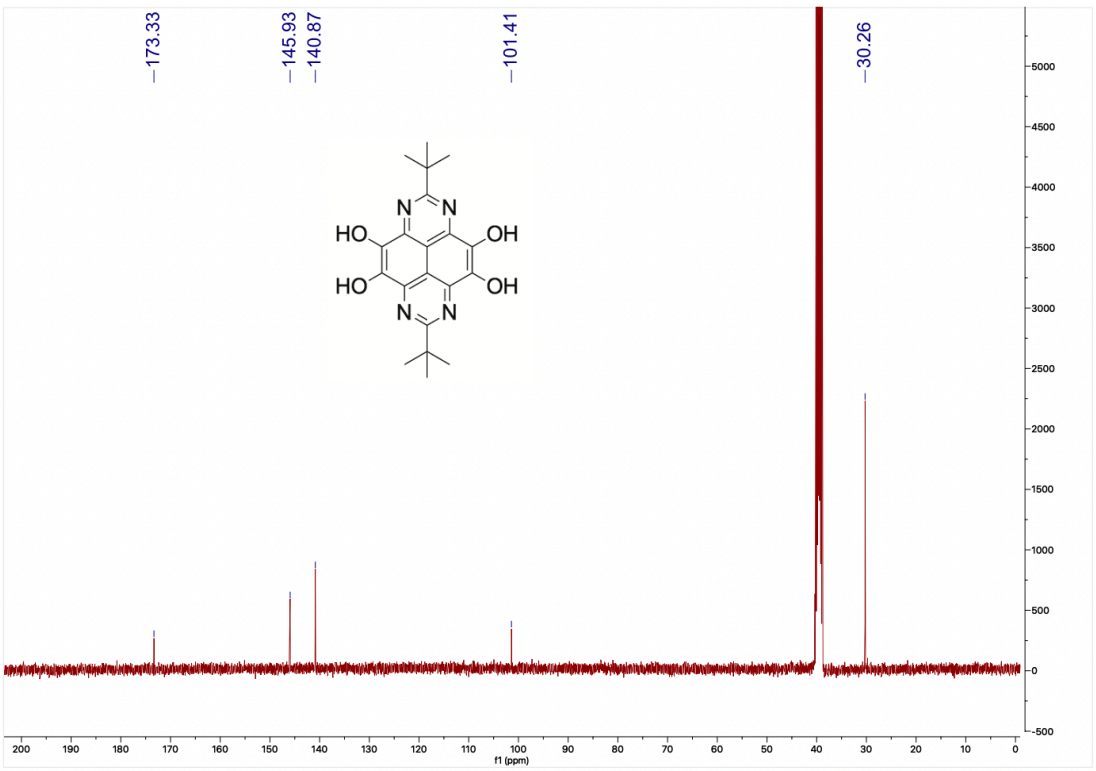

A 2. 5 ^{13}C of compound **3** in DMSO-d_6.

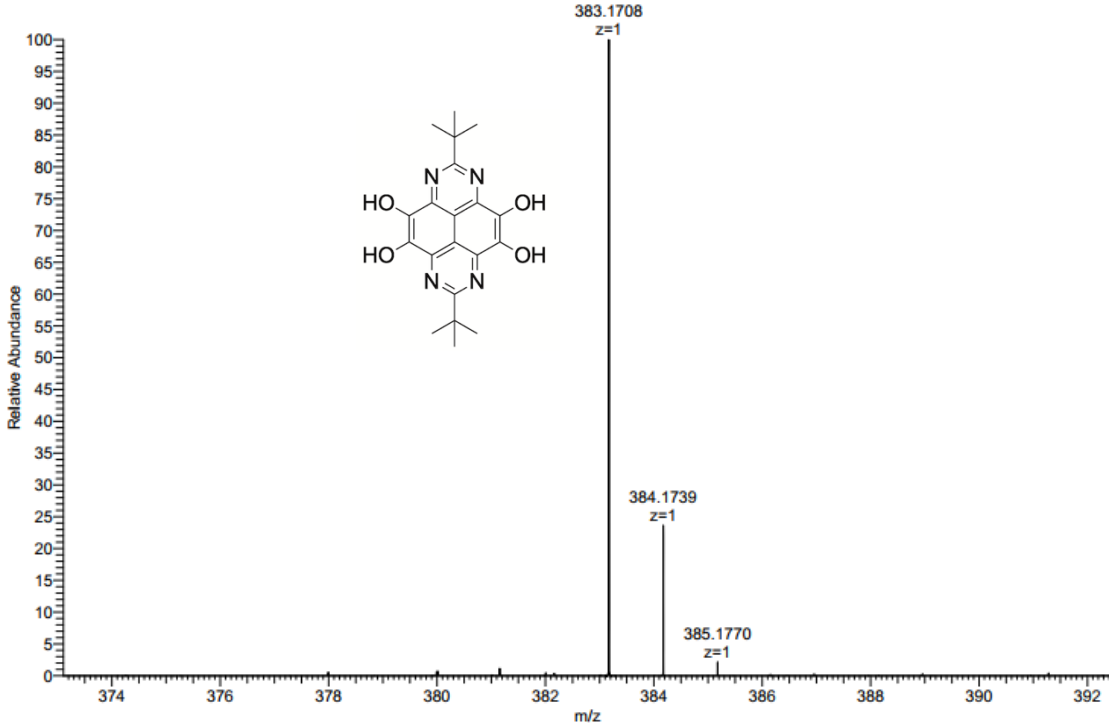

A 2. 6 HR-MS of compound **3**.

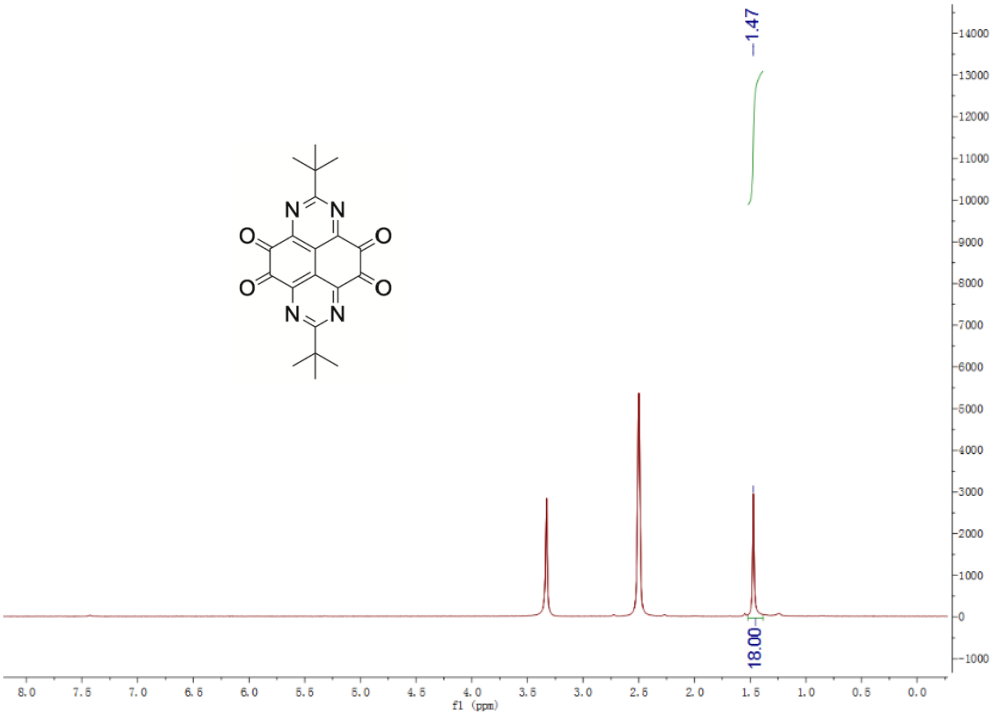

A 2. 7 ^{1}H NMR of compound **4** in DMSO-d_6.

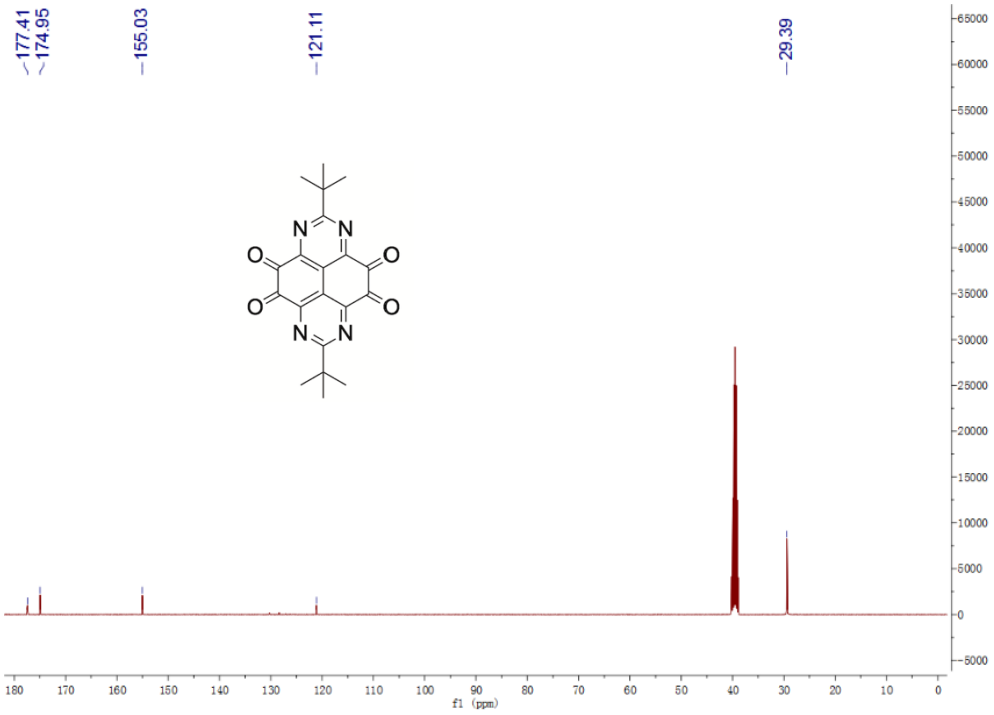

A 2. 8 ^{13}C of compound **4** in DMSO-d_6.

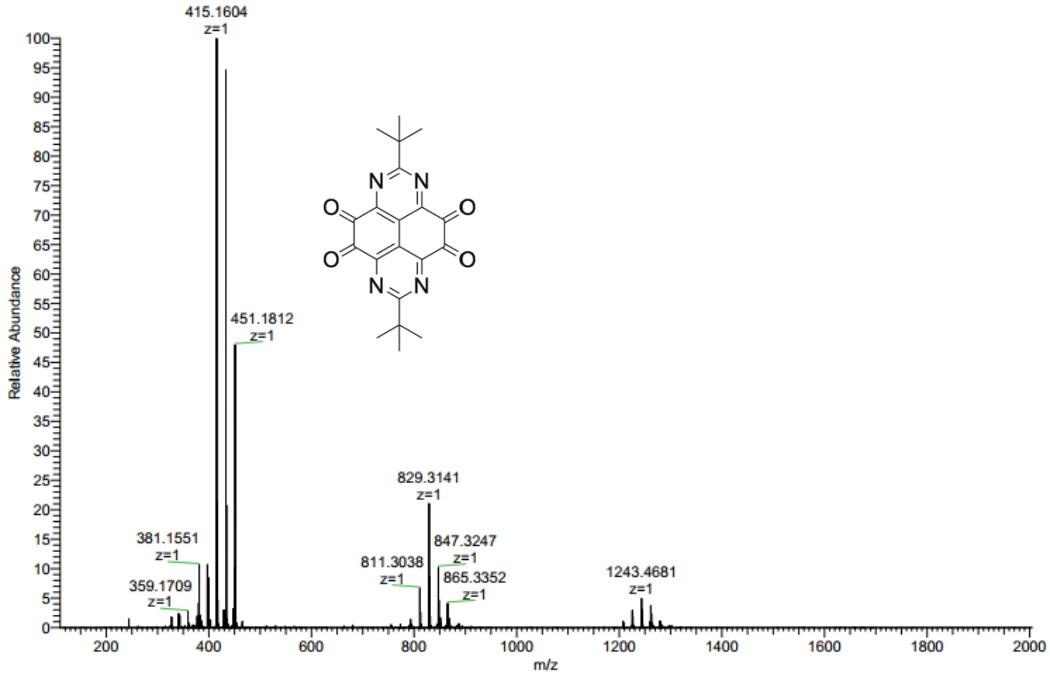

A 2. 9 HR-MS of compound **4**.

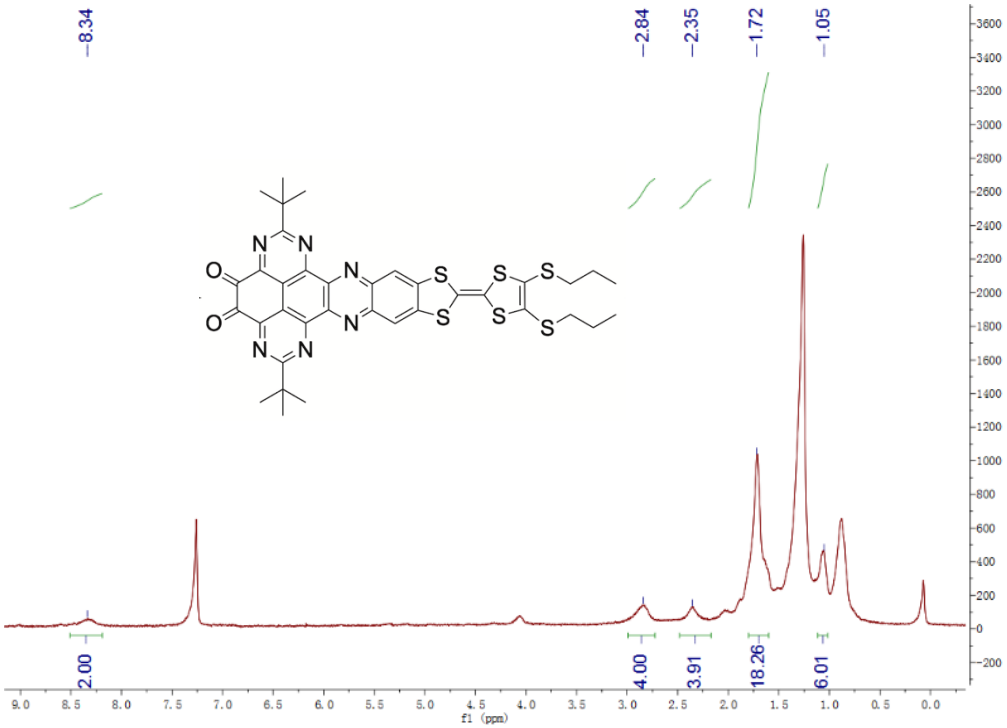

A 2. 10 ^{1}H NMR of compound **5** in $CDCl_3$.

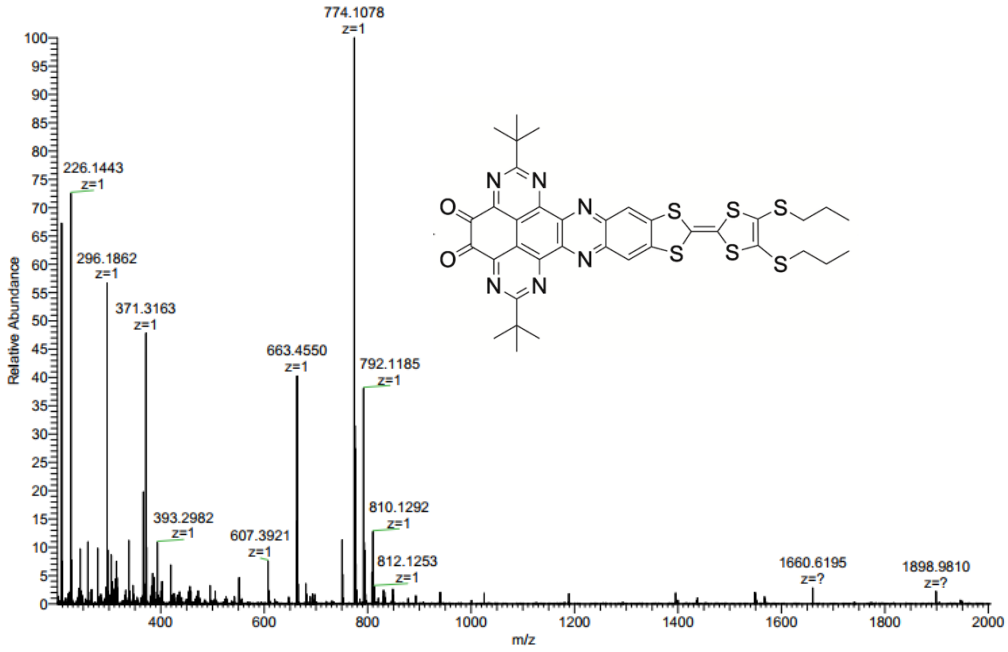

A 2. 11 HR-MS of compound **5**.

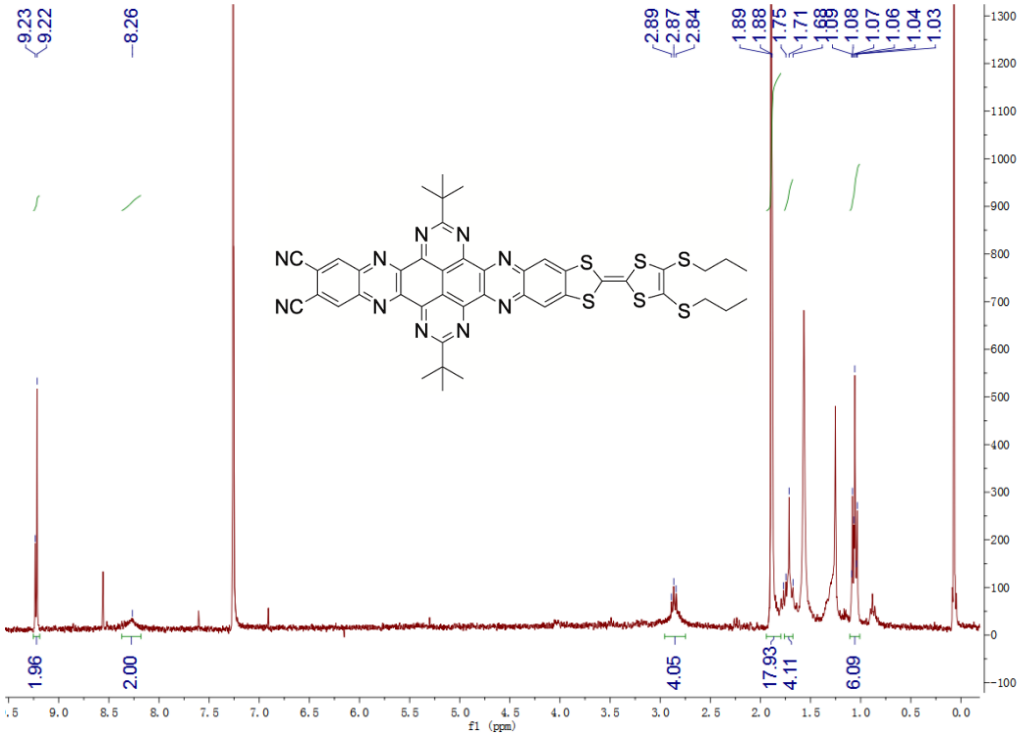

A 2. 12 ^{1}H NMR of compound **6** in $CDCl_3$.

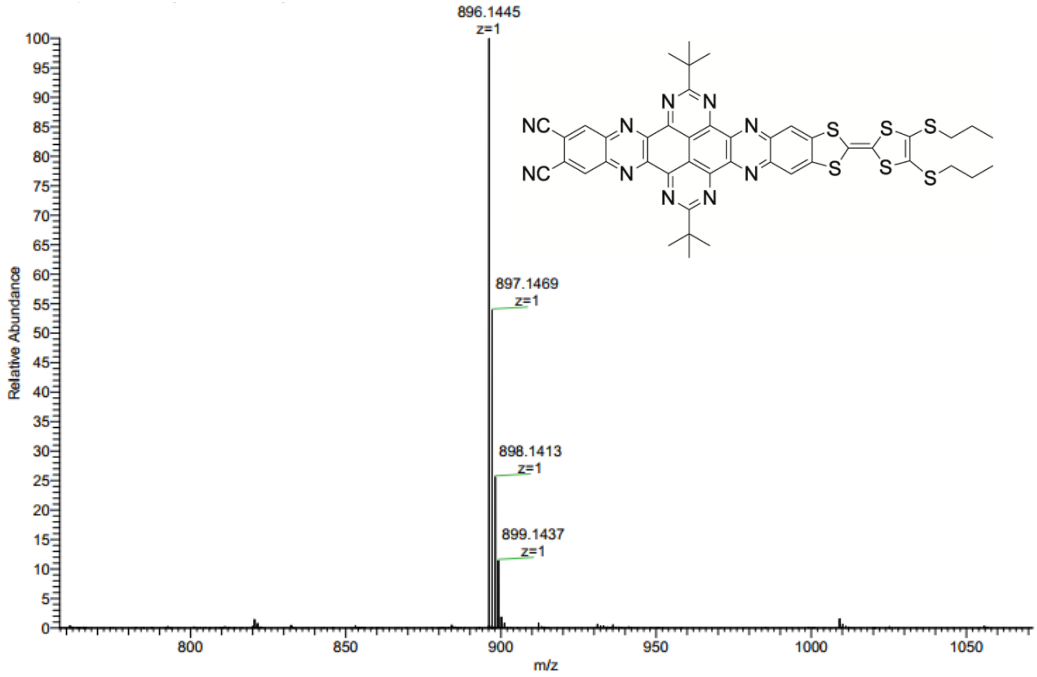

A 2. 13 HR-MS of compound **6**.

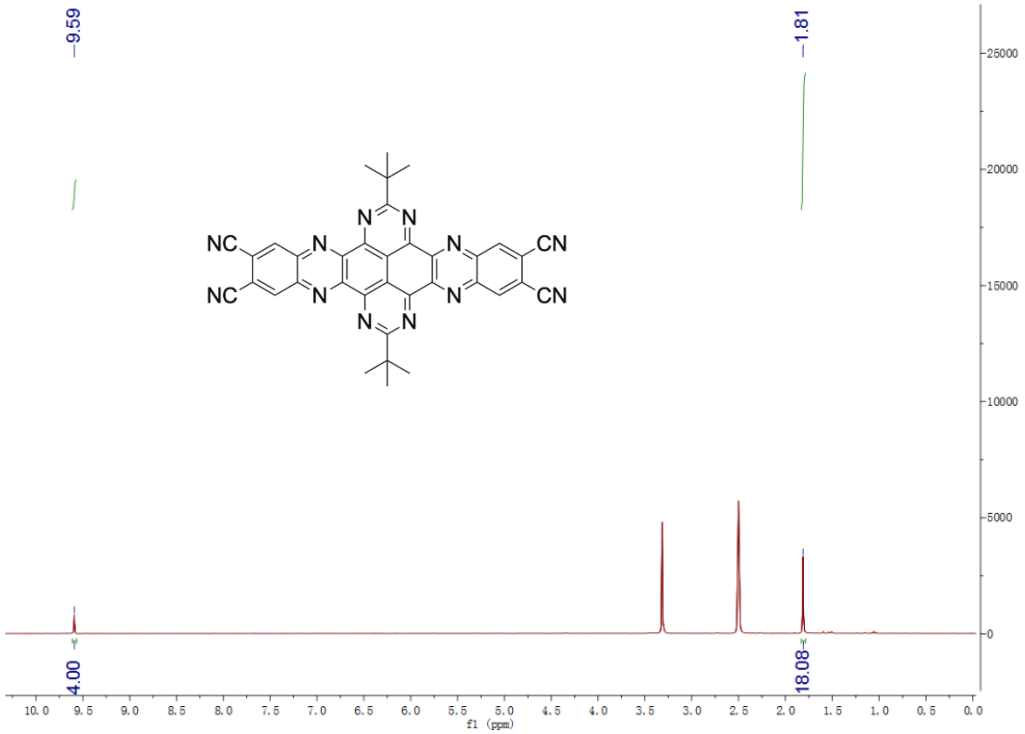

A 2. 14 ^{1}H NMR of compound **7** in DMSO-d_6.

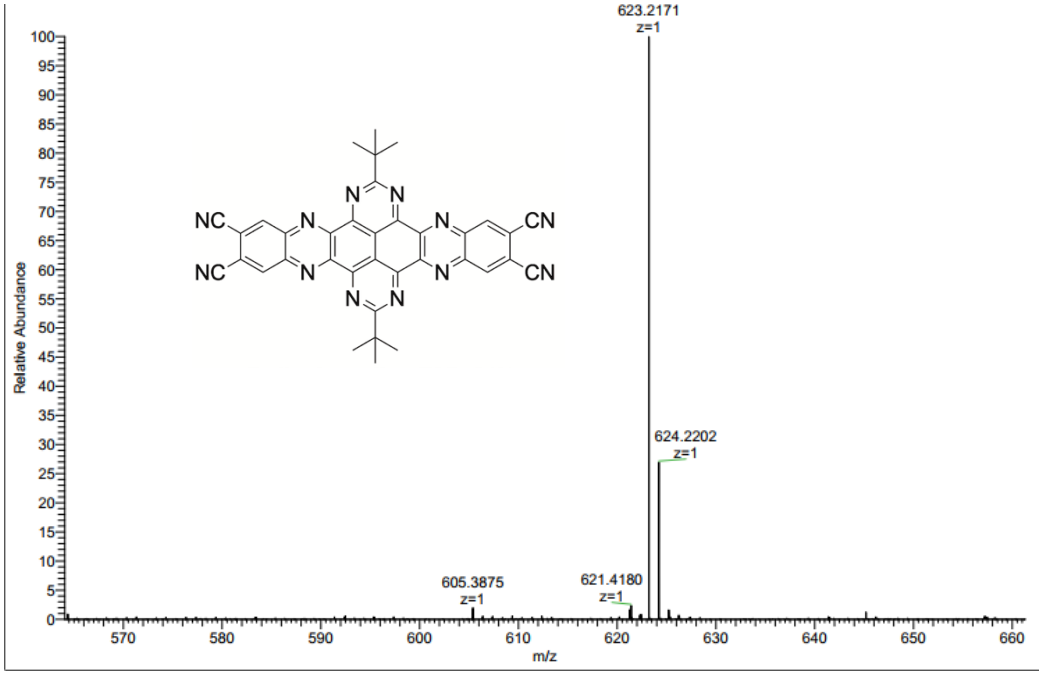

A 2. 15 HR-MS of compound **7**.

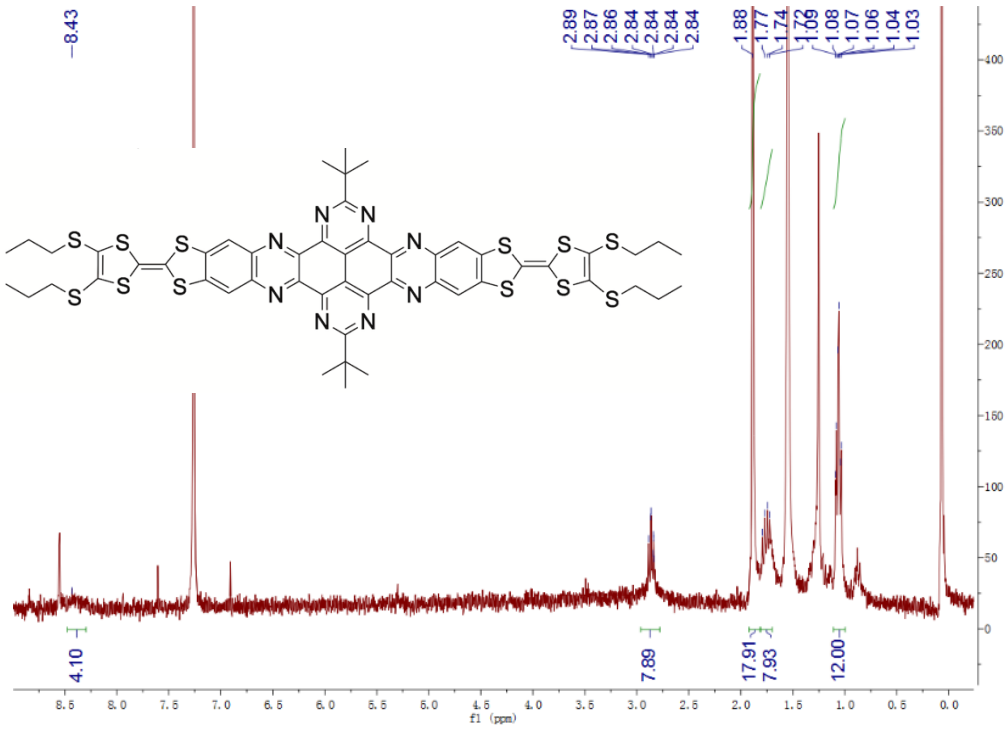

A 2. 16 ^{1}H NMR of compound **8** in $CDCl_3$.

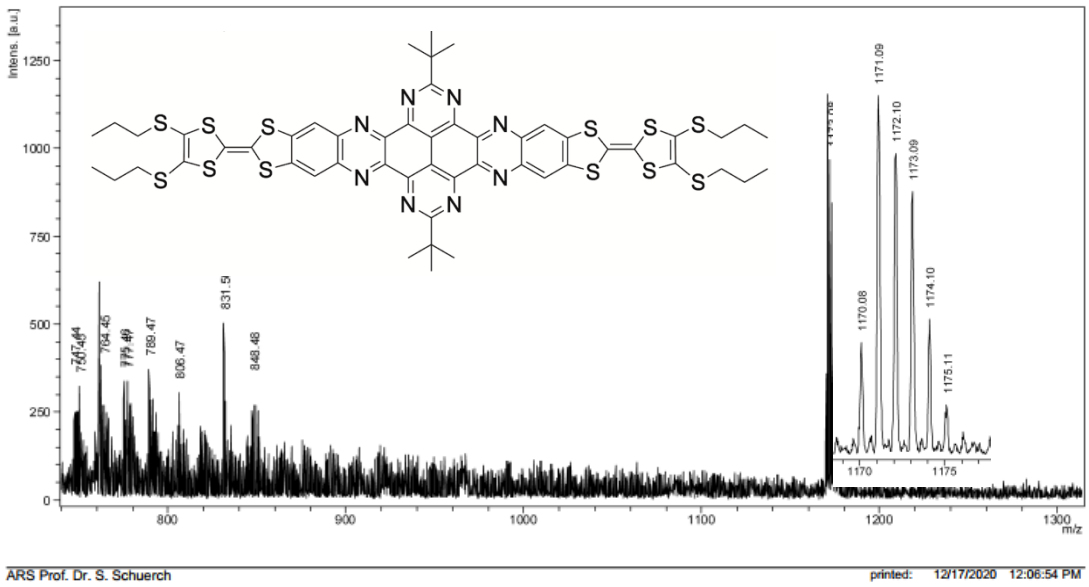

A 2. 17 MALDI-TOF-MS of compound **8**.

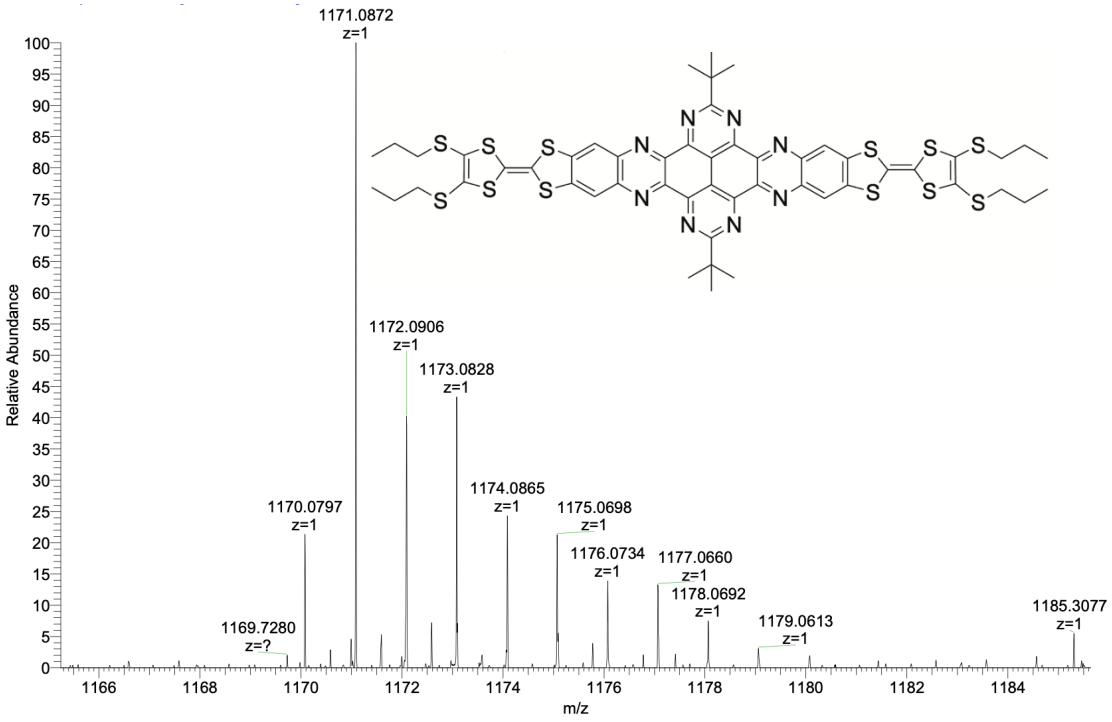

A 2. 18 HR-MS of compound **8**.

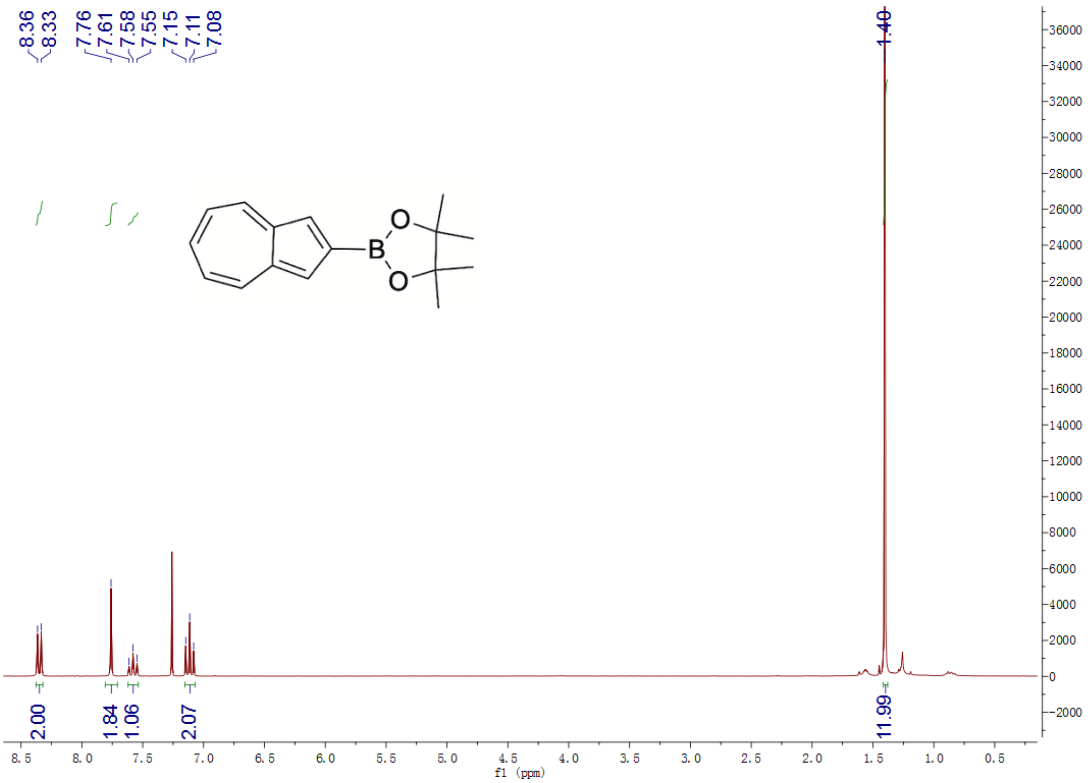

A 2. 19 ^{1}H NMR of compound **9** in $CDCl_3$.

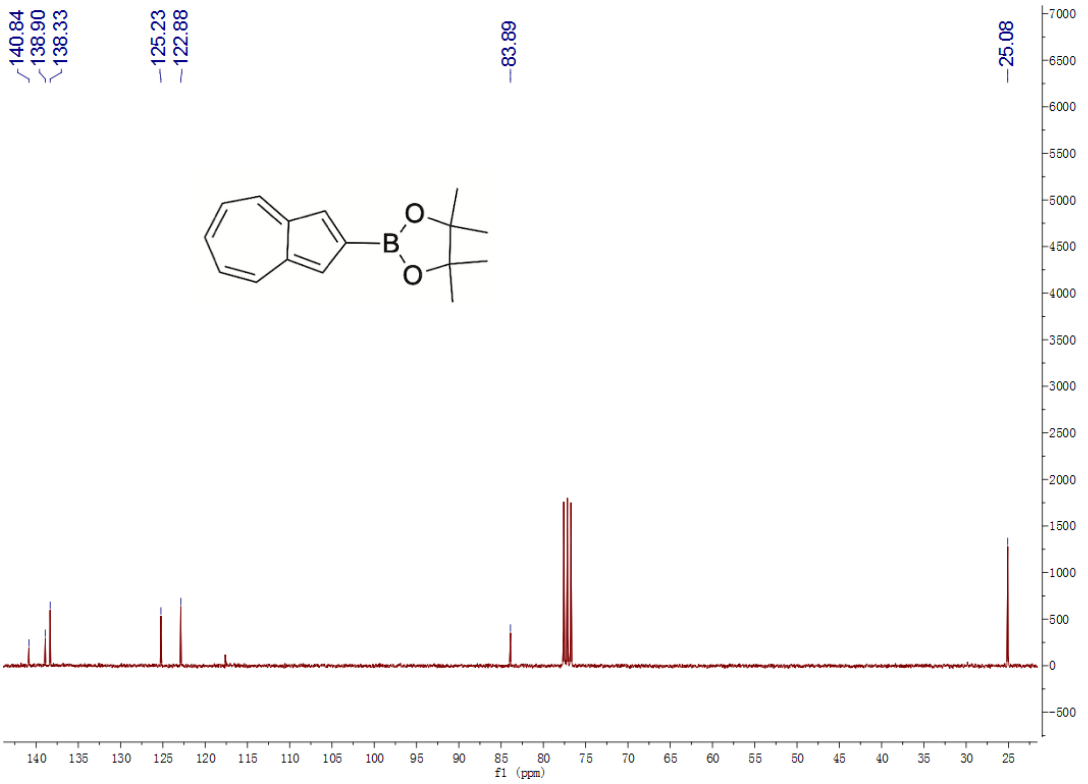

A 2. 20 ^{13}C of compound **9** in $CDCl_3$.

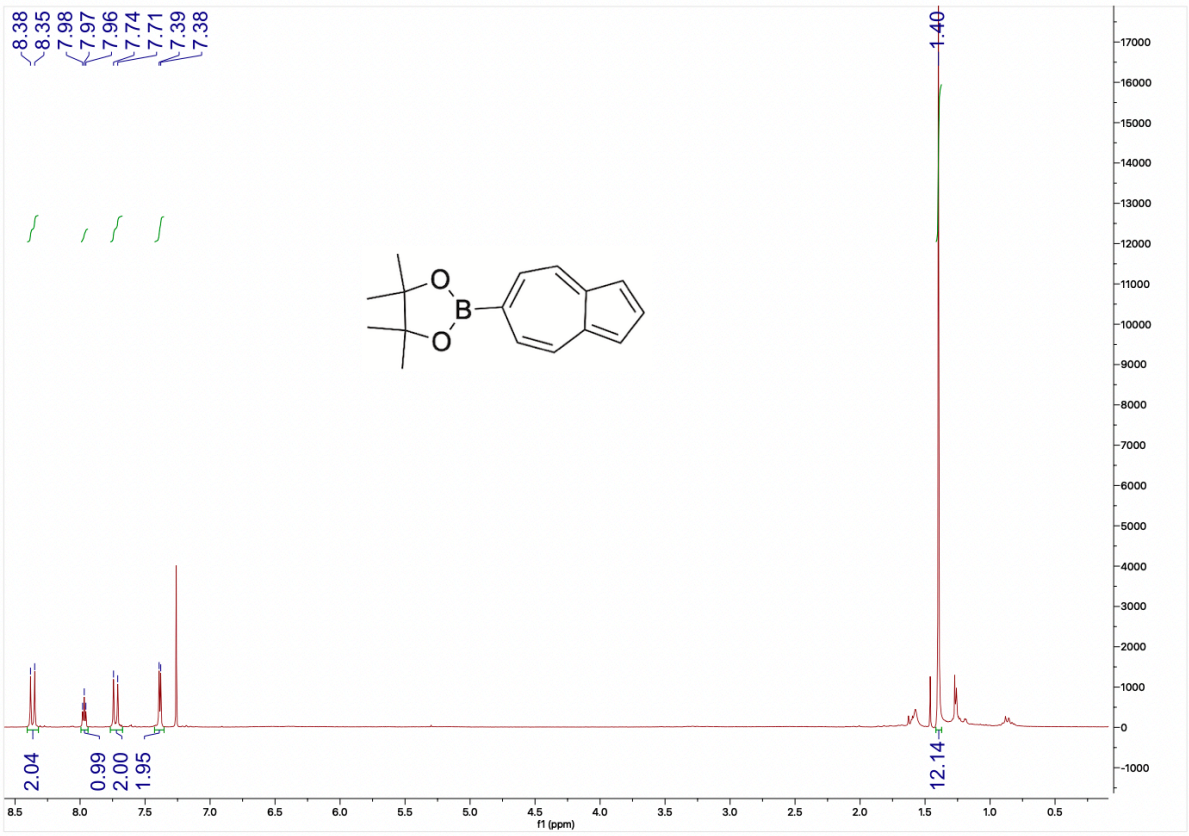

A 2. 21 ^{1}H NMR of compound **10** in $CDCl_3$.

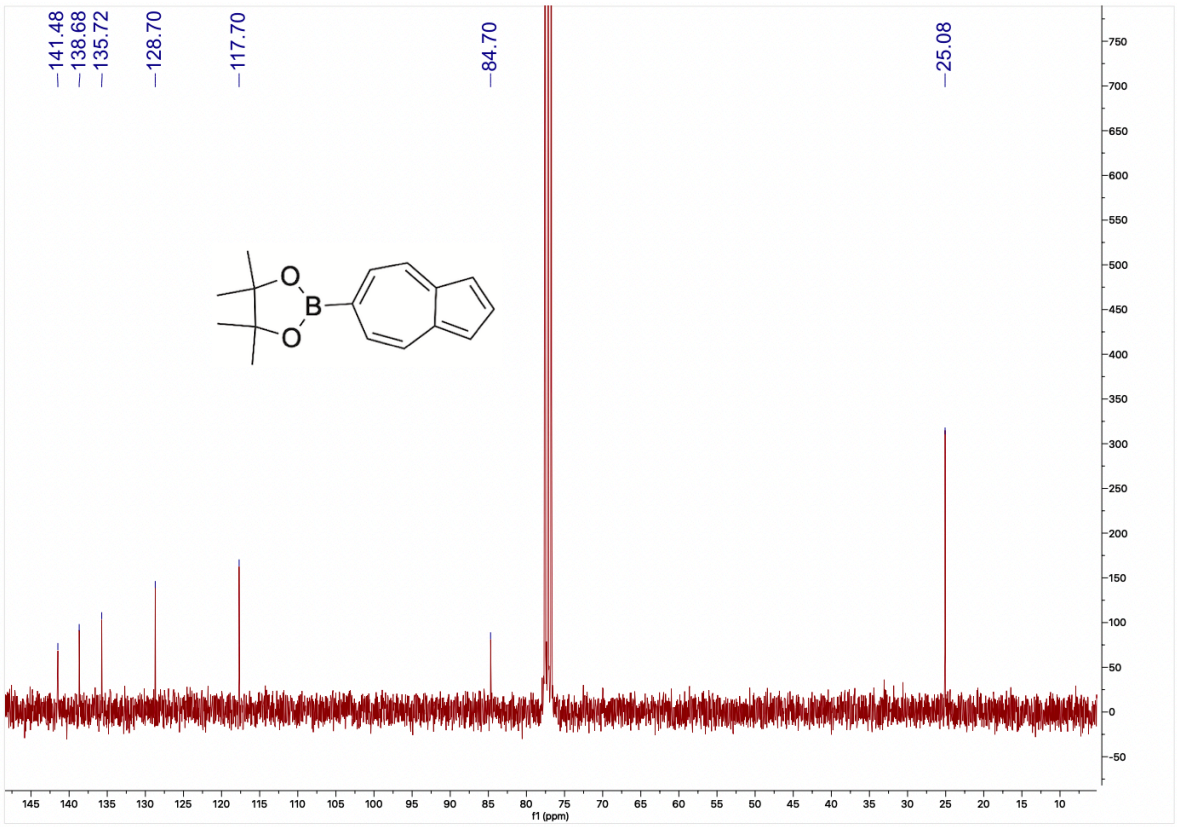

A 2. 22 ^{13}C of compound **10** in $CDCl_3$.

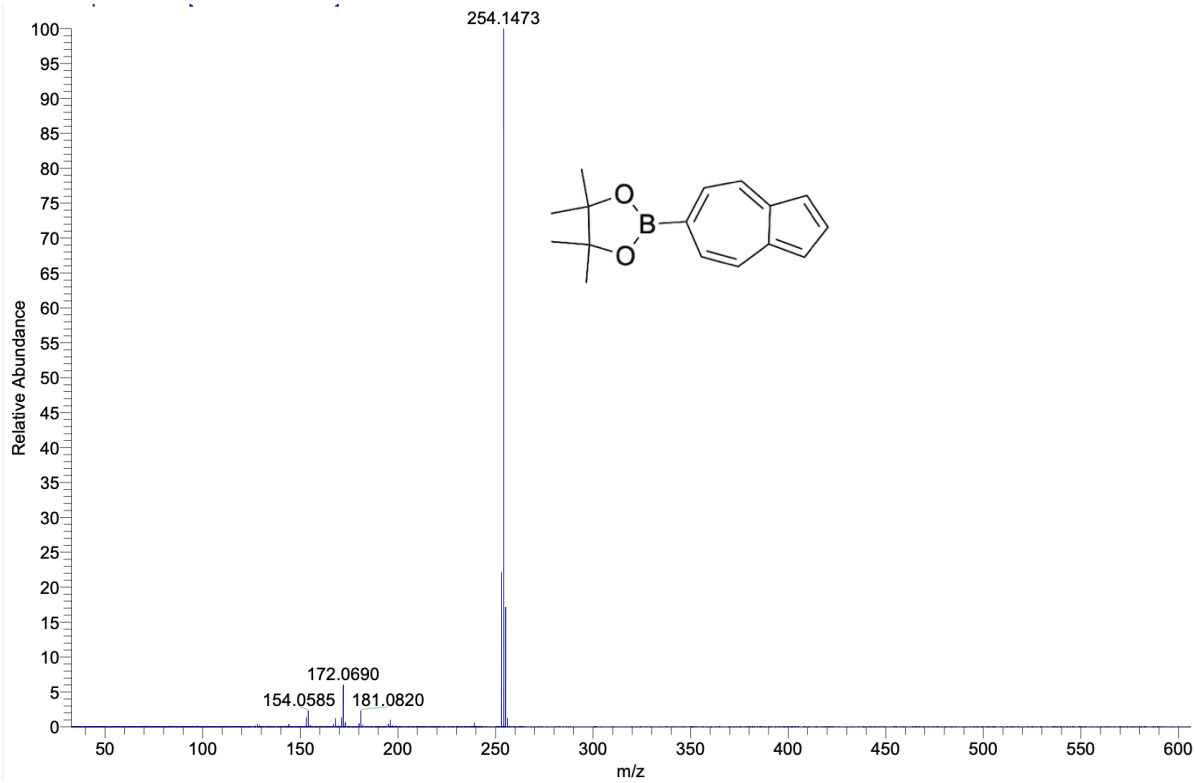

A 2. 23 HR-MS of compound **10**.

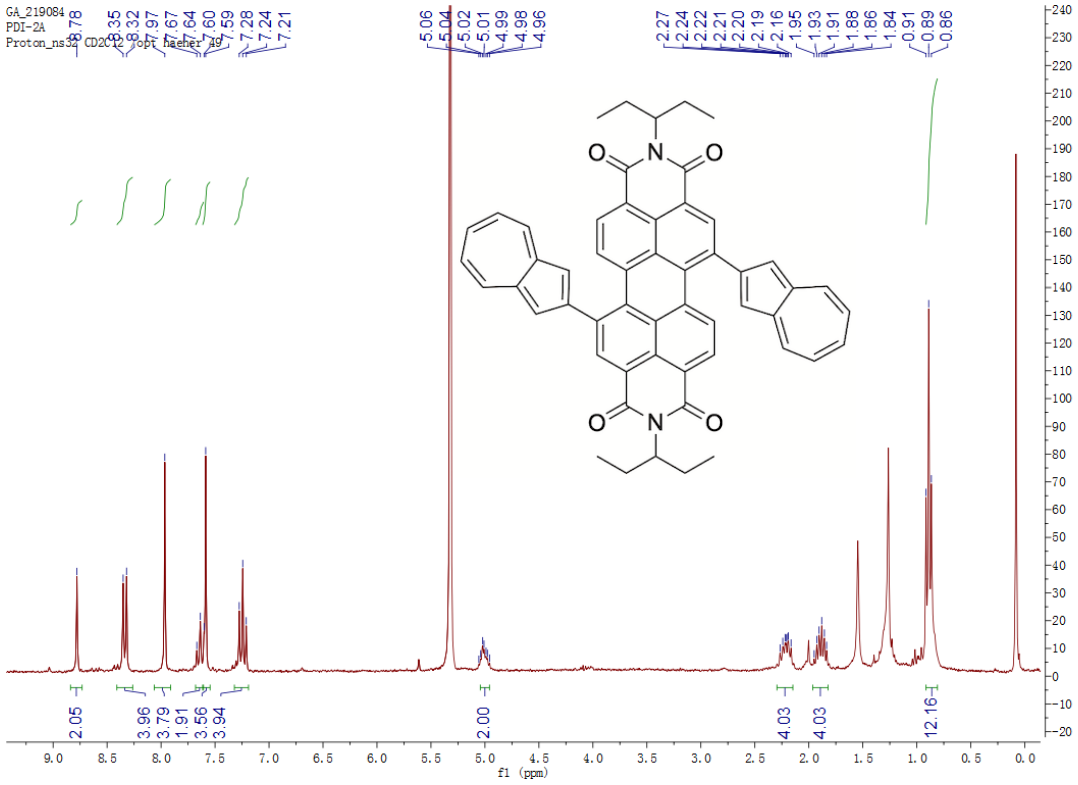

A 2. 24 ^{1}H NMR of compound **12** in CD_2Cl_2.

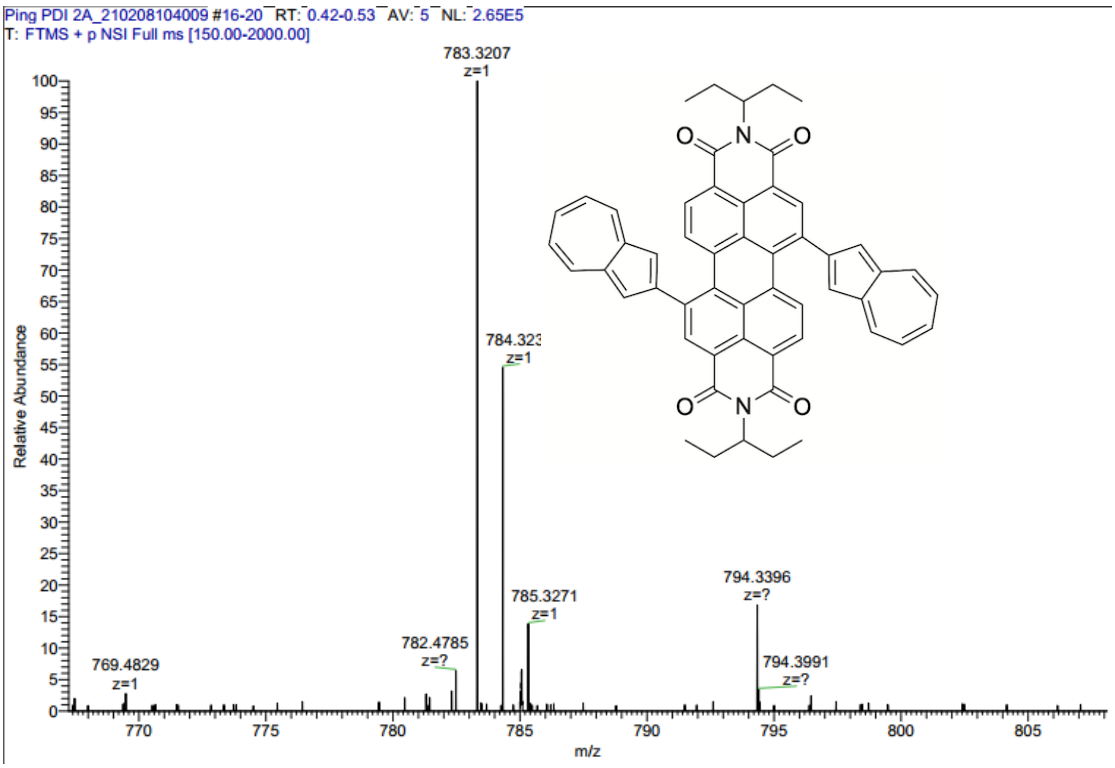

A 2. 25 HR-MS of compound **12**.

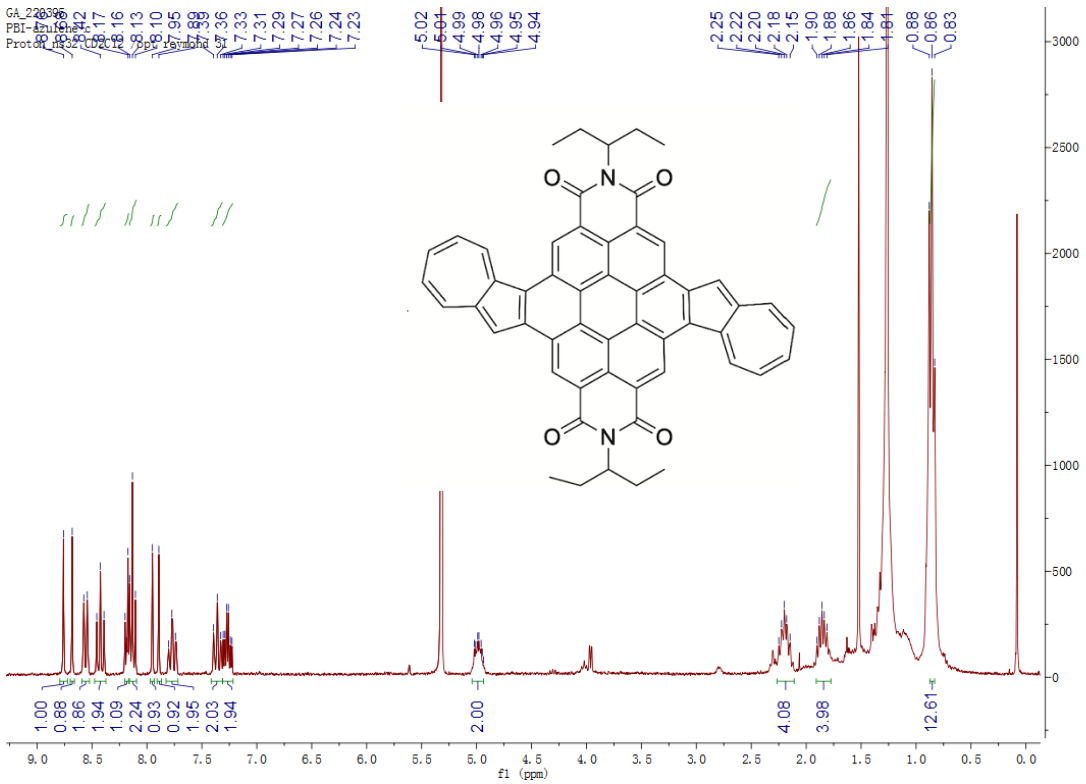

A 2. 26 ^{1}H NMR of compound **13** in CD_2Cl_2.

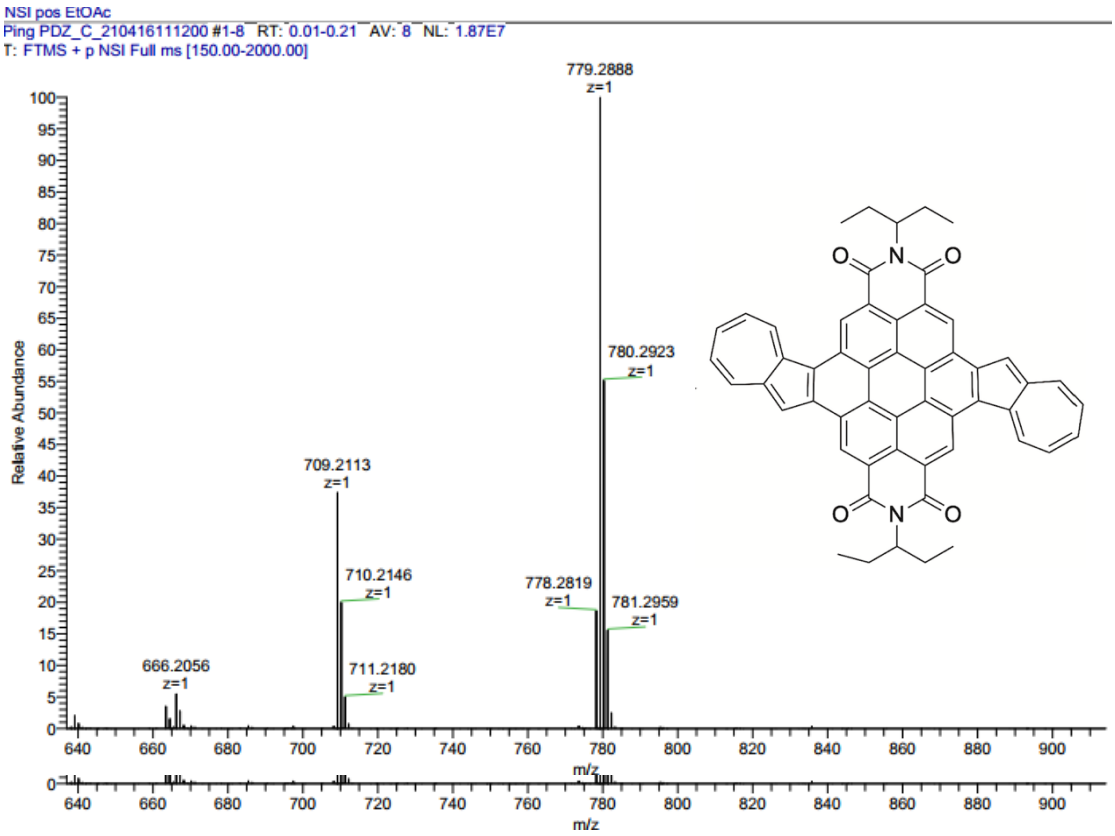

A 2. 27 HR-MS of compound **13**.

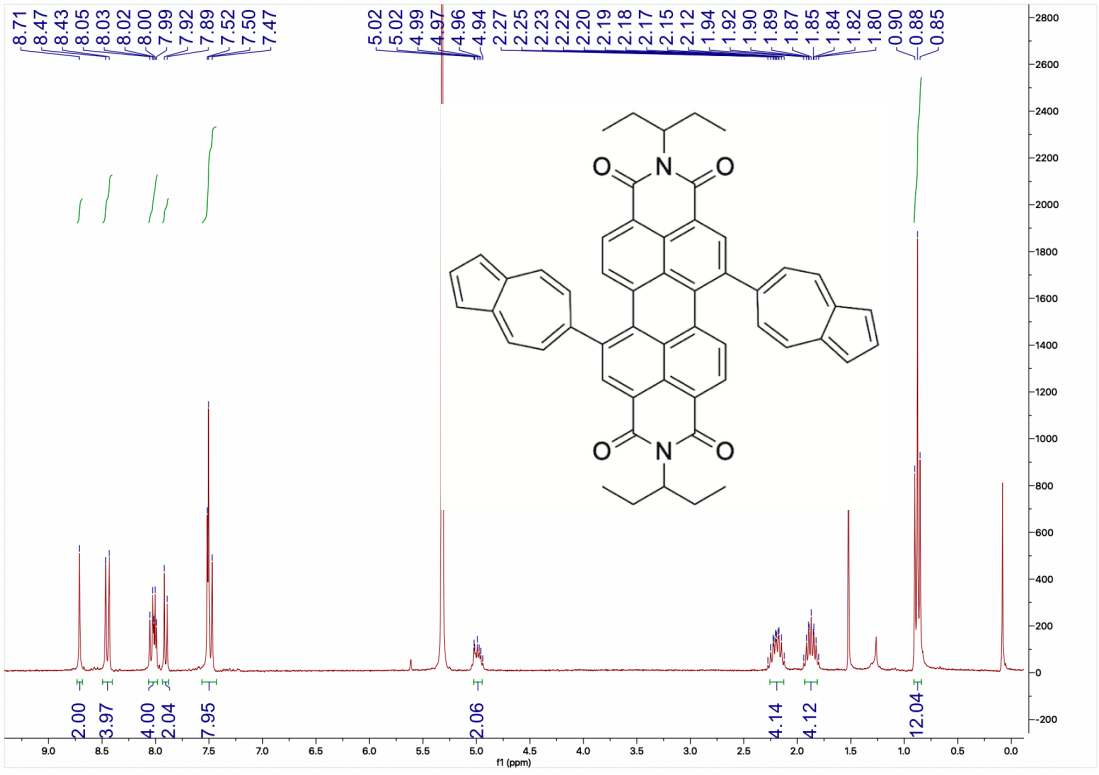

A 2. 28 ^{1}H NMR of compound **14** in CD_2Cl_2.

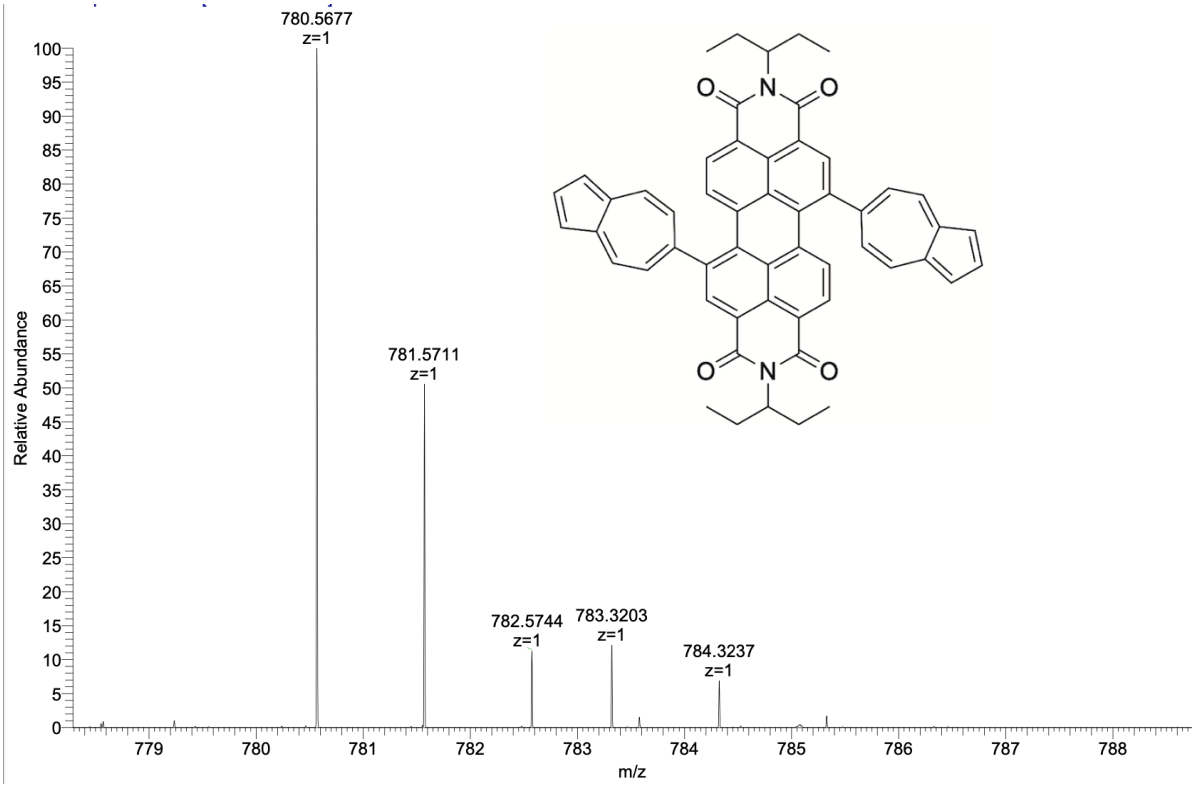

A 2. 29 HR-MS of compound **14**.

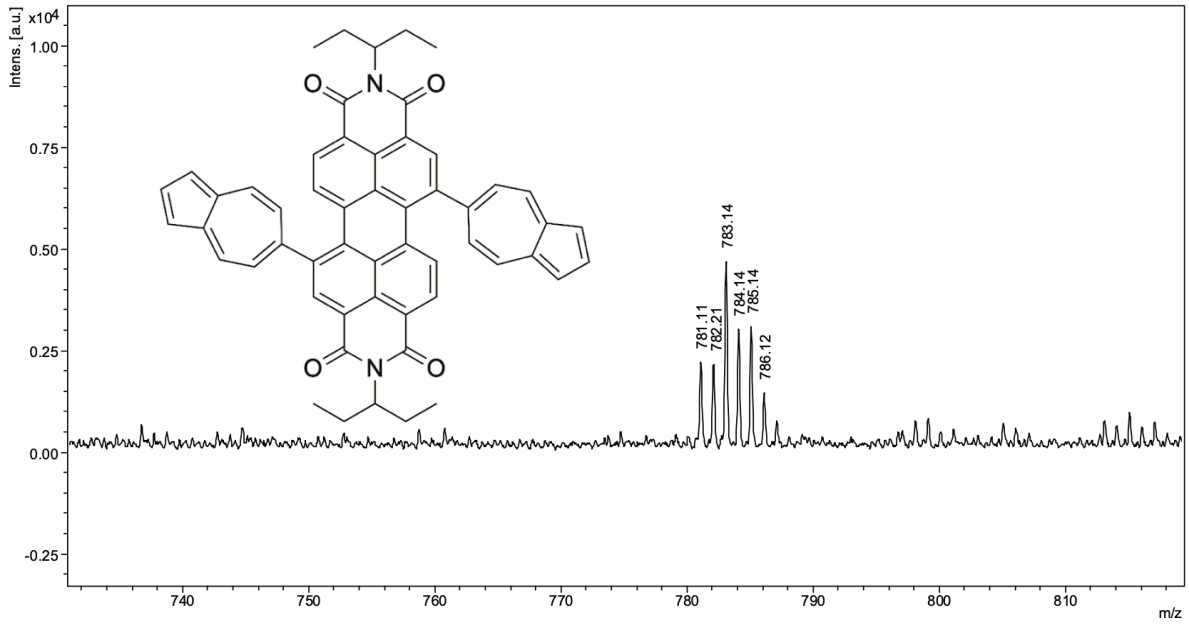

A 2. 30 MALDI-TOF-MS of compound **14**.

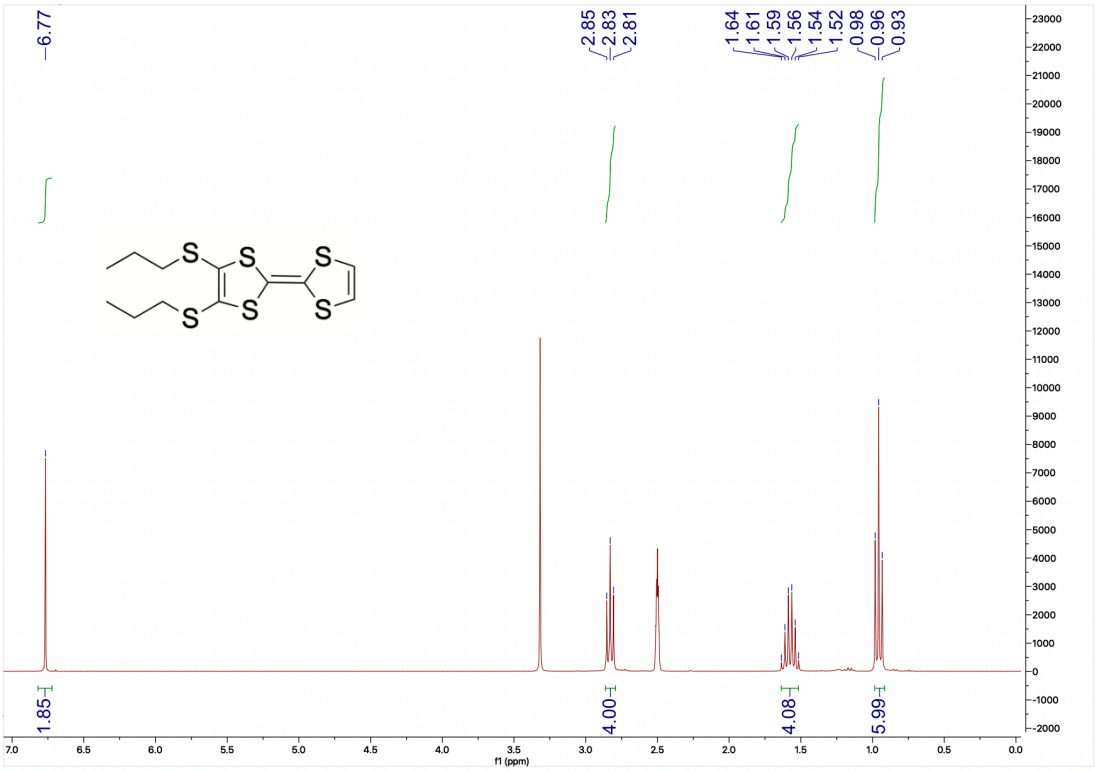

A 2. 31 ^{1}H NMR of compound **15** in DMSO-d_6.

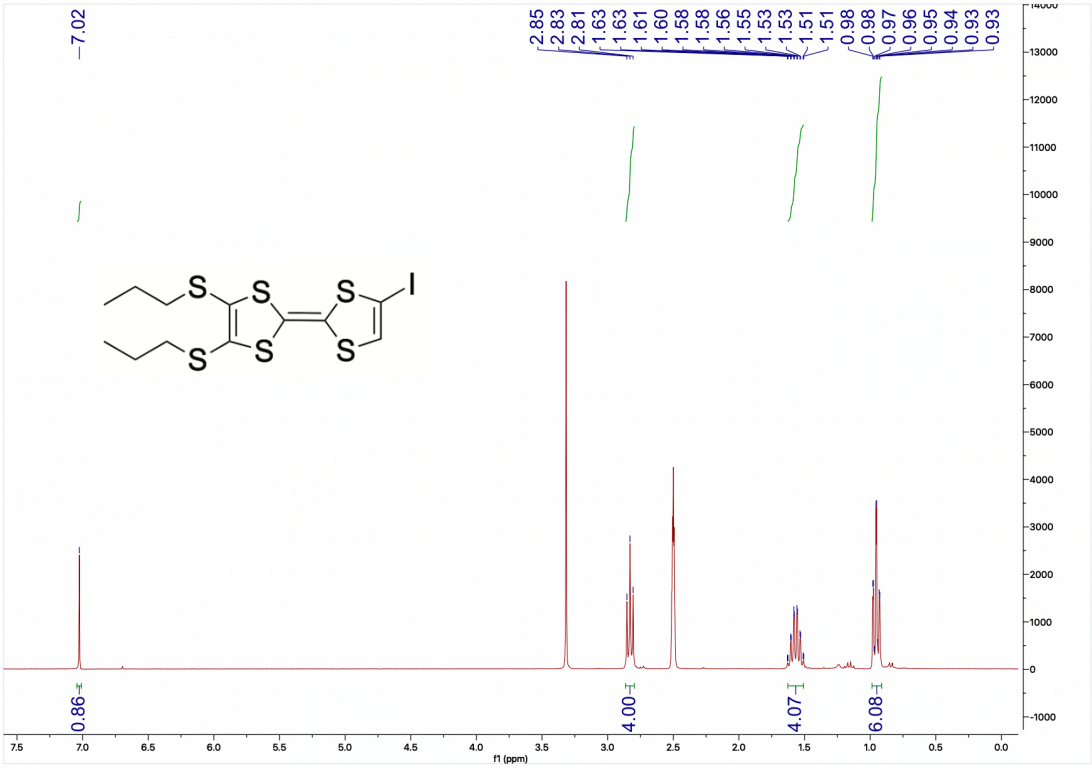

A 2. 32 ^{1}H NMR of compound **16** in DMSO-d_6.

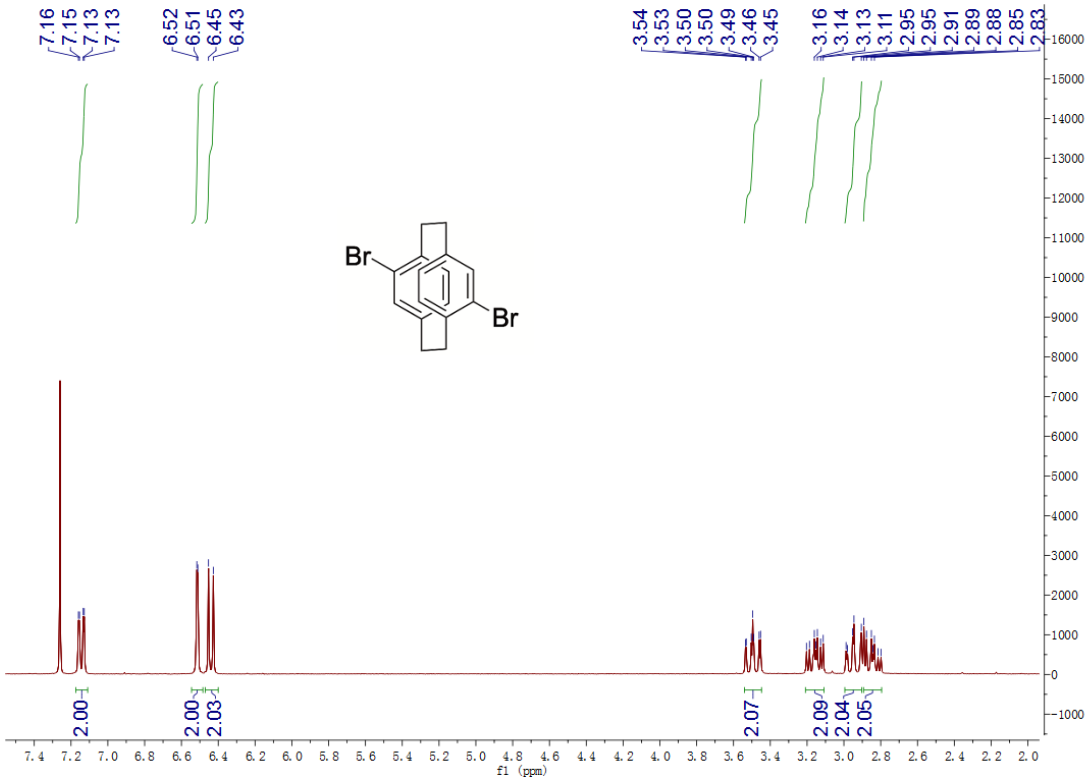

A 2. 33 ^{1}H-NMR of compound **18** in $CDCl_3$.

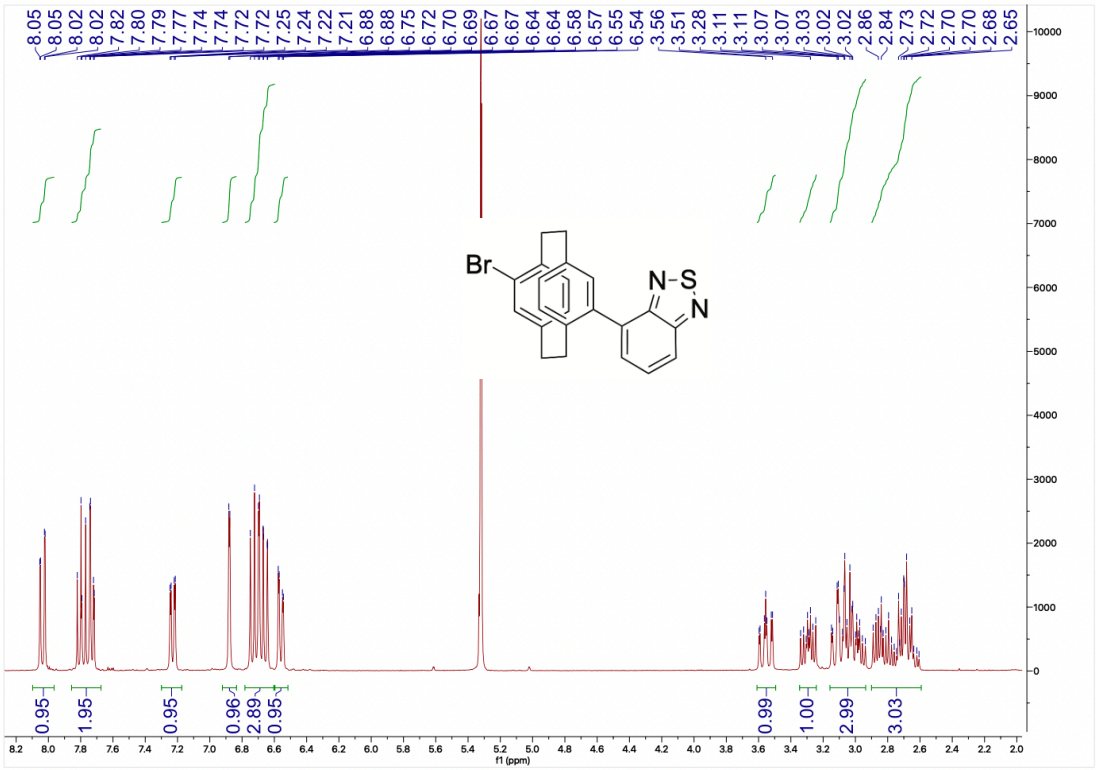

A 2. 34 ^{1}H NMR of compound **19** in CD_2Cl_2.

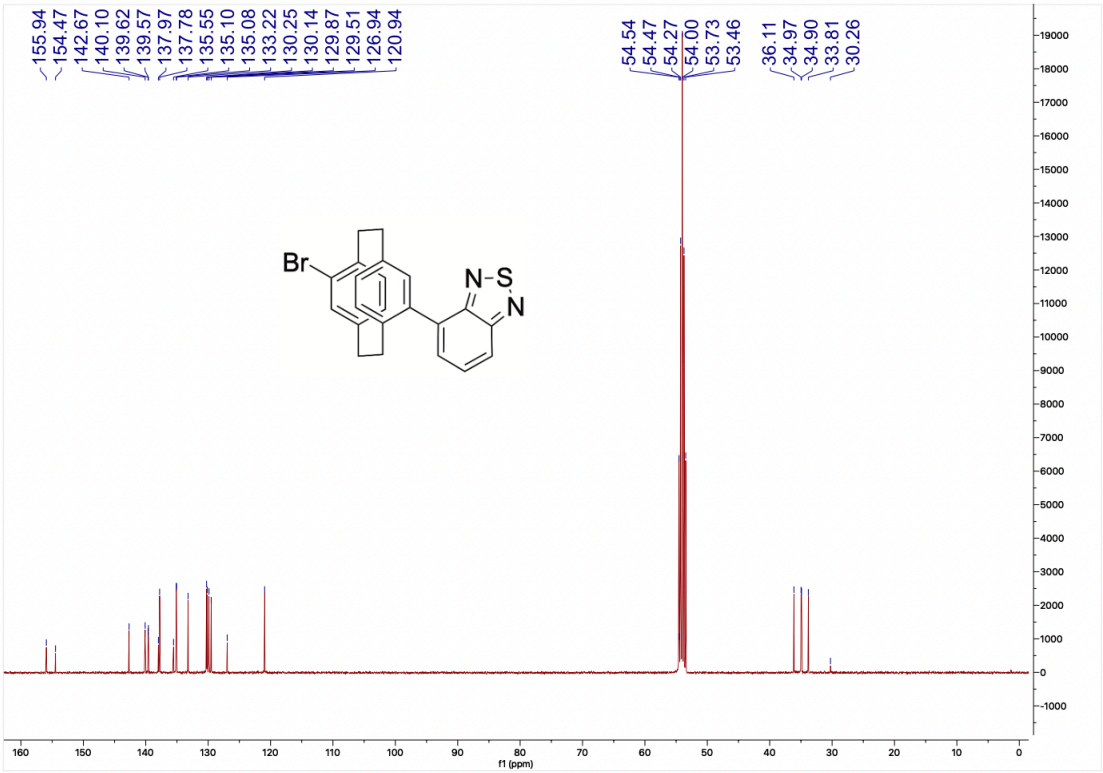

A 2. 35 ^{13}C of compound **19** in CD_2Cl_2.

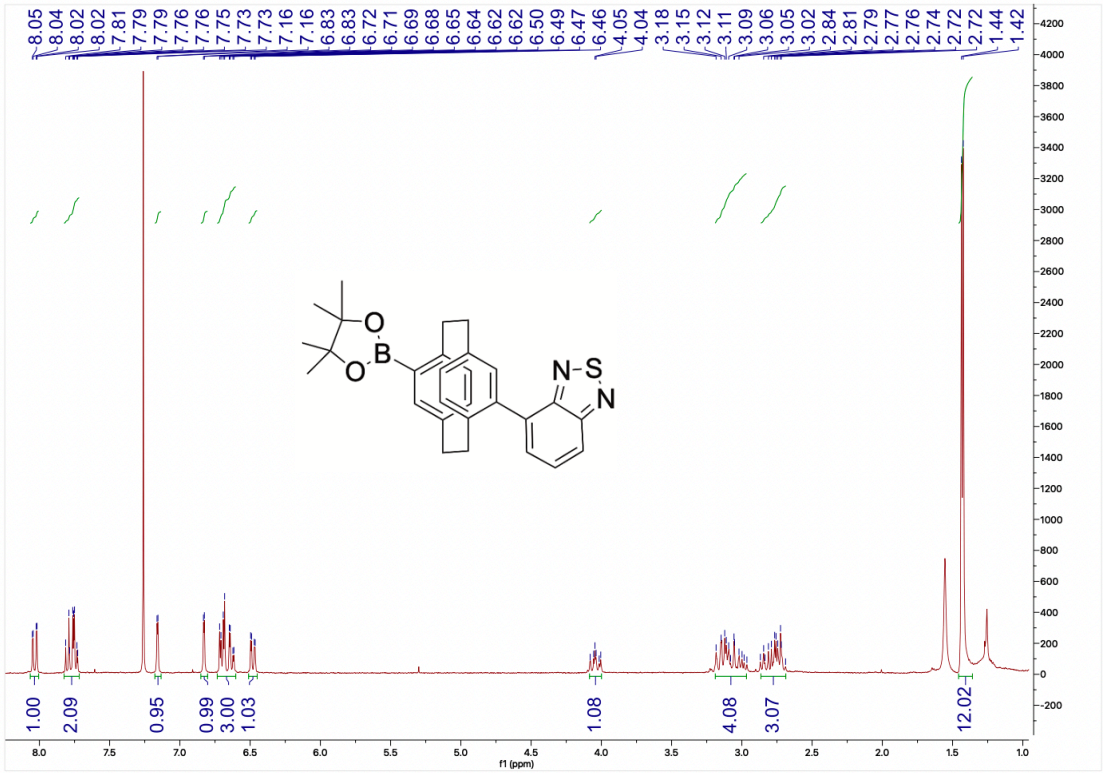

A 2. 36 ^{1}H NMR of compound **20** in $CDCl_3$.

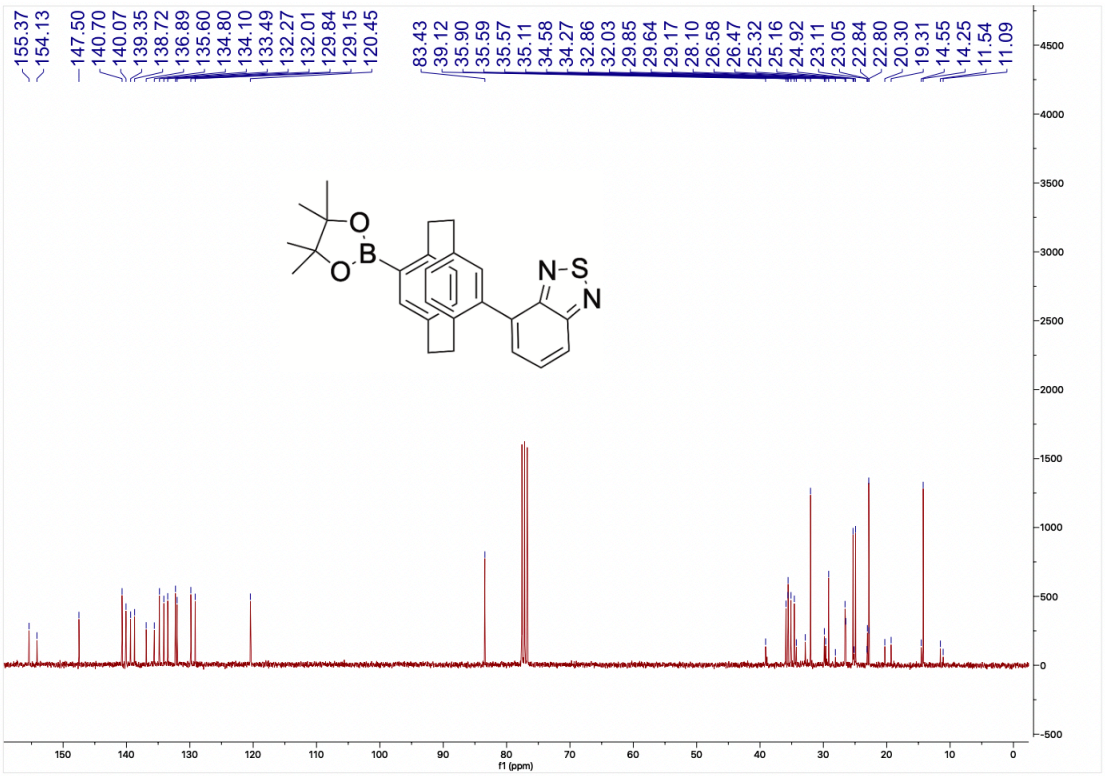

A 2. 37 ^{13}C of compound **20** in $CDCl_3$.

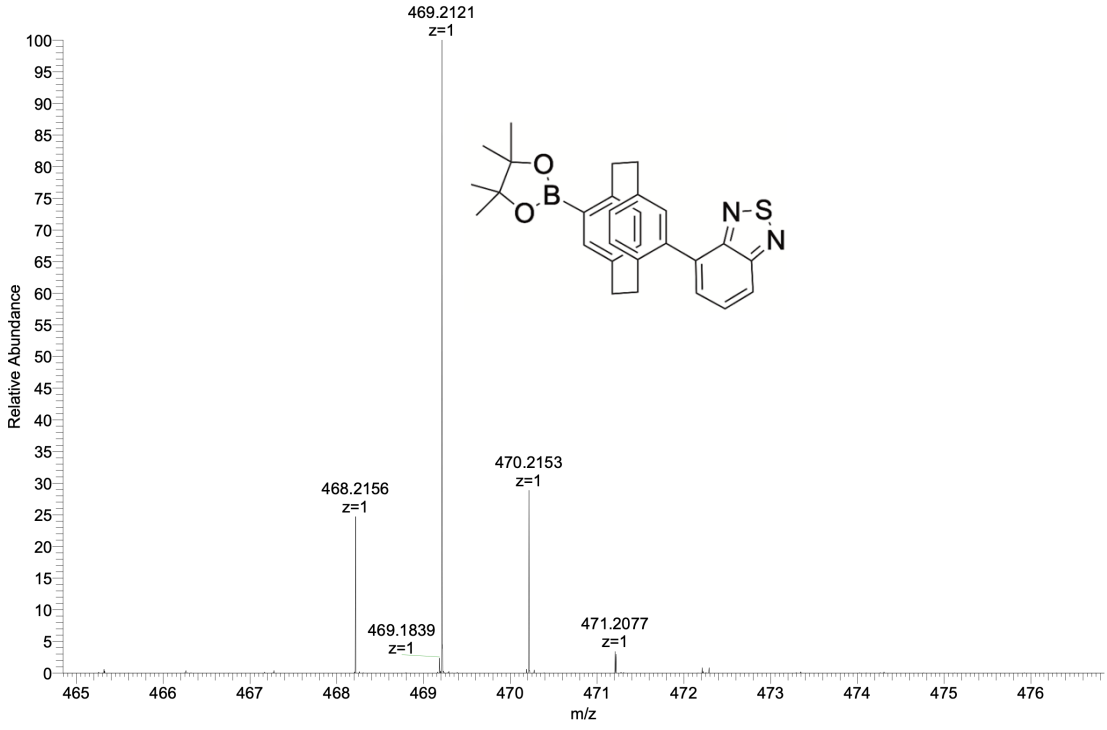

A 2. 38 HR-MS of compound **20**.

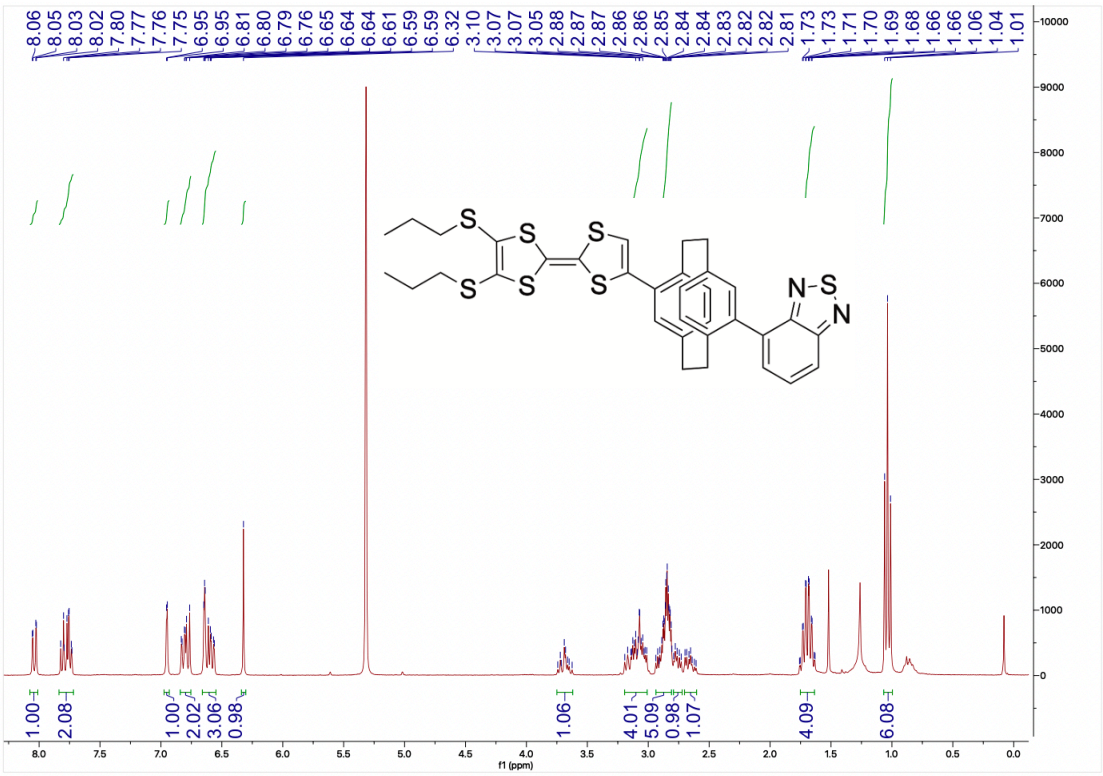

A 2. 39 ^{1}H NMR of compound **21** in CD_2Cl_2.

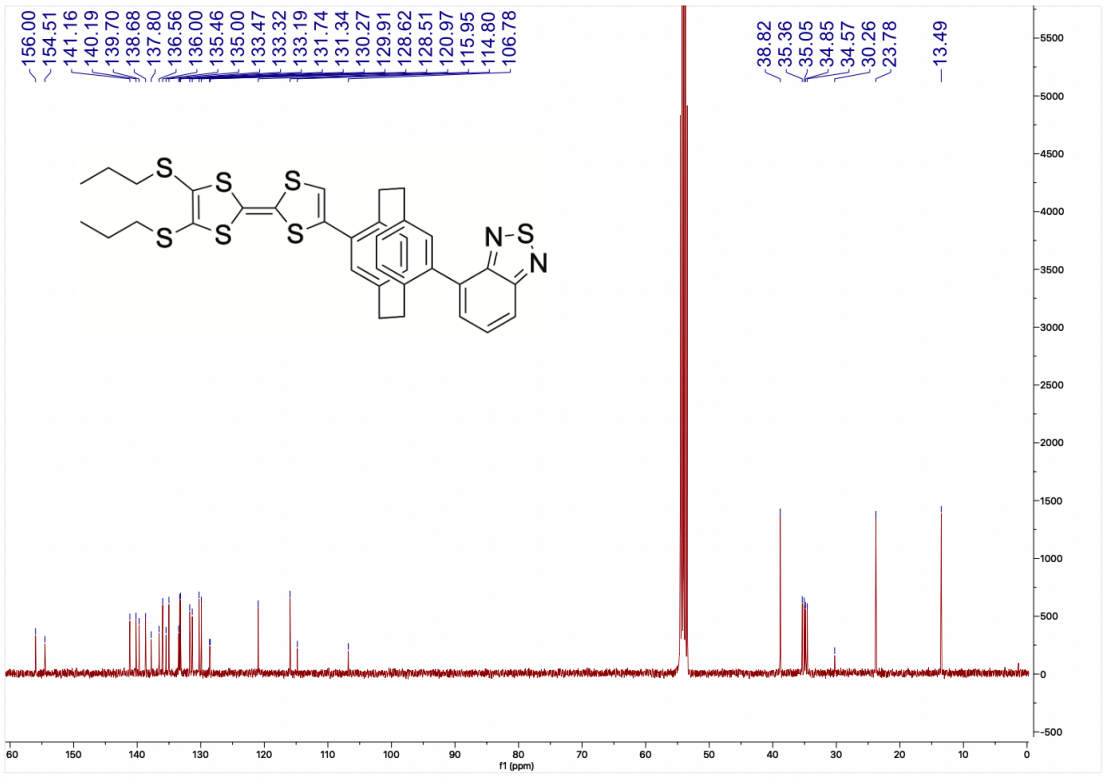

A 2. 40 ^{13}C of compound **21** in CD_2Cl_2.

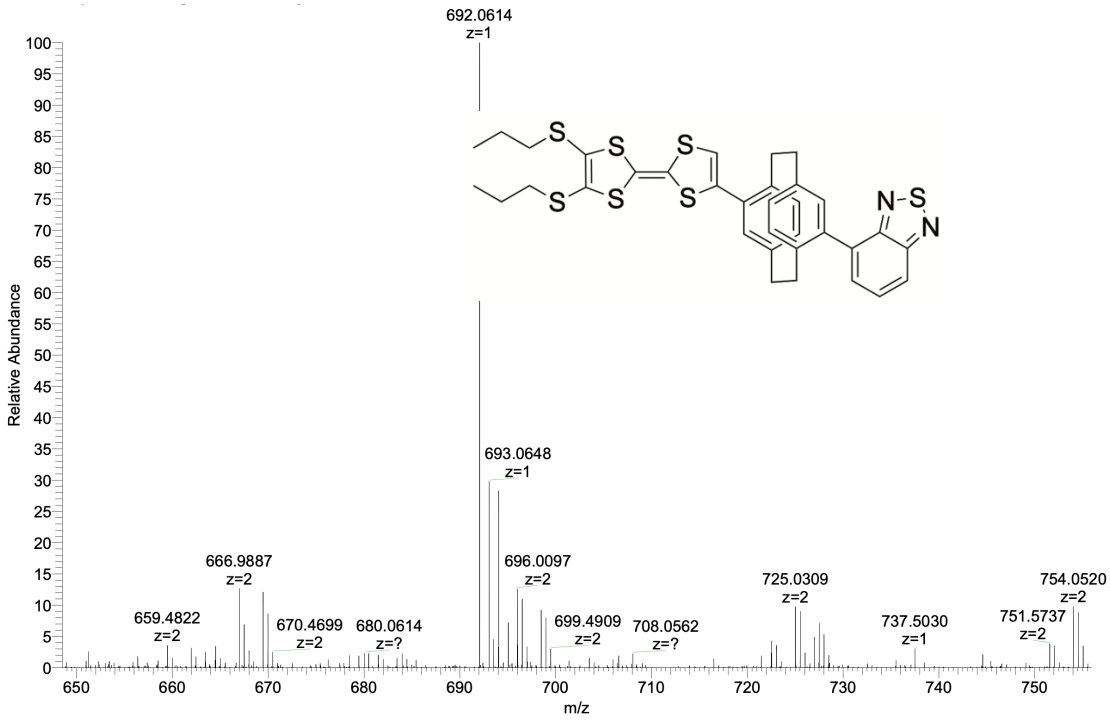

A 2. 41 HR-MS of compound **21**.

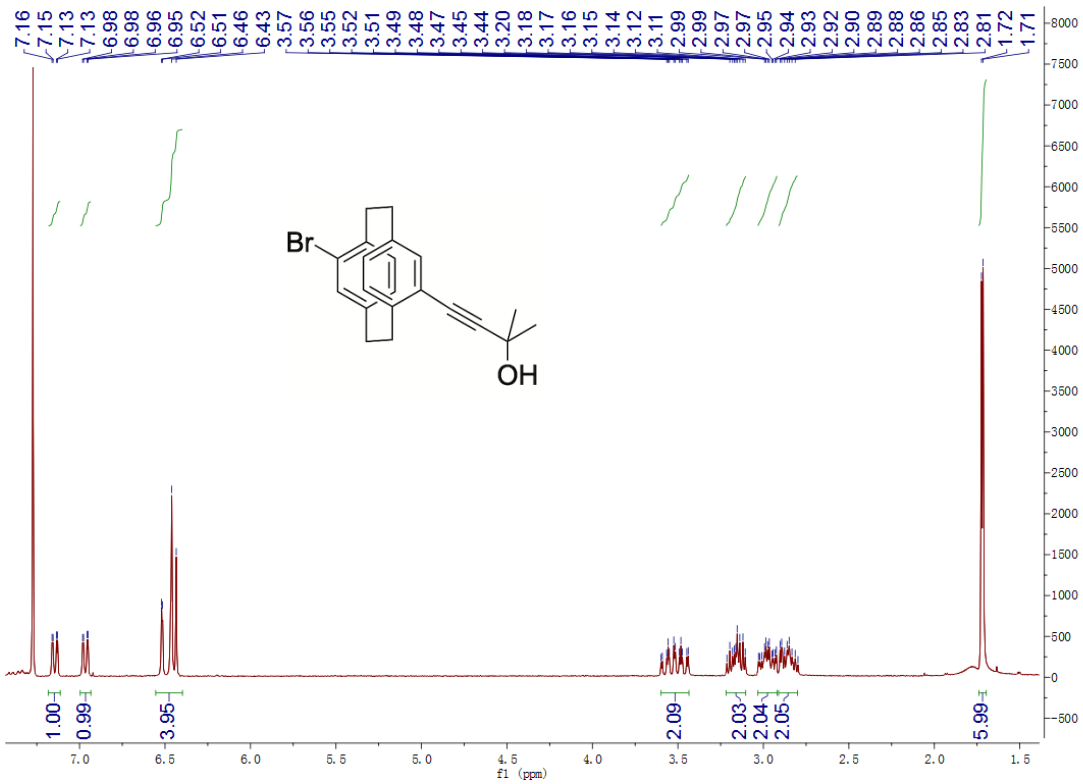

A 2. 42 ^{1}H NMR of compound **22** in $CDCl_3$.

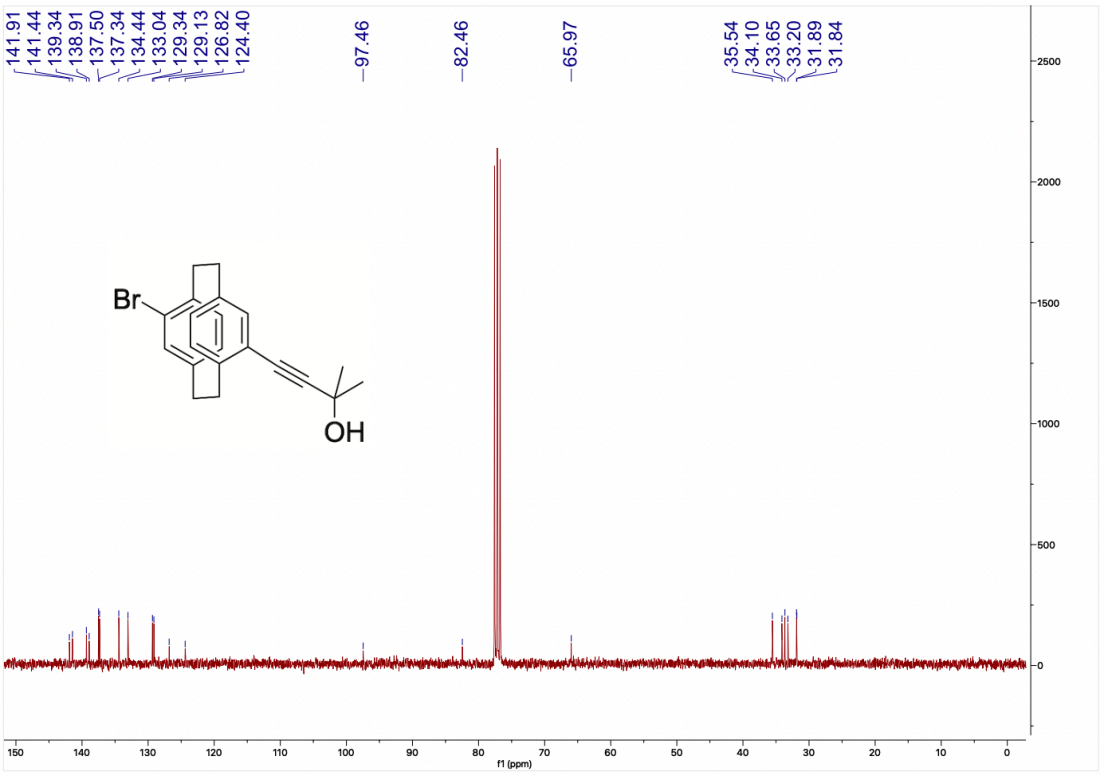

A 2. 43 ^{13}C of compound **22** in $CDCl_3$.

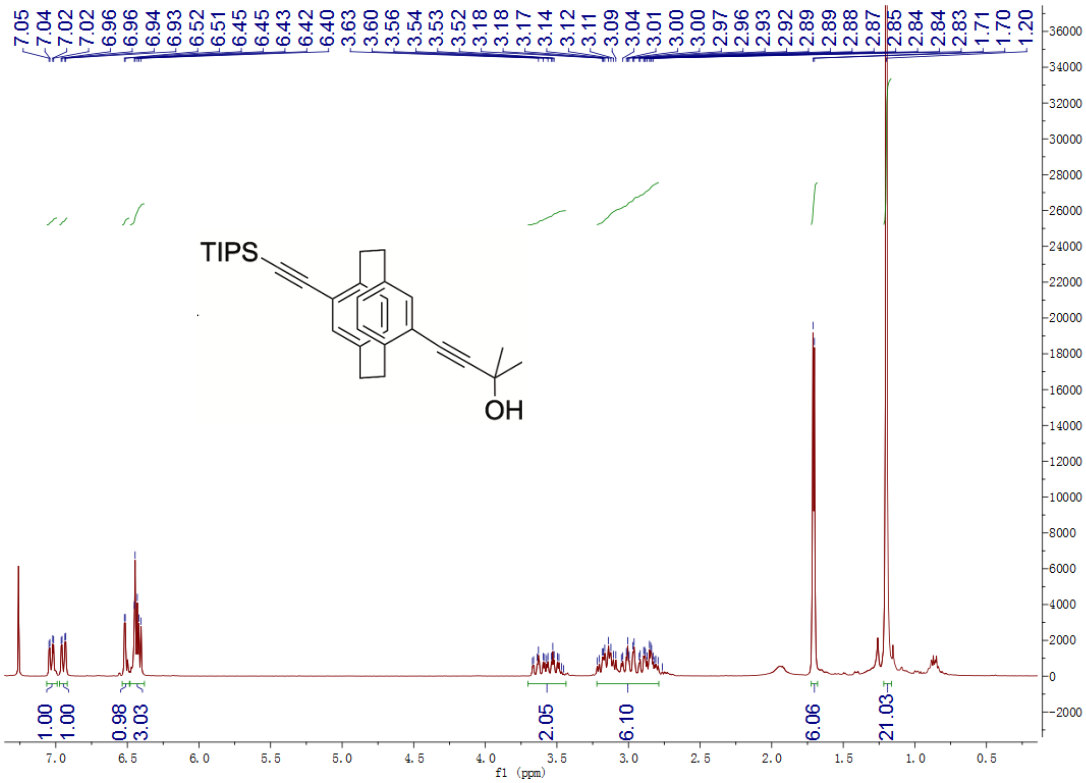

A 2. 44 ^{1}H NMR of compound **23** in $CDCl_3$.

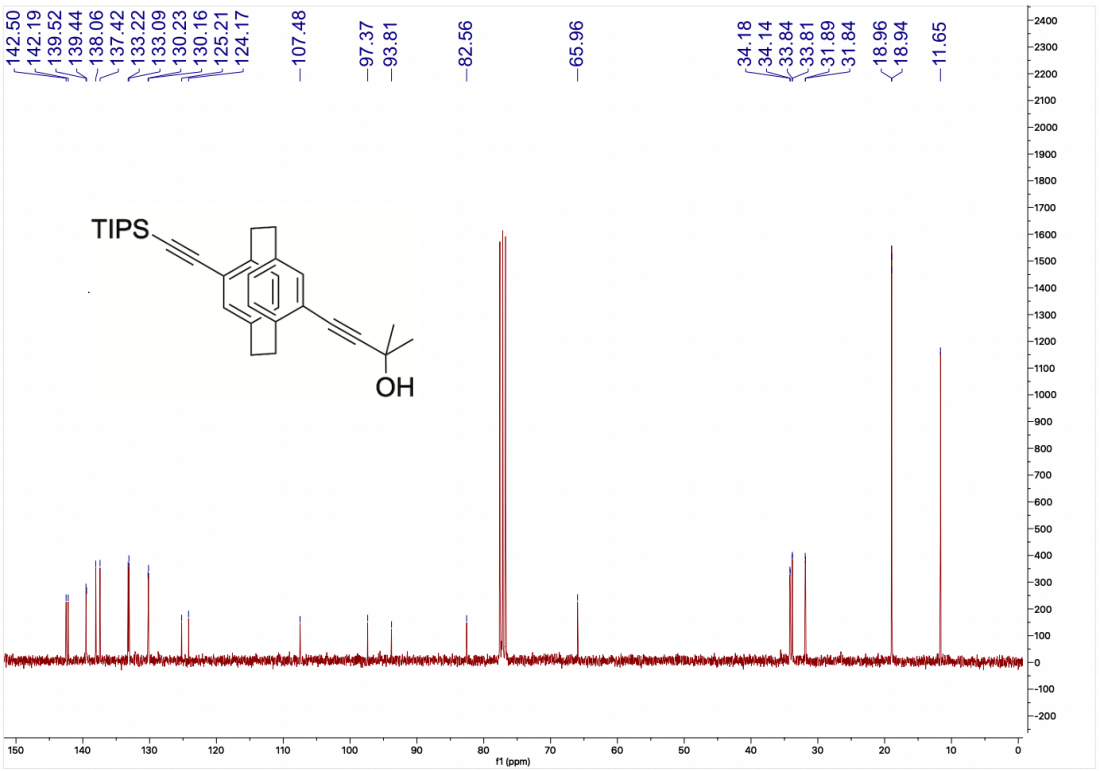

A 2. 45 ^{13}C of compound **23** azulene in $CDCl_3$.

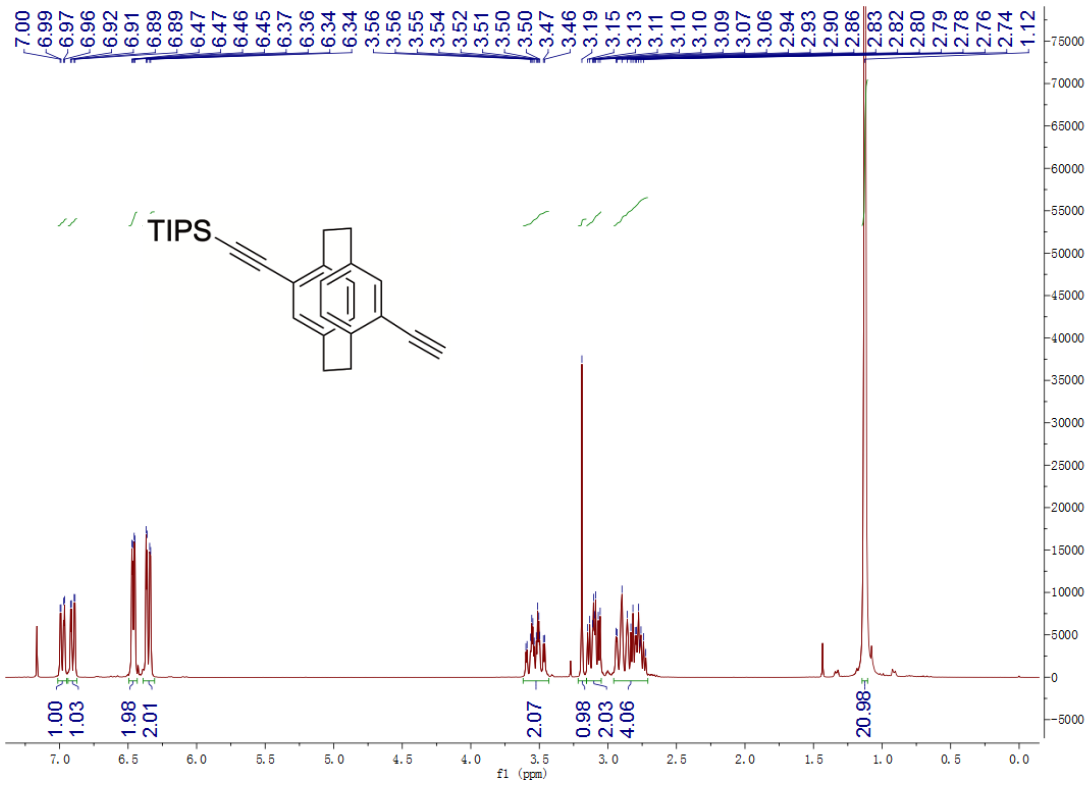

A 2. 46 ^{1}H NMR of compound **24** in $CDCl_3$.

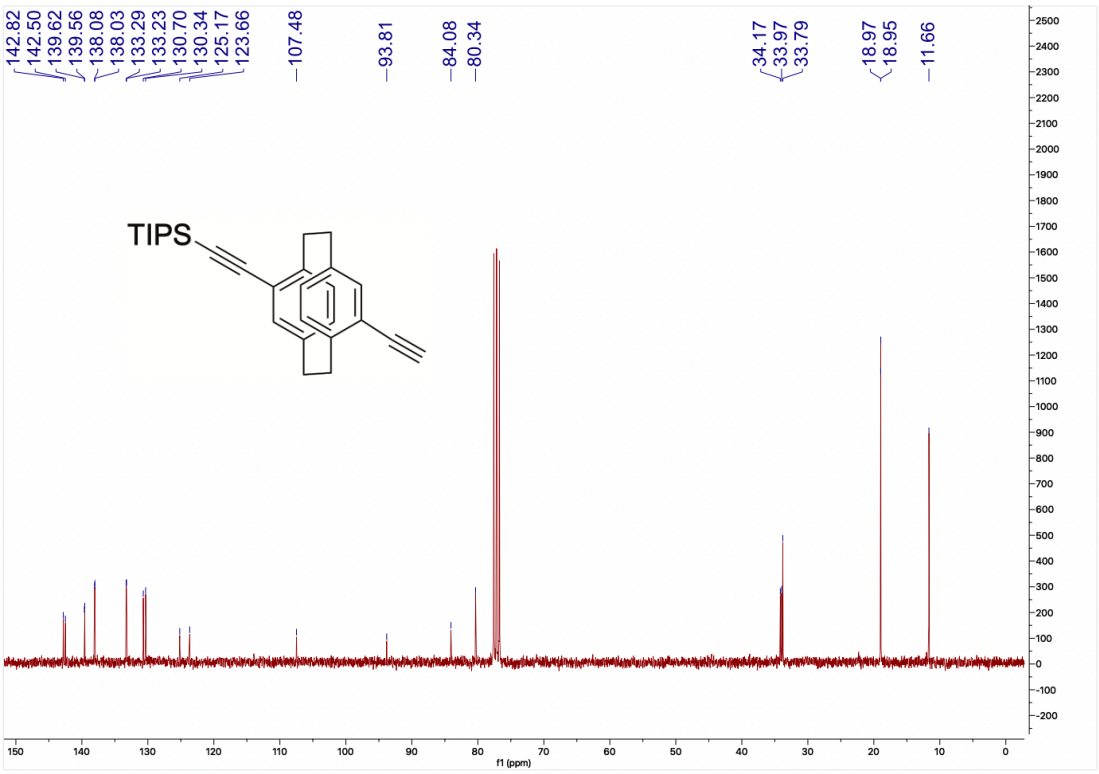

A 2. 47 ^{13}C of compound **24** in $CDCl_3$.

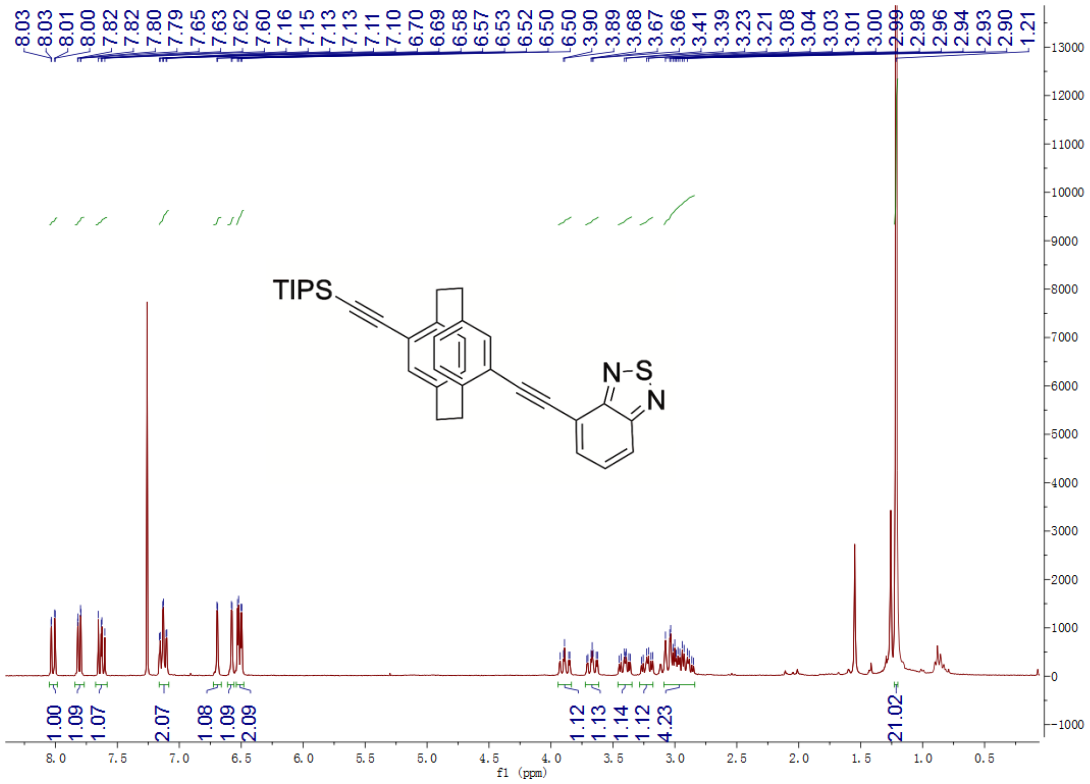

A 2. 48 ^{1}H NMR of compound **25** in $CDCl_3$.

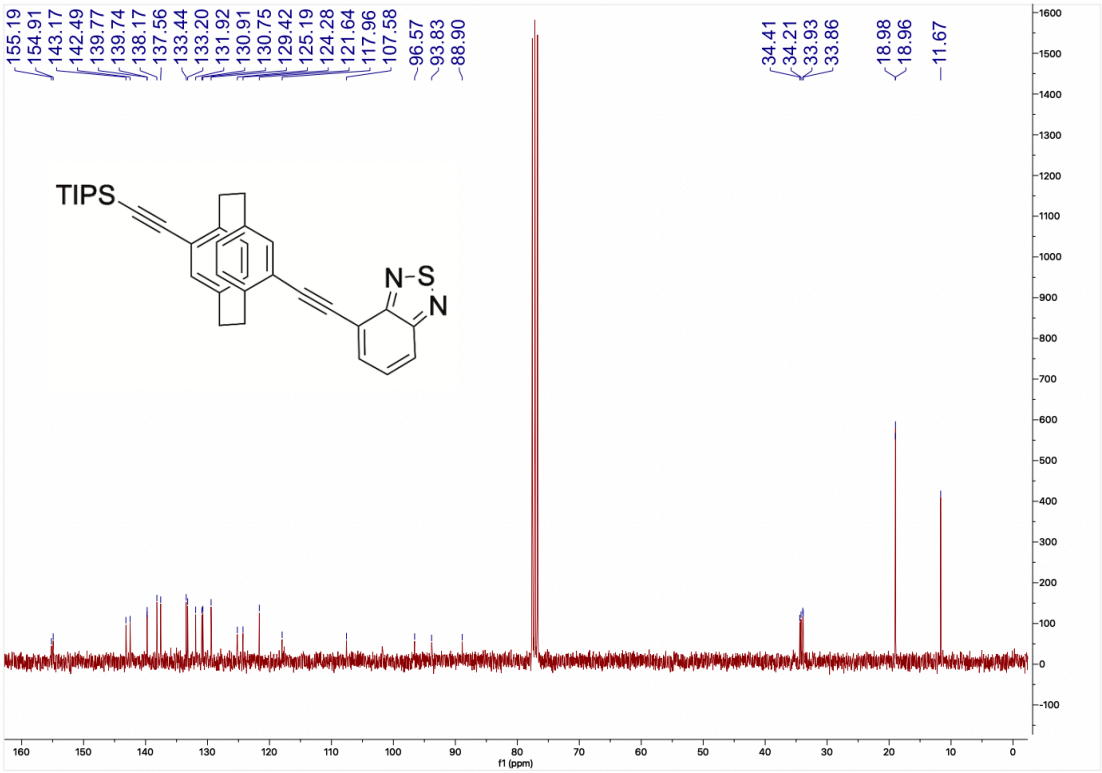

A 2. 49 ^{13}C of compound **25** in $CDCl_3$.

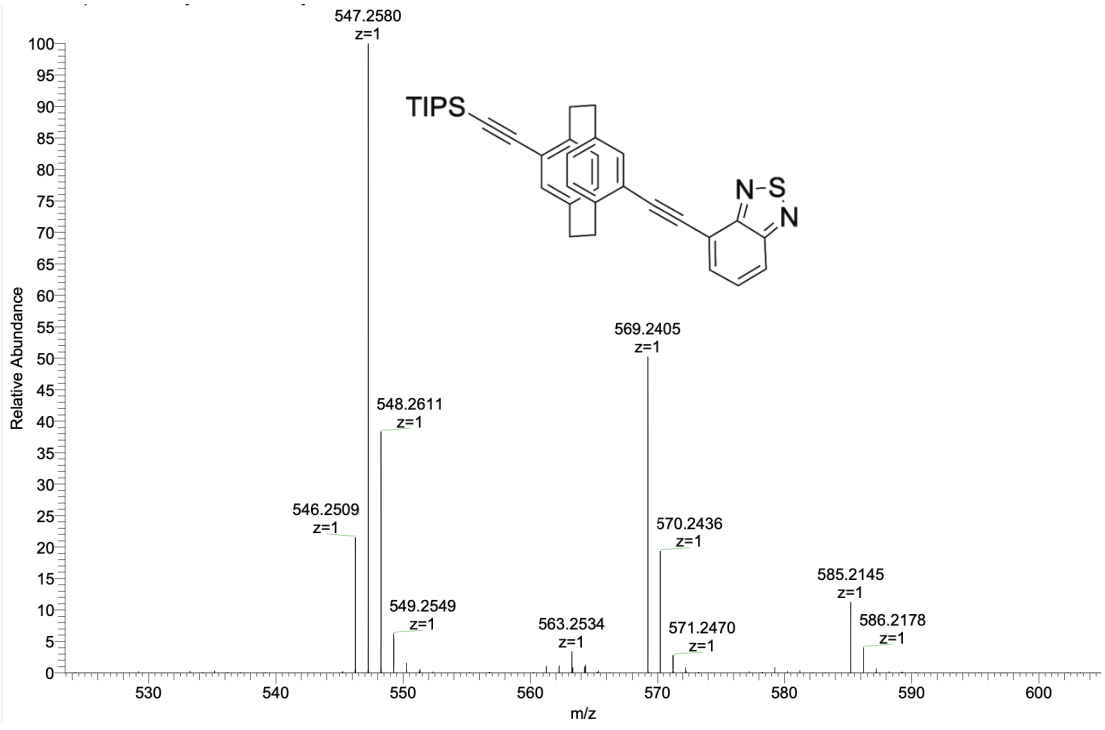

A 2. 50 HR-MS of compound **25**.

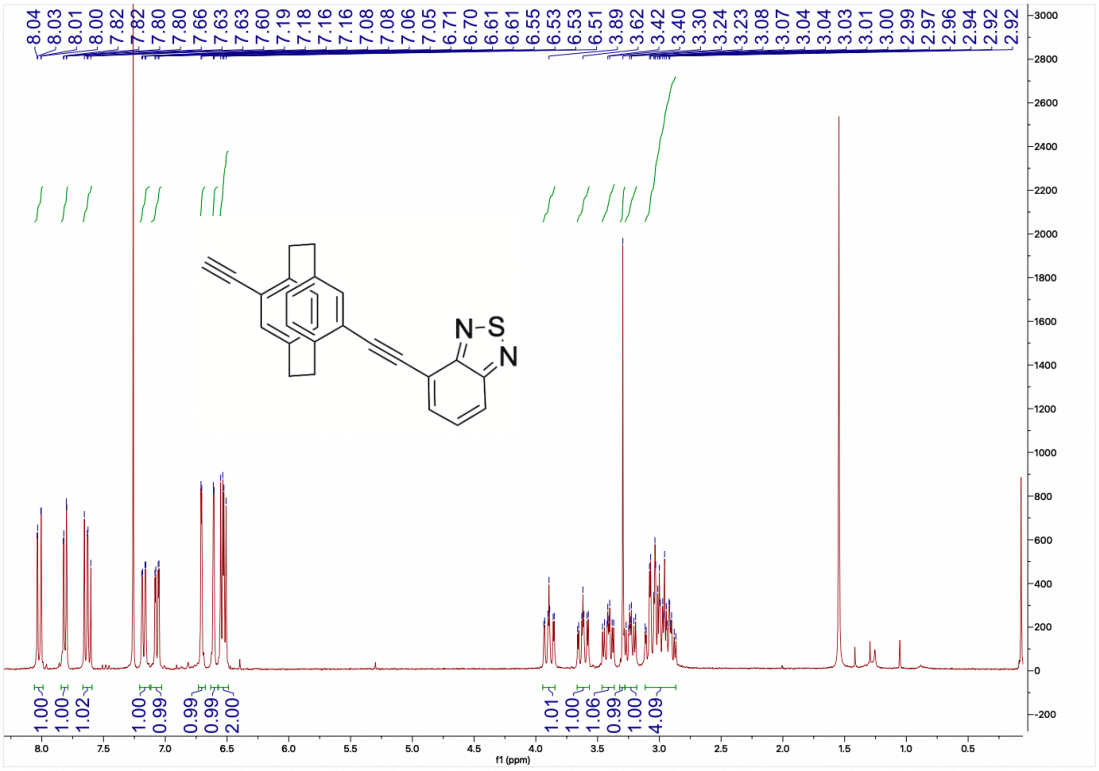

A 2. 51 ^{1}H NMR of compound **26** in $CDCl_3$.

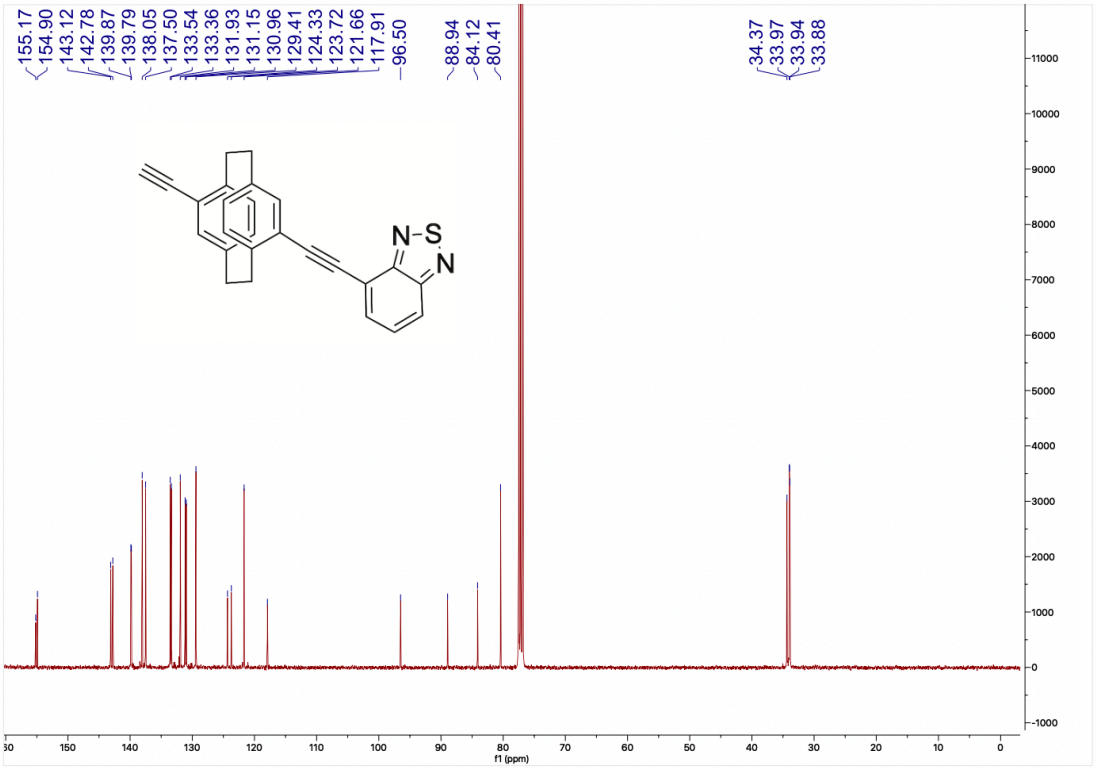

A 2. 52 ^{13}C of compound **26** in $CDCl_3$.

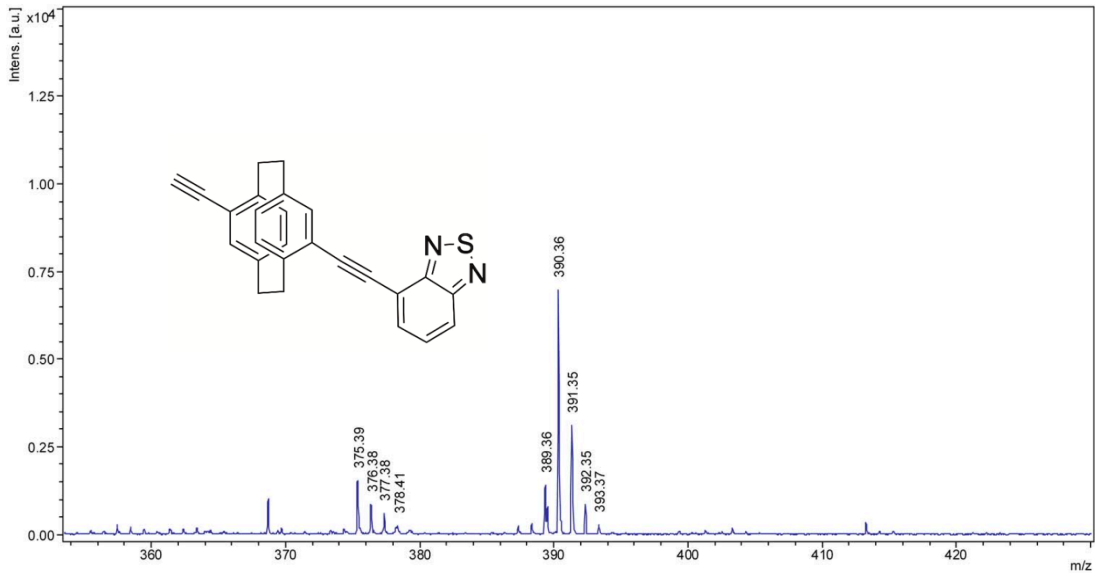

A 2. 53 MALDI-TOF-MS of compound **26**.

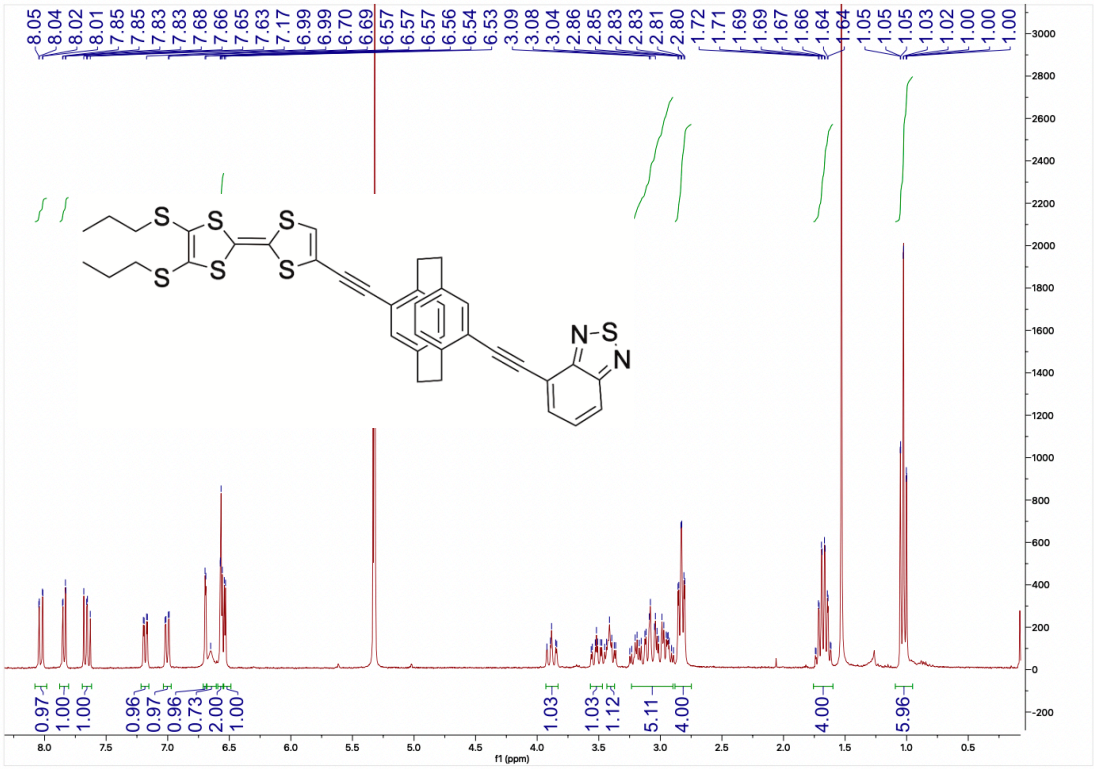

A 2. 54 ^{1}H NMR of compound **27** in CD_2Cl_2.

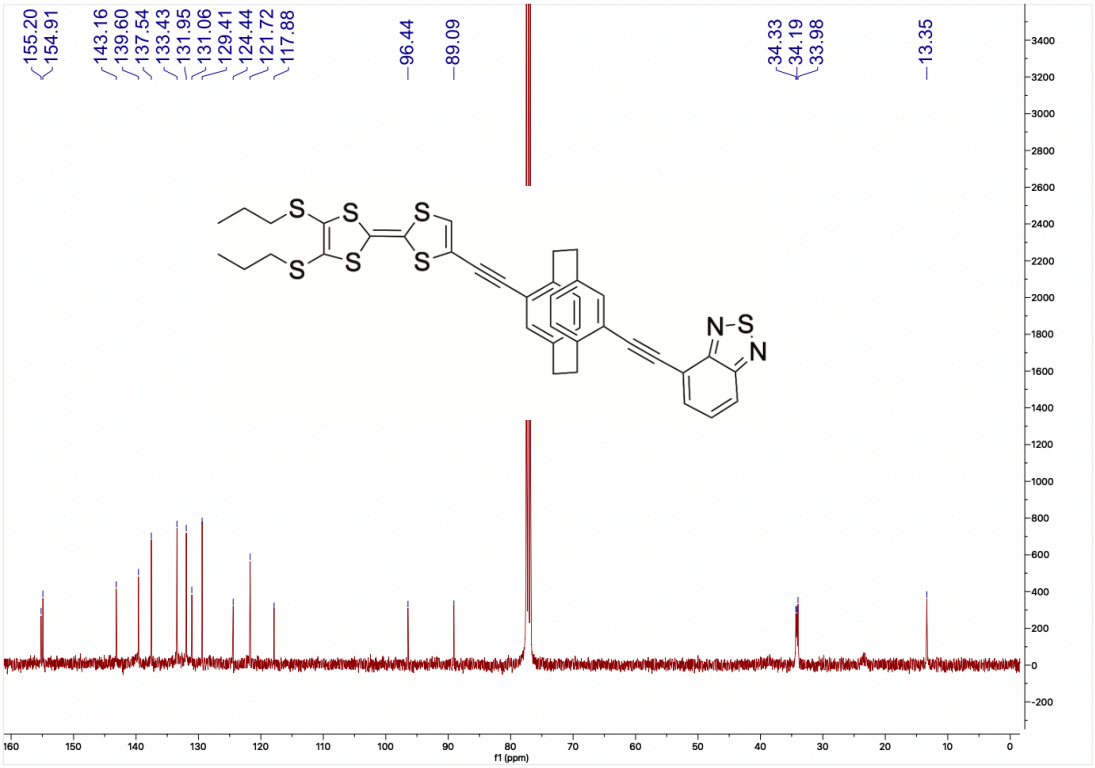

A 2. 55 ^{13}C of compound **27** in $CDCl_3$.

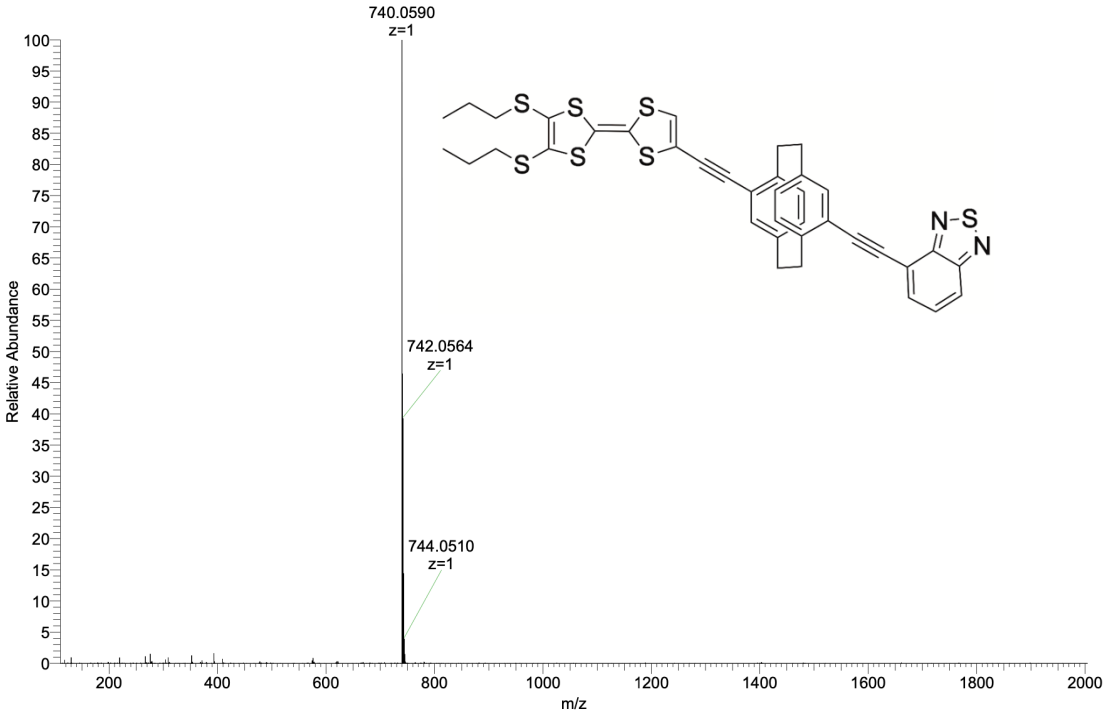

A 2. 56 HR-MS of compound **27**.

Declaration of consent

on the basis of Article 18 of the PromR Phil.-nat. 19

Name/First Name: Zhou Ping

Registration Number: 18-125-286

Study program: Chemistry and Molecular Sciences

Bachelor ☐ Master ☐ Dissertation ☑

Title of the thesis: Investigation on Intramolecular Charge Transfer in π-Conjugated Donor and Acceptor Ensembles

Supervisor: PD Dr. Shi-Xia Liu
Prof. Dr. Robert Häner

I declare herewith that this thesis is my own work and that I have not used any sources other than those stated. I have indicated the adoption of quotations as well as thoughts taken from other authors as such in the thesis. I am aware that the Senate pursuant to Article 36 paragraph 1 litera r of the University Act of September 5th, 1996 and Article 69 of the University Statute of June 7th, 2011 is authorized to revoke the doctoral degree awarded on the basis of this thesis.
For the purposes of evaluation and verification of compliance with the declaration of originality and the regulations governing plagiarism, I hereby grant the University of Bern the right to process my personal data and to perform the acts of use this requires, in particular, to reproduce the written thesis and to store it permanently in a database, and to use said database, or to make said database available, to enable comparison with theses submitted by others.

Bern 30.06.2022

Place/Date

ping zhou

Signature 周萍

Curriculum Vitae

Ping Zhou

Personal Information

Date and place of birth	June 8, 1992, Anhui Province, China
Address	Frohbergweg 4, CH-3012 Bern, Switzerland
Phone	+41764539088
E-mail	pingzhou0608@outlook.com

Education

10/2018-present	PhD student, the group of Prof. Robert Häner, Department of Chemistry, Biochemistry and Pharmaceutical Sciences, Bern University, Switzerland
09/2015-07/2018	M.S. in Inorganic Chemistry and Biochemistry, College of Life and Environment Sciences, Shanghai Normal University, China.
09/2011-07/2015	B.S. in Materials Chemistry, School of Chemistry and Materials Engineering, Fuyang Normal University, China.

Publications

1. J. Liu, R. Pawlak, X. Wang, Philipp D'Astolfo, C. Drechsel, **P. Zhou**, S. Decurtins, U. Aschauer, S.-X. Liu, W. Wulfhekel, E. Meyer. Proximity-Induced Superconductivity in Atomically Precise Nanographene. arXiv:2202.00460 [*cond-mat.supr-con*], submitted on 1 Feb 2022.

2. **P. Zhou**, U. Aschauer, S. Decurtins, T. Feurer, R. Häner and S.-X. Liu. Effect of *tert*-Butyl Groups on Electronic Communication Between Redox Units in Tetrathiafulvalene-Tetraazapyrene Triads. *Chem. Commun.,* **2021**, *57*, 12972 -12975.

3. **P. Zhou**, U. Aschauer, S. Decurtins, T. Feurer, R. Häner and S.-X. Liu. Chemical Control of Photoinduced Charge-Transfer Direction in a Tetrathiafulvalene-Fused Dipyrrolylquinoxaline Difluoroborate Dyad. *Chem. Commun.,* **2020**, *56*, 13421-13424.

4. M. Volland, **P. Zhou**, L. Wibmer, R. Häner, S. Decurtins, S.-X. Liu and D. Guldi. Nanographene Favors Electronic Interactions with an Electron Acceptor Rather Than an Electron Donor in a Planar Fused Push–Pull Conjugate. *Nanoscale*, **2019**, *11*, 1437-1441.

5. **P. Zhou**, L. Pan, G. Deng, Z. Zhou, H. Zhao, C. Peng and S. Yang. Fe@Fe_3Ge_2 Nanoparticles for MR Imaging-Guided NIR-Driven Photodynamic Therapy in Vivo. *J. Mater. Chem. B*, **2019**, *7*, 5661-5668.

6. G. Deng, **P. Zhou**, Z. Zhou, X. Wang, H. Yang, and S. Yang. Amplified Photoacoustic Imaging of Tumor through In Situ Cycloaddition. *Part. Part. Syst. Charact.*, **2019**, *36*, 1900042-1900048.

7. **P. Zhou**, H. Zhao, Q. Wang, Z. Zhou, J. Wang, G. Deng, X. Wang, Q. Liu, H. Yang, S. Yang. Photoacoustic-Enabled Self-Guidance in Magnetic-Hyperthermia Fe@Fe_3O_4 Nanoparticles for Theranostics In Vivo. *Adv. Healthcare Mater.*, **2018**, *7*, 1701201- 1701209.

8. H. Zhao, **P. Zhou**, K. Huang, G. Deng, Z. Zhou, J. Wang, M. Wang, Y. Zhang, H. Yang, S. Yang. Amplifying Apoptosis Homing Nanoplatform for Tumor Theranostics. *Adv. Healthcare Mater.*, **2018**, *7*, 1800296-1800305. (**Equal contribution**)

9. H. Zhao, M. Wang, **P. Zhou**, Q. Wang, Z. Zhou, D. Wang, H. Yang, and S. Yang. RGD-Conjugated Titanium Dioxide Nanoparticles: Targeted Near-Infrared Photothermal Therapy for a_vb_3 Integrin Overexpressed Cancer Cells. *J. Mater. Sci.*, **2017**, *52*, 13356–13364.

10. J. Wang, H. Zhao, Z. Zhou, **P. Zhou**, Y. Yan, M. Wang, H. Yang, Y. Zhang, and S. Yang. MR/SPECT Imaging Guided Photothermal Therapy of Tumor-Targeting Fe@Fe_3O_4Nanoparticles in Vivo with Low Mononuclear Phagocyte Uptake. *ACS Appl. Mater. Interfaces.*, **2016**, 8, *31*, 19872–19882.